NOTICE

The quality of this microform is heavily dependent upon the quality of the original thesis submitted for microfilming. Every effort has been made to ensure the highest quality of reproduction possible.

If pages are missing, contact the university which granted the degree.

Some pages may have indistinct print especially if the original pages were typed with a poor typewriter ribbon or if the university sent us an inferior photocopy.

Previously copyrighted materials (journal articles, published tests, etc.) are not filmed.

Reproduction in full or in part of this microform is governed by the Canadian Copyright Act, R.S.C. 1970, c. C-30.

AVIS

La qualité de cette microforme dépend grandement de la qualité de la thèse soumise au microfilmage. Nous avons tout fait pour assurer une qualité supérieure de reproduction.

S'il manque des pages, veuillez communiquer avec l'université qui a conféré le grade.

La qualité d'impression de certaines pages peut laisser à désirer, surtout si les pages originales ont été dactylographiées à l'aide d'un ruban usé ou si l'université nous a fait parvenir une photocopie de qualité inférieure.

Les documents qui font déjà l'objet d'un droit d'auteur (articles de revue, tests publiés, etc.) ne sont pas microfilmés.

La reproduction, même partielle, de cette microforme est soumise à la Loi canadienne sur le droit d'auteur, SRC 1970, c. C-30.

Canada

COMPUTER-AIDED ANALYSIS AND DESIGN FOR EXTRUSION DIES

by

Fock Lee Heng

B.A.Sc. Chem. Eng.

A Thesis

Submitted to the School of Graduate Studies

in Partial Fulfilment of the Requirements for

the Degree of Master of Applied Science

in

Chemical Engineering

University of Ottawa

September, 1987

ISBN 0-315-46778-9

UNIVERSITÉ D'OTTAWA
UNIVERSITY OF OTTAWA

Abstract

Various polymer flows through extrusion dies have been studied by using the Lubrication Approximation Theory (LAT) and Finite Element Method (FEM). These include flow through an orifice, flow through annular dies, wire coating and wire-coating coextrusion. Free surfaces and interfaces are present. Newtonian and shear-thinning inelastic viscosity models have been used under isothermal and nonisothermal conditions. Thermal boundary conditions ranging from isothermal to adiabatic have been investigated. A Streamline-Upwind/Petrov-Galerkin scheme for quadrilateral elements has been incorporated into the FEM to stabilize the solution for highly convective nonisothermal flows. Free surfaces and interfaces are determined through a relaxation iterative technique that allows no cross flow to the surface. A double-node technique has been implemented in the FEM for multi-layered flows occurring in coextrusion.

Flows of Newtonian fluids through capillary dies of variable length showed that the swell is reduced from 13% for long dies to 8% for an orifice (zero length), thus exhibiting reverse trends from Non-Newtonian viscoelastic fluids. The flow through converging and diverging annular dies

showed the influence that die design has on the thickness and diameter swell of parisons (plastic tubes).

Nonisothermal studies showed that the full energy equation has to be considered in polymer melt flows, even in the case of straight channels. This is because radial temperature gradients exist that cause radial flow that cannot be safely neglected. Comparison with other studies based on such simplifications showed that the errors involved in omitting radial gradients and components can be appreciable.

Wire-coating studies revealed that very good agreement with experiments for high-speed operations is achieved when correct viscosity data are used and thermal-balance boundary conditions are imposed. The analysis showed why an empirical industrial die design employed by Du Pont Co. works. The criteria required include a streamlined flow with no recirculation present, as well as the development of smooth die stresses with no "hump" near the impact region. These observations have been used in constructing new designs for wire-coating coextrusion of two resins. In addition a rather flat, horizontal interface should be achieved within the die for better operation.

A new die design for wire-coating coextrusion of High-Density Poly-

Ethylene (HDPE) and Poly-Styrene (PS) has been successfully deduced, as evidenced by the corresponding analysis. Such design met all criteria for a variety of operating conditions pertaining to wire speeds, melt temperatures and coating thicknesses, typical of industrial operations.

Acknowledgements

In presenting this thesis, I wish to express my sincere appreciation to Dr. E. Mitsoulis, my supervisor, for his constant guidance, inspiration and encouragement throughout the course of this study.

Furthermore, I would like to thank the Department of Chemical Engineering, University of Ottawa and the National Science and Engineering Research Council of Canada for the financial support in the form of assistanceship for this project.

Finally, I owe my gratitude to my parents, family and fiancée in Malaysia for their constant encouragement, which was indispensable in completing this study.

Contents

List of Figures

List of Tables

Nomenclature

a_i	constants in viscosity expressions, dimensionless
A	area, m^2
b	constant in viscosity expression, dimensionless
B	swell ratio, dimensionless
c	constant in viscosity expression, dimensionless
c_o	integration constant
C_p	heat capacity, $J/kg\ K$
d	extrudate diameter, m
	diameter, m
D	capillary/orifice diameter, m
e	unit vector, dimensionless
E	activation energy, $J/kgmol$
f	constant in viscosity expression, dimensionless
F	tension, N
$\{F\}$	load vector
g	acceleration due to gravity, m/s^2

GS	gum space, m
h	gap width, m
	thickness, m
	length, m
h_T	heat transfer coefficient, $J/m^2\ s\ ^\circ C$
H	characteristic length in r-direction, m
I_2	second invariant of the rate-of-strain tensor, s^{-2}
$[J]$	Jacobian matrix
k	thermal conductivity, $J/m\ s\ K$
$[K]$	global stiffness matrix
l	length in z-direction, m
L	length of die in z-direction, m
	capillary/orifice length, m
	area coordinate in an element, dimensionless
L_f	taper length, m
m	consistency index of power-law model, $Pa\ s^n$
M	length in gum space, m
n	power-law index, dimensionless

$\overline{n}$	unit outward normal vector
N	interpolation (shape) function, dimensionless
	length in gum space, m
p	pressure, Pa
$\dot{q}$	heat rate, J/s
q	heat flux, $J/m^2\ s$
Q	volumetric flowrate, m^3/s
Q_d	heat of viscous dissipation, $J/m^3\ s$
r	radius, m
	radial global coordinate, m
R	radius, m
	molar energy constant, $J/kgmol\ K$
s	thickness of the temperature boundary layer, m
t	time, s
$\overline{t}$	unit tangential vector
T	temperature, $°C$ or K
$\overline{T}$	surface traction, Pa
u	velocity in the r-direction, m/s

v	velocity, m/s
V	boundary velocity, m/s
	characteristic velocity, m/s
w	velocity in the z-direction, m/s
W	weighting function, dimensionless
x	gap in gum space, m
$\{X\}$	vector of nodal unknowns
z	axial distance, m
	axial global coordinate, m
	gap in gum space, m

Greek Letters

α	ratio of interface position to outer wall, dimensionless
	taper angle, *deg*
β	temperature shift factor, K^{-1}
	taper angle, *deg*
$\dot{\gamma}$	rate-of-strain, s^{-1}

	shear rate, s^{-1}
$\bar{\dot{\gamma}}$	characteristic shear rate, s^{-1}
Γ	boundary surface area, m^2
ΔP	pressure drop, Pa
η	apparent viscosity, $Pa\ s$
	radial local coordinate, dimensionless
$\bar{\eta}$	characteristic viscosity, $Pa\ s$
θ	azimuthal global coordinate, deg
κ	ratio of inner wall position to outer wall, dimensionless
λ	relaxation factor, dimensionless
	ratio of zero shear stress position to outer wall, dimensionless
μ	Newtonian viscosity, $Pa \cdot s$
ξ	axial local coordinate, dimensionless
ρ	density, kg/m^3
τ	extra stress, Pa
	shear stress, Pa
τ_{rz}	shear stress, Pa
$\bar{\tau}$	characteristic stress, Pa

ϕ	taper angle, *deg*
ψ	stream function, m^3/s
ω	vorticity, s^{-1}

Subscripts

a	ambient
air	air
A	fluid A
b	boundary
B	fluid B
c	coating
d	die
en	entrance
ex	exit
f	free surface
	boundary film
i	i^{th} node

	i^{th} coordinate
	inner
j	j^{th} coordinate
m	melt
max	maximum
n	normal to a surface
new	new
N	Newtonian
opt	optimum
p	power-law
	constant pressure
	extrudate
r	r-direction
res	reservoir
s	surroundings
t	tangential to a surface
	torpedo
T	temperature

w	wire
z	z-direction
η	η-direction
ξ	ξ-direction
τ	constant stress
o	origin/initial/reference/outer/exit
I	fluid I
II	fluid II
∞	infinite distance

Superscripts

-1	inverse of a matrix
(e)	element
i	present iteration
T	transpose of a vector or a matrix
$*$	dimensionless quantity

Overscripts

$\vec{}$	vector
$=$	matrix
$\tilde{}$	local value
$\hat{}$	local value
$\dot{}$	rate

Dimensionless Groups

Bi	Biot Number $= \frac{(\partial T/\partial r)_b H}{T_s - T_b}$
Br	Brinkman Number $= \frac{\bar{\eta} V^2}{k T_o}$
C	Capacitance Parameter $= \frac{R_w}{2H} \frac{(\rho C_p)_w}{(\rho C_p)_m}$
Gz	Graetz Number $= \frac{\rho C_p V H^2}{kL}$
Na	Nahme Number $= \frac{\beta \bar{\eta} V^2}{k}$
Nu	Nusselt Number $= \frac{h_T R_c}{k_{air}}$
Pe	Peclet Number $= \frac{\rho C_p V H}{k}$
Re	Reynolds Number $= \frac{\rho V H}{\bar{\eta}}$

Mathematical Symbols

Δ	increment
∂	differential operator
∇	vector differential operator
∇^2	Laplace operator
$\frac{D}{Dt}$	substantial derivative
$\sum_i$	summation over i
$\{\ \}$	column vector
$[\ ]$	matrix
$\|\ \|$	magnitude
	determinant of a matrix

Chapter 1

Introduction

1.1 Polymer Melt Flow in Extrusion Dies

Since the development of polymerization reactions and the tremendous growth of the polymer industry, plastics have literally been omnipresent in every part of everyday life. Enormous efforts have been made to study the behaviour of such new materials and to be able to predict reasonably their characteristics during processing, usually in the form of a melt. A variety of shaping processes exists nowadays, such as extrusion, injection molding, blow molding, film blowing, fiber spinning, calendering, wire coating, to name just a few. Although each process is suited for different products,

almost all plastics (approximately 95%) pass at some point through an extruder to be compressed, conveyed down the screw channel and then melted before being shaped into the desired form or product. A typical schematic diagram of a plasticating extruder is shown in Figure 1.1, along with the various zones encountered (from Agur and Vlachopoulos, 1982).

While a variety of experimental and theoretical studies has been done on extruders with varying degrees of success (Agur and Vlachopoulos, 1982), the plastics industry remains primarily interested in the design of the last section of the extruder, i.e. the extrusion die. Dies come in a variety of shapes and sizes, from the simplest circular hole for the production of plastic fibers and rods to sophisticated three-dimensional sheeting dies for shaping huge plastics sheets; they can be annular for pipe formations for example, or with a moving inner cylinder, as in the process of wire coating; they can combine different polymer streams in a variety of ways to produce multilayered products, as in the process of coextrusion, which has received great attention in the last decade.

Until recently, the design of extrusion dies has been mainly based on the empirical approach of a series of experiments under varying conditions to determine the optimum geometry needed. Extensive and expensive ex-

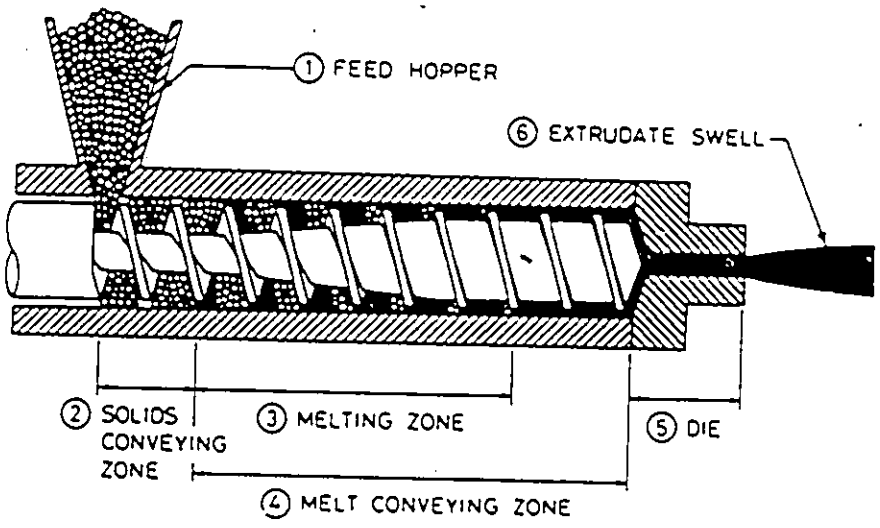

Figure 1.1: Schematic Diagram of a Plasticating Extruder.

periments have been the norm for a variety of melts to determine such quantities as the length and opening gap for a die to give certain dimensions to the product, or the pressure drop needed for a certain extrusion throughput (flow rate). Taking into account the unusual behaviour of plastics due to their viscoelastic nature, one of the biggest headaches even for the simplest problem of extrusion through a capillary die, is what should be the die diameter to produce a certain extrudate diameter and at what flow rate. This, of course, happens because of an interesting and important phenomenon exhibited by plastics, called "extrudate swell," which accounts for considerable increase in the extrudate cross-section when the material comes out of the die.

Apart from the effect of the geometry on the flow, another important parameter is the polymer melt itself, since different materials flow differently and therefore obey different constitutive relations. Extensive experiments have also been carried out to determine the properties of polymer melts. The data obtained called for a need to correlate their properties and establish appropriate mathematical relationships. Such relationships can be used to model these materials and understand their behaviour under processing conditions by performing numerical simulations.

In the last ten years, the rapid development of computers has allowed the numerical solution of many complicated problems with a variety of sophisticated methods such as the numerical method of finite elements (FEM). The main advantages of this method are:

(a) its ability to easily handle complex geometries and boundary conditions and

(b) its flexibility to solve many different types of problems with only slight modifications of the same computer program.

The question of a powerful numerical method seems more or less to have been settled with the application of FEM in flow problems. One shortcoming of the method seems to be its rather involved formulation which requires a good understanding of variational principles, matrix algebra and computer programming skills. However, computer programs can become "user-friendly" with appropriate pre-processing of input data and post-processing of output data, that greatly simplify the numerical simulations for a series of parametric studies. In that form then, the computer programs can be used by a non-expert on the numerical method itself.

1.2 Review of Numerical Simulation of Polymer Melt Flow in Extrusion Dies

The numerical simulation of polymer melt flows has been the object of many investigations in recent years. Calculations have been performed using several numerical methods, such as perturbation, collocation, finite difference methods (FDM), finite element methods (FEM) and quite recently, boundary element methods (BEM) (Bush and Tanner, 1983). The emphasis has been shifted progressively towards FEM, because of their ability to incorporate complicated geometrical boundaries. The major conclusions of these research efforts have been summarized by Crochet and Walters (1983) and Mitsoulis et al. (1984). A brief summary is also given here.

A helpful classification of polymer melt flows includes:

- Flows dominated by the shear viscosity (nearly viscometric flows)
- Complex flows involving inelastic or highly elastic fluids

In the first category, due to the geometry of the flow field, the fluid elasticity has only a minor effect on the streamlines. This is typical of constrained flows inside oblong extrusion dies, and the Lubrication Approxi-

mation Theory (LAT) can be applied as explained in standard textbooks (McKelvey, 1962; Middleman, 1977; Tadmor and Gogos, 1979). Shear-thinning effects (see Figure 1.2) may remain though quite important and a generalized Newtonian fluid (power-law fluid, for example) can be used to account for such behaviour. Numerical methods for calculating Newtonian flow can be adapted without difficulty to meet the variable-viscosity complication. A Picard iterative technique may be used, in which the velocity is updated by means of the previous velocity field. Up to now, the FDM has been the most popular numerical technique and there are numerous publications in the literature based on its applications to melt flow problems through extrusion dies (Carley, 1959; McKelvey, 1962; Bagley and Storey, 1963; Fenner, 1967; Fenner and Williams, 1967; Middleman, 1977; Uhland, 1977; Winter, 1977; Han and Rao, 1978; Carley et al., 1979; Tadmor and Gogos, 1979; Basu, 1981; Chin et al., 1984; Sornberger et al., 1986).

In the second category, for flow predictions in arbitrary geometries, the FDM has recently been replaced by the FEM because of its flexibility to handle complex shapes that dies may have. The FEM has been exploited for purely viscous (inelastic) fluids by Caswell and Tanner (1978), Wagner and Mitsoulis (1985), Mitsoulis (1986c), Pittman and Rashid (1986) for

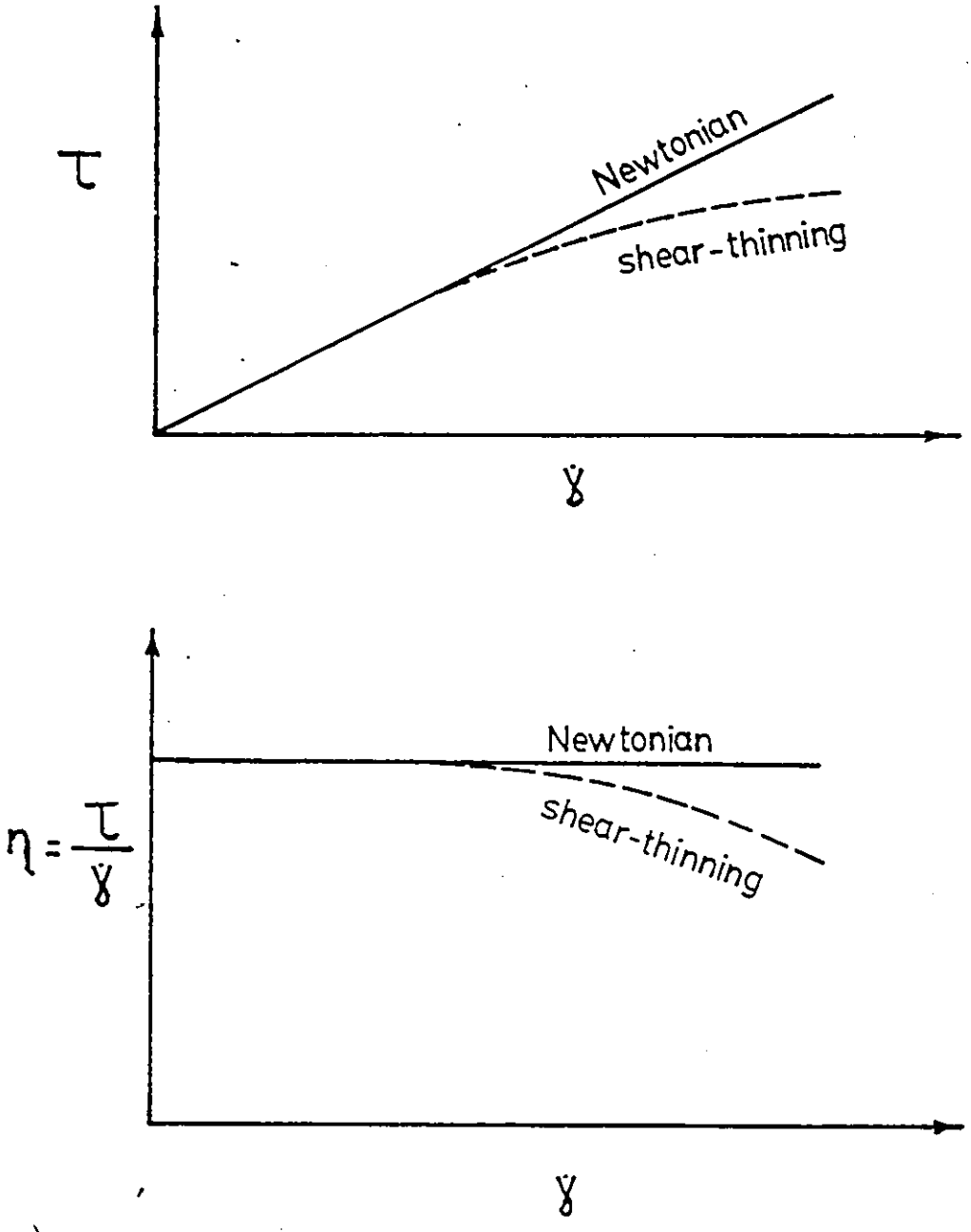

Figure 1.2: Typical Shear Stress and Shear Viscosity vs. Shear Rate Curves for Newtonian and Shear-Thinning Fluids.

the design of wire-coating dies, by Crochet and Keunings (1981) for conical dies, by Crochet and Keunings (1983) for fiber-spinning dies, by Mitsoulis et al. (1984) for slit and capillary dies, by Mitsoulis (1986b) for annular dies, by Sornberger et al. (1986) for coat-hanger dies and by Mitsoulis (1986a) and Mavridis et al. (1987) for coextrusion dies.

For highly elastic fluids flowing in complex geometries, there has been a tremendous activity since 1980 to predict viscoelastic behaviour using a variety of viscoelastic constitutive models and usually the FEM. All these efforts have been reviewed recently by Mitsoulis (1986e). Unfortunately, up to now the results have been rather discouraging due to numerical breakdown of the computations (divergence of the solution) and/or wrong predictions for cases where convergence had been attained. Due to the unresolved nature of the problem of viscoelasticity, only purely viscous (inelastic) models will be considered in this work.

1.3 Objectives

The objectives of this study are to solve the governing conservation and constitutive equations for polymer melt flows inside extrusion dies. In par-

ticular, two programs will be developed, one based on the Lubrication Approximation Theory (LAT) for quick determination of such quantities as pressure drop vs. flow rate, etc., and another based on the Finite Element Method (FEM) for a full analysis of flows in axisymmetric geometries.

The emphasis for the LAT program will be its user-friendliness and generality for any polymer melt flow inside almost parallel channels with moving or stationary boundaries and various layers of different melts.

For the FEM program, the emphasis will be in developing and implementing a numerical scheme to successfully solve the energy equation for highly convective flows and thus suppress spurious temperature oscillations that have plagued other previous numerical simulations (Wagner and Mitsoulis, 1985; Wagner, 1987). Another feature to be implemented and used for coextrusion flows will be the handling of interfaces when two melts travel together inside an extrusion die, along with the free surfaces present upon exit of the melts to the atmosphere.

The flow of polymer melts in extrusion dies will be considered as steady-state, incompressible, creeping flow (inertia forces negligible). Constitutive models considered in this study will be purely viscous (inelastic) and will include:

(a) Newtonian fluid

(b) Generalized Newtonian fluid (shear-thinning models with or without temperature-dependent viscosity).

Shear-thinning models used in this study will be the power law, a quadratic model and a logarithmic model which can adequately describe experimental viscosity data for polymer melts.

The programs developed will be tested against known analytical and numerical solutions and thus their accuracy will be established. They then will be used for the analysis of several polymer melt flow problems in axisymmetric extrusion dies. From the analysis, new or modified die designs will be deduced for flow of some typical polymer melts used in industrial applications.

1.4 Outline of Thesis

Chapter 2: The equations of conservation of mass, momentum and energy are introduced and simplified using the appropriate assumptions. The models and the constitutive equations available for the description of flow of polymer melts in extrusion dies are also presented.

The relevant dimensionless groups are discussed and the appropriate boundary conditions are outlined.

Chapter 3: The two methods of solution are presented. The Lubrication Approximation Theory (LAT) is briefly discussed and its implementation is given for the case of two fluids flowing side-by-side. The Finite Element formulation (FEM) of the continuity and momentum equations (velocities-pressure or u-w-p formulation) is briefly presented for axisymmetric flows. Then the Streamline-Upwind/Petrov-Galerkin scheme for the energy formulation is detailed along with a new finite element discretization scheme for bilinear quadrilaterals. Also included are a stream function formulation and a method for handling problems with free surfaces and interfaces occurring in coextrusion.

Chapter 4: Results from preliminary runs and test runs are presented to confirm the workability of the finite element method and the new upwinding technique for handling highly convective nonisothermal flows. The validity and accuracy of the results is checked against analytical and other numerical methods.

Chapter 5: The process of high-speed wire coating is examined with ma-

jor emphasis on thermal effects. Results from LAT and FEM are presented and compared with other numerical results available in the literature as well as with experimental data from an industrial operation.

Chapter 6: The process of wire-coating coextrusion is examined with major emphasis on thermal effects and their influence on the interface location. Results from LAT and FEM are presented and compared with other numerical results available in the literature. Deductions for effective coextrusion die design are given based on the analysis.

Chapter 7: The results of this thesis are summarized for the various problems examined and the different methods used. Conclusions and recommendations for future work are presented.

Chapter 2

Mathematical Modelling of Polymer Melt Flow

This chapter presents an introduction on the importance and need for analyzing and predicting the behaviour of polymer melts as they flow through processing equipment. The general conservation equations for the flow analysis are presented along with the constitutive equations used for polymer melts. Finally, the reduction of these equations for steady-state flows in axisymmetric geometries is given under the appropriate assumptions.

2.1 Introduction

The determination of the velocity, pressure and temperature fields of polymer melts inside extrusion dies is of considerable practical interest in the plastics industry. The results of the above primary variables can be used to evaluate other quantities of practical importance, such as flow rates, power requirements, stresses and strains, heat dissipated, extrudate swell, etc. Such information can be used in the design of processing dies.

An analysis of polymer melt flows through processing equipment requires simultaneous consideration of the mass, momentum and energy conservation principles. These equations must also accommodate appropriate constitutive equations that relate stresses to the velocity gradients. The geometry of the equipment enters in the specification of the boundaries. Because of the complexity of the differential equations involved and their domain of integration, nearly all problems require numerical methods for their solution. Except for a few highly simplified (Newtonian or power-law) constitutive equations that can describe some melt flows in simple geometries, it is often very difficult or impossible to obtain solutions that represent adequately the behaviour of polymer melts. In order to obtain a

manageable and solvable form of the equations for the analysis of a very difficult problem, some assumptions based on experience are necessary. Some of the simplifications adopted are described later in this chapter.

Extensive experiments have been carried out to determine the properties of polymer melts. Correlations of these properties can be used to model these materials and allow for the understanding of their behaviour under processing conditions by performing numerical simulations.

The single most important and readily measurable property of polymer melts is the shear viscosity. Some typical viscosity vs. shear rate curves are shown in Figure 2.1 for an LDPE melt (Meissner, 1971). It is seen that at low shear rates, the viscosity is almost constant (Newtonian regime), but at moderate to high shear rates it decreases exhibiting the "shear-thinning" behaviour, which is typical of pseudoplastic materials such as polymer melts. Empirical correlations have been found and used extensively for polymer melts under certain conditions. The use of a power-law model in viscometric flows, for example, is a widely accepted constitutive relationship that describes adequately the shear-thinning behaviour of polymer melts in shear flows. Although such a relation was an improvement over the idealized linear Newtonian models, it tends to overestimate the

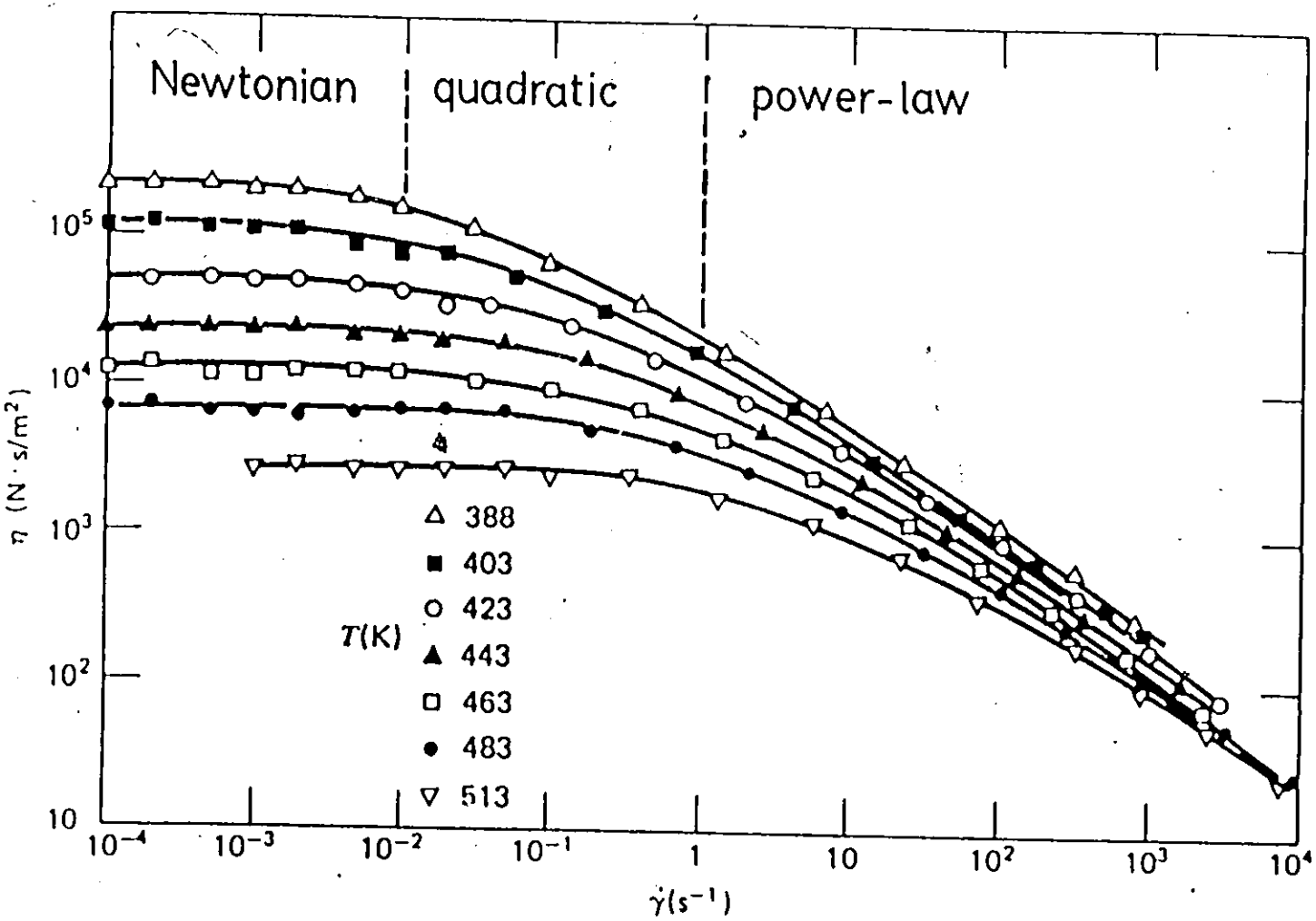

Figure 2.1: Viscosity Curves of a Low Density Polyethylene (LDPE) Melt at Different Temperatures (Meissner, 1971).

shear viscosity of most polymer melts in relatively low shear rate range. Therefore an improvement would be to include a Newtonian model in the low shear rate range and a quadratic model in the mid-shear rate range. Such empirical relationships have gained more popularity during the past few years for numerical simulations.

Although able to represent the shear viscosity quite well, the above models fail to account for the elastic effects that most polymers exhibit in practice. As a result, new models that would presumably describe reality adequately have been developed by several researchers (Bird et al., 1977). Unfortunately most investigations in the literature have shown that such models, when implemented in the numerical simulation, have failed to converge at moderate to high elasticity levels that are usually encountered in practical situations (Mitsoulis, 1986e). Therefore, the current work is limited to studies of purely viscous (inelastic) fluids.

2.2 Conservation Equations

In general tensorial form the conservation equations are (Bird et al., 1960):

Mass:

$$\frac{D\rho}{Dt} + \rho(\nabla \cdot \overline{v}) = 0 \tag{2.1}$$

Momentum:

$$\rho\frac{D\overline{v}}{Dt} = -\nabla p + \nabla \cdot \overline{\overline{\tau}} + \rho\overline{g} \tag{2.2}$$

Energy:

$$\rho C_p\frac{DT}{Dt} = -\nabla \cdot \overline{q} + \overline{\overline{\tau}} : \nabla\overline{v} \tag{2.3}$$

Assuming that:

(a) the melt is incompressible (constant density), the continuity equation for conservation of mass (Equation 2.1) reduces to:

$$\nabla \cdot \overline{v} = 0 \tag{2.4}$$

The incompressibility assumption is not valid when large pressure gradients are present. However, for most polymer melts under usual processing conditions, Equation 2.4 is indeed applicable.

The equation of conservation of momentum involves a balance between inertia, viscous, pressure and body forces. Because polymer melt flows are

very slow flows with extremely small Reynolds numbers ($Re \ll 1$) (Pearson, 1985), it may be assumed that:

(b) inertia effects are negligible in comparison with viscous and pressure forces.

We also assume that:

(c) body forces (such as gravity) are negligible in comparison with viscous and pressure forces.

(d) the flow is steady ($\frac{\partial}{\partial t} = 0$), which applies to many polymer processes.

Thus, the conservation of momentum (Equation 2.2) reduces to:

$$0 = -\nabla p + \nabla \cdot \bar{\bar{\tau}} \tag{2.5}$$

Turning to the conservation of energy (Equation 2.3), the following assumptions are usually made for polymer melts:

(e) the thermal conductivity k is constant.

(e) the specific heat at constant pressure C_p is constant.

The resulting energy equation with convective, conductive and viscous dissipation terms respectively, is:

$$\rho C_p \bar{v} \cdot \nabla T = k \nabla^2 T + \bar{\bar{\tau}} : \nabla \bar{v} \tag{2.6}$$

2.3 Constitutive Equations

To solve the above equations we also need constitutive equations that relate the extra stress tensor $\bar{\bar{\tau}}$ to the rate-of-strain tensor $\bar{\bar{\dot{\gamma}}}$:

$$\bar{\bar{\dot{\gamma}}} = \nabla\bar{v} + (\nabla\bar{v})^T \tag{2.7}$$

2.3.1 Newtonian Fluid

For Newtonian fluids we have

$$\bar{\bar{\tau}} = \mu\bar{\bar{\dot{\gamma}}} = \mu\dot{\gamma}_{ij} \tag{2.8}$$

where μ is a constant viscosity coefficient.

2.3.2 Generalized Newtonian Fluid

The generalized Newtonian fluid includes a variable, non-Newtonian viscosity η and it has the form:

$$\bar{\bar{\tau}} = \eta(\dot{\gamma})\bar{\bar{\dot{\gamma}}} = \eta(\dot{\gamma})\dot{\gamma}_{ij} \tag{2.9}$$

The apparent viscosity $\eta(\dot{\gamma})$ is a function of the magnitude $|\dot{\gamma}|$ of the rate-of-strain tensor $\bar{\bar{\dot{\gamma}}}$, which is given by the expression

$$|\dot{\gamma}| = \sqrt{\frac{1}{2}I_2} \tag{2.10}$$

I_2 is the scalar second invariant of $\bar{\bar{\dot{\gamma}}}$, given by (summation convention adopted):

$$I_2 = (\bar{\bar{\dot{\gamma}}} : \bar{\bar{\dot{\gamma}}}) = \dot{\gamma}_{ij}\dot{\gamma}_{ji} = \sum_i \sum_j \dot{\gamma}_{ij}\dot{\gamma}_{ji} \tag{2.11}$$

The form of the function $\eta(\dot{\gamma})$ gives rise to various empirical relations introduced in the literature to fit experimental data (see Figure 2.1). The relations used in this analysis are:

(a) The power-law model of Ostwald and de Waele (Bird et al., 1960).

The most widely used model in industrial applications is the power-law fluid with an apparent viscosity η given by:

$$\eta(\dot{\gamma}) = m|\dot{\gamma}|^{n-1} \tag{2.12}$$

where m is usually referred to as the consistency index ($Pa{\cdot}s^n$) and n is the power-law index (dimensionless). Both constants m and n can be determined experimentally, using commercially available viscometers. This model describes adequately the descending linear region of the plot of $\log\eta$ vs. $\log\dot{\gamma}$, which is the most important region for practical applications.

(b) Intermediate quadratic model (Carley et al., 1979).

This model takes care of the region between the Newtonian region

(low shear rates) and the power-law region (high shear rates). The apparent viscosity takes the following form:

$$\eta(\dot{\gamma}) = \frac{\tau}{\dot{\gamma}} \tag{2.13}$$

where

$$\log \tau = a(\log \dot{\gamma})^2 + b(\log \dot{\gamma}) + c \tag{2.14}$$

with a, b and c being the correlated parameters.

(c) Full quadratic model (Agur and Vlachopoulos, 1982).

This is a stand-alone model with temperature as one of its independent variables. The apparent viscosity takes the following form:

$$\ln \eta = a_1 + a_2 \ln \dot{\gamma} + a_3(\ln \dot{\gamma})^2 + a_4 T + a_5 T^2 + a_6 T \ln \dot{\gamma} \tag{2.15}$$

where a_1, a_2, a_3, a_4, a_5 and a_6 are correlated parameters. It has the advantage of taking temperature into consideration. It allows the viscosity curves at different temperatures to converge together as $\dot{\gamma}$ increases; this is the general behaviour of most polymer melts at high shear rates (see Figure 2.1).

Unlike model (c) models (a), (b) and the Newtonian model allow a nonisothermal analysis to be carried out through the exponential relation

(Bird et al., 1977):

$$\eta = \eta_o \exp(-\beta(T - T_o)) \tag{2.16}$$

where η_o is the viscosity at the reference temperature T_o, η is the viscosity at T, and β is a temperature shift constant.

Although all of the above listed models have been used in the literature for the solution of various problems, the power-law fluid still remains the most popular model for calculations. All the above models are useful for calculating flow rates and shearing forces in steady-state shear flows, such as flows in tubes, slits, rotating disks and cone-and-plate flows. They cannot describe normal-force phenomena, any time-dependent phenomena, or phenomena connected with flows other than steady shear. The power-law model can describe the shear-thinning behaviour of polymer melts over wide shear rate ranges for $n < 1$. Although elasticity is not included, the power-law model is used successfully in predicting the behaviour of many polymer processes, especially in constrained flows inside processing equipment.

2.4 Governing Equations for Axisymmetric Flows

The flow of polymer melts inside processing equipment is three-dimensional in nature. However, a large class of extrusion flows occurs inside tubular or annular dies for manufacture of plastic rods, pipes, insulated wires, etc. Such geometries conveniently allow the use of cylindrical coordinates (r, θ and z). In addition, no changes in the θ-direction could be safely assumed. The flow can thus be considered as axisymmetric. Due to axisymmetry, the three-dimensional problem can be fully described as two-dimensional with two independent variables, namely r and z.

For axisymmetric flows, the continuity equation can be written as (Bird et al., 1960):

$$\frac{\partial v_r}{\partial r} + \frac{v_r}{r} + \frac{\partial v_z}{\partial z} = 0 \tag{2.17}$$

The equation of conservation of momentum gives:

$$0 = -\frac{\partial p}{\partial r} + \frac{\partial \tau_{rr}}{\partial r} + \frac{\tau_{rr}}{r} + \frac{\partial \tau_{rz}}{\partial z} - \frac{\tau_{\theta\theta}}{r} \tag{2.18}$$

$$0 = -\frac{\partial p}{\partial z} + \frac{\partial \tau_{rz}}{\partial r} + \frac{\tau_{rz}}{r} + \frac{\partial \tau_{zz}}{\partial z} \tag{2.19}$$

and the equation of conservation of energy yields:

$$\rho C_p \left(v_r \frac{\partial T}{\partial r} + v_z \frac{\partial T}{\partial z} \right) = k \left(\frac{1}{r} \frac{\partial T}{\partial r} + \frac{\partial^2 T}{\partial r^2} + \frac{\partial^2 T}{\partial z^2} \right) + \tau_{rr} \frac{\partial v_r}{\partial r} + \tau_{\theta\theta} \frac{v_r}{r} + \tau_{rz} \frac{\partial v_z}{\partial r} + \tau_{zr} \frac{\partial v_r}{\partial z} + \tau_{zz} \frac{\partial v_z}{\partial z} \tag{2.20}$$

It should be noted that because of the symmetry of the stress tensor, $\tau_{rz} = \tau_{zr}$. Thus, only four stress components are needed for axisymmetric flows. This simplifies the analysis by using a stress vector $(\tau_{rr}, \tau_{zz}, \tau_{rz}, \tau_{\theta\theta})$ and a corresponding rate-of-strain vector $(\dot{\gamma}_{rr}, \dot{\gamma}_{zz}, \dot{\gamma}_{rz}, \dot{\gamma}_{\theta\theta})$.

For axisymmetric flows, the Newtonian constitutive equation gives:

$$\tau_{rr} = 2\mu \frac{\partial v_r}{\partial r} \tag{2.21}$$

$$\tau_{\theta\theta} = 2\mu \frac{v_r}{r} \tag{2.22}$$

$$\tau_{zz} = 2\mu \frac{\partial v_z}{\partial z} \tag{2.23}$$

$$\tau_{rz} = \mu \left(\frac{\partial v_z}{\partial r} + \frac{\partial v_r}{\partial z} \right) = \tau_{zr} \tag{2.24}$$

The generalized Newtonian constitutive equation has the same form as the above, except that the constant viscosity μ is replaced by the apparent viscosity $\eta(\dot{\gamma})$. For the power-law model, $\eta(\dot{\gamma})$ is given by:

$$\eta(\dot{\gamma}) = m \left(\frac{1}{2} I_2 \right)^{(n-1)/2} = m \left[\frac{1}{2} \left(\dot{\gamma}_{rr}^2 + \dot{\gamma}_{\theta\theta}^2 + \dot{\gamma}_{zz}^2 + 2\dot{\gamma}_{rz}^2 \right) \right]^{(n-1)/2} \tag{2.25}$$

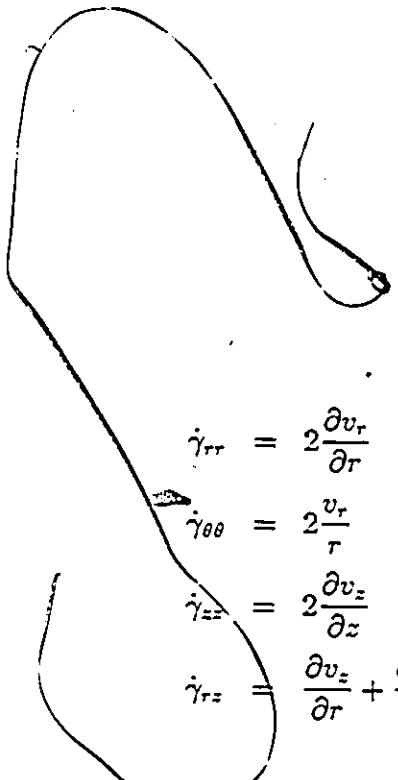

where

$$\dot{\gamma}_{rr} = 2\frac{\partial v_r}{\partial r} \tag{2.26}$$

$$\dot{\gamma}_{\theta\theta} = 2\frac{v_r}{r} \tag{2.27}$$

$$\dot{\gamma}_{zz} = 2\frac{\partial v_z}{\partial z} \tag{2.28}$$

$$\dot{\gamma}_{rz} = \frac{\partial v_z}{\partial r} + \frac{\partial v_r}{\partial z} = \dot{\gamma}_{zr} \tag{2.29}$$

The above constitutive equations in the form presented here were substituted in the momentum and energy Equations 2.18–2.20 and used in a fully two-dimensional finite element analysis to simulate the behaviour of polymer melts in several axisymmetric problems.

2.5 Dimensionless Groups

Before proceeding with the boundary conditions necessary for the solution of the governing conservation and constitutive equations, it is interesting to examine the relevant dimensionless numbers in extrusion flows. The various dimensionless groups are used to characterize the relative significance of each term in the conservation equations of momentum and energy. The dimensionless groups are calculated at a reference temperature T, a char-

acteristic length H and a characteristic velocity V. It is appropriate then to define a characteristic shear rate

$$\bar{\dot{\gamma}} = \frac{V}{H} \tag{2.30}$$

and a characteristic viscosity

$$\bar{\eta} = \eta(\bar{\dot{\gamma}}, T) \tag{2.31}$$

With the above definitions at hand, we can now define the relevant dimensionless groups of interest in the analysis:

1. Reynolds number

$$Re = \left. \frac{\rho V H}{\bar{\eta}} \right|_T \tag{2.32}$$

The Reynolds number is a measure of the relative importance of inertia forces compared to viscous forces in the equation of momentum. For polymer melt flows in general, $Re \ll 1$ (Pearson, 1985) and the creeping flow approximation is valid. As a result, the inertia terms are not included in the calculations.

2. Peclet number

$$Pe = \left. \frac{\rho C_p V H}{k} \right|_T \tag{2.33}$$

The Peclet number is a measure of convective heat transfer with regard to conductive heat transfer. High Pe values indicate a flow dominated by convection. An example of such flows is high-speed wire coating (Pe up to 100,000). From a numerical point of view these flows are notorious because of instabilities that manifest themselves in the form of spurious oscillations in the temperature field (Roache, 1976; Hüebner and Thornton, 1982). Special "upwinding" techniques must then be used to remedy the oscillations (Hughes and Brooks, 1979, 1982; Brooks and Hughes, 1982).

3. Graetz number

$$Gz = \left.\frac{\rho C_p V H^2}{kL}\right|_T = Pe \left.\frac{H}{L}\right|_T \tag{2.34}$$

where L is the axial length of the die. The Graetz number can be understood to be the ratio of the time required for heat conduction from the center of the channel to the wall and the average residence time in the channel. As with Pe, a large value of Gz means that heat convection in the flow direction is more important than conduction toward the walls.

4. Nahme number

$$Na = \left.\frac{\beta\bar{\eta}V^2}{k}\right|_T \tag{2.35}$$

The Nahme number is a measure of viscous dissipation effects compared to conduction, hence an indicator of coupling of the energy and momentum equations. For values of Na greater than 0.1–0.5 (depending on geometry and thermal boundary conditions), the viscous dissipation leads to considerable coupling of the conservation equations and a nonisothermal analysis is necessary.

In some studies (Mitsoulis and Vlachopoulos, 1984a), the Brinkman number defined by:

$$Br = \left.\frac{\bar{\eta}V^2}{kT_o}\right|_T \tag{2.36}$$

has been used instead of the Nahme number. However, as pointed out by Winter (1977), Br contains the arbitrary temperature level T_o and may, therefore, have very different values for similar processes. The value of Br does not give any information on the extent of the coupling between the equations of motion and energy.

5. Biot number

$$Bi = \frac{(\partial T/\partial r)_b H}{T_s - T_b} \tag{2.37}$$

where H is the local annular gap, T_s is some temperature of the surroundings and T_b is the local boundary temperature. The Biot number is a measure of the relative importance of heat transfer mode at the boundaries. A high value of Bi ($Bi > 100$) approaches isothermal wall conditions ($Bi = \infty$), while a low value of Bi ($Bi < 1$) describes poor heat transfer to the surroundings (nearly adiabatic case, for which $Bi = 0$) (Winter, 1977, 1978).

6. Capacitance parameter

$$C = \frac{R_w}{2H} \frac{(\rho C_p)_w}{(\rho C_p)_m} \tag{2.38}$$

where $(\rho C_p)_w$ and $(\rho C_p)_m$ are the thermal capacitance of the metallic core in an annulus and that of the melt, respectively. The capacitance parameter C is used to account for the energy stored in the boundary during thermal development. The thermal capacitance (ρC_p) is in the same order of magnitude for polymer melts and for metals (Winter, 1978), and therefore it cannot be ignored in nonisothermal studies.

2.6 Boundary Conditions

The solution of the conservation equations 2.17–2.20 can be obtained by imposition of proper boundary conditions. In order to solve boundary-value problems such as in material flows through processing equipment, a rather complete set of boundary conditions is necessary.

There are basically two types of boundary conditions (Huebner and Thornton, 1982):

1. Essential boundary conditions (or fixed boundary conditions), and
2. Natural boundary conditions (or flux boundary conditions).

The first type refers to the primary variables, e.g. velocities for the flow analysis, temperatures for the thermal analysis, and stream function values for a flow analysis based on stream function formulation. The second type of boundary conditions refers to the secondary variables (usually derivatives of the primary variables), e.g. surface tractions for the flow analysis, heat fluxes for the thermal analysis and velocities for the stream function formulation.

More specifically, for flow problems the following set of boundary conditions is available (Ben-Sabar and Caswell, 1979):

1. V_n, V_t pure velocity conditions; specify V_n, V_t

2. T_n, T_t pure surface tractions conditions; specify T_n, T_t

3. T_n, V_t or V_n, T_t mixed conditions; specify T_n, V_t or V_n, T_t

where the subscripts n and t represent the components of a vector in the normal and tangential direction to a surface, respectively. In flow problems velocity conditions (type 1) are most commonly encountered. However, in materials processing the appearance of free surfaces requires the specification of surface tractions (type 2). Such surface tractions can be air drag, drawdown force, surface tension, etc.

Boundary conditions for the energy equation require the specification of either T or q_n on the entire surface. The following set is available (Ben-Sabar and Caswell, 1979):

1. temperature conditions; specify T

2. (a) heat flux conditions; specify q_n

   (b) 'linear' radiation boundary conditions; specify $q_n = h_T(T - T_a)$

Condition 2(a) is specified on a boundary where the heat flux exchange is known exactly. A special case for 2(a) is $q_n = 0$ (adiabatic condition), where

no heat exchange exists at the boundary. Other cases involve specification of finite values for q_n. In reality, however, the exact heat exchange at the boundary is unknown. Condition 2(b) allows for more flexibility in this respect by introducing the general surface heat transfer coefficient h_T and the controlled temperature T_a. Generally, the temperature at the boundary T is unknown. Note that a special case for 2(b) is when the temperature at the boundary T is equal to T_a, i.e. the boundary temperature is being controlled at a known temperature T_a. This case is commonly known as the isothermal wall condition.

The boundary conditions for the stream function are (Huebner and Thornton, 1982):

1. stream function conditions; specify ψ

2. velocity conditions; specify $\partial\psi/\partial\overline{n}$

where $\partial\psi/\partial\overline{n}$ represents the tangential velocity at the surface.

For stratified multiphase flows of two or more components in coextrusion processes, additional boundary conditions are necessary at the interfaces. A schematic diagram of a fluid-fluid interface is shown in Figure 2.2. In such cases, the interface is modelled as a continuous surface with zero thickness.

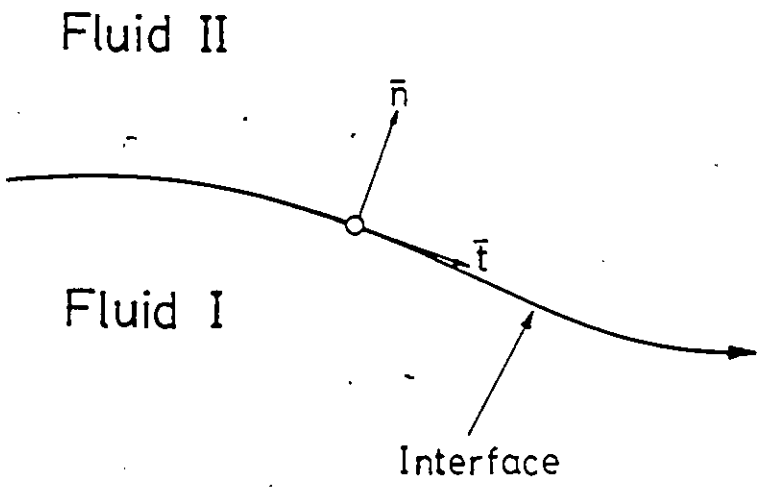

Figure 2.2: Schematic Diagram of a Fluid-Fluid Interface.

As a result, there is a discontinuity of fluid properties across the interface.

At the interface, by assuming only pressure and viscous forces are in effect (i.e. neglecting surface tension effects), the boundary conditions for flow analysis are (Mitsoulis, 1986a; Mavridis et al., 1987):

1. kinematic conditions

$$v_{t,I} = v_{t,II} \tag{2.39}$$

$$v_{n,I} = v_{n,II} = 0 \tag{2.40}$$

2. tangential stress conditions

$$\eta_I \left(\frac{\partial v_{t,I}}{\partial \bar{n}} + \frac{\partial v_{n,I}}{\partial \bar{t}} \right) = \eta_{II} \left(\frac{\partial v_{t,II}}{\partial \bar{n}} + \frac{\partial v_{n,II}}{\partial \bar{t}} \right) \tag{2.41}$$

3. normal stress conditions

$$-p_I + 2\eta_I \frac{\partial v_{n,I}}{\partial \bar{n}} = -p_{II} + 2\eta_{II} \frac{\partial v_{n,II}}{\partial \bar{n}} \tag{2.42}$$

where v_t and v_n are the velocities tangential and normal to the interface, respectively, η are the apparent viscosities and p are the pressures. Subscripts I and II denote fluids I and II, respectively.

At the interface, the boundary conditions for the energy equation are:

1. temperature conditions

$$T_I = T_{II} \tag{2.43}$$

2. heat flux conditions

$$q_{n,I} = q_{n,II} \tag{2.44}$$

At the interface, the boundary conditions for the stream function are:

1. stream function conditions

$$\psi_I = \psi_{II} \tag{2.45}$$

2. velocity conditions

$$\frac{\partial \psi_I}{\partial \overline{n}} = \frac{\partial \psi_{II}}{\partial \overline{n}} \tag{2.46}$$

Therefore, a complete set of boundary conditions is necessary for the solution of the conservation equations 2.17–2.20. The specific boundary conditions to be applied depend upon the problem at hand. Having outlined the governing equations and the types of boundary conditions involved, we embark in the next Chapter upon formulating the methods for their solution.

Chapter 3

Methods of Solution

3.1 Introduction

The numerical methods used in this study are the Lubrication Approximation Theory (LAT) and the Finite Element Method (FEM). Both methods will be briefly discussed here. Most of the material covered in this chapter can also be found in Mitsoulis (1984), Huebner and Thornton (1982) and Basu (1981), and it is included here for the sake of completeness.

3.2 Lubrication Approximation Theory

The Lubrication Approximation Theory has been used to reduce the governing two-dimensional partial differential equations to a one-dimensional ordinary differential equation. As such, LAT is only valid for extrusion dies with geometries which are approximately horizontal (i.e. small angles present, see Figure 3.1). Only the isothermal analysis for LAT is discussed.

Consider the momentum conservation equations 2.18 and 2.19, and the domain shown in Figure 3.1 where:

- ϕ is the angle the outer wall makes with the axis,
- V_o is the velocity of the outer wall, and
- V_i is the velocity of the inner wall.

If ϕ is small ($< 10°$) (Middleman, 1977)

$$v_r \ll v_z \tag{3.1}$$

$$\frac{\partial p}{\partial r} \ll \frac{\partial p}{\partial z} \tag{3.2}$$

$$\frac{\partial v_z}{\partial z} \ll \frac{\partial v_z}{\partial r} \tag{3.3}$$

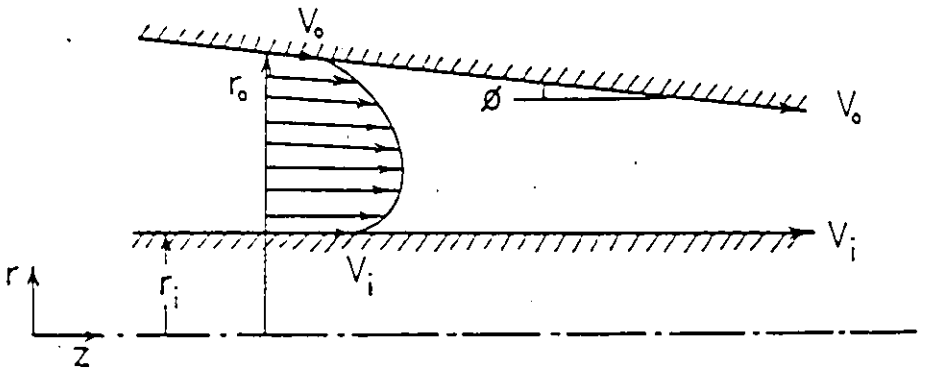

Figure 3.1: Schematic Diagram for Flow in an Annulus.

then Equation 2.18 is eliminated and Equation 2.19 reduces to an ordinary differential equation

$$\frac{dp}{dz} = \frac{d\tau_{rz}}{dr} + \frac{\tau_{rz}}{r} \tag{3.4}$$

with boundary conditions

$$\begin{aligned} &\text{at} \quad r = r_i \quad , \quad v_z = V_i \\ &\text{at} \quad r = r_o \quad , \quad v_z = V_o \end{aligned} \tag{3.5}$$

for the more general case of an annulus. Note that r_i and r_o are the inner and outer radius of the annulus, respectively. In addition, no-slip condition is assumed, i.e. the polymer melt at the inner wall takes the inner wall velocity (V_i) and the polymer melt at the outer wall takes the outer wall velocity (V_o).

The governing equation, Equation 3.4, is integrated to give

$$\tau_{rz} = \frac{dp}{dz}\frac{r}{2} + \frac{c_o}{r} \tag{3.6}$$

where c_o is the integration constant. In general, Equation 3.6 cannot be solved analytically due to the complicated constitutive equations involved (Rao, 1979).

Equation 3.6 is also applicable for each individual fluid in multilayer coextrusion processes. In order to illustrate the method of solution used,

the coextrusion process of two layers is considered. Referring to Figure 3.2, fluid A forms the inner layer and fluid B forms the outer layer in the final product. In general, these two fluids will have different flow rates given by:

$$Q_A = 2\pi \int_{mR_o}^{\alpha R_o} v_{z(A)}(r) r \, dr \tag{3.7}$$

$$Q_B = 2\pi \int_{\alpha R_o}^{R_o} v_{z(B)}(r) r \, dr \tag{3.8}$$

where αR_o is the interface radius. Also note that in fully developed flow

$$\frac{dp}{dz} = \frac{\partial p_A}{\partial z} = \frac{\partial p_B}{\partial z} \tag{3.9}$$

Two additional boundary conditions, besides Equation 3.5, are required at the interface:

$$\begin{aligned} &\text{at} \quad r = \alpha R_o \quad , \quad v_{z(A)} = v_{z(B)} \\ &\text{at} \quad r = \alpha R_o \quad , \quad \tau_{rz(A)} = \tau_{rz(B)} \end{aligned} \tag{3.10}$$

For coextrusion of two layers, dp/dz, c_o, and the interface location are unknown. Thus, an iterative procedure is used. In the beginning of the iterative procedure, we assume dp/dz, c_o and the interface location. The shear stresses are evaluated at the specified radial positions. With an appropriate constitutive equation relating the viscosity to the shear stress for each layer, the shear rates at each radial position could be obtained by

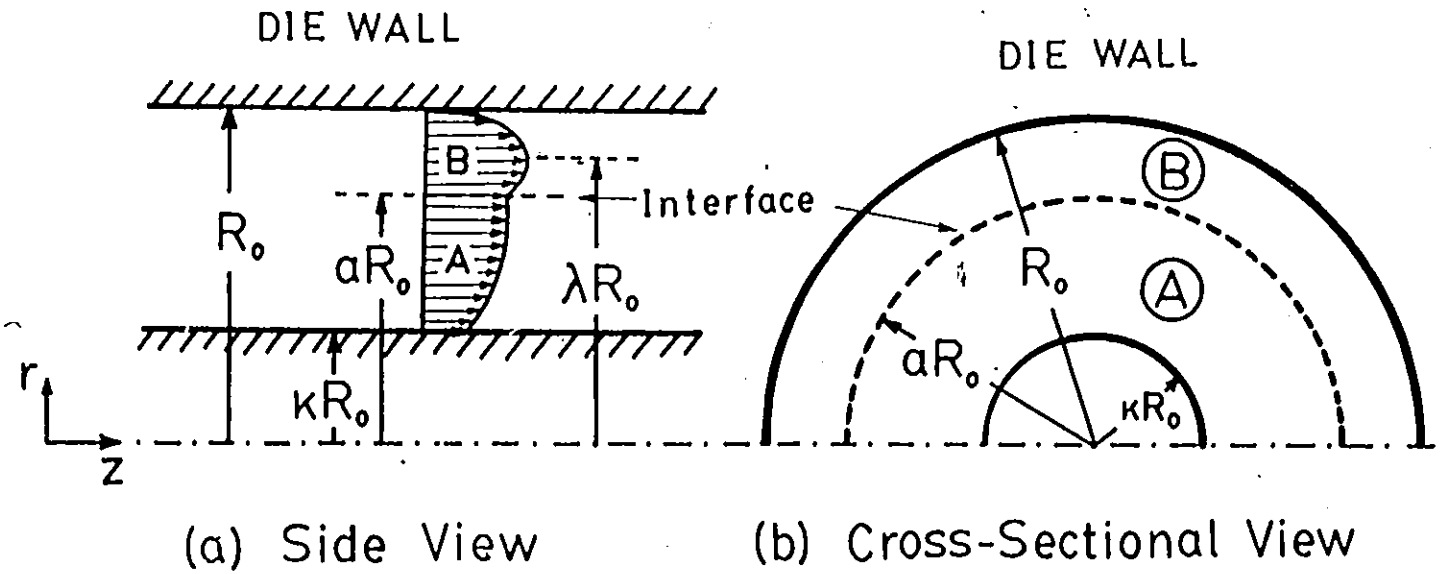

Figure 3.2: Schematic Diagram for Coextrusion of Two Layers in an Annulus.

using

$$\dot{\gamma} = \frac{\tau_{rz}}{\eta} \tag{3.11}$$

Note that two nodes, one in each fluid, must have the same coordinates. These nodes will ensure the continuity of the shear stress and velocity at the interface. The shear rates at these two nodes, in general, will be different. The shear rates are then integrated from the inner wall to the outer wall by

$$v_{z(A)}(r) = \int_{\alpha R_o}^{\kappa R_o} \dot{\gamma}\, dr + V_i \tag{3.12}$$

$$v_{z(B)}(r) = \int_{R_o}^{\alpha R_o} \dot{\gamma}\, dr + v_{z(A)}(\alpha R_o) \tag{3.13}$$

using the inner wall velocity as the initial condition and assuming the velocity is continuous at the interface. Since the position of the interface, the value of dp/dz and c_o are arbitrary, the velocity profile thus obtained does not usually satisfy the velocity boundary condition at the outer wall (die wall). The velocity profile in each layer is integrated by using Equations 3.7 and 3.8 to get the flow rates of each fluid. At correct values of dp/dz, c_o and the interface location, the volumetric flow rates should be equal to the specified flow rates of the polymers and the velocity at the die wall should equal V_o. If any of these conditions is violated, the values of dp/dz, c_o and

the interface location are simultaneously changed using numerical differentiation and a Newton-Raphson scheme in a matrix form (Maron, 1982) and the procedure is repeated until convergence occurs.

For extrusion of a single layer, all of the above still holds. The only difference is instead of using two different constitutive equations, only one is used throughout. In doing so, the shear rate at the interface is also continuous. The location of the interface becomes immaterial in this case.

For extrusion dies with a variable gap (Figure 3.1), this process is carried out at a specified increment in the z-direction until the full length of the die is analyzed. Then, the integration of the pressure gradient throughout the length of the die will yield the pressure profile in the axial direction:

$$P|_z = -\int \left(\frac{dp}{dz}\right) dz \tag{3.14}$$

where $P|_z$ is the pressure at any axial location before the die exit. In addition, integrating the shear stresses along the wall surface gives the tension profile in the axial direction:

$$F|_z = -2\pi \int \tau_{rz} r \, dz \tag{3.15}$$

where $F|_z$ is the tension at any axial location before the die exit.

Although simple in formulation and fast in execution, the LAT fails to account for the nonisothermal, two-dimensional case encountered in actual situations. As a result, a more elaborate numerical method is required to perform the full analysis. This method is discussed as follows.

3.3 Finite Element Method for Axisymmetric Flows

The Finite Element Method (FEM) is a numerical analysis technique for obtaining approximate solutions to a wide variety of engineering problems. The main advantage of FEM over other numerical methods (notably, finite difference) is its ability to solve problems in irregular and complex geometries with unusual boundary conditions (Vlachopoulos, 1977). Once the general differential conservation equations have been cast in their equivalent finite element formulation, a computer program can be written and used for different situations with only minor changes. These may include the geometry, boundary conditions and material properties that are particular to each problem.

In the FEM, the differential equations are solved in an area rather than

a point. As a result, the differential equations must be recast in an approximate integral form which is the basis for the FEM formulation. Several methods are available for reducing the differential conservation equations to suitable integral equations. These include (Huebner and Thornton, 1982):

- the *direct approach*, based on the direct stiffness method of structural analysis
- the *variational approach*, based on the calculus of variations
- the *weighted residuals approach*, based on Galerkin's method
- the *energy balance approach*, based on the balance of thermal and/or mechanical energy of a system

Mitsoulis (1984) has used the variational approach for both flow and heat transfer analysis. This approach, however, is only applicable for a limited class of differential equations. On the other hand, the weighted residuals approach (Galerkin's method) provides a convenient means to cast any differential equation into integral form and will be adopted in this work.

Another point concerns the discretization of the domain into small subdomains, called finite elements. For the flow analysis, the same discretiza-

tion scheme used by Mitsoulis (1984) is employed. However, due to persistent difficulties in obtaining oscillation-free temperature solutions in highly convective flows, a different discretization scheme has been used for the solution of the energy equation.

3.3.1 Velocity-Pressure (u-w-p) Formulation

Using the method of weighted residuals (Huebner and Thornton, 1982), the continuity and momentum Equations 2.17–2.19 are written as the following integral equations:

$$\int_{A^{(e)}} \left[\frac{\partial v_r}{\partial r} + \frac{v_r}{r} + \frac{\partial v_z}{\partial z} \right] W_i \, dA = 0 \tag{3.16}$$

$$\int_{A^{(e)}} \left[-\frac{\partial p}{\partial r} + \frac{\partial \tau_{rr}}{\partial r} + \frac{\tau_{rr}}{r} + \frac{\partial \tau_{rz}}{\partial z} - \frac{\tau_{\theta\theta}}{r} \right] W_i \, dA = 0 \tag{3.17}$$

$$\int_{A^{(e)}} \left[-\frac{\partial p}{\partial z} + \frac{\partial \tau_{rz}}{\partial r} + \frac{\tau_{rz}}{r} + \frac{\partial \tau_{zz}}{\partial z} \right] W_i \, dA = 0 \tag{3.18}$$

where W_i are the weighting functions, and $A^{(e)}$ is the solution domain for element (e). Then by applying integration by parts using Green's theorem (Huebner and Thornton, 1982), Equations 3.16–3.18 become:

$$\int_{A^{(e)}} \left[\frac{\partial v_r}{\partial r} + \frac{v_r}{r} + \frac{\partial v_z}{\partial z} \right] W_i \, dA = 0 \tag{3.19}$$

$$\int_{A^{(e)}} \left[(-p + \tau_{rr}) \frac{\partial W_i}{\partial r} + \tau_{rz} \frac{\partial W_i}{\partial z} + \left(\frac{\tau_{rr}}{r} - \frac{\tau_{\theta\theta}}{r} \right) W_i \right] dA = \int_{\Gamma^{(e)}} T_r W_i \, d\Gamma \tag{3.20}$$

$$\int_{A^{(e)}} \left[(-p + \tau_{zz}) \frac{\partial W_i}{\partial z} + \tau_{rz} \frac{\partial W_i}{\partial r} + \frac{\tau_{rz}}{r} W_i \right] dA = \int_{\Gamma^{(e)}} T_z W_i \, d\Gamma \tag{3.21}$$

where $\Gamma^{(e)}$ is the boundary for element (e) that also lies on the domain boundary; T_r and T_z are the r and z components of the surface traction $\overline{T}$ given by:

$$T_r = (\tau_{rr} - p) n_r + \tau_{rz} n_z \tag{3.22}$$

$$T_z = \tau_{rz} n_r + (\tau_{zz} - p) n_z \tag{3.23}$$

where n_r and n_z denote direction cosines of the outward unit normal vector $\overline{n}$. By relating the stresses to the rates-of-strain through an appropriate constitutive equation, Equations 3.19–3.21 may now be discretized. This must be done by an appropriate choice of element. Once an element has been chosen, the continuous function that relates the nodal values of the field variables and sometimes the nodal values of their derivatives to anywhere else within the element has been fixed. These continuous functions are called "interpolation functions." Mathematical considerations require that the interpolation functions for velocity should be higher by one order than the interpolation functions for pressure (Taylor and Hood, 1973).

Thus, a quadratic triangular element as shown in Figure 3.3 is chosen. The velocities v_r (or u) and v_z (or w) are interpolated by a quadratic polynomial whereas the pressure p is interpolated by a linear polynomial. Thus, we have

$$u = \sum_{i=1}^{6} N_i u_i \tag{3.24}$$

$$w = \sum_{i=1}^{6} N_i w_i \tag{3.25}$$

$$p = \sum_{i=1}^{3} L_i p_i \tag{3.26}$$

where N_i are the "interpolation (shape) functions." These are related to the "natural (area) coordinates" L_i for a triangle by the expressions

$$\begin{aligned} N_1 &= L_1(2L_1 - 1) \quad , \quad N_4 = 4L_1L_2 \\ N_2 &= L_2(2L_2 - 1) \quad , \quad N_5 = 4L_2L_3 \\ N_3 &= L_3(2L_3 - 1) \quad , \quad N_6 = 4L_3L_1 \end{aligned} \tag{3.27}$$

The natural coordinates L_i are defined by

$$L_i = \frac{A_i}{A} \tag{3.28}$$

where the areas A_i and A are given in standard textbooks (e.g. Huebner and Thornton, 1982). In addition, the derivatives of u and w could be

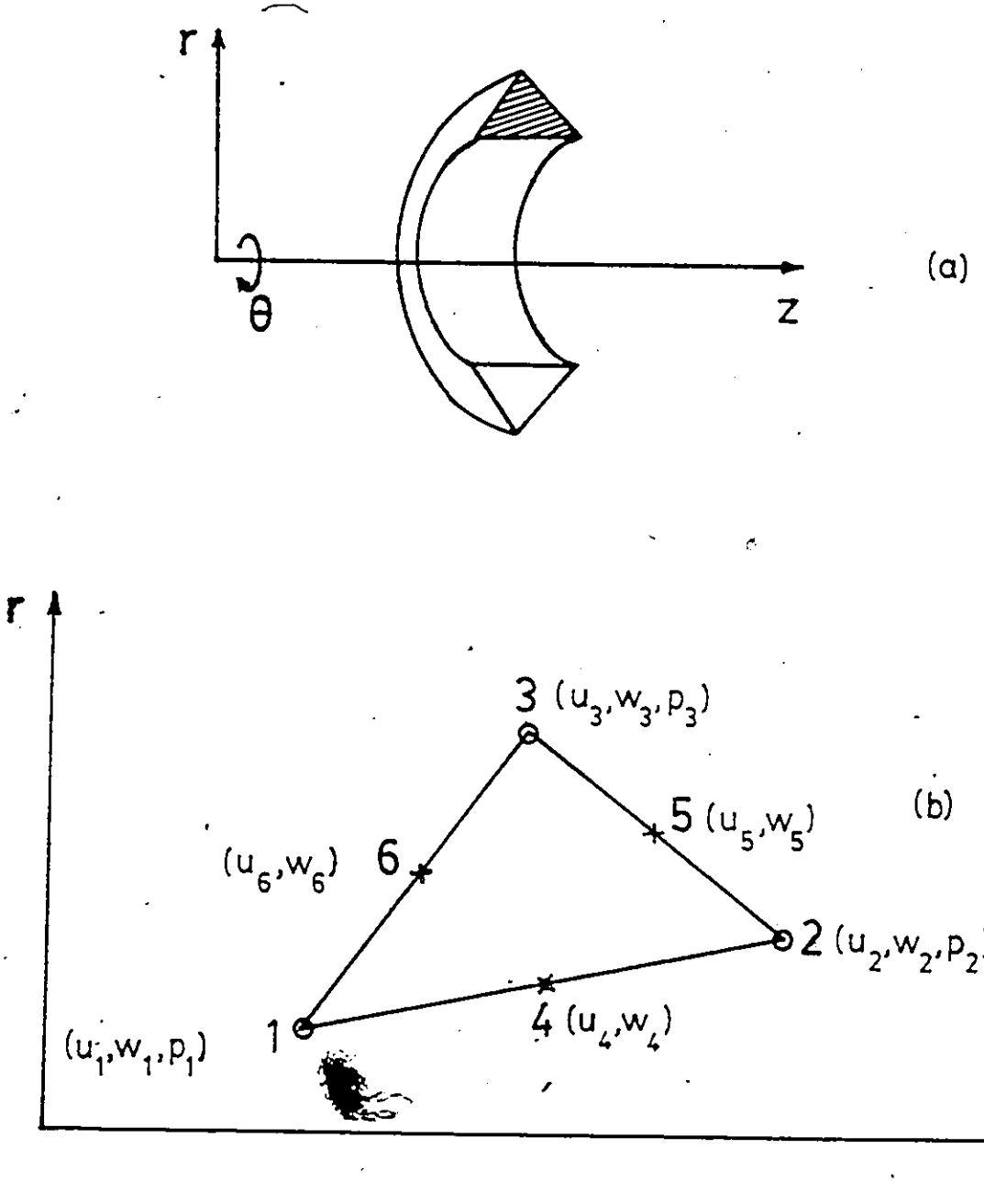

Figure 3.3: (a) Axisymmetric Ring Element with Triangular Cross Section.

(b) A Quadratic Triangular Element for u-w-p Formulation.

obtained as

$$\begin{aligned} \frac{\partial u}{\partial r} &= \sum_{i=1}^{6}\left(\frac{\partial N_i}{\partial r}\right)u_i \quad , \quad \frac{\partial u}{\partial z} = \sum_{i=1}^{6}\left(\frac{\partial N_i}{\partial z}\right)u_i \\ \frac{\partial w}{\partial r} &= \sum_{i=1}^{6}\left(\frac{\partial N_i}{\partial r}\right)w_i \quad , \quad \frac{\partial w}{\partial z} = \sum_{i=1}^{6}\left(\frac{\partial N_i}{\partial z}\right)w_i \end{aligned} \tag{3.29}$$

Galerkin's method consists of substituting the weighting functions W_i by the corresponding interpolation functions N_i and L_i, i.e.:

$$\int_{A^{(e)}}\left[\frac{\partial v_r}{\partial r}+\frac{v_r}{r}+\frac{\partial v_z}{\partial z}\right]L_i\,dA = 0 \tag{3.30}$$

$$\int_{A^{(e)}}\left[(-p+\tau_{rr})\frac{\partial N_i}{\partial r}+\tau_{rz}\frac{\partial N_i}{\partial z}+\left(\frac{\tau_{rr}}{r}-\frac{\tau_{\theta\theta}}{r}\right)N_i\right]dA = \int_{\Gamma^{(e)}}T_r N_i\,d\Gamma \tag{3.31}$$

$$\int_{A^{(e)}}\left[(-p+\tau_{zz})\frac{\partial N_i}{\partial z}+\tau_{rz}\frac{\partial N_i}{\partial r}+\frac{\tau_{rz}}{r}N_i\right]dA = \int_{\Gamma^{(e)}}T_z N_i\,d\Gamma \tag{3.32}$$

Equations 3.30–3.32 when applied at the nodes of the discretized flow domain along with the appropriate boundary conditions, provide as many equations as there are unknown nodal velocity and pressure variables.

By choosing an appropriate number of Gaussian integration points, Equations 3.30–3.32 are numerically integrated over an element. As the domain of interest contains many elements, the contributions from all the elements are taken into account by a global assemblage procedure. The final matrix equation is of the form

$$[K]\{X\} = \{F\} \tag{3.33}$$

where $[K]$ is a symmetric stiffness matrix, $\{X\}$ is the vector of the nodal unknowns and $\{F\}$ a load vector containing body forces and surface tractions. Then the boundary conditions are introduced by a standard procedure (Huebner and Thornton, 1982). Solving Equation 3.33 with a standard matrix solver gives the solution of u, w and p at the appropriate nodes in the domain. For a generalized Newtonian fluid, a successive substitution scheme (Picard method) is used for the non-linear system of equations because of its simplicity and wider range of convergence (Mitsoulis and Vlachopoulos, 1984b).

For the analysis of coextrusion of stratified multilayer flows, there is a discontinuity of fluid properties across the interface. In order to satisfy the boundary conditions at the interface (Equations 2.39–2.42), the pressures at the interface must be discontinuous. The discontinuity of pressures comes from the following analysis (Mitsoulis, 1986a; Mavridis et al., 1987):

The continuity equation at the interface, for incompressible fluids, may be written for each fluid:

Fluid I

$$\frac{\partial v_{t,I}}{\partial \bar{t}} + \frac{\partial v_{n,I}}{\partial \bar{n}} = 0 \tag{3.34}$$

Fluid *II*

$$\frac{\partial v_{t,II}}{\partial \bar{t}} + \frac{\partial v_{n,II}}{\partial \bar{n}} = 0 \tag{3.35}$$

Taking the derivatives of Equation 2.39:

$$\frac{\partial v_{t,I}}{\partial \bar{t}} = \frac{\partial v_{t,II}}{\partial \bar{t}} = \frac{\partial v_t}{\partial \bar{t}} \tag{3.36}$$

and substituting into Equations 3.34 and 3.35 gives:

$$\frac{\partial v_{n,I}}{\partial \bar{n}} = \frac{\partial v_{n,II}}{\partial \bar{n}} = -\frac{\partial v_t}{\partial \bar{t}} \tag{3.37}$$

Substituting Equation 3.37 into 2.42, and rearranging the latter Equation gives:

$$(p_{II} - p_I) = 2(\eta_I - \eta_{II})\frac{\partial v_t}{\partial t} \tag{3.38}$$

Equation 3.38 states that there will be a pressure discontinuity whenever $\eta_I \neq \eta_{II}$ and $\partial v_t/\partial \bar{t} \neq 0$. This discontinuity invalidates the continuous approximation adopted by a standard application of the finite-element method and requires a special treatment.

In order to handle such discontinuity in the pressure, a double-node technique (Mitsoulis, 1986a; Mavridis et al., 1987) is used. This technique involves using a discontinuous finite-element grid having two values for the primitive variables (velocities and pressure) on two different nodes at the

same spatial location. Primitive variables that are continuous are specified as such, interface boundary conditions are applied directly, and the finite jump in the discontinuous variables is determined from the solution of the global system.

Referring to Figure 3.4, at the interface, nodes i and $i+1$, j and $j+1$, and k and $k+1$ have the same coordinates, respectively, i.e.:

$$\begin{aligned} r_i &= r_{i+1} \quad , \quad z_i = z_{i+1} \\ r_j &= r_{j+1} \quad , \quad z_j = z_{j+1} \\ r_k &= r_{k+1} \quad , \quad z_k = z_{k+1} \end{aligned} \tag{3.39}$$

In addition, the velocities at these nodes are constrained as follows:

$$\begin{aligned} \overline{v}_{i+1} &= \overline{v}_i \\ \overline{v}_{j+1} &= \overline{v}_j \\ \overline{v}_{k+1} &= \overline{v}_k \end{aligned} \tag{3.40}$$

However, pressures at these nodes are unconstrained. In general, for two-dimensional flows, pressures are not equal at the interface. By using this double-node discretization technique, the FEM formulation for single-layer flows can be applied to stratified multilayer flows with only minor changes in the computer program.

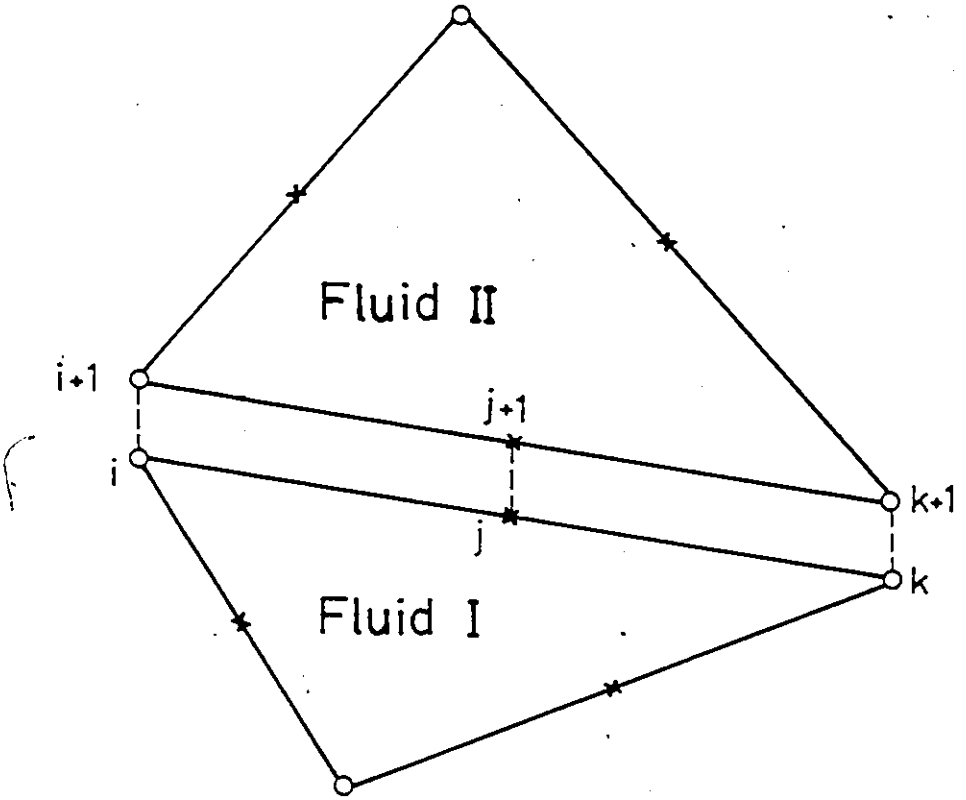

Figure 3.4: Double Nodes at the Interface.

3.3.2 Temperature Formulation

Using the method of weighted residuals (Huebner and Thornton, 1982) with weighting functions W_i, Equation 2.20 is put in the form:

$$\int_{A^{(e)}} \left[k \left(\frac{1}{r}\frac{\partial T}{\partial r} + \frac{\partial^2 T}{\partial r^2} + \frac{\partial^2 T}{\partial z^2} \right) + Q_d + \rho C_p \left(v_r \frac{\partial T}{\partial r} + v_z \frac{\partial T}{\partial z} \right) \right] W_i dA = 0 \tag{3.41}$$

where $A^{(e)}$ is the solution domain for element (e), and Q_d is the viscous dissipation term. We also assume constant and isotropic material properties (k, ρ and C_p). Then by applying integration by parts using Green's theorem (Huebner and Thornton, 1982), Equation 3.41 becomes:

$$\begin{aligned} &\int_{A^{(e)}} k \left(\frac{\partial W_i}{\partial r}\frac{\partial N_j}{\partial r} + \frac{\partial W_i}{\partial z}\frac{\partial N_j}{\partial z} + \frac{1}{r} W_i \frac{\partial N_j}{\partial r} \right) \{T\}^{(e)} \, dA \\ &\quad + \int_{A^{(e)}} \rho C_p W_i \left(v_r \frac{\partial N_j}{\partial r} + v_z \frac{\partial N_j}{\partial z} \right) \{T\}^{(e)} \, dA \\ &\quad + \int_{\Gamma^{(e)}} (\overline{q} \cdot \overline{n}) W_i d\Gamma - \int_{A^{(e)}} Q_d W_i dA = 0 \end{aligned} \tag{3.42}$$

where

$\{T\}^{(e)}$ = temperature at the nodes for element (e)

$\overline{q} \cdot \overline{n}$ = normal outward heat flux at the boundary $\Gamma^{(e)}$ for element (e)

$A^{(e)}$ = solution domain for element (e)

$\Gamma^{(e)}$ = boundary for element (e)

W_i = weighting function for node i of element (e)

N_i = interpolation function for node i of element (e)

In standard Galerkin formulation, $W_i \equiv N_i$. The solution is not oscillatory if the convective term is relatively small compared with the conductive term. But if the opposite is true, the temperature solution will be oscillatory (Huebner and Thornton, 1982). The degree of oscillations depends very much on the relative magnitude of the convective term to the conductive term, which is measured by the Peclet number (Pe) defined previously (Equation 2.33). In order to suppress the oscillations, a consistent Steamline-Upwind/Petrov-Galerkin (SU/PG) formulation developed by Hughes and Brooks (1979, 1982) and Brooks and Hughes (1982) has been implemented. Further details of this method can be found in Appendix A.

Bilinear isoparametric Lagrangian quadrilaterals are used to discretize the domain of interest. An example of this element is shown in Figure 3.5. It has four nodes with four straight edges. Therefore, two quadratic triangular elements could be used to form four bilinear elements (Figure 3.6). The temperatures and coordinates at the four nodes are linearly interpolated as follows:

$$T = \sum_{i=1}^{4} N_i(\xi,\eta)T_i \tag{3.43}$$

$$\begin{aligned} r &= \sum_{i=1}^{4} N_i(\xi,\eta)r_i \\ z &= \sum_{i=1}^{4} N_i(\xi,\eta)z_i \end{aligned} \tag{3.44}$$

where N_i's are given by:

$$\begin{aligned} N_1(\xi,\eta) &= \frac{1}{4}(\xi-1)(\eta-1) \\ N_2(\xi,\eta) &= -\frac{1}{4}(\xi+1)(\eta-1) \\ N_3(\xi,\eta) &= \frac{1}{4}(\xi+1)(\eta+1) \\ N_4(\xi,\eta) &= -\frac{1}{4}(\xi-1)(\eta+1) \end{aligned} \tag{3.45}$$

In the above r and z are global coordinates and ξ and η are local coordinates. In order to perform the integration on Equation 3.42, transformation

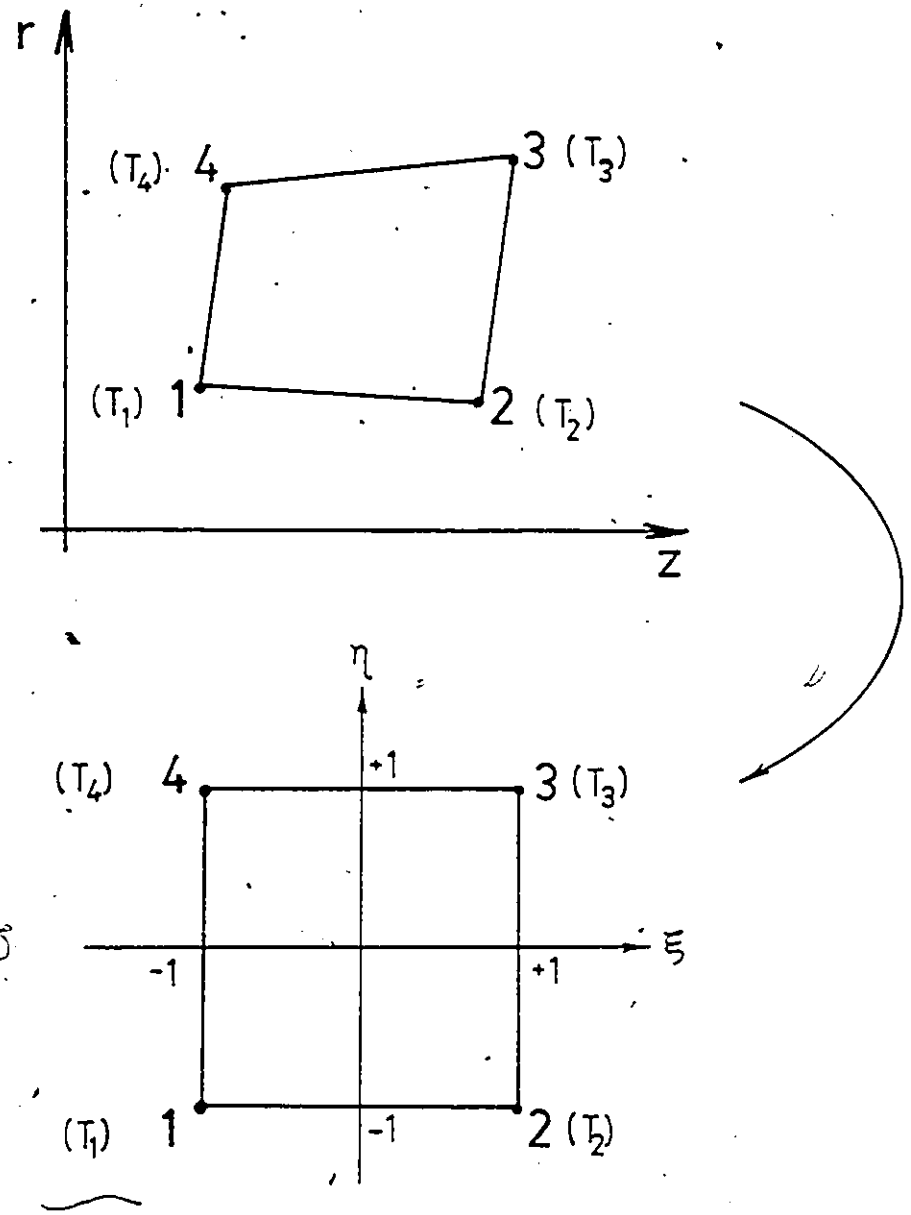

Figure 3.5: Bilinear Isoparametric Quadrilateral Element.

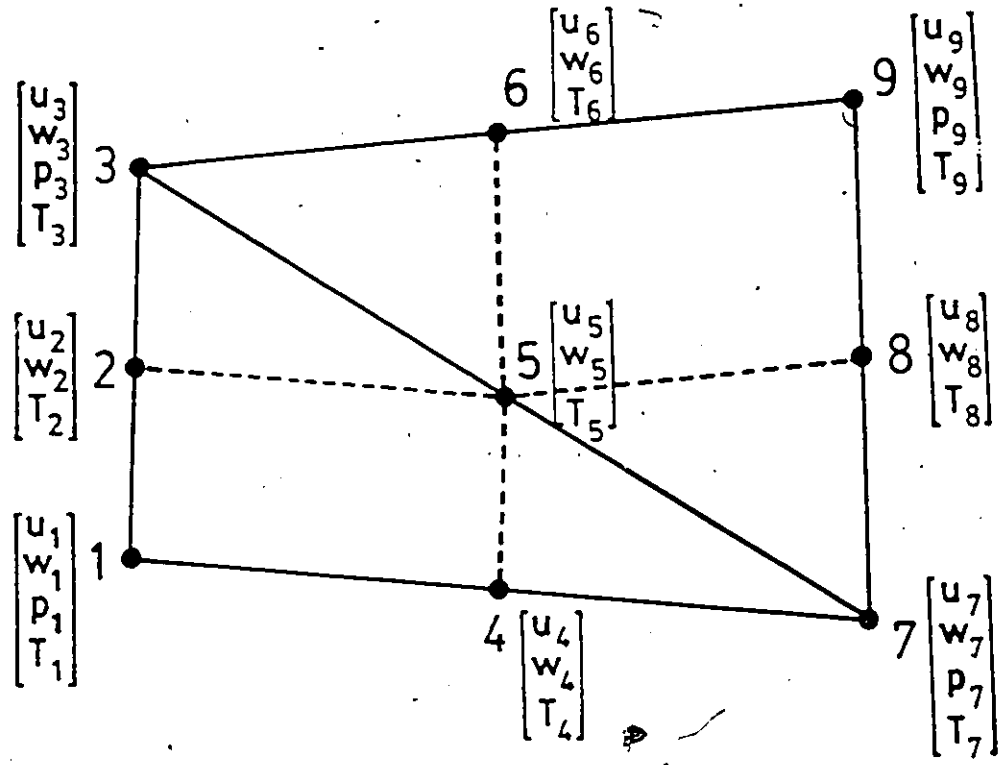

Figure 3.6: Two 6-Node Quadratic Triangles for u-w-p Formulation Subdivided into Four 4-Node Bilinear Quadrilaterals for Temperature/Stream Function Formulation (Dashed Lines).

of coordinates is required using the Jacobian matrix:

$$\begin{Bmatrix} \frac{\partial()}{\partial\xi} \\ \frac{\partial()}{\partial\eta} \end{Bmatrix} = \begin{bmatrix} \frac{\partial r}{\partial\xi} & \frac{\partial z}{\partial\xi} \\ \frac{\partial r}{\partial\eta} & \frac{\partial z}{\partial\eta} \end{bmatrix} \begin{Bmatrix} \frac{\partial()}{\partial r} \\ \frac{\partial()}{\partial z} \end{Bmatrix} = [J] \begin{Bmatrix} \frac{\partial()}{\partial r} \\ \frac{\partial()}{\partial z} \end{Bmatrix} \tag{3.46}$$

where () represents any variable and $[J]$ defines the Jacobian matrix:

$$[J] = \begin{bmatrix} \frac{\partial r}{\partial\xi} & \frac{\partial z}{\partial\xi} \\ \frac{\partial r}{\partial\eta} & \frac{\partial z}{\partial\eta} \end{bmatrix} \tag{3.47}$$

$[J]$ is evaluated by substituting Equation 3.44 into Equation 3.47. Thus, from Equation 3.46:

$$\begin{Bmatrix} \frac{\partial()}{\partial r} \\ \frac{\partial()}{\partial z} \end{Bmatrix} = [J]^{-1} \begin{Bmatrix} \frac{\partial()}{\partial\xi} \\ \frac{\partial()}{\partial\eta} \end{Bmatrix} \tag{3.48}$$

To complete the evaluation of the integral in Equation 3.42, the area $drdz$ is

$$drdz = |J|\, d\xi d\eta \tag{3.49}$$

where $|J|$ is the determinant of $[J]$.

Equation 3.42 is numerically integrated over an element using the appropriate Gaussian integration points. Again, a global assemblage of the individual elements gives rise to a matrix equation of the form similar to Equation 3.33 where $[K]$ is generally unsymmetric (if the convection term

is included), and $\{F\}$ is a load vector containing the viscous dissipation term and the appropriate fixed and/or natural boundary conditions.

3.3.3 Stream Function Formulation

In fluid mechanics the stream function ψ and the vorticity ω are of great importance. For axisymmetric flows these are defined by

$$r\,u = -\frac{\partial \psi}{\partial z} \quad , \quad r\,w = \frac{\partial \psi}{\partial r} \tag{3.50}$$

$$\omega = \frac{\partial w}{\partial r} - \frac{\partial u}{\partial z} \tag{3.51}$$

Taking the derivatives of Equation 3.50 and substituting into Equation 3.51 gives

$$\nabla^2 \psi = -\omega \tag{3.52}$$

The above equation is called the Poisson equation and is valid for any axisymmetric flow of any fluid. Its usefulness lies in the fact that enables us to visualize the flow field by constructing streamlines from the stream function ψ.

The same finite element formulation used for temperatures (bilinear elements) can also be used for the stream function ψ, by realizing that the

energy equation with no convection satisfies a Poisson equation of the form

$$k\,\nabla^2 T = -Q_d \tag{3.53}$$

where $Q_d = \bar{\bar{\tau}} : \nabla \bar{v}$ is the viscous dissipation term. Comparison with Equation 3.52 shows the equivalence for $k = 1$, $T = \psi$, and $Q_d = \omega$. A solution of a flow field (u-w-p formulation) gives ω, and the stream function can, therefore, be obtained *a posteriori* by solving the Poisson equation with the FEM and the appropriate boundary conditions.

3.4 Free Surface/Interface Flows

Flows with free surfaces/interfaces in polymer processing are encountered whenever a fluid exits from a die to the atmosphere (free surface flows) or when two fluids meet in the die (e.g. interface formation in coextrusion flows). These problems are particularly difficult to solve since not only the flow characteristics (velocities, pressures, temperatures, etc.) are unknown but also the location of the free surface/interface that forms part of the boundary is unknown. The only condition that makes this class of problems solvable is the fact that no fluid can flow through a free surface/interface,

which are streamlines. Hence, at the free surface/interface

$$\overline{n} \cdot \overline{v} = 0 \tag{3.54}$$

where $\overline{n}$ is the unit outward normal vector to the surface and $\overline{v}$ the velocity vector.

The FEM is very attractive for free surface/interface problems because of the ability of the elements to deform and take the shape of the flowing fluid. A simple procedure originally developed by Nickell et al. (1974) is to assume at first a location for the free surface (usually an extension of the solid boundary line that the fluid last encountered) and solve the system of conservation equations for these boundaries. Once the velocity field has been found, a streamline can be constructed based on the velocities u and w found on that surface and the equation that defines a streamline, i.e.

$$\frac{w}{dz} = \frac{u}{dr} \tag{3.55}$$

Integration of Equation 3.55 can be carried out (usually numerically by applying Simpson's rule) to locate a new surface $h_{new}(z)$ which is given by

$$h_{new}(z) = h_o + \int_0^l \frac{u}{w}\, dz \tag{3.56}$$

where $h_o = h_{new}(0)$ and l is the length in the z-direction. The old surface

is then updated using:

$$h^{i+1}(z) = h^i(z) + \lambda[h_{new}(z) - h^i(z)] \tag{3.57}$$

where $h^{i+1}(z)$ is the updated surface, $h^i(z)$ is the old surface, and λ is a relaxation factor.

With the updated boundary, the system of conservation equations is solved again in the new domain. Recent velocities are used to compute a new surface and the process is repeated until no change in the location of the free surface is observed.

Mitsoulis (1986,1987) extended Nickell et al.'s approach to handle interfaces in coextrusion flows. The same method has been used quite recently by Mavridis et al. (1987). In most cases of free surface flows from extrusion dies, $\lambda = 1$ (Picard-like iteration) gives satisfactory convergence. However, for interface problems, when Picard iteration fails to converge, an underrelaxation factor $\lambda = 0.5$ is recommended (Mavridis et al., 1987).

Finally, a more general procedure for handling unusual free surfaces/interfaces in complex flows has been developed by Kistler (1984), and is known as u-w-p-h formulation. In this, the coordinates h_i of the free surface/interface are not decoupled from the system of equations, but solved for simultane-

ously with the other primary variables. A grand Newton's scheme has also been implemented for the u-w-p-h formulation, having a quadratic convergence. However, extensive computer storage and execution time are considered the main drawbacks of this new method (Kistler and Scriven, 1984).

Chapter 4

Preliminary Tests and Results

Before proceeding with the numerical analysis of actual extrusion processes, the finite element program was tested against some well-known one- and two-dimensional cases. Comparisons were made with analytical solutions (whenever available) or numerical solutions reported in the literature.

The ability of FEM to determine the location of unknown *a priori* free surfaces was tested in the isothermal extrusion of Newtonian fluids. The flow of Newtonian fluids through an orifice was first analyzed. Following that, the flow of Newtonian fluids through converging and diverging annular dies was examined. The purpose was to investigate the effect of geometry on the swelling phenomena associated with the extrudate. In addition, these

tests also serve to evaluate the validity of the velocities-pressure formulation used.

In order to perform nonisothermal analysis, the temperature program developed was tested against several one-dimensional problems that have analytical solutions. The one-dimensional heat conduction-convection problem with no source term was first analyzed. Then, a convective heat transfer problem with a source term was solved. These tests serve to evaluate the validity of the new temperature program developed.

4.1 Flow of a Newtonian Fluid through an Orifice

Plastic rods are made by the extrusion of polymer melts through tubular dies. Upon exiting from the die, viscoelastic fluids exhibit a considerable increase in the cross-sectional area of the emerging jet. This phenomenon is usually called "extrudate swell" (die swell). The extent of swelling for a polymer fluid depends very much on the length-to-diameter ratio (L/D) of the die. A typical polymer melt behaviour is shown in Figure 4.1 (Vlachopoulos, 1981), where B is the swell ratio (d/D). An orifice of zero

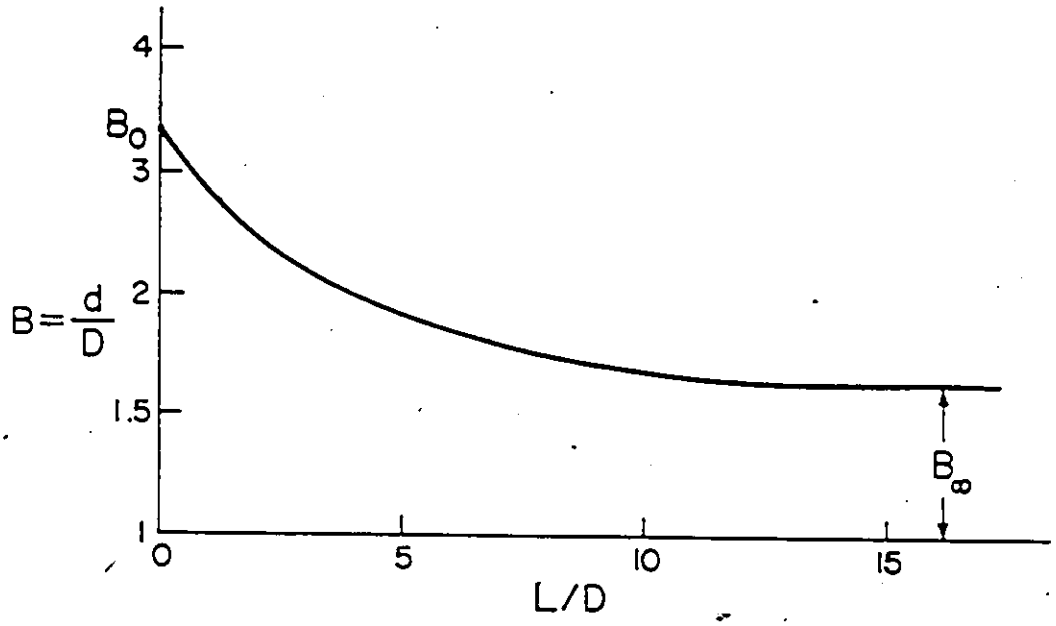

Figure 4.1: Variation of Polymer Extrudate Swell with L/D Ratio.

length produces the maximum swelling B_o, whereas a sufficiently long die produces an asymptotic value B_∞ which depends on the polymer melt used and the flow rate. Various attempts in the literature to numerically simulate the swelling phenomena associated with polymer melts have not shown promising results so far (Crochet and Walters, 1983). However, at the time of writing this thesis, Tanner (1987) apparently has successfully simulated the extrudate swell phenomenon for an LDPE melt using a viscoelastic model with strain history.

Although inelastic in nature, the Newtonian fluid has also been observed to swell (Middleman and Gavis, 1961). The numerical predictions of this swelling phenomenon from a long capillary tube have been quite successful (Tanner, 1973; Allan, 1977; Omodei, 1979; Chang et al., 1979). However, no work has been done to investigate the effect of L/D for an orifice (capillary die with $L/D \ll 1$) on the swelling of a Newtonian jet.

In this analysis, the diameter of the reservoir is four times the diameter of the orifice (also known as a 4:1 contraction). Nguyen and Boger's experiments (1979) have shown that the flow kinematics depend little on contraction ratio, in the range between 4:1 and 12:1. Thus, a contraction ratio of 4:1 is sufficient to represent the flow of polymer melts from a large

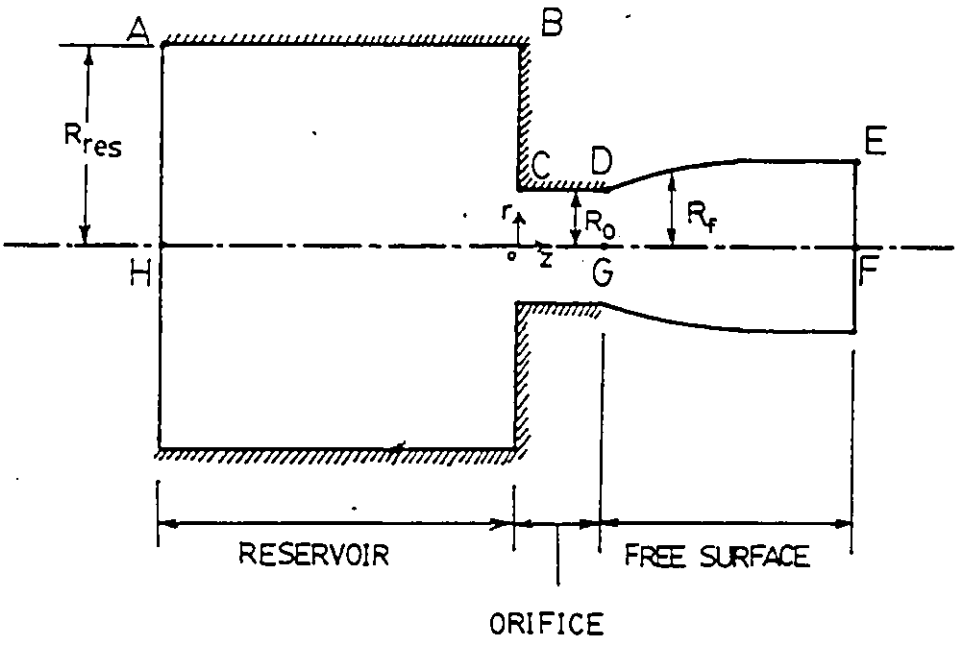

Figure 4.2: Schematic Diagram for the Flow of a Newtonian Fluid through an Orifice.

reservoir into a small capillary. The L/D (orifice length/orifice diameter) ratios investigated in this study are: 0.5, 0.15, 0.1, 0.05 and 0.0. The physical system for the analysis of this flow problem is illustrated in Figure 4.2 and is representative of flow of polymer melts from a reservoir through an orifice before being extruded into the atmosphere. Due to symmetry, the calculation was done on only half of the domain (area bounded by ABCDEFGHA). In all cases, the boundary conditions were assigned as follows:

1. Along boundary AH, the well-known fully-developed Poiseuille velocity profile was imposed (Bird et al., 1960):

$$v_z = v_{z,max}\left[1 - \left(\frac{r}{R_{res}}\right)^2\right] \tag{4.1}$$

$$v_r = 0 \tag{4.2}$$

where

$$0 < r < R_{res} \tag{4.3}$$

Note that $v_{z,max}$ is the maximum axial velocity at the centerline.

2. Along boundary ABCD, no-slip boundary condition was prescribed:

$$v_z|_{r=R_{res}} = 0 \tag{4.4}$$

$$v_r|_{r=R_{res}} = 0 \tag{4.5}$$

3. Along boundary FGH, zero radial velocities were assigned due to symmetry:

$$v_r|_{r=0} = 0 \tag{4.6}$$

4. Along boundary EF, the surface traction normal to the surface was set to zero,

$$\overline{T} \cdot \overline{n} = 0 \tag{4.7}$$

and the velocity tangential to the plane was set to zero:

$$\overline{v} \cdot \overline{t} = v_r = 0 \tag{4.8}$$

5. Along boundary DE, the zero surface traction condition was set:

$$\overline{T} \cdot \overline{n} = 0 \tag{4.9}$$

Since only Newtonian fluids are considered and the results are in dimensionless form, the actual values of $v_{z,max}$ and R_{res} do not affect the swelling.

A typical FEM grid used for the u-w-p formulation is shown in Figure 4.3. All the grids used have 336 u-w-p elements and 741 nodes (13 nodes across and 57 nodes along). Different distributions of the grid were used for different L/D ratios. A denser grid is used near the orifice to

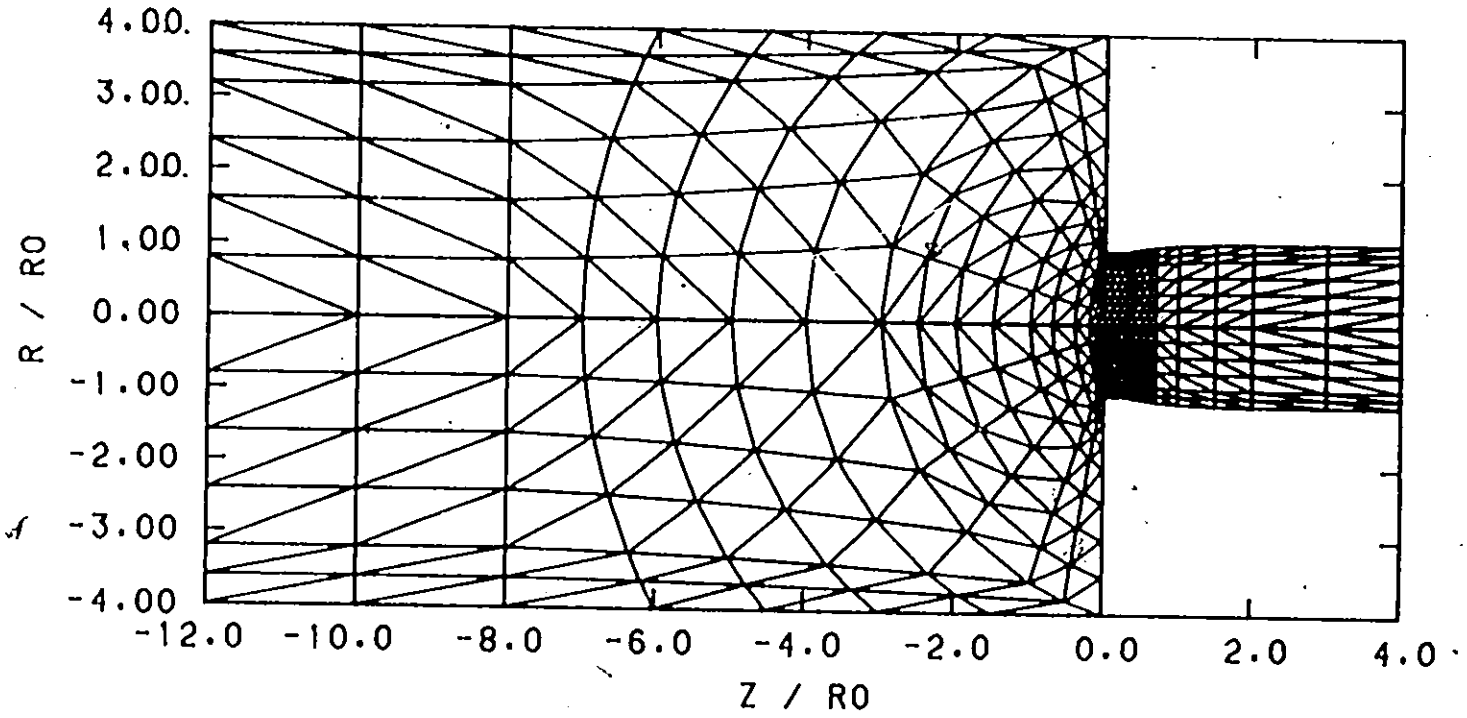

Figure 4.3: Finite Element Grid for the Flow of a Newtonian Fluid through an Orifice ($L/D = 0.15$).

better capture the stress singularity at the entry point C and exit point D (Mitsoulis, 1984). In addition, it is also used to capture the shape of the free surface, which is rapidly changing after leaving the die. The use of such dense grids ensures that the results are virtually free from mesh influence.

The stream function formulation was also employed in order to visualize the flow field via streamlines. Referring to Figure 4.2, the boundary conditions used were:

1. Along boundary ABCDE:

$$\psi = 0 \tag{4.10}$$

2. Along boundary FGH:

$$\psi = \psi|_{R_{rec}} \tag{4.11}$$

3. Along boundary AH:

$$\frac{\partial \psi}{\partial n} = 0 \tag{4.12}$$

4. Along boundary EF:

$$\frac{\partial \psi}{\partial n} = 0 \tag{4.13}$$

Note that $\psi|_{R_{rec}}$ is a measure of the total volumetric flow rate of the system

under investigation. Integrating Equation 4.1 gives

$$\begin{aligned} \psi|_{R_{res}} &= \int_0^{R_{res}} v_z\, r\, dr \\ &= v_{z,max}\, \frac{R_{res}^2}{4} \end{aligned} \tag{4.14}$$

using the definition of the stream function.

The only non-linearity present in this problem is the unknown *a priori* free surface. The successive substitution method (Picard iteration) was used to determine the free surface. Initially, boundary CDE (Figure 4.2) was assumed to be a straight line. The free surface (boundary DE) was then updated at each iteration. Convergence is assumed when the location of a free surface reaches a stable value i.e. deviation of the present location from the previous one is less than 0.1%. In each case, four iterations were required to attain this criterion. The average computation time (CPU time) required for each L/D run was approximately 120 seconds.

Diameter swell ratio (or simply diameter swell) was used to determine the degree that the Newtonian fluid swells. In this context, diameter swell is defined as

$$B = \text{diameter swell} = \frac{\text{extrudate radius}}{\text{orifice radius}} = \frac{\text{EF}}{\text{DG}} \tag{4.15}$$

where both the distances EF and DG are shown in Figure 4.2. The diameter

Table 4.1: Diameter Swell for the Flow of a Newtonian Fluid through an Orifice.

L/D Ratio	Diameter Swell, B
0.50	1.132
0.15	1.131
0.10	1.124
0.05	1.114
0.00	1.082

swell for each L/D run is tabulated in Table 4.1 and plotted on Figure 4.4.

As can be seen, the diameter swell reaches a plateau (about 13% swell ratio) when $L/D > 0.15$. Any increase in the L/D of the orifice will not significantly affect the swell ratio ($< 0.1\%$). As a result, the diameter swell for $L/D = 0.15$ and $L/D \to \infty$ are virtually the same. On the other hand, a decrease in the L/D causes the swell to decrease. In a limiting case, when $L/D = 0$, the Newtonian fluid swells about 8%. In all cases, the free surfaces attained their final values within an axial distance equal to three times the radius of the orifice and remained unchanged farther downstream. An example of the shape of the free surface for the $L/D = 0.15$ case is shown

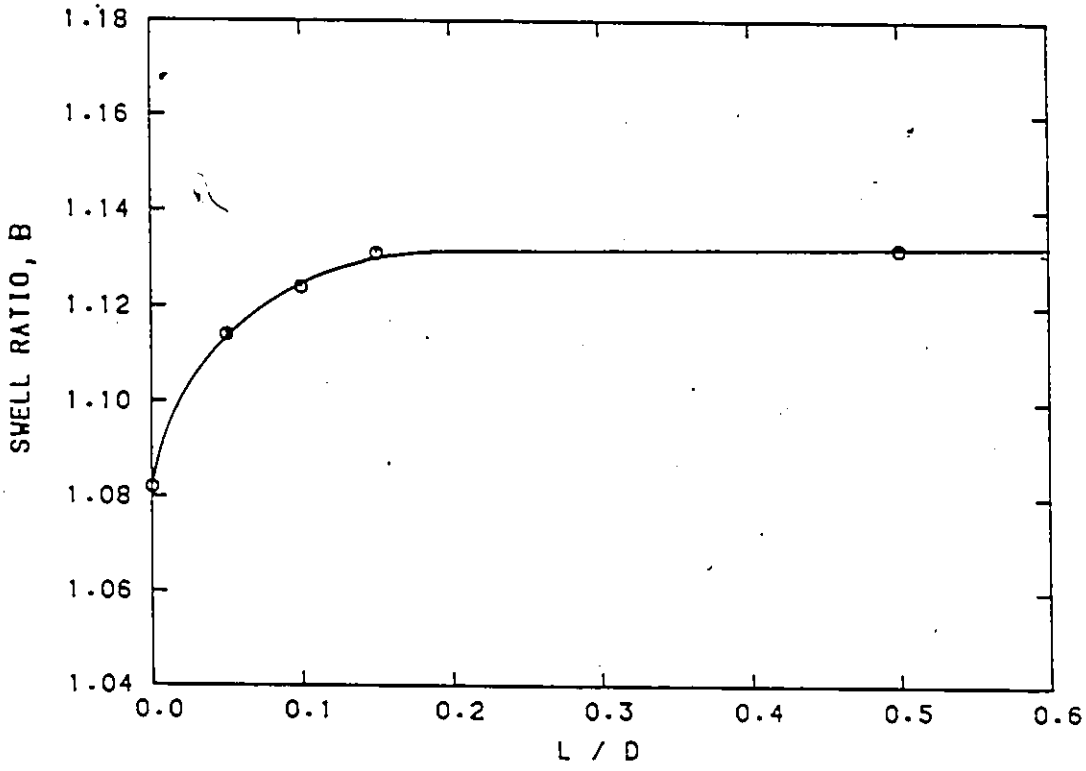

Figure 4.4: Diameter Swell for the Flow of a Newtonian Fluid through an Orifice.

in Figure 4.5. Note that the ordinate of the graph is highly exaggerated with respect to the abscissa.

For a Newtonian fluid emerging from a capillary die the swelling ratio was found to be 13.2% (refer to Table 4.1 for $L/D = 0.5$). The numerical results available in the literature (for $L/D \rightarrow \infty$) have shown that the swelling ratio depends slightly on the finite element grid. The results range from 12.6% (Crochet and Keunings, 1980) to 14.3% (Crochet and Keunings, 1982b). Recently, Tanner (1982) used a boundary element method and determined the Newtonian swell as being 12.844%, while calculations with very refined finite element grids have given 12.855% (Tanner, 1982) and 13% (Omodei, 1979).

The flow field is visualized through velocity vectors and streamlines. An example of the velocity field for $L/D = 0$ and streamline pattern for $L/D = 0.15$ are shown in Figures 4.6 and 4.7, respectively.

As can be seen from these graphs, in the area near the corner of the reservoir, the flow is very weak resembling an almost stagnant region. Negative small velocities also appear and the direction of the arrows reveals the existence of a small and weak vortex forming in the corners. This is best demonstrated via the streamlines. The stream function has been normal-

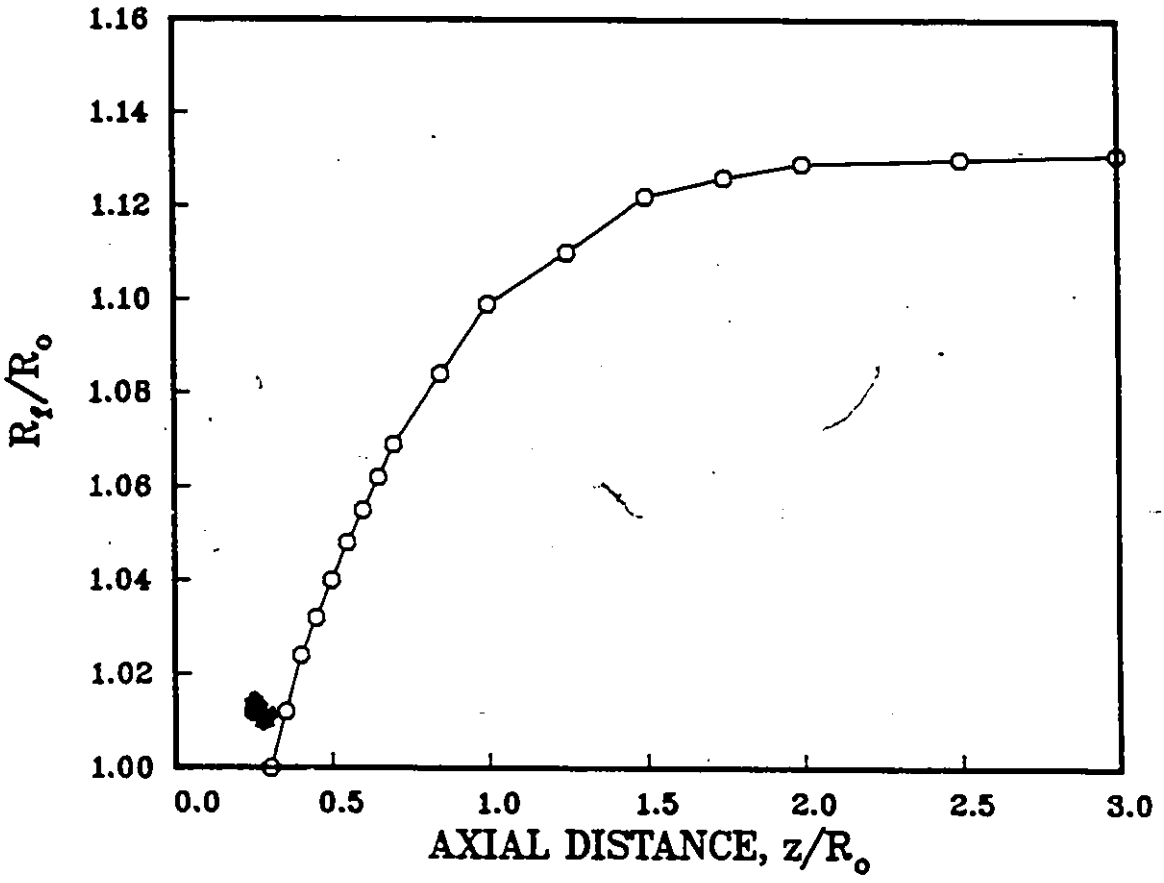

Figure 4.5: Shape of Free Surface for the Flow of a Newtonian Fluid through an Orifice ($L/D = 0.15$).

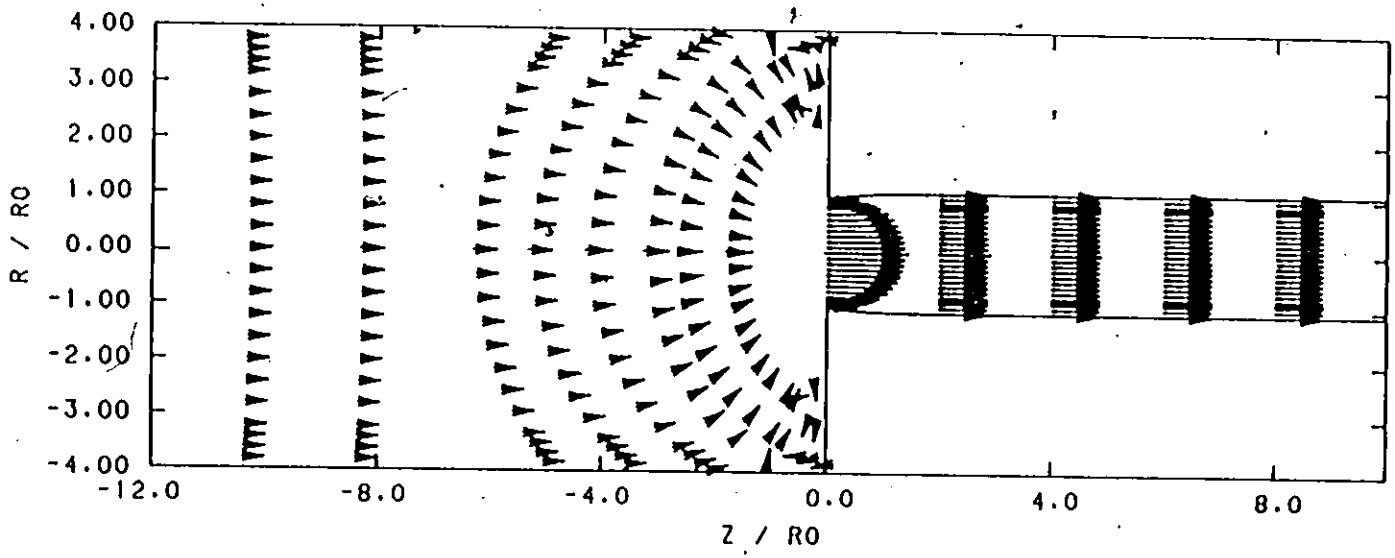

Figure 4.6: Velocity Field for the Flow of a Newtonian Fluid through an Orifice ($L/D = 0$).

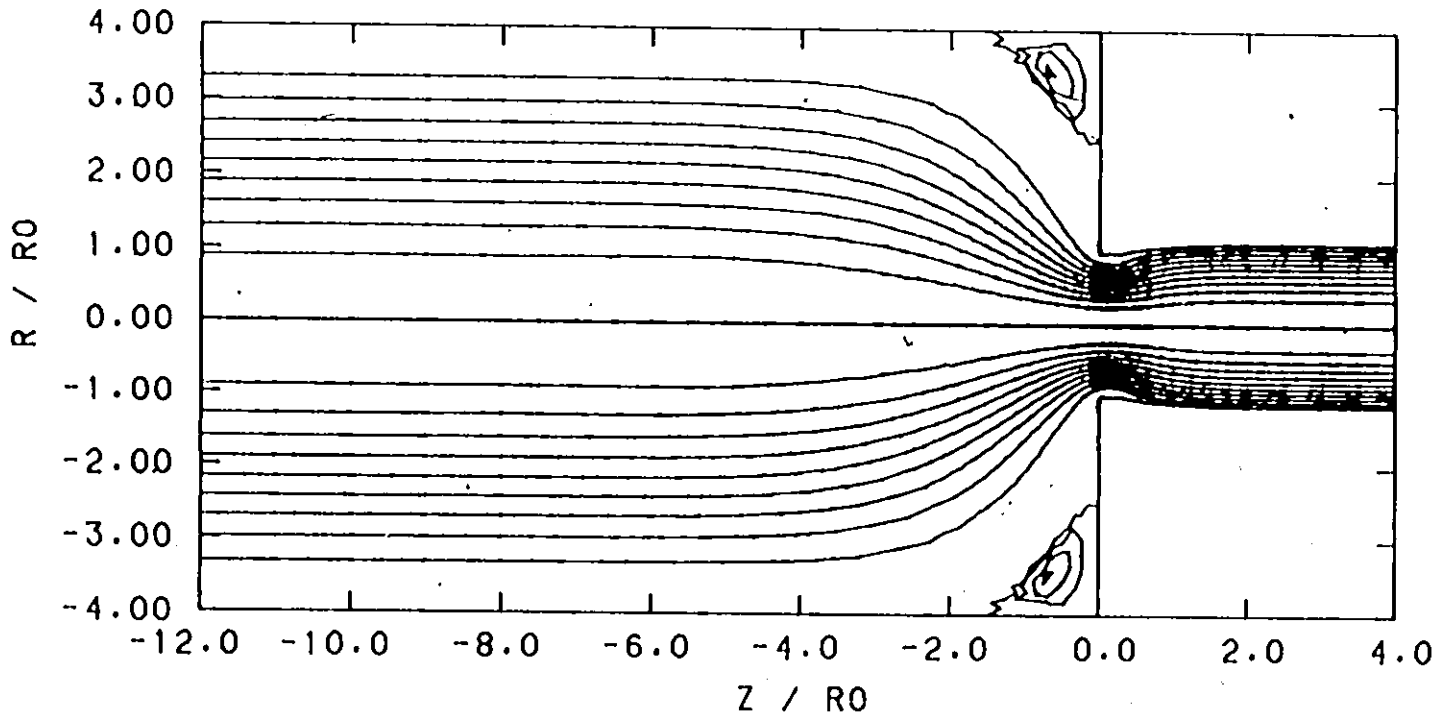

Figure 4.7: Streamlines for the Flow of a Newtonian Fluid through an Orifice ($L/D = 0.15$).

ized to take the value of 0 at the wall and 1 at the centerline. The corner vortex has an intensity that reaches a minimum value of -0.002, i.e. 0.2% of the fluid flow in the domain examined is recirculating in the corner.

The present results (diameter swell) have shown excellent agreement with those available in the literature (experimental and numerical). This, in turn, gives us confidence that the u-w-p and free-surface formulations are numerically sound. The behaviour of Newtonian fluids, however, is totally different from that of viscoelastic fluids (compare Figures 4.1 and 4.4). This is another indication that other mechanisms must be involved in the flow of viscoelastic fluids. However, such an investigation is beyond the scope of the present study.

4.2 Flow of a Newtonian Fluid through Converging and Diverging Annular Dies

Plastic pipes are formed by the extrusion of polymer melts through annular dies. Converging or diverging annular dies are commonly used in the plastics industry for extrusion. For polymer melts the simulations have been pursued with a variety of constitutive equations with unclear results

so far (Crochet and Walters, 1983). Meanwhile experimental research has shifted from the simplest die design of a straight capillary tube to more sophisticated annular dies used for pipe formations (Orbey and Dealy, 1984). There is a need to understand the effect of such complicated annular die designs on the extrudate. In order to decouple the effect of geometry and non-Newtonian viscoelastic nature of the fluids, it is essential to consider first the Newtonian fluid behaviour. The case of Newtonian extrudate swell from a straight annulus has been examined by Mitsoulis (1986). Newtonian swell from converging and diverging capillaries (conical dies) has also been studied (Allan, 1977).

The experimental work of Orbey and Dealy (1984) has been performed on a variety of tapered annular dies to study the effect of die design on the swelling of different HDPE melts. It is the purpose of this section to provide the corresponding results from numerical calculations on Newtonian fluids of various diameter ratios and convergence angles in flow through tapered annular dies.

A schematic diagram of extrusion through a tapered annular die is given in Figure 4.8. Two independent swell ratios can be defined in the case of an annular extrudate: the diameter swell B_1, and the thickness swell, B_2,

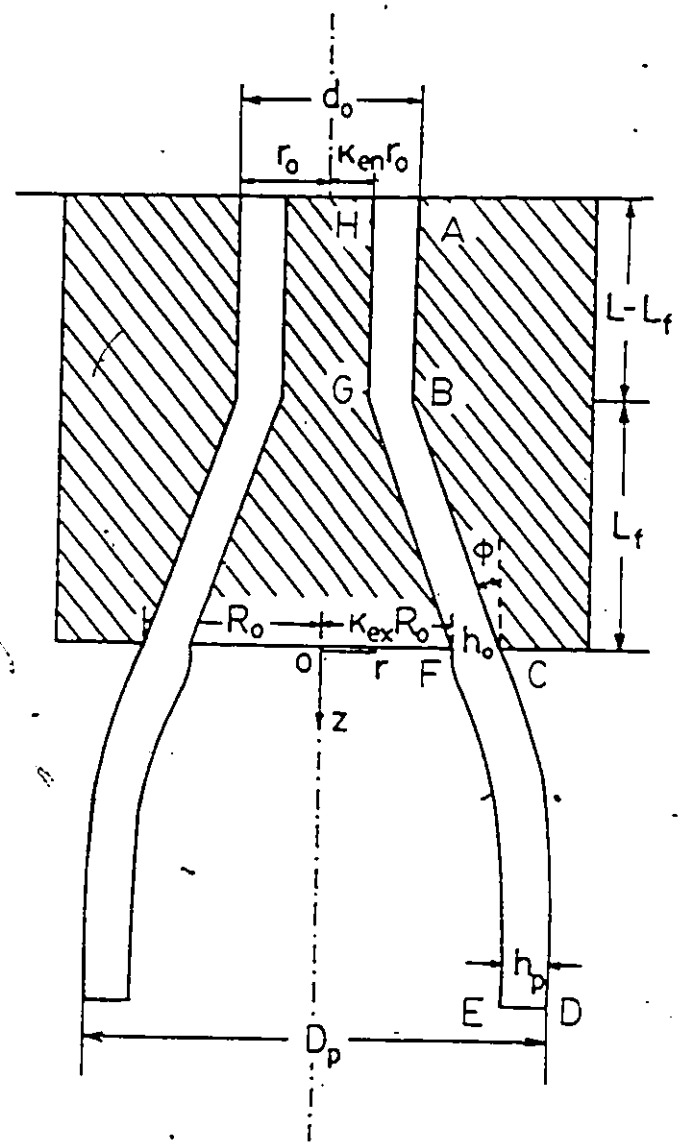

Figure 4.8: Schematic Diagram for Extrusion through a Tapered Annular Die

defined by:

$$B_1 = \frac{D_p}{D_o} \tag{4.16}$$

$$B_2 = \frac{h_p}{h_o} \tag{4.17}$$

A third swell ratio, the inner diameter swell, B_3, follows from the above definitions:

$$B_3 = \frac{D_p - 2h_p}{D_o - 2h_o} \tag{4.18}$$

Due to symmetry, only half of the domain (area bounded by ABCDE-FGHA) need be considered. The appropriate boundary conditions include:

1. Along boundary AH, a fully developed velocity profile is imposed. The velocity profile is (Bird et al., 1960):

$$v_z = \left(-\frac{dp}{dz}\right)\frac{r_o^2}{4\mu}\left[1 - \left(\frac{r}{r_o}\right)^2 + 2\lambda^2 \ln\left(\frac{r}{r_o}\right)\right] \tag{4.19}$$

$$v_r = 0 \tag{4.20}$$

where

$$\lambda^2 = \frac{1 - \kappa_{cn}^2}{2\ln(1/\kappa_{cn})} \tag{4.21}$$

and

$$\kappa_{cn} < \frac{r}{r_o} < 1 \tag{4.22}$$

Again, since only Newtonian fluids are considered, the actual values of $\partial p/\partial z$ and μ are not important. Thus, they are arbitrarily chosen.

2. Along ABC and FGH, there is no slip at the boundary, i.e.:

$$v_r = 0 \tag{4.23}$$

$$v_z = 0 \tag{4.24}$$

3. At the end plane of the discretization (boundary DE), the velocity tangential to the plane was set to zero, i.e.:

$$\overline{v} \cdot \overline{t} = 0 \tag{4.25}$$

4. At the free surface (boundary CD and EF), the usual zero surface traction condition was imposed:

$$\overline{T} \cdot \overline{n} = 0 \tag{4.26}$$

The finite element calculations were carried out for the geometries given by Orbey and Dealy (1984). The effect of different converging and diverging angles was also examined. In all cases the finite element grid was extended $10h_o$ upstream and $10h_o$ downstream of the exit, except for the case of a 10°–diverging angle where the entry was extended $17h_o$ upstream. Such

entrance and exit lengths are sufficient to justify the imposition of a fully developed velocity profile upstream and $v_r = 0$ downstream. Special care must be taken when selecting the finite element grid. From previous experience and after several trials, a grid was chosen having 464 u-w-p elements, 1003 nodes (17 points across) with a total of 2,120 non-zero degrees of freedom (unknowns). The grid was selectively dense where most drastic changes are expected to occur.

Figure 4.9 shows the final finite element grid and the streamlines for a 20°–diverging annular die. The stream function has been normalized between 0 (outer streamline) and 1 (inner streamline) with increments of 0.1 in between. Figure 4.10 shows a typical velocity field for a 20°–converging annular die. The velocity vectors have been normalized by the average velocity upstream.

The various die designs used are summarized in Table 4.2 and the corresponding results concerning swell ratios are summarized in Table 4.3. The results of the diameter swell, inner diameter swell and thickness swell for cases 1 to 6 are shown in Figures 4.11a, 4.11b and 4.11c, respectively.

A run for straight annulus (case 1) with $\kappa_{en} = \kappa_{ex} = 0.75$ is included. For case 1, the diameter swell, inner diameter swell and thickness swell are

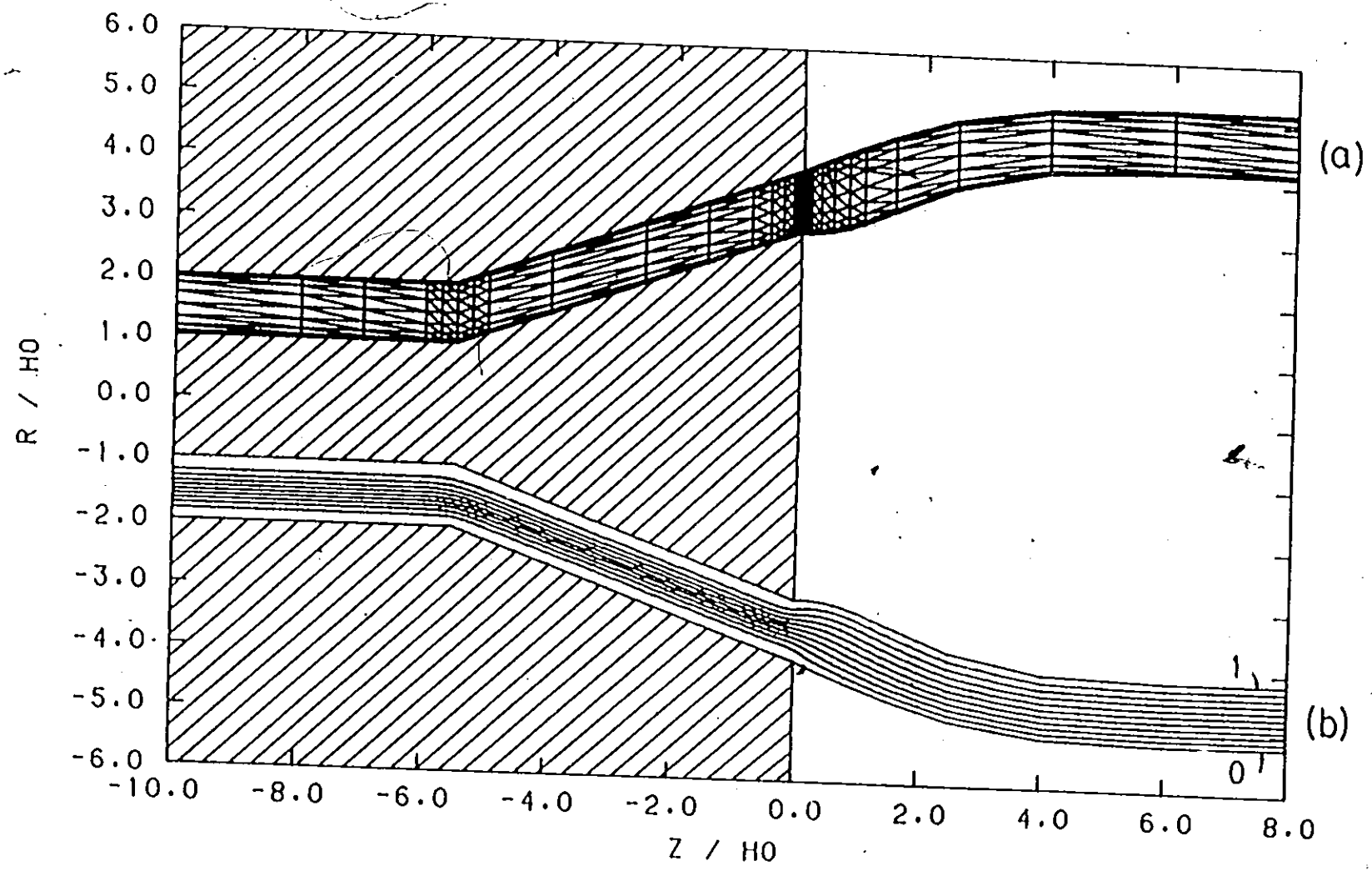

Figure 4.9: Analysis of Annular Newtonian Extrudate Swell. Diverging Die, $\kappa_{en} = 0.5$, $\kappa_{ez} = 0.75$, $\phi = 20°$, $L_f = 5.5h_o$: (a) Finite Element Grid, and (b) Streamlines.

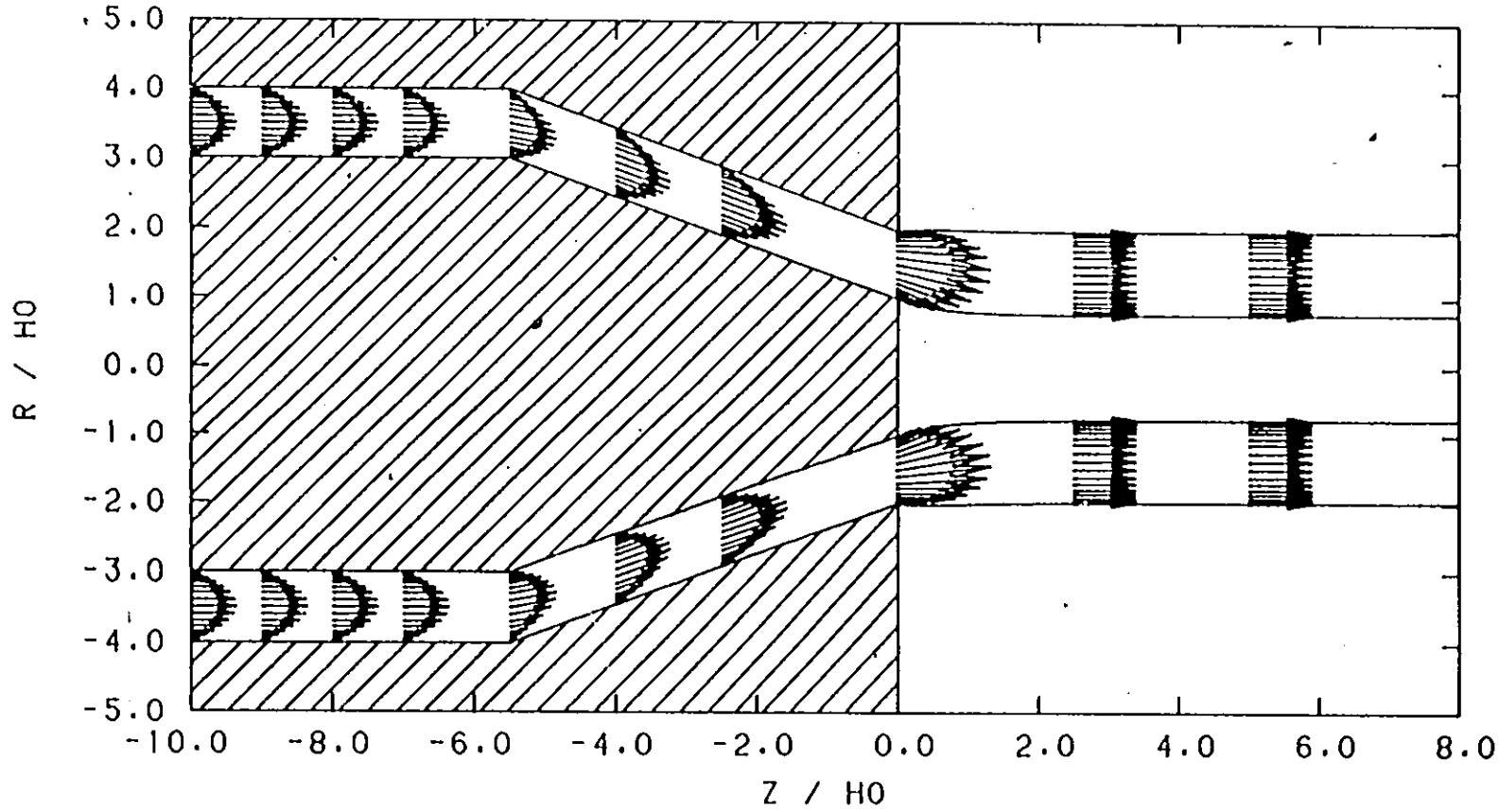

Figure 4.10: Velocity Field from the Analysis of Annular Newtonian Extrudate Swell. Converging Die, $\kappa_{en} = 0.75$, $\kappa_{ex} = 0.5$, $\phi = -20°$, $L_f = 5.5h_o$. (Vectors Drawn to Scale).

Table 4.2: Various Die Designs for Newtonian Fluids in Tapered Annular Dies.

Case	Entry Diameter Ratio κ_{en}	Exit Diameter Ratio κ_{ex}	Taper Angle ϕ	Taper Length L_f
1*	0.75	0.75	0	∞
2	0.50	0.75	10	11.3 h_o
3*	0.50	0.75	20	5.5 h_o
4	0.50	0.75	25	4.3 h_o
5	0.50	0.75	30	3.5 h_o
6	0.50	0.75	35	2.9 h_o
7	0.67	0.75	10	5.5 h_o
8	0.75	0.67	-10	5.5 h_o
9*	0.75	0.50	-20	5.5 h_o
10	0.50	0.50	0	∞

* Die design employed by Orbey and Dealy (1984).

Table 4.3: Effect of Die Design on Extrudate Swell for Newtonian Fluids in Tapered Annular Dies.

Case	Diameter Swell B_1 %	Inner Diameter Swell B_3 %	Thickness Swell B_2 %
1*	5.64	1.69	17.47
2	15.71	16.99	11.88
3*	29.79	37.86	5.59
4	39.11	51.30	2.52
5	49.94	66.78	-0.01
6	65.97	89.41	-4.34
7	15.83	17.19	11.75
8	-0.16	-1.09	21.63
9*	-0.01	-23.09	21.69
10	8.87	1.70	16.05

* Die design employed by Orbey and Dealy (1984).

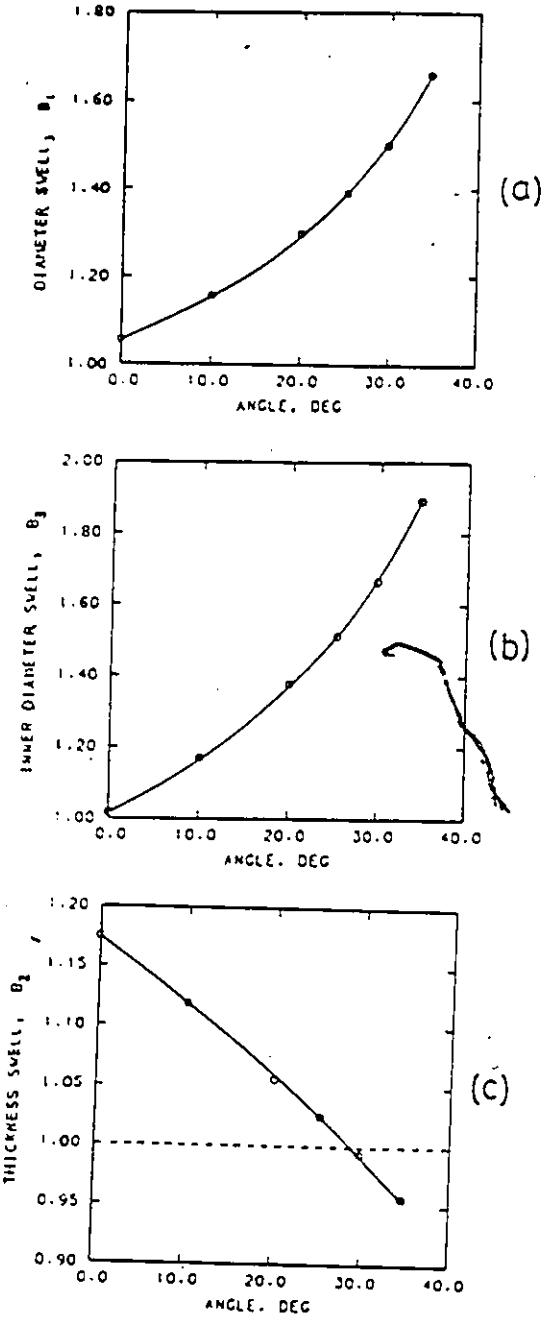

Figure 4.11: Swell Ratios vs. Diverging Angle for Newtonian Fluids Extruded from Tapered Annular Dies ($\kappa_{en} = 0.5$, $\kappa_{ex} = 0.75$): (a) Outer Diameter Swell. (b) Inner Diameter Swell. (c) Thickness Swell.

5.64%, 1.69% and 17.47%, respectively. Mitsoulis (1986) obtained exactly the same values as this work. In addition, the results of Crochet and Keunings (1980) are 5.5% (B_1), 1.6% (B_3) and 17% (B_2). The close agreement between this work and the numerical solutions available in the literature is readily seen.

Figures 4.11a and 4.11b show that the diameter and inner diameter swells increase rapidly with ϕ (diverging angle). On the other hand, the thickness swell decreases, becoming negative (in %) at about 30° (Figure 4.11c). The maximum diverging angle employed was 35°. Attempts to analyze angles beyond 35° failed because no convergence for the free surface could be obtained.

Table 4.3 also shows some other results with converging angles. Cases 1, 3 and 9 correspond to the die designs given by Orbey and Dealy (1984). They found out that for all resins examined, the diameter swell was always highest for the converging, followed by the straight and then the diverging dies. The contrary is borne out by our calculations for Newtonian fluids. The thickness swell depended on the resin, whereas for Newtonian fluids the sequence is highest for divergent and lowest for convergent dies. Obviously, other mechanisms take place in flow of viscoelastic fluids through tapered

annular dies that cannot be explained by Newtonian fluid mechanics.

4.3 One-Dimensional Heat Transfer without Source Term

The area of convection-dominated phenomena has proven to be one of the most difficult areas to satisfactorily deal with by numerical methods (Hughes and Brooks, 1979). This section is set out to evaluate the behaviour of the conventional and Streamline-Upwind/Petrov-Galerkin (SU/PG) finite element formulations. A "classical" one-dimensional (z-direction) steady-state flow without source term (viscous dissipation) is considered.

For the one-dimensional problem in the z-direction with no viscous dissipation term, the equation of conservation of energy (2.20) reduces to:

$$\frac{d^2T}{dz^2} - \frac{\rho C_p w}{k}\frac{dT}{dz} = 0 \tag{4.27}$$

with the imposed boundary conditions

$$T|_{z=0} = 1 \tag{4.28}$$

$$T|_{z=L} = 0 \tag{4.29}$$

where L is the length of the solution domain. The problem has a simple exact solution:

$$T = \frac{e^{(Pe/L)z} - e^{Pe/L}}{1 - e^{Pe/L}} \tag{4.30}$$

where

$$Pe = \frac{\rho C_p w L}{k} \tag{4.31}$$

is the Peclet number of the system. The bilinear quadrilateral Lagrangian element was used in the temperature formulation to discretize the solution domain. Since the problem is only one-dimensional, the finite elements used are rectangular in shape with equal area.

Huebner and Thornton (1982) had shown that their upwinding solution was inferior to the conventional formulation at low Pe number ($Pe = 0.2$), as shown in Figure 4.12. However, at high Pe number, the upwinding solution showed good agreement with the analytical solution, whereas the conventional finite element solution yielded temperatures with such large oscillations that the results were worthless ($Pe = 25$). Although the upwinding solution they obtained was better than the conventional finite element solution, there were still discrepancies between the numerical and the analytical solutions.

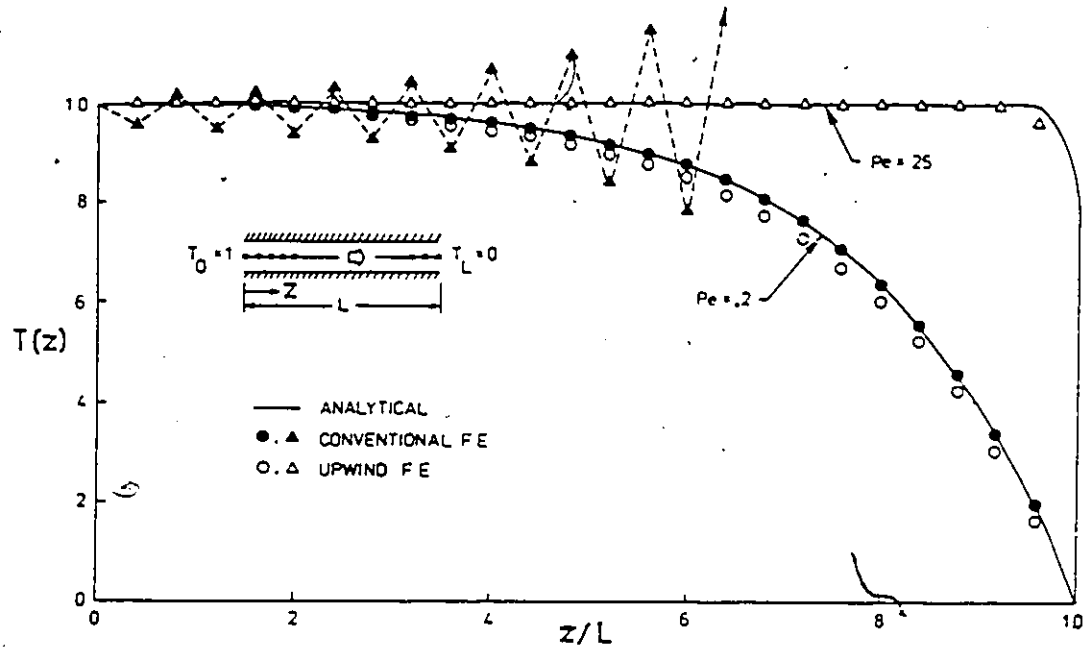

Figure 4.12: Solution for One-Dimensional Heat Transfer without Source Term (Huebner and Thornton, 1982).

With SU/PG, however, the solution agrees with the analytical solution up to seven significant figures for whatever *Pe* values used. An example is shown in Table 4.4. Although the dimensionless element length used is 0.02 (50 finite elements), a series of runs showed that the SU/PG method of solution is independent of the element dimension (sometimes known as "superconvergence quality"). On the other hand, the conventional Galerkin method of solution is highly dependent on the element dimension (accuracy increases with grid density).

Some other types of elements were also employed. These are: quadratic triangular element (no upwinding), linear triangular element (no upwinding), linear triangular element (upwinding, Mitsoulis, 1984), linear triangular element (upwinding, Mizukami, 1985). In each case, an equal number of nodes were used. At high enough *Pe* (> 100), these methods failed miserably.

Table 4.4: Comparison between SU/PG, Conventional* and Analytical Solutions for One-Dimensional Heat Transfer (without Viscous Dissipation) at $z/L = 0.98$ (Dimensionless Element Length = 0.02).

Pe	Conventional* Solution	SU/PG Solution	Analytical Solution
1	0.03132	0.03132	0.03132
10	0.18183	0.18128	0.18128
20	0.33333	0.32968	0.32968
40	0.57143	0.55067	0.55067
60	0.75000	0.69880	0.69880
100	1.00000	0.86466	0.86466

* Conventional Galerkin finite element solution with bilinear element.

4.4 One-Dimensional Convective Heat Transfer with Source Term

Leonard (1979) has shown that some upwind formulations give very poor results when a source term (e.g. viscous dissipation) is present. However, Brooks and Hughes (1982) showed that the SU/PG solution gives nearly exact results. The test case used (Leonard, 1979) is solved again in order to reproduce Brooks and Hughes' results.

For one-dimensional heat transfer with source term, the equation of conservation of energy (2.20) reduces to:

$$-\rho C_p w \frac{dT}{dz} = Q_d \tag{4.32}$$

where Q_d (the viscous dissipation term) is given by

$$\begin{aligned} 0 \le z \le 6 \quad &, \quad Q_d = 1 - 0.25\,z \\ 6 < z \le 8 \quad &, \quad Q_d = 0.25\,(z-6) - 0.5 \\ z > 8 \quad &, \quad Q_d = 0 \end{aligned} \tag{4.33}$$

The boundary conditions are:

$$\begin{aligned} \text{at} \quad z = 0 \quad &, \quad T = 0 \\ \text{at} \quad z = 15 \quad &, \quad dT/dz = 0 \end{aligned} \tag{4.34}$$

The bilinear elements used are again rectangles of equal area. Since this is a one-dimensional problem, the width of the element is not important. The length of the element was fixed at 1.0. There are altogether 15 elements. The material properties (ρ and C_p) and constant velocity (w) were taken to be unity.

The solution for this system is tabulated in Table 4.5. In addition, the analytical solution and the classical upwinding solution (inconsistent Petrov-Galerkin scheme) are included (Brooks and Hughes, 1982). The agreement between the SU/PG and the analytical solution is excellent, the maximum deviation being about 4%. On the other hand, the classical upwinding solution is highly degraded due to the incorrect treatment of the source term.

From the above it becomes evident that the Streamline-Upwind/Petrov-Galerkin scheme applied to bilinear quadrilateral elements is best suited for the treatment of the energy equation for problems dominated by convection and viscous dissipation such as these occurring in polymer melt flows. The preliminary tests and results of this chapter showed the excellent agreement obtained for benchmark problems and built confidence in the numerical methods. Having thus established their accuracy, we embark upon solving

Table 4.5: Comparison of Different Schemes for One-Dimensional Convective Heat Transfer with Source Term.

—	Temperature Solution		
x	Classical	SU/PG	Exact
0.0	0.00	0.000	0.000
1.0	0.74	0.875	0.875
2.0	1.25	1.500	1.500
3.0	1.50	1.875	1.875
4.0	1.50	2.000	2.000
5.0	1.25	1.875	1.875
6.0	0.83	1.458	1.500
7.0	0.59	1.083	1.125
8.0	0.54	0.979	1.000
⋮	⋮	⋮	⋮
15.0	0.54	0.979	1.000

some difficult polymer extrusion problems with free surfaces and interfaces and dominated by convection and viscous dissipation effects.

Chapter 5

Computer-Aided Analysis and Design of Wire-Coating Extrusion Dies

Isothermal and nonisothermal analyses of wire-coating extrusion dies are performed. The isothermal analysis of Newtonian and power-law fluid flow in a particular die design employed by Du Pont Co. is carried out using the Lubrication Approximation Theory (LAT) and the Finite Element Method (FEM). The full two-dimensional nonisothermal analysis is then carried out by implementing the Streamline-Upwind/Petrov-Galerkin (SU/PG) tem-

perature formulation. The nonisothermal analysis is first performed on a simple die design used by Carley et al. (1979), and a comparison is made between their findings and FEM results. Finally, the die employed by Du Pont Co. is analyzed using a commercially available wire-coating LDPE resin (Alathon 3535) for which experimental data is available. Comparisons are made between theory and experiment and a new criterion is developed for optimum operation.

5.1 Introduction - The Wire-Coating Process

The wire-coating process is a continuous extrusion process for primary insulation of conducting wires with molten polymers for mechanical strength and environmental protection purposes.

Various details of the wire-coating process and a literature survey on the numerical simulation of wire-coating has been provided in a recent comprehensive review by Mitsoulis (1986). As a result, only a summary is included in this section.

Most numerical analyses of wire-coating dies have been done on the

pressure-type die. The early studies were performed by using the LAT and assuming isothermal flow. Using these simplifications, both Newtonian and power-law fluids have been analyzed (Carley, 1959; McKelvey, 1962; Bagley and Storey, 1963; Fenner and Williams, 1967; Fenner, 1970; Han and Rao, 1978).

The first full two-dimensional analysis was done by Caswell and Tanner (1978). The FEM was used to analyze the whole flow field. That work, however, was mainly concerned with isothermal flows of Newtonian and power-law fluids.

Inclusion of the energy equation in the analysis has also been done (Carley et al., 1979; Winter, 1978). However, these studies were carried out by neglecting the $v_r(\partial T/\partial r)$ term in the energy equation.

Recently, a full two-dimensional nonisothermal analysis has been performed by Wagner and Mitsoulis (1985) and Mitsoulis (1986) using FEM. However, the temperature field, in some cases, was plagued by numerical instabilities due to the temperature formulation employed.

The need, therefore, arises to perform a more reliable two-dimensional nonisothermal analysis of the wire-coating process, using the SU/PG temperature formulation discussed in Chapter 3.

5.2 Mathematical Modelling of Wire Coating

A schematic diagram for a wire-coating extrusion unit is shown in Figure 5.1. The polymer melt flowing in the die is surrounded by three distinct components:

1. The *die wall*, which forms the outer boundary for the annulus configuration. It is stationary at all times.

2. The *torpedo* or *guider tip*, which forms the inner boundary before the melt meets the wire. It is stationary during the process.

3. The *wire*, which is travelling at a constant speed. It is concentric with the center-line of the die and forms the last part of the inner boundary.

From here on, the section of the die bounded by the die wall and the torpedo will be called the "annular section," while the section bounded by the die wall and the wire will be called the "die section."

The torpedo, although stationary during a wire-coating process, is adjustable to different positions before the coating operation. Haas and Skewis

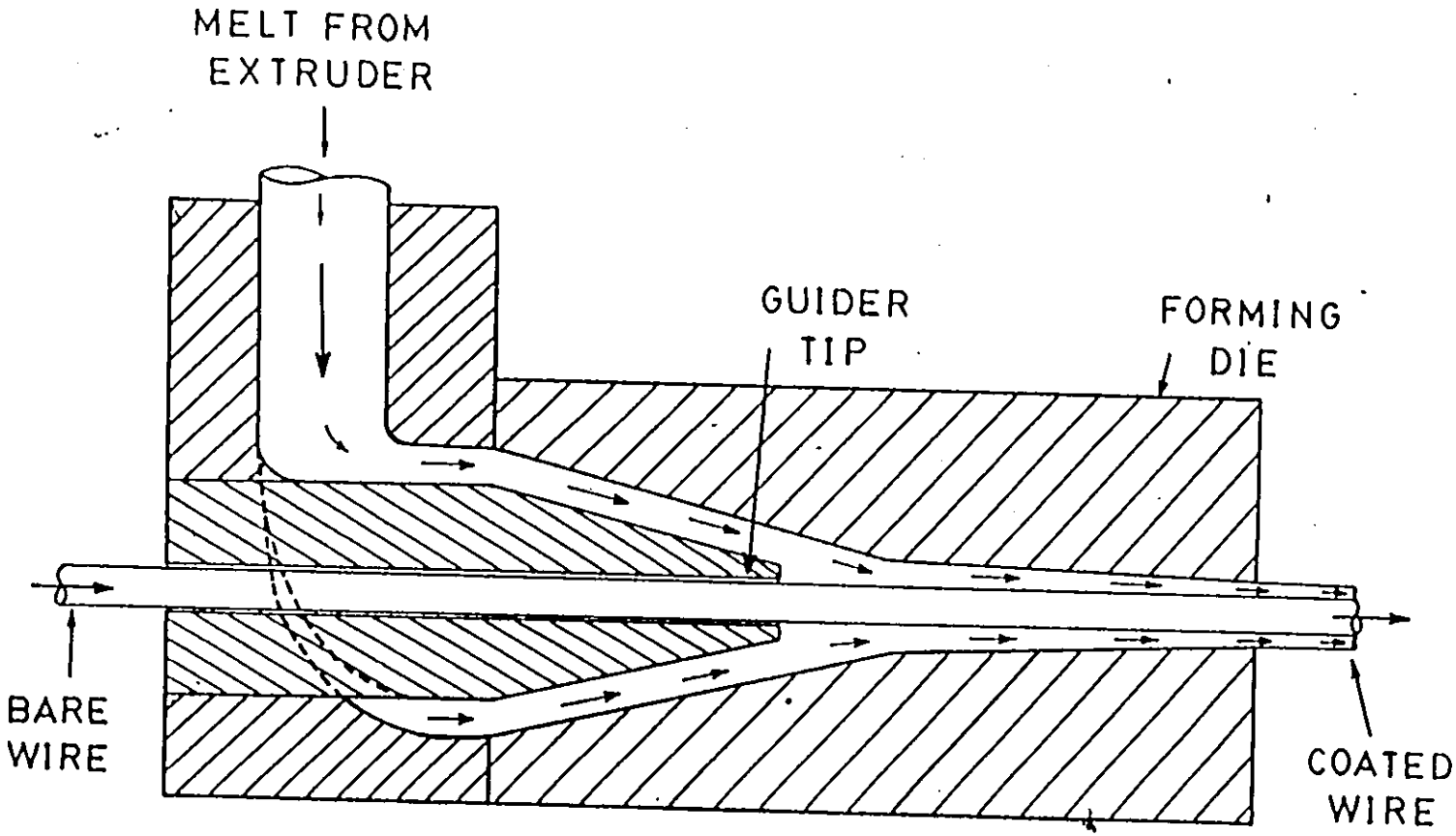

Figure 5.1: Schematic Diagram of a Wire-Coating Extrusion Unit.

(1974) claimed that the location of the torpedo greatly affects the quality of the coated wire. The location of the torpedo is defined by the "gum space." Referring to Figure 5.2, the gum space (GS) is defined as shown.

Figure 5.3 shows the domain of interest for the analysis along with the relevant notation. Due to symmetry, only half of the domain need be considered. For LAT the area bounded by EFGAHDE is analyzed (without free surface), whereas for FEM the area bounded by EFGAHBCDE is analyzed (with free surface).

For LAT, the boundary conditions used are (no-slip assumed):

1. Along boundaries ED (die wall) and FGA (torpedo), $v_z = 0$.

2. Along boundary AH (wire surface), $v_z = V_w$.

where V_w is the wire velocity.

For FEM, the boundary conditions for the u-w-p formulation are (no-slip assumed):

1. Along boundary EF, a fully developed velocity profile for Newtonian fluid is imposed. The velocity profile is (Bird et al., 1960):

$$v_z = \left(-\frac{dp}{dz}\right)\frac{r_o^2}{4\mu}\left[1 - \left(\frac{r}{r_o}\right)^2 + 2\lambda^2 \ln\left(\frac{r}{r_o}\right)\right] \qquad (5.1)$$

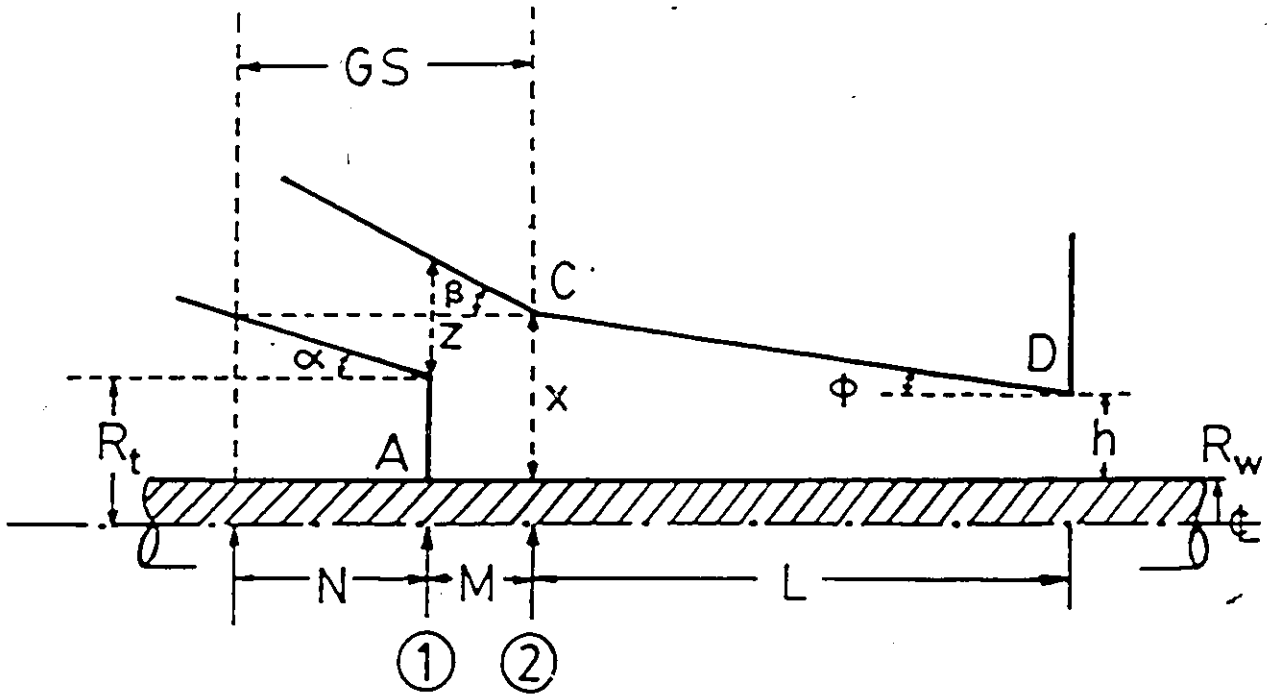

Figure 5.2: The "Gum Space" Concept and Relevant Notation.

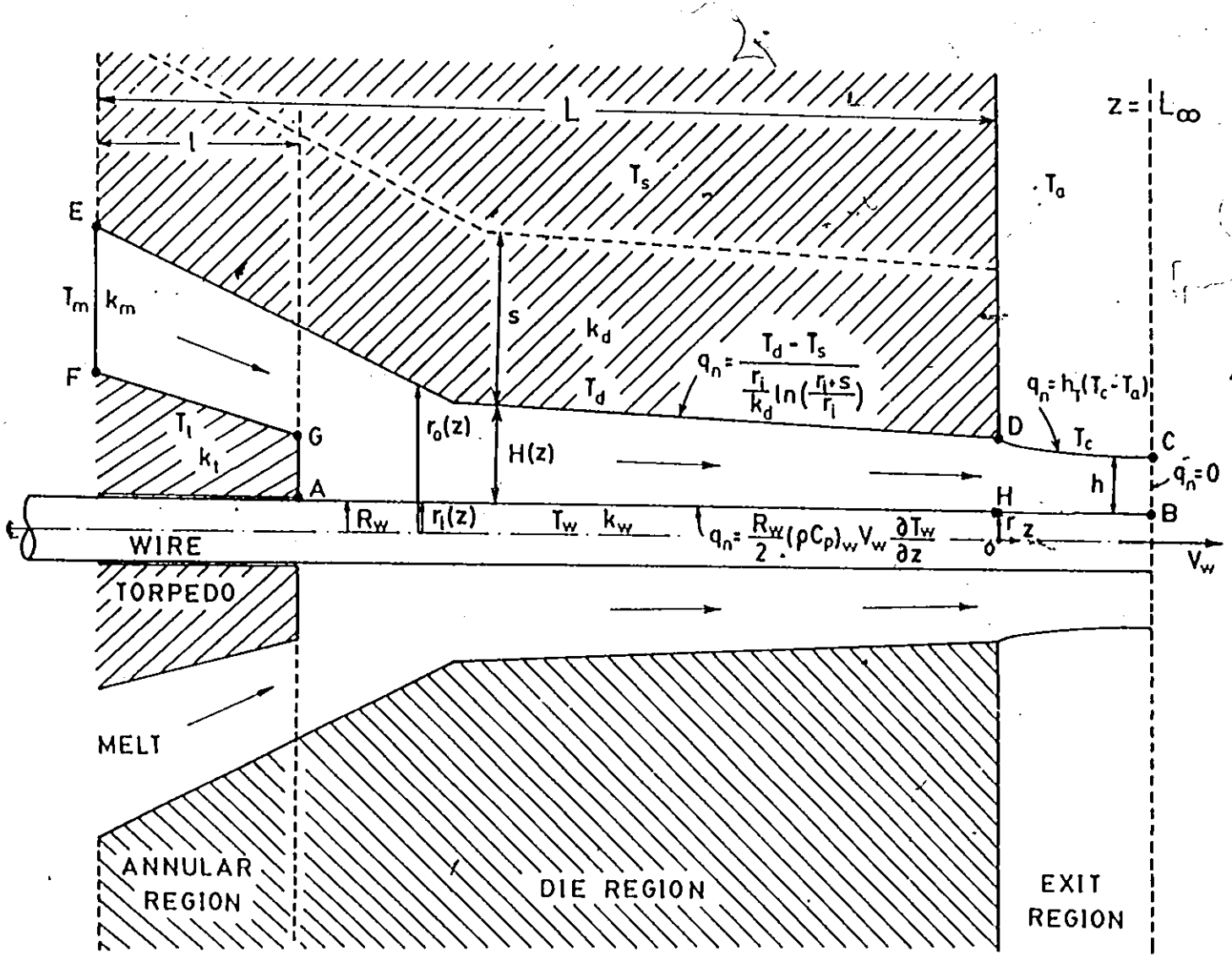

Figure 5.3: Notation for Fluid Flow and Heat Transfer Analysis in a Wire-Coating Extrusion Die.

$$v_r = 0 \tag{5.2}$$

where

$$\lambda^2 = \frac{1 - \kappa_{en}^2}{2\ln(1/\kappa_{en})} \tag{5.3}$$

and

$$\kappa_{en} < \frac{r}{r_o} < 1 \tag{5.4}$$

2. Along boundaries ED and FGA, no-slip is assumed:

$$v_r = 0 \,, \tag{5.5}$$

$$v_z = 0 \tag{5.6}$$

3. Along boundary BC (outflow plane of the domain), the velocity tangential to the plane is set to zero:

$$\overline{v} \cdot \overline{t} = v_r = 0 \tag{5.7}$$

4. Along boundary DC (free surface), the usual zero surface traction condition is imposed:

$$\overline{T} \cdot \overline{n} = 0 \tag{5.8}$$

The boundary conditions for the temperature formulation only apply in nonisothermal analysis. They can be (Figure 5.3):

1. Isothermal wall condition:

$$T = T_m \tag{5.9}$$

where T_m is the temperature of the melt coming in from the extruder (assumed to be constant at the end of the extruder, due to the large gap).

2. Adiabatic condition:

$$q_n = 0 \tag{5.10}$$

where q_n is the heat flux normal to the surface.

3. Heat balance condition:

   (a) at the die wall surface (refer to Appendix B for details of derivation):

$$q_n = \frac{k_w}{r_o \ln(1 + s/r_o)}(T - T_s) \tag{5.11}$$

where

k_w = thermal conductivity of the die wall (assumed constant)

r_o = radius of the die wall

T = unknown temperature at the die wall

T_s = known controlled temperature in the die at a distance s away from the die wall

s = distance from the die wall to a location in the die where temperature is being controlled

(b) at the free surface, using the definition of heat transfer coefficient (Holman, 1981):

$$q_n = h_T(T - T_a) \tag{5.12}$$

where

h_T = heat transfer coefficient to the air

T = unknown temperature at the free surface

T_a = ambient temperature

(c) at the wire surface (refer to Appendix B for the details of derivation):

$$q_n = \frac{R_w}{2}(\rho_w C_{pw}) V_w \frac{\partial T}{\partial z} \tag{5.13}$$

where

R_w = wire radius

ρ_w = density of wire

C_{pw} = heat capacity of wire

V_w = wire velocity

dT/dz = unknown axial temperature gradient

In actual situations, due to the complex geometry of the die, the heat-balance boundary conditions are two-dimensional in nature, and further FEM analysis within the solid boundaries is necessary. However, such an analysis would consume a large amount of computing resources. Since the main area of interest is the melt flowing in the die, the above heat-balance conditions were derived based on some assumptions listed below. As a result, these heat-balance conditions are only approximate and serve to illustrate the effects of intermediate boundary conditions, i.e. neither isothermal wall nor adiabatic wall.

The assumptions involved in using Equation 5.11 are:

(a) The heat transfer in the die is one-dimensional, i.e. the axial heat transfer is neglected ($\partial T/\partial z = 0$).

(b) There is no heat sink or source in the die.

(c) The thermal conductivity of the die wall, k_w, is independent of temperature.

(d) $q_n = q_r$ (radial heat flux component) i.e. the axial heat flux component is neglected ($q_z = 0$).

The assumption involved in using Equation 5.12 is:

(a) h_T is independent of temperature.

The assumptions involved in using Equation 5.13 are:

(a) The radial temperature gradient in the wire is negligible compared with the axial gradient ($\partial T/\partial r \ll \partial T/\partial z$).

(b) ρ_w and C_{pw} are independent of temperature.

To obtain streamlines *a posteriori* from the solution of the flow field, boundary conditions for the stream function are needed. Referring to Figure 5.3, these are:

1. Along boundary FGAHB:

$$\psi = 0 \tag{5.14}$$

2. Along boundary CDE:

$$\psi = Q/(2\pi) \tag{5.15}$$

3. Along boundaries BC and EF:

$$\frac{\partial \psi}{\partial n} = 0 \tag{5.16}$$

where Q is the volumetric flow rate.

5.3 Isothermal Wire Coating

Many of the earlier numerical simulations for the wire-coating process have been done by assuming isothermal flows. In addition, these simulations were mainly concerned with the flow in the die section, i.e. the annular region was entirely neglected. When only a slightly tapered die wall is involved, the use of LAT is justified. However, the torpedo is also an integrated part of a wire-coating die. Thus, a full analysis of wire-coating dies should include both the annular and the die sections. In such cases, however, the use of LAT is not so easily justified.

The purpose of this section is to analyze the flow field in a full die using both LAT and FEM, the former being a one-dimensional and the latter a two-dimensional analysis. The LAT has been implemented in a computer program developed. The program was written based on Fenner's analysis

(1970). More details can be found in an internal report by Heng (1986). The behaviour of both Newtonian and power-law fluids are studied.

In this section, the analysis is carried out in a die used for high-speed industrial operations by Du Pont Co. (Haas and Skewis, 1974). The details for such a die are as shown in Figure 5.4. For such a die, Haas and Skewis claimed that the quality of the coated wire depends on the location of the torpedo (thus the GS). They concluded, after experimental investigations, that a GS=$4.9R_w$ is the optimum design for this die. Wagner (1987) has performed a thorough isothermal analysis on the same die with GS=$7.9R_w$. It is, then, the intention of this section to compare these two designs (see Figure 5.9 for the differences in the designs).

For this isothermal analysis, a constant melt temperature is assumed throughout the flow domain. The isothermal temperature is assumed to be (Haas, 1986):

$$T = T_m = 232°C \tag{5.17}$$

where T_m is the temperature of the melt coming in from the extruder. In addition, the final coated wire radius is set at $1.8R_w$ i.e. the coating thickness is 80% of the wire radius.

The flow of Newtonian and power-law fluids in Du Pont's die with

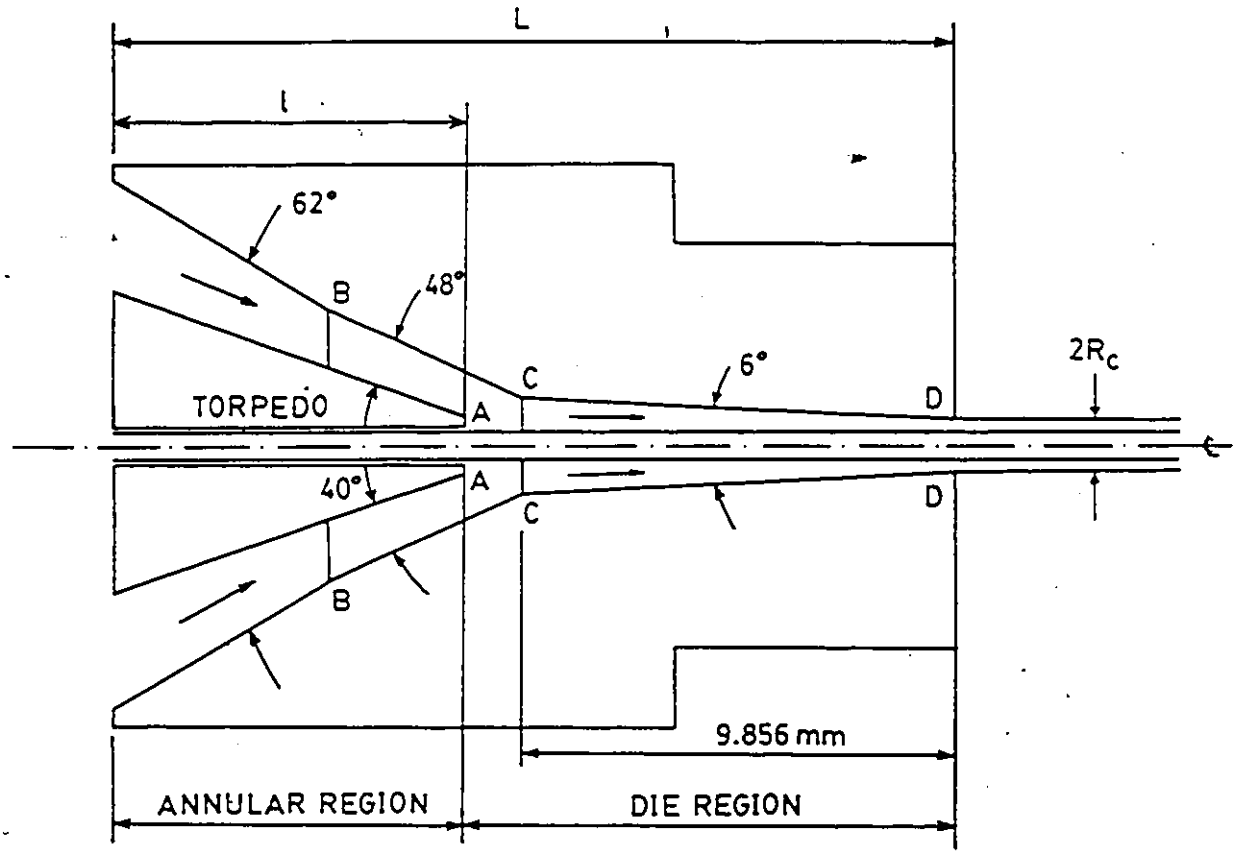

TIP DIAMETER AA = 1.28 mm
DIAMETER BB = 6.08 mm
DIAMETER CC = 2.176 mm
DIAMETER DD = 1.152 mm

WIRE DIAMETER = 0.64 mm
TORPEDO LENGTH l = 8.032 mm
OVER-ALL LENGTH L = 19.2 mm

Figure 5.4: Die Design Employed by Du Pont (Piece 22-1S) (Haas and Skewis, 1974).

GS=$4.9R_w$ is studied. Power-law indices of $n = 1$, 0.75, 0.5 and 0.25 are used. Note that the Newtonian fluid is a special case of the power-law fluid with $n = 1$. The results of primary interest are: pressure (P), die shear stress (τ_d), wire shear stress (τ_w) and wire tension (F). These results are made dimensionless by introducing the characteristic shear stress:

$$\overline{\tau} = m\left(\frac{V_w}{R_w}\right)^n \tag{5.18}$$

where m is the consistency index and n is the power-law index. The dimensionless variables are:

- dimensionless pressure,

$$P^* = \frac{P}{\overline{\tau}} \tag{5.19}$$

- dimensionless die shear stress,

$$\tau_d^* = \frac{\tau_d}{\overline{\tau}} \tag{5.20}$$

- dimensionless wire shear stress,

$$\tau_w^* = \frac{\tau_w}{\overline{\tau}} \tag{5.21}$$

- dimensionless wire tension,

$$F^* = \frac{F}{\overline{\tau} R_w^2} \tag{5.22}$$

where R_w is the wire radius.

The LAT results are obtained by using 100 nodes along the annular region and 100 nodes along the die region. For each axial cut, 100 nodes are used across the flow channel, giving a total of 20,000 nodal points in the domain. Despite such a great number of nodes, the execution time is extremely fast (a few CPU *secs*), and this is typical of problems described by an ordinary differential equation.

Figures 5.5, 5.6 and 5.7 show the axial pressure, die and wire shear stress, and wire tension profiles, respectively. The corresponding results for GS=$7.9R_w$ taken from Wagner's thesis (1987) are also included. The behaviour of the operating variables has been discussed by Wagner (1987) and will not be repeated here.

The $4.9R_w$-GS design exhibits extremely similar behaviour to the $7.9R_w$ design. A look at the pressure (P^*) profiles (Figure 5.5) shows only discrepancies close to the torpedo. This is understandable, since bringing the torpedo closer allows a smaller area for flow, thus a higher pressure is required. The positive pressure gradient (dP^*/dz) discussed by Wagner (1987) is still present. He explains that such behaviour can be used as a criterion to determine the presence of recirculation. A look at the stresses

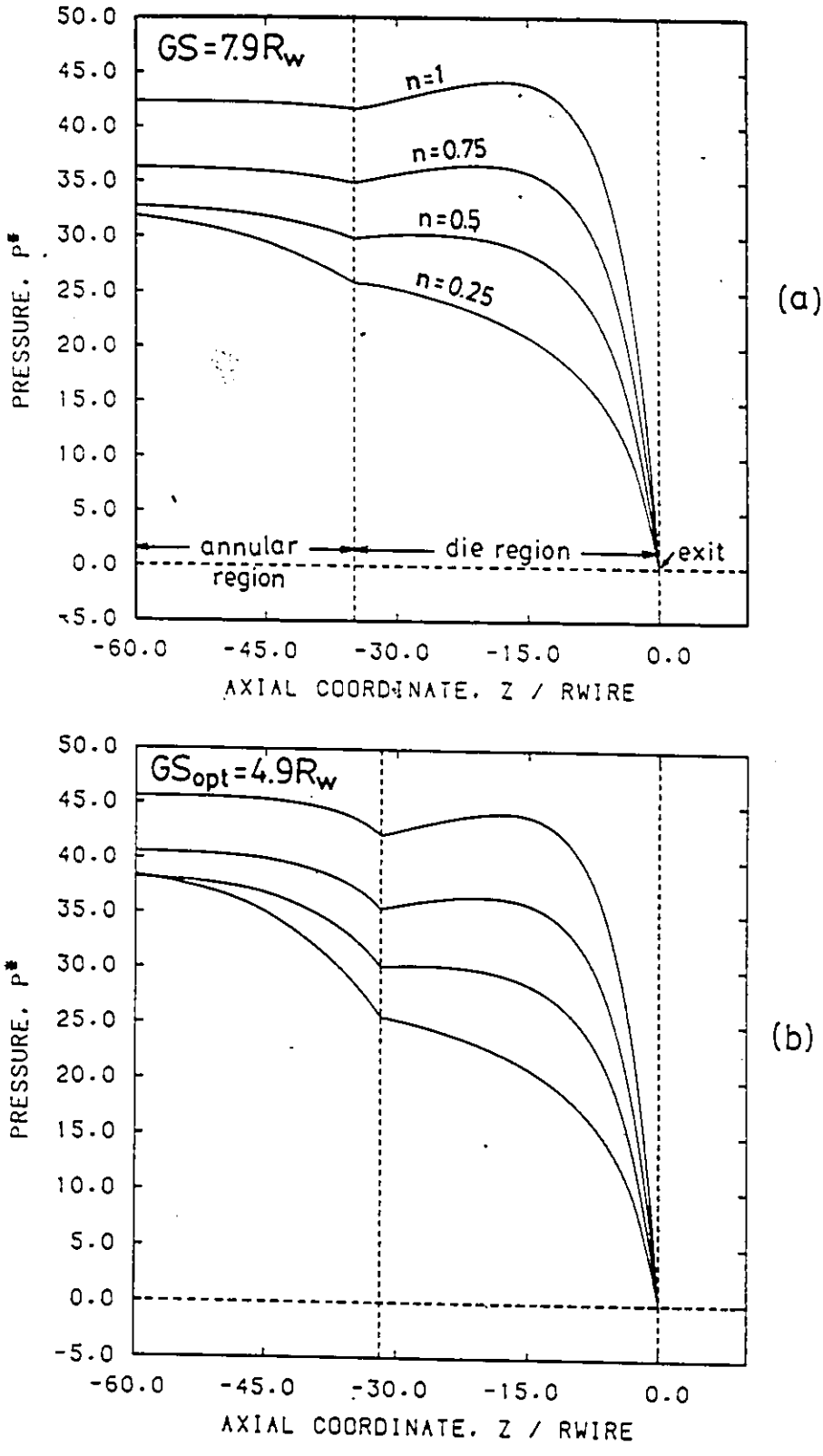

Figure 5.5: Dimensionless Pressure Profiles along Du Pont's Die for Power-law Fluids Using the LAT: (a) GS=7.9R_w. (b) GS=4.9R_w.

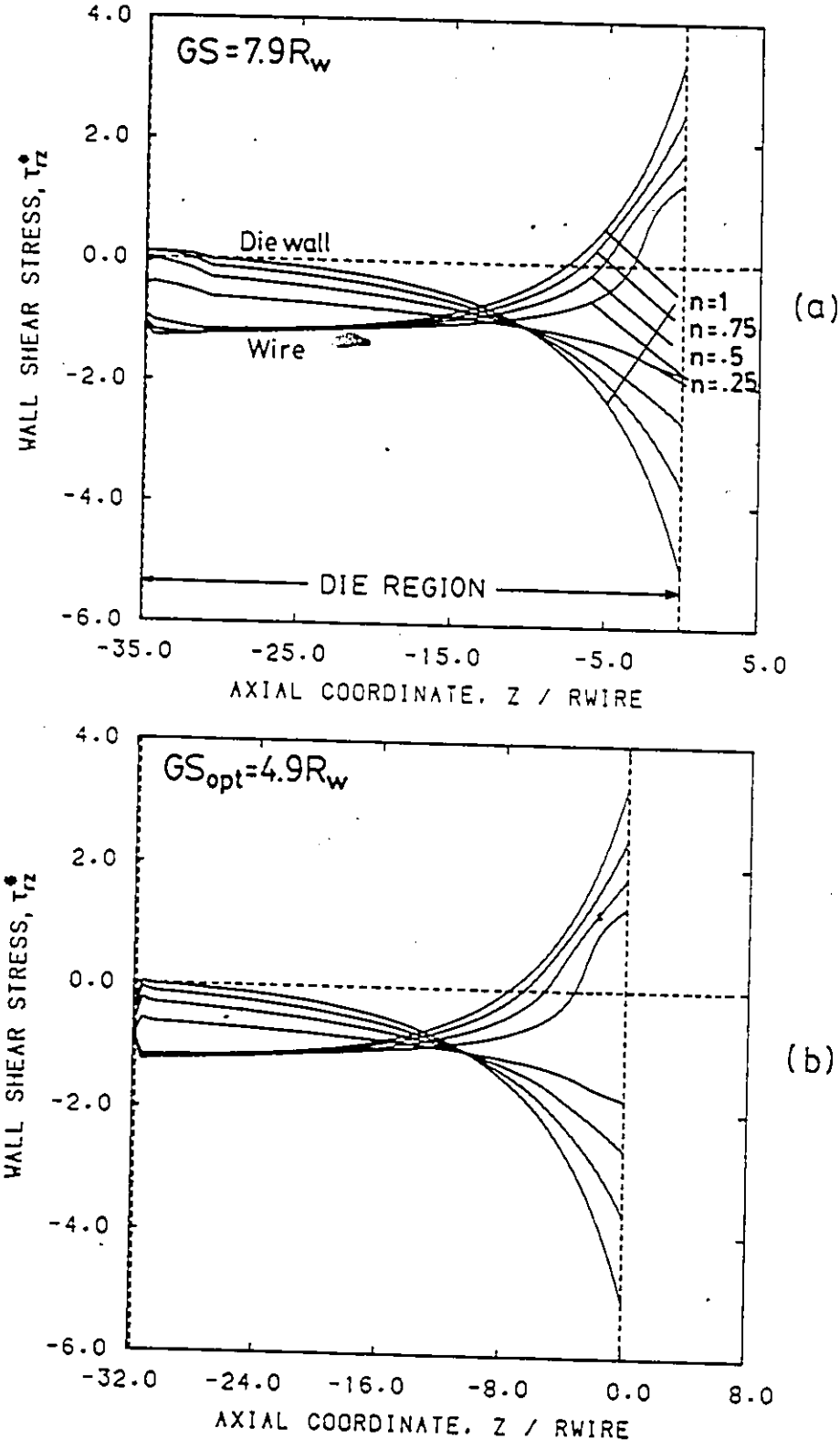

Figure 5.6: Dimensionless Shear Stress Profiles along the Die Wall and Wire in Du Pont's Die for Power-law Fluids Using the LAT: (a) GS=$7.9R_w$. (b) GS=$4.9R_w$.

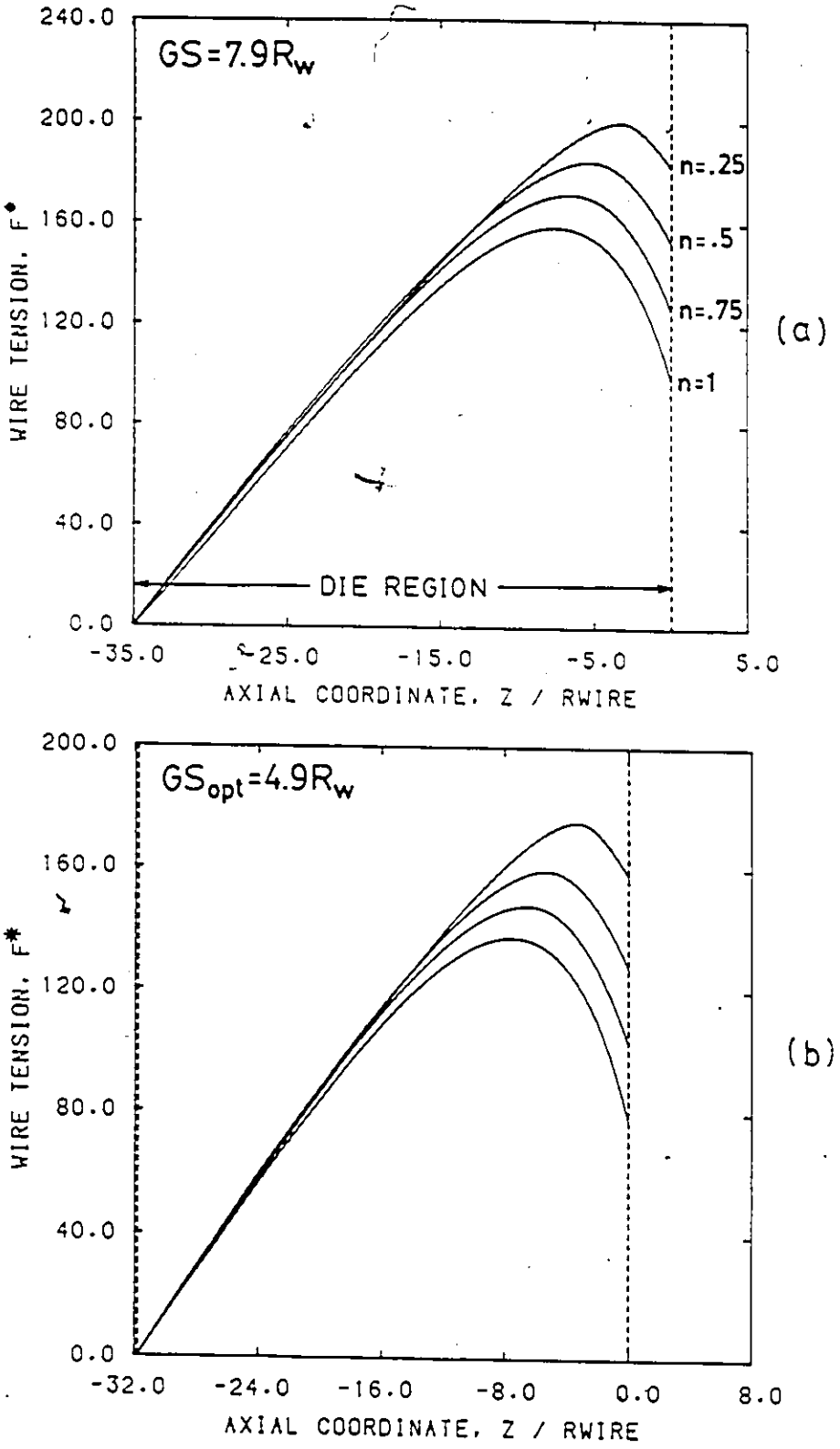

Figure 5.7: Dimensionless Wire Tension Profiles along Du Pont's Die for Power-law Fluids Using the LAT: (a) GS=7.9R_w. (b) GS=4.9R_w.

(τ^*) in Figure 5.6 shows similar behaviour. A slight discrepancy for the die wall stress occurs close to the end of the annular region. The $4.9R_w$-GS design has die stresses which are always less than zero. The $7.9R_w$-GS design, however, might start from a positive value, reaching zero in the early stage of the die section, and becoming negative farther downstream. It is believed that this positive die stress behaviour, rather than the positive pressure gradient behaviour, should be used as a criterion to determine the presence of recirculation. Schematically, this is shown in Figure 5.8. As can be seen, the die shear stress can only be positive when back-flow exists. Further analysis using FEM (see Figure 5.10) has confirmed this point. The wire tension profiles for the $4.9R_w$-GS case (Figure 5.7) show very similar behaviour to the $7.9R_w$-GS case.

The two-dimensional FEM is used to study the same domain. There are a total of 216 u-w-p elements and 511 nodes. A section of the grids for the two designs are shown in Figure 5.9. The boundary conditions for the u-w-p formulation are as described in the mathematical modelling section of this chapter. The streamlines obtained for the $4.9R_w$-GS and $7.9R_w$-GS designs are plotted in Figure 5.10. Wagner (1987) found a small recirculation at the die wall for the $7.9R_w$-GS design. By moving the torpedo a little deeper into

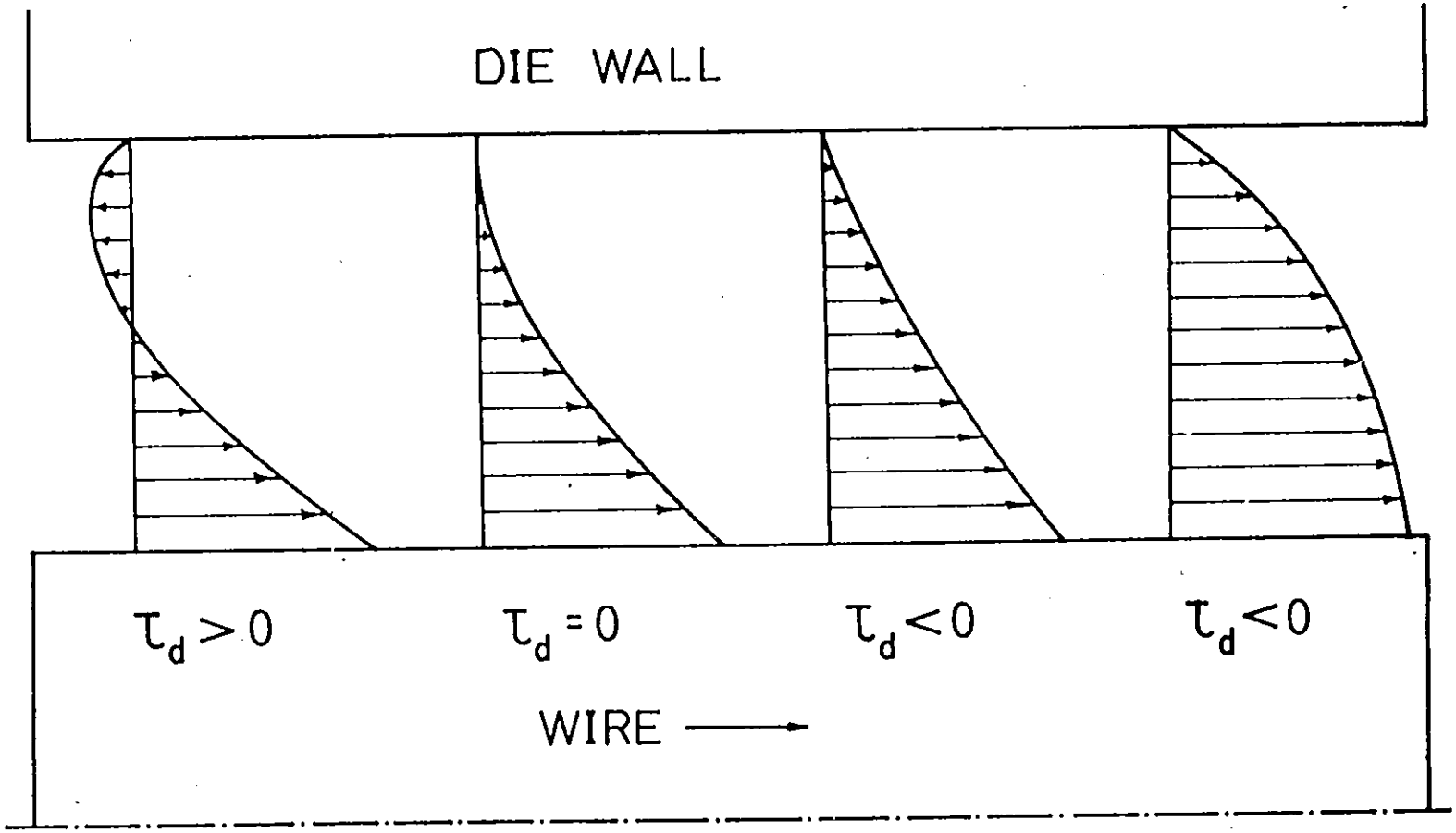

Figure 5.8: Schematic Diagram of Radial Velocity Profiles in Wire Coating and the Corresponding Die Shear Stresses.

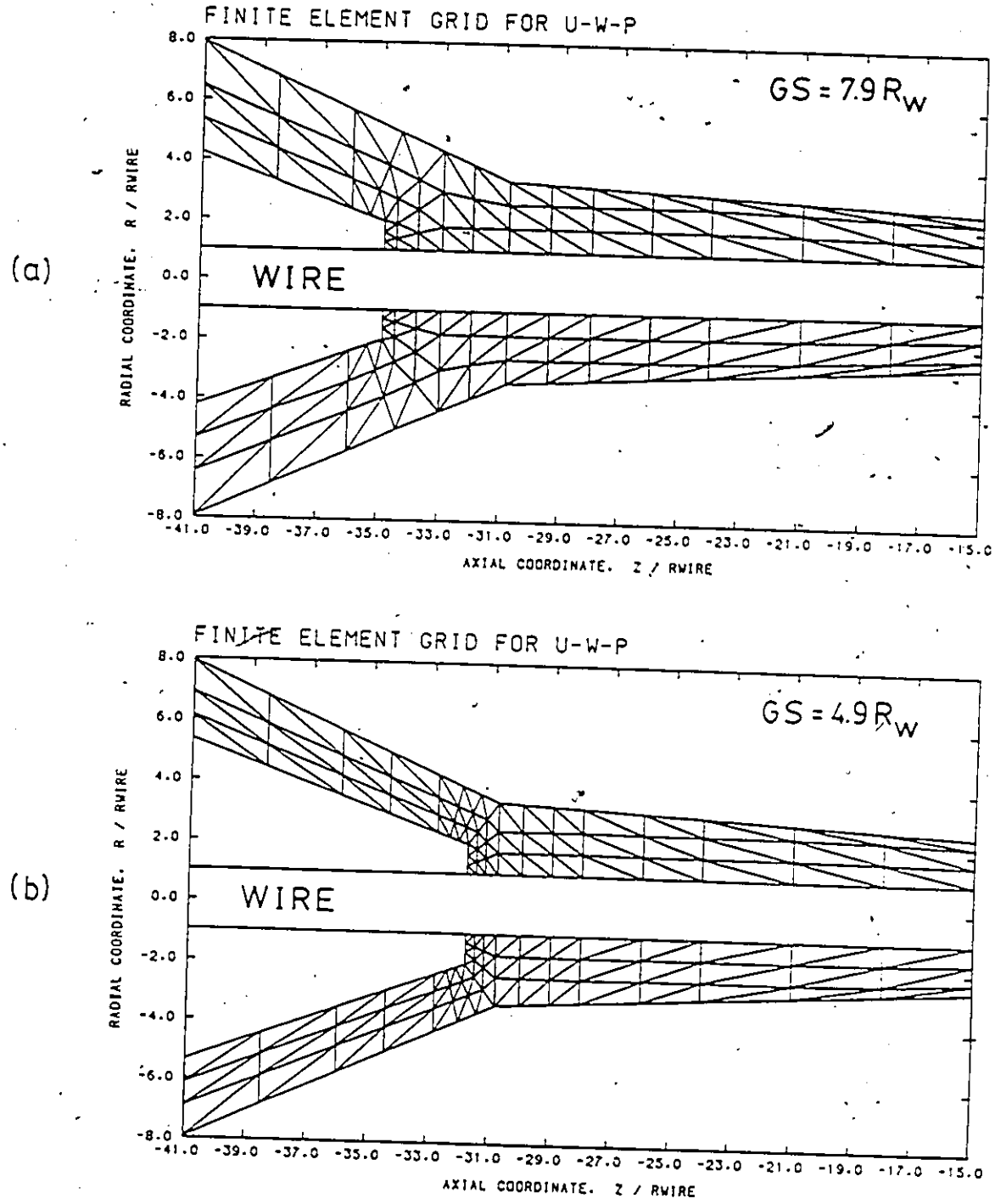

Figure 5.9: Finite Element Grid for u-w-p Formulation near the Impact Region of Du Pont's Die: (a) GS=7.9R_w. (b) GS=4.9R_w.

the die ($4.9R_w$ GS), the recirculation disappears. Obviously, the $4.9R_w$-GS design gives a better "streamlined" flow by eliminating the almost stagnant region (region where recirculation occurs).

The major differences between the two designs were found to exist close to the end of the annular region. Both the LAT and FEM have shown no significant differences between the two designs. The most interesting aspect is the elimination of the recirculation for the $4.9R_w$-GS design.

5.4 Nonisothermal Wire Coating

The majority of nonisothermal studies in wire-coating dies have been preformed by neglecting the $v_r(\partial T/\partial r)$ term in the energy equation. In this section, the full two-dimensional energy equation is solved using the new temperature formulation (discussed in Chapter 3) and the results are compared to those obtained by neglecting radial convection in earlier work (Endo's die, Carley et al., 1979). Following that, the die employed by Du Pont Co. is analyzed for a commercially used wire-coating resin (Alathon 3535) for which experimental data is available. In this analysis, the effect of thermal boundary conditions and the concept of optimum gum space are

(a)

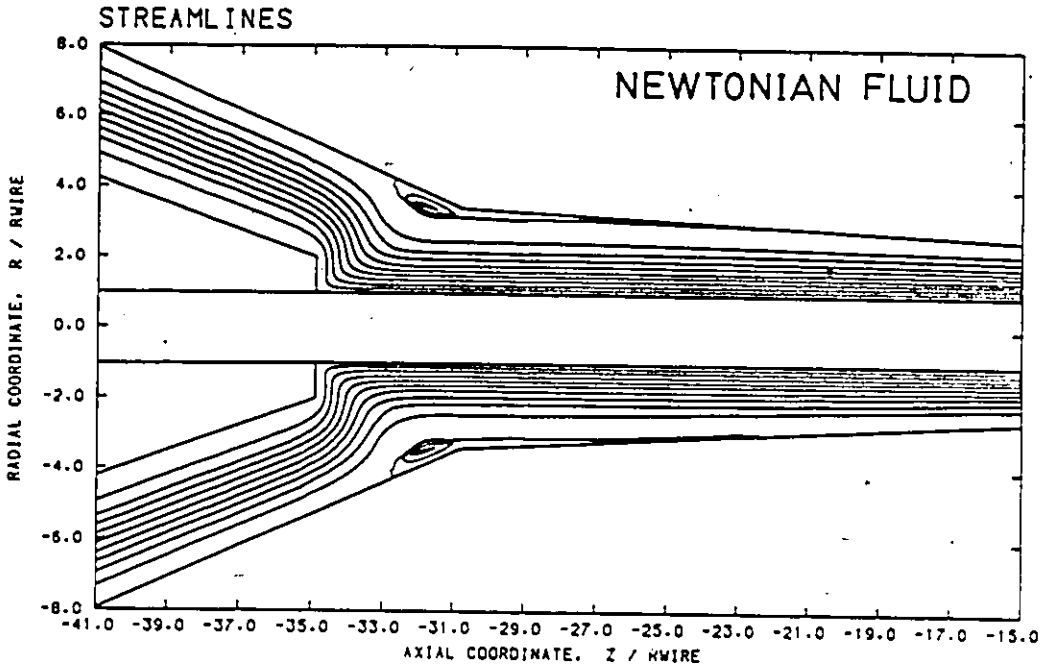

(b)

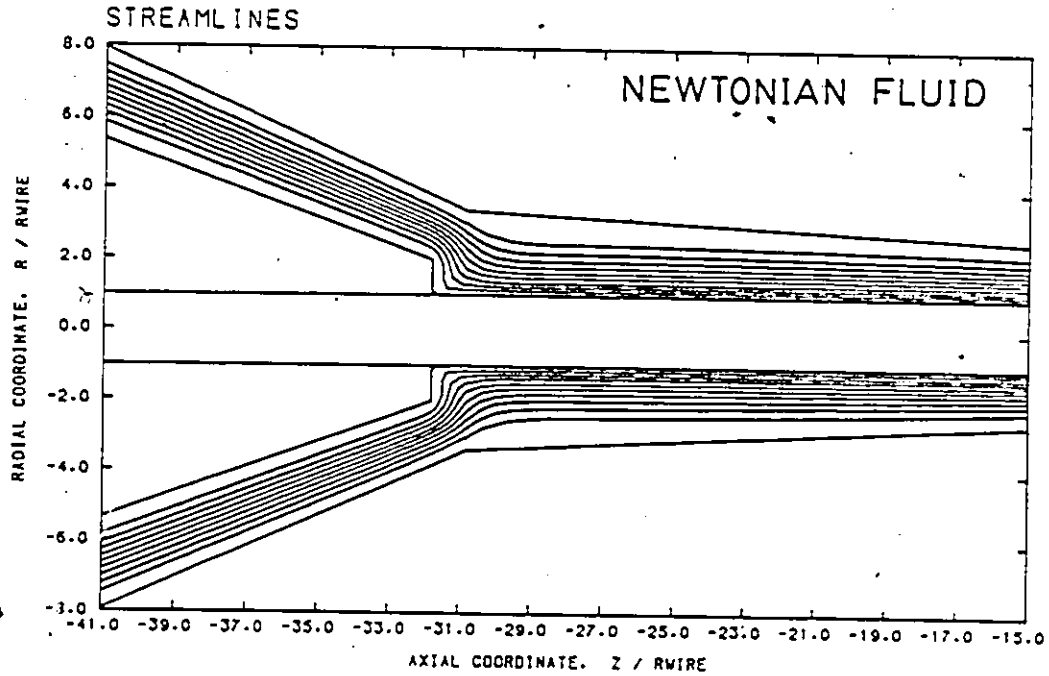

Figure 5.10: Streamline Patterns for a Newtonian Fluid near the Impact Region of Du Pont's Die: (a) GS=7.9R_w. (b) GS=4.9R_w.

also being examined.

5.4.1 Comparison with Previous Results (Endo's Die)

Endo (1976) (also Carley et al., 1979) solved the coupled momentum and energy equations in a simple wire-coating die (as shown in Figure 5.11) using the Finite Difference Method (FDM). Due to numerical instabilities encountered, the radial convection term $v_r(\partial T/\partial r)$ in the conservation of energy equation was dropped in their calculations.

In this section, their problem is reworked with the FEM. The new temperature formulation (discussed in Chapter 3) is used to solve the full energy equation. Current findings are compared to the FDM results. The physical properties of LDPE (Carley et al., 1979) are summarized as follows:

Density:	$\rho_a = 0.914$	g/cm^3 at room temperature
	$\rho_m = (1.143 + 0.00089T)^{-1}$	g/cm^3 for $T > 127°C$
Specific heat:	$(C_p)_m = 2.078 + 0.00337T$	$J/g\,°C$
Thermal conductivity:	$k_m = 0.00329$	$J/cm\,s\,°C$

The above physical properties are evaluated at the entry melt temperature

$$T_m = 226.8°C$$

and assumed constant throughout the die.

The three-region viscosity curve employed is (Carley et al., 1979):

Newtonian regime:

$$\log \tau = \log \dot{\gamma} + \log \mu_o \qquad \dot{\gamma} \leq \dot{\gamma}_N \tag{5.23}$$

Transition regime:

$$\log \tau = a(\log \dot{\gamma})^2 + b \log \dot{\gamma} + c \qquad \dot{\gamma}_N \leq \dot{\gamma} \leq \dot{\gamma}_p \tag{5.24}$$

Power-law regime:

$$\log \tau = n \log \dot{\gamma} + \log f \qquad \dot{\gamma} \geq \dot{\gamma}_p \tag{5.25}$$

where $\dot{\gamma}_N = 0.01\ s^{-1}$, $\dot{\gamma}_p = 1600\ s^{-1}$, $\mu_o = 40,000\ poise$, $a = -0.06408$, $b = 0.7437$, $c = 4.346$, $n = 0.333$ and $\log f = 5.004$ for the reference temperature, $T_o = 206°C$.

The temperature dependence of viscosity was handled as follows (Carley et al., 1979):

$$\eta_T = \eta_o \exp\left[\frac{E_\tau}{R}\left(\frac{1}{T_o} - \frac{1}{T}\right)\right] \tag{5.26}$$

where η_T and η_o are the viscosities at absolute temperatures T and T_o (K), the reference temperature, E_τ is the activation energy at constant stress (refer to Appendix C for details) and R is the molar energy constant. The

values for these quantities are: $T_o = 479\ K$, $E_\tau = 48{,}900\ J/gmol$, $R = 8.310\ J/gmol\,K$.

The operating requirement consists of coating a No. 22 AWG wire ($R_w = 0.03215\ cm$) with a final cold (room temperature) coating of $0.0254\ cm$ (79% of R_w) at $V_w = 2032\ cm/s$.

Referring to Figure 5.11, the die is $1.27\ cm$ long with a 3°-tapered angle. The analysis done by Carley et al. (1979) is only restricted to within the die. However, a free surface extended $11.8R_w$ beyond the exit is included in this study so that the boundary conditions at the outflow plane can be more appropriately specified. The corresponding dimensionless groups are summarized as follows (referring to Appendix C for details of calculations):

$$Re = 0.86 \ , \ Pe = 32{,}800$$

$$Na = 147 \ , \ Gz = 656$$

It is interesting to note the low value of Re number justifying the creeping flow assumption but the high values of the Pe and Na numbers, indicating a convection-dominated flow with strong viscous dissipation.

The boundary conditions for the u-w-p formulation are as follows (refer to Figure 5.11):

1. Along AB, the fully developed Newtonian velocity profile is specified.

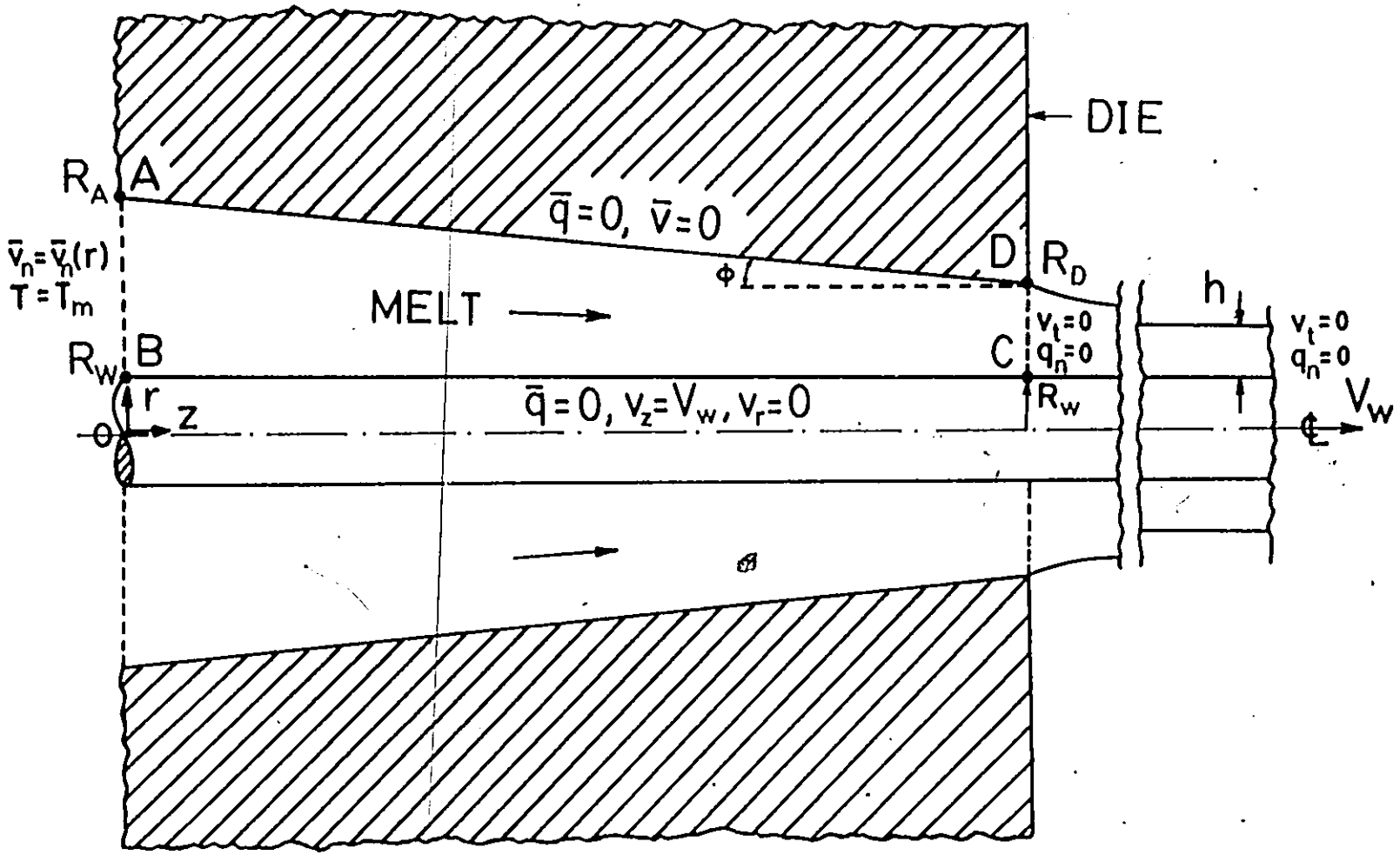

Figure 5.11: Schematic Diagram for Endo's Die along with Notation and Boundary Conditions.

(Rao, 1979).

2. Along AD, no-slip boundary condition is assumed, i.e. $v_r = v_z = 0$.

3. Along the wire surface, no-slip boundary condition is assumed, i.e. $v_r = 0$, $v_z = V_w$.

4. Along the free surface, zero surface traction is prescribed, i.e. $\overline{T} \cdot \overline{n} = 0$.

5. Along the outflow plane, zero radial velocity is prescribed, i.e. $\overline{v} \cdot \overline{t} = v_r = 0$.

The thermal boundary conditions are (refer to Figure 5.11):

1. Along AB, the temperature is assumed to be $T_m = 226.8°C$.

2. Along other boundaries, adiabatic conditions are assumed, i.e. $\overline{q} = 0$.

A section of the discretized domain is shown in Figure 5.12. Both the u-w-p and temperature grids are included. All elements have equal length (z-direction). A total of 1040 u-w-p (2080 bilinear) elements, and 2227 nodes (17 nodes across, 131 nodes along) are used. Such dense grids give solutions which are virtually independent of mesh layout.

The pressure profile from the FEM is shown in Figure 5.13. Also included are Endo's results (1976). An overall pressure drop of 11.5 MPa

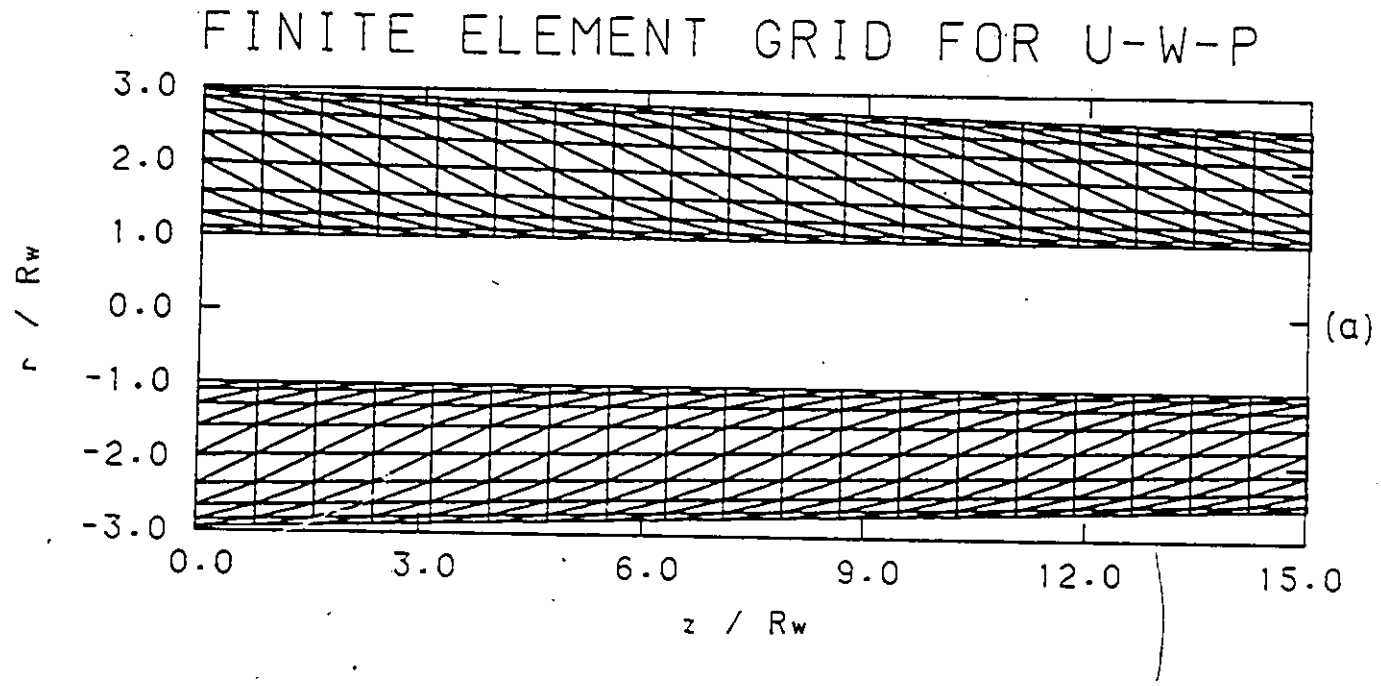

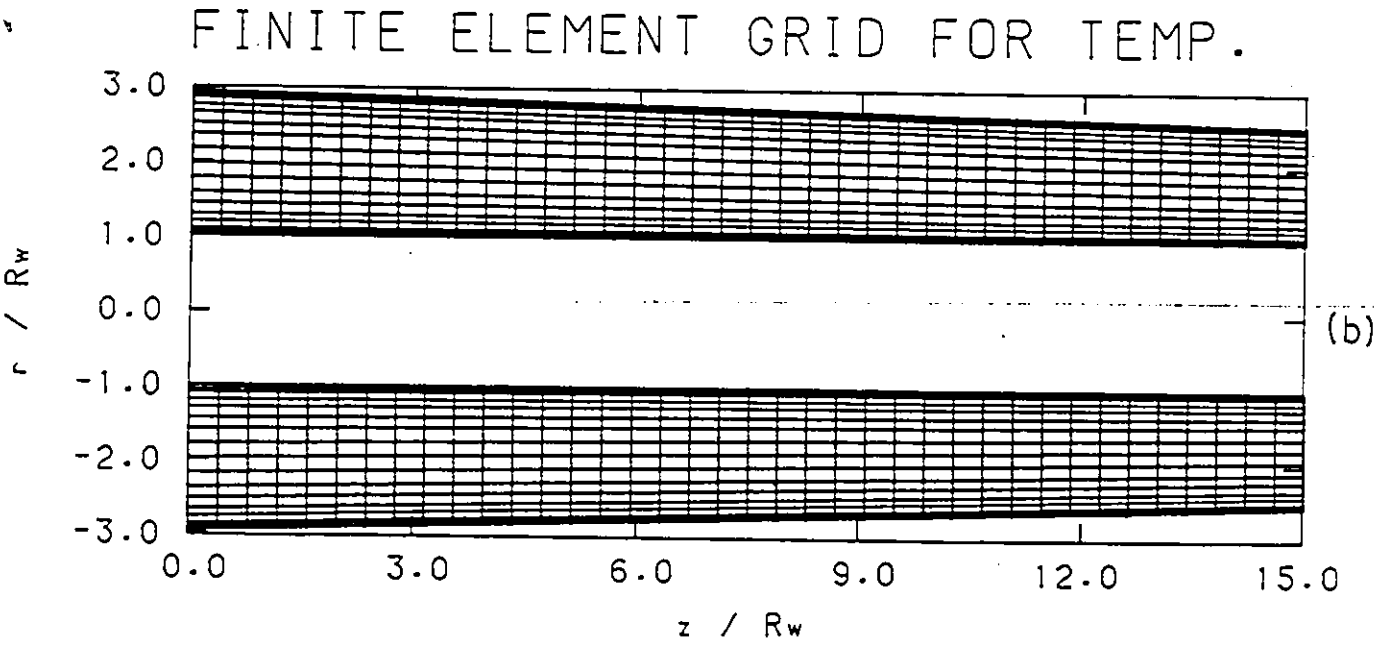

Figure 5.12: Finite Element Grid for Endo's Die: (a) u-w-p Grid. (b) Temperature Grid.

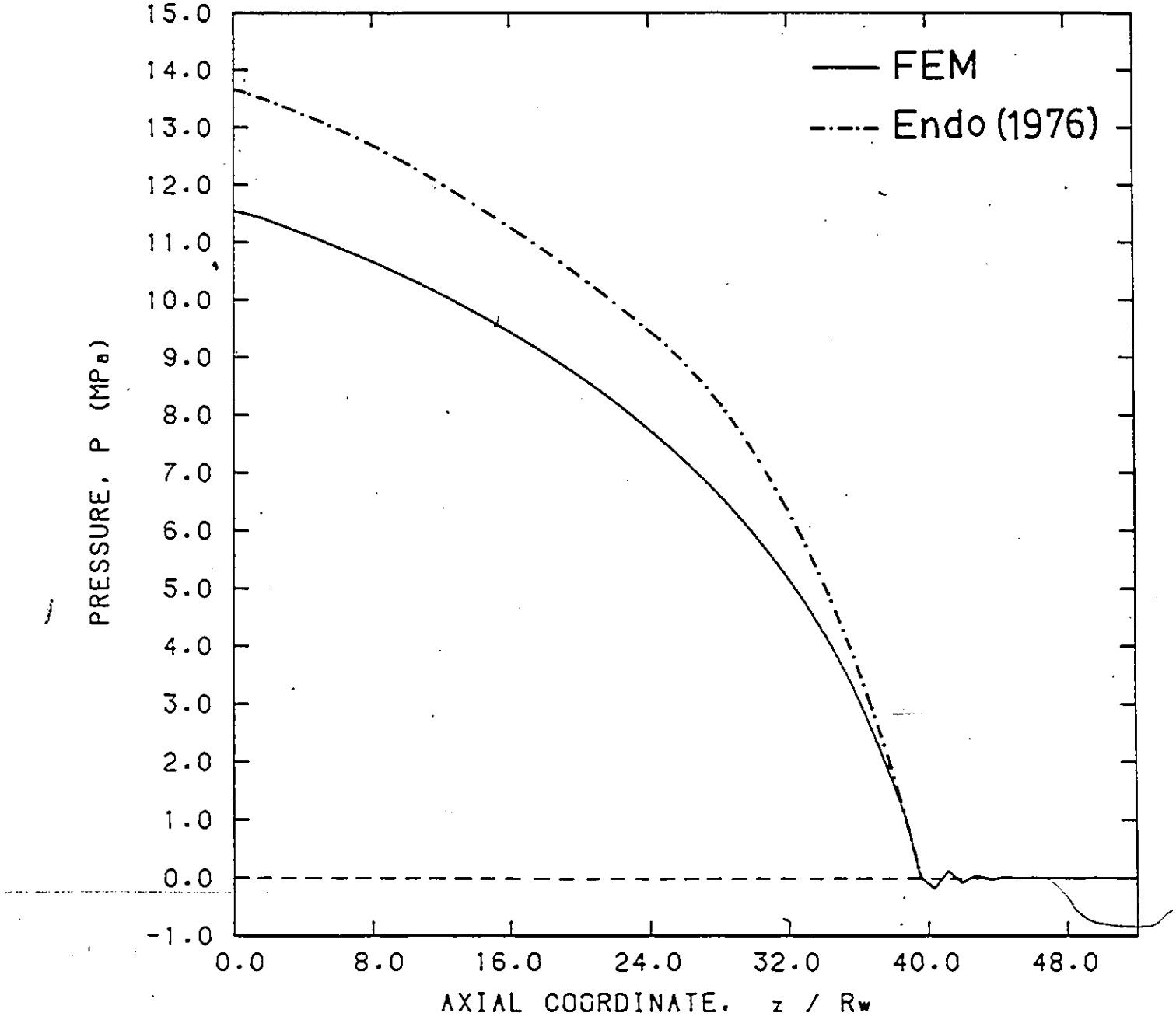

Figure 5.13: Pressure Distribution in Endo's Die.

is obtained as compared to 13.7 MPa from Endo (1976), a discrepancy of about 17%. A look at the radial temperature profile at the die exit (Figure 5.14) shows a significantly higher temperature at the die wall. It is possible, then, to obtain a lower pressure drop due to a reduction in the temperature-sensitive viscosity. Referring to Figure 5.14, it is seen that dropping the v_r-component greatly underestimates the maximum temperature. The term $v_r(\partial T/\partial r)$ serves to convect heat to the walls, thus altering the flow and temperature fields. This in turn affects the overall pressure drop in the system. It is also interesting to note that a trial run with $v_r(\partial T/\partial r)$ set to zero in the new temperature program gave about the same pressure drop as the one found by Carley et al. (1979). These findings clearly demonstrate the errors involved by not considering the v_r-component in the energy equation. In addition, Endo's temperature profile shows a reduction in temperature from the maximum as the die wall is approached. This is highly unrealistic because the adiabatic boundary condition should produce a flat temperature profile after a maximum has been reached (Uhland, 1977; Basu, 1981). The radial velocity profile at the die exit is also shown (Figure 5.15). As can be seen, a more pluggish profile is obtained from the FEM. This can also be attributed to the higher tem-

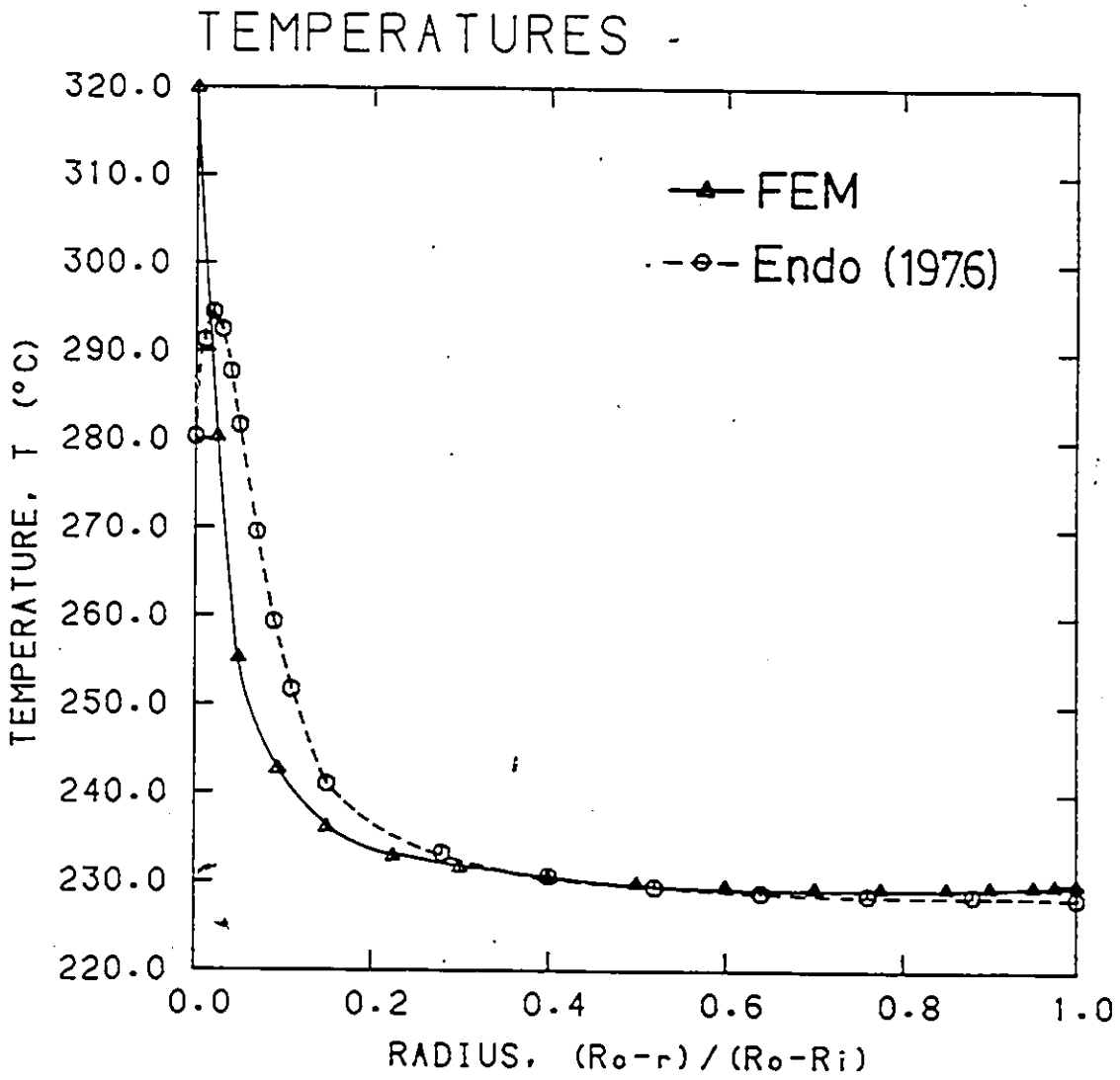

Figure 5.14: Radial Temperature Profile at the Die Exit in Endo's Die.

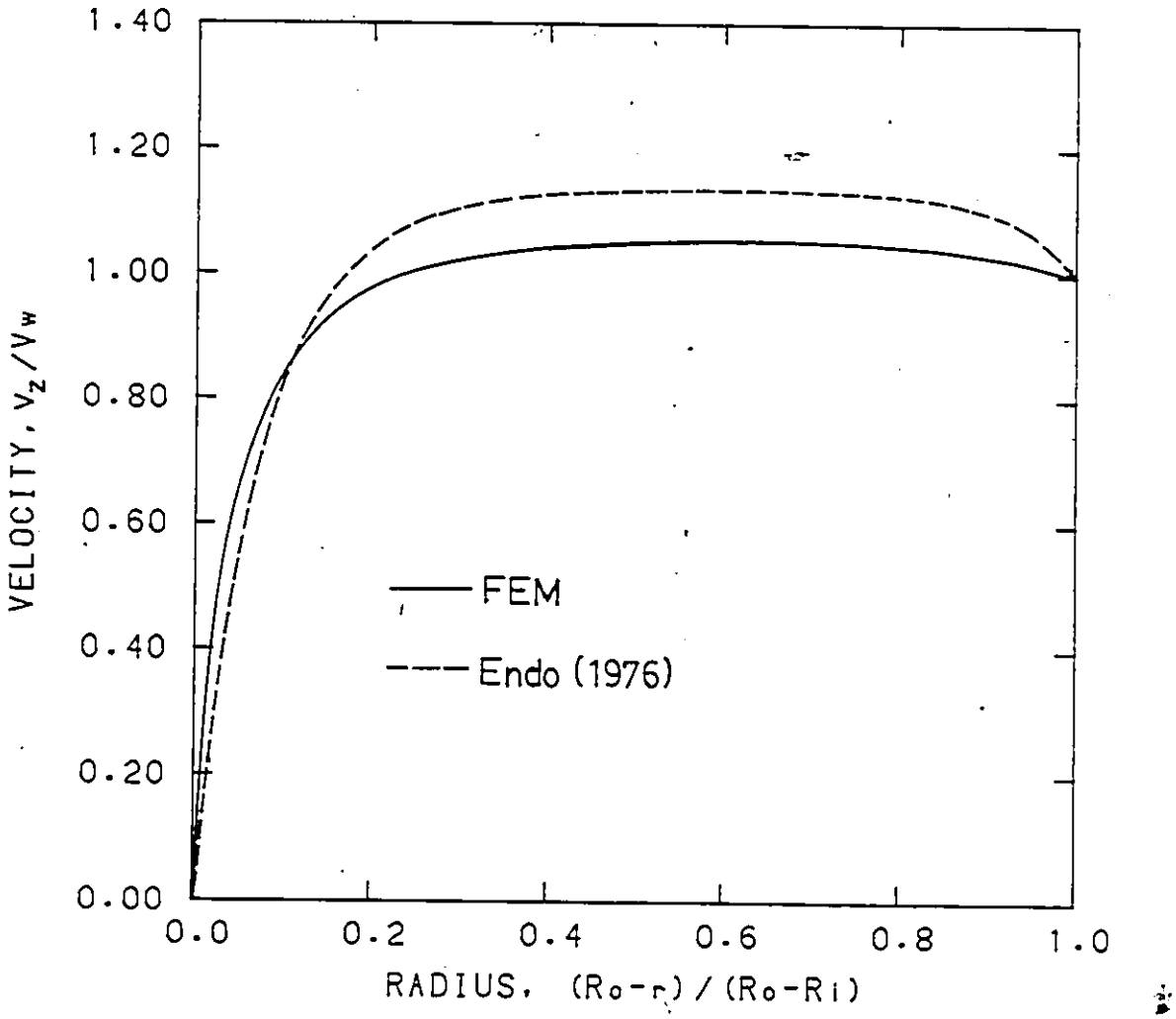

Figure 5.15: Radial Velocity Profile at the Die Exit in Endo's Die.

perature achieved at the die wall, which tends to give a steeper velocity gradient.

Figure 5.16 shows the maximum temperature distribution. The high temperature achieved at the die exit is mostly due to the singularity present, which gives rise to tremendous viscous dissipation. Also included is the wire temperature rise (Figure 5.17). A different discretization (linear triangular elements) for the Streamline-Upwind/Petrov-Galerkin (SU/PG) scheme as proposed by Mizukami (1985) has also been employed. The maximum temperature and wire temperature distribution produced by this upwinding scheme are also included in Figures 5.16 and 5.17, respectively. The highly oscillatory temperature solution illustrates the failure of the linear triangles in treating flows dominated by convection and viscous dissipation effects (high Peclet and Nahme number flows). It has been pointed out by Hughes and Brooks (1982) that this particular upwinding scheme is exact for rectangles and highly skewed quadrilaterals introduce errors. Since triangles are a degenerate form of rectangles (highly skewed), they are expected to be inferior in suppressing the spurious oscillations.

The present analysis shows that the implementation of the Streamline-Upwind/Petrov-Galerkin scheme in bilinear elements is necessary in order

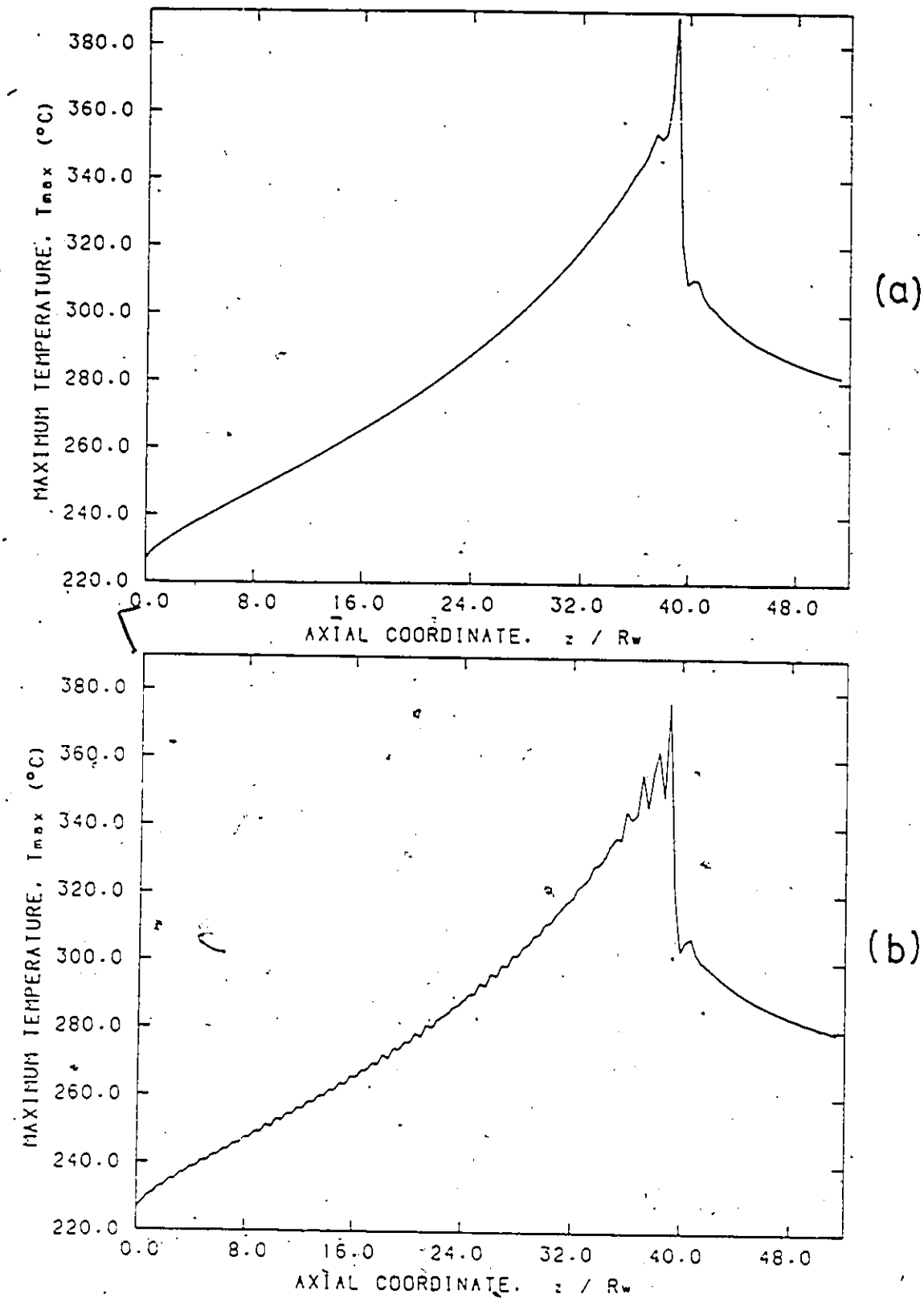

Figure 5.16: Maximum Temperature Distribution in Endo's Die: (a) Bilinear Quadrilaterals. (b) Linear Triangles.

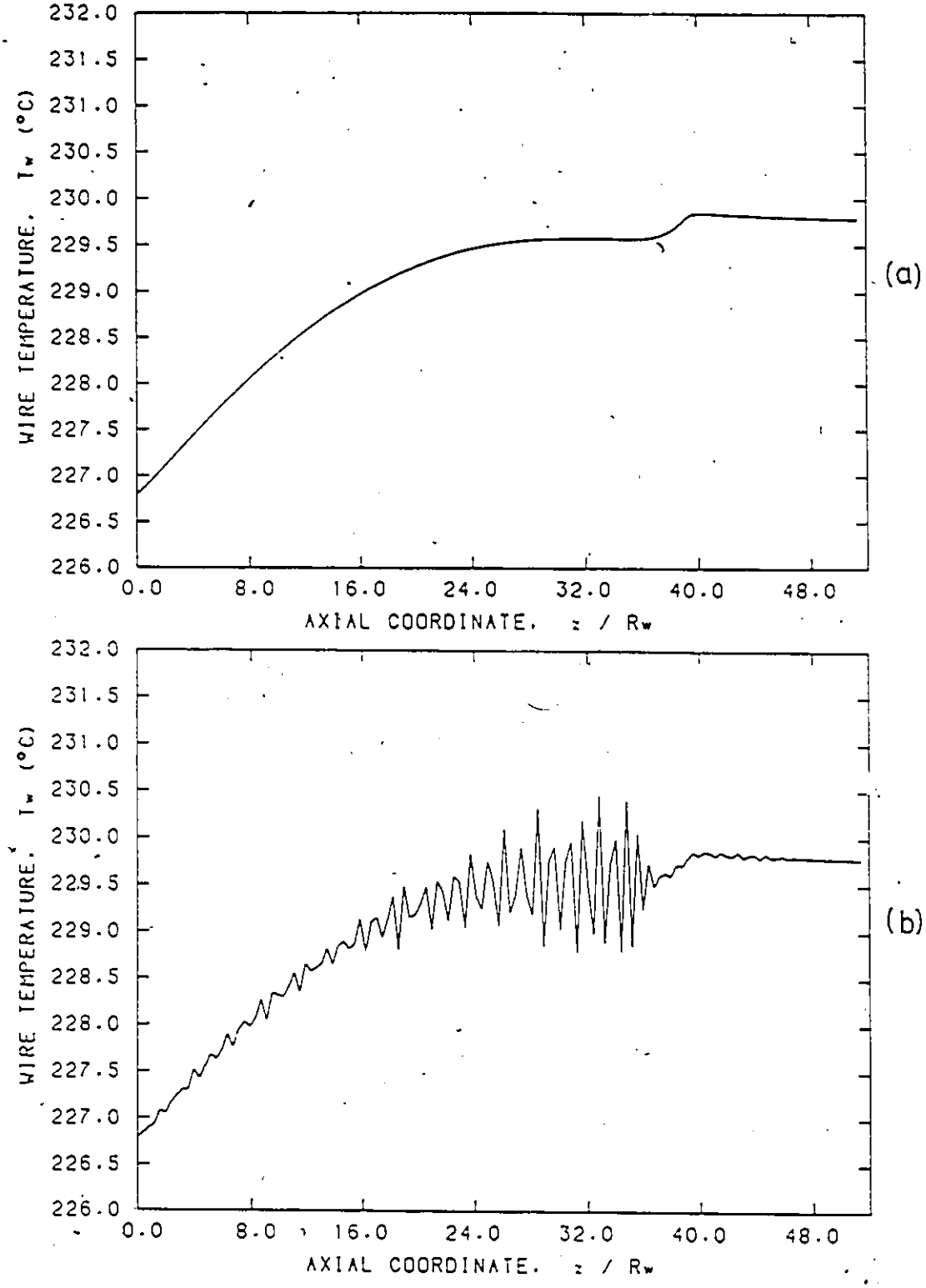

Figure 5.17: Wire Temperature Rise in Endo's Die: (a) Bilinear Quadrilaterals. (b) Linear Triangles.

to obtain accurate solution of the full energy equation for nonisothermal polymer melt flows. In addition, when the full energy equation is considered, the temperatures reach higher values and in turn the pressure drops in the system are lowered. These errors would increase as the taper angle is increased and as the *Pe* and *Na* numbers become larger.

5.4.2 Influence of Die Design and Thermal Boundary Conditions (Du Pont's Die)

(a) Design A (GS=7.9R_w)

The nonisothermal analysis of LDPE (Alathon-3535) in Du Pont's die is first carried out for the 7.9R_w-GS design (Design A) for which experimental data is available (Haas and Skewis, 1974). The effect of various types of thermal boundary conditions (isothermal, adiabatic and heat balances) is investigated. Following that, the 4.9R_w-GS design (Design B) with heat-balance boundary conditions is studied and the results are compared with the 7.9R_w-GS design.

The physical properties of LDPE (Basu, 1981) are summarized as follows:

Density:	$\rho_a = 0.918$	g/cm^3 at $T = 23°C$
	$\rho_m = 0.8772 - 0.00059T$	g/cm^3 for $T > 150°C$
Specific heat:	$(C_p)_m = 2.079 + 0.003376T$	$J/g\,°C$
Thermal conductivity:	$k_m = 0.00326$	$J/cm\,s\,°C$

The viscosity curves for Alathon-3535 were experimentally determined by Tzoganakis (1986). The following viscosity function (refer to Chapter 2, Equation 2.15) is used to curve-fit the data via linear regression (Agur and Vlachopoulos, 1982):

$$\ln \eta = a_1 + a_2 \ln \dot{\gamma} + a_3 (\ln \dot{\gamma})^2 + a_4 T + a_5 T^2 + a_6 T \ln \dot{\gamma} \qquad (5.27)$$

with

$$a_1 = 10.68 \quad , \quad a_2 = -0.7614 \quad , \quad a_3 = -0.007190$$

$$a_4 = 0.003535 \quad , \quad a_5 = -4.473 \times 10^{-5} \quad , \quad a_6 = 0.001131$$

For the heat-balance thermal boundary conditions, the following additional data are used:

Density of copper wire	$\rho_w = 8.913\ g/cm^3$
Specific heat of copper wire	$(C_p)_w = 0.2136\ J/g\,°C$
Thermal conductivity of copper wire	$k_w = 3.894\ J/cm\,s\,°C$

Thermal conductivity of stainless steel (die)	$k_d = 0.4673\ J/cm\,s\,°C$
Thermal conductivity of tungsten (torpedo)	$k_t = 1.5\ J/cm\,s\,°C$
Heat transfer coefficient	$h_T = 0.0047\ J/cm^2\,s\,°C$
Ambient air temperature	$T_a = 23\ °C$
Body die temperature	$T_s = 232\ °C$
Torpedo temperature	$T_t = 232\ °C$
Distance for controlled temperature in die	$s = 0.35\ cm\ (\approx 11R_w)$
Distance for controlled temperature in torpedo	$s \approx 0\ cm$

The physical properties for the metals are taken from Perry and Green (1984) and evaluated at $232°C$. Note that the values of s are set arbitrarily but within reasonable limits for the analysis. The heat transfer coefficient has been evaluated according to Phuoc and Tanner (1980) based on the experimental data of Acierno et al. (1971) (see Appendix D for details). It was found out from the nonisothermal analysis that the value of h_T does not affect the overall results in the die (which are of main interest).

The boundary conditions imposed for the analysis have been presented in Section 5.2. For isothermal wall conditions ($Bi = \infty$), the temperatures

on all boundaries are set to

$$T_o = 232\,^{\circ}C \tag{5.28}$$

which is assumed to be the temperature of the melt at the die entrance (Haas,1986). For adiabatic conditions ($Bi = 0$),

$$\overline{q} = 0 \tag{5.29}$$

is prescribed everywhere except at the die entrance where the temperature is set to the temperature of the melt at the die entrance. For the heat-balance boundary conditions, and referring to the Section 5.2 and Figure 5.3, an arbitrary value of $s = 0.35$ was chosen. This corresponds to $30 < Bi < 130$. Due to the complicated geometry of the die wall, the values for the Bi obtained are only approximate.

A series of runs was carried out for each set of thermal boundary conditions. The results are obtained for four different wire speeds: 100, 500, 1000 and 2000 cm/s. In each case the final coated wire radius is $1.8R_w$, i.e. coating thickness is 80% of wire radius. From the work of Wagner and Mitsoulis (1985), Carley et al. (1979) and Winter (1978), it is apparent that the temperature rise due to viscous dissipation occurs only in a very thin layer close to the walls while the rest of the melt passes under almost isother-

mal conditions at die temperature (entrance melt temperature, 232 $°C$). Therefore, the melt density is assumed to be at 232 $°C$, i.e. $\rho_m = 0.74$, and stay constant throughout the domain. Taking the density difference between the cold melt (solid at 23 $°C$) and the hot melt (at 232 $°C$) into consideration, a coating thickness of $h_m = 0.94R_w$ is required to give a final cold coating of $h = 0.8R_w$. This density difference is accounted for in all the runs of this section.

The FEM grid employed consists of 1200 u-w-p elements (2400 bilinear quadrilaterals) and 2567 nodes, with 151 nodes along the die length and 17 nodes radially. The grids are shown in Figure 5.18 for the u-w-p formulation and in Figure 5.19 for the temperature/stream function formulation. The use of such dense grids guarantees results which are free from mesh influences.

The pressure profiles are similar to those obtained from the isothermal analysis. However, the overall pressure drops obtained are always lower for the nonisothermal case, due to a reduction in the temperature-sensitive viscosity. Table 5.1 presents a summary of pressure drop data for all these cases. The results from the nonisothermal analysis and the experimental data (Haas and Skewis, 1974) are also plotted in Figure 5.20. As can

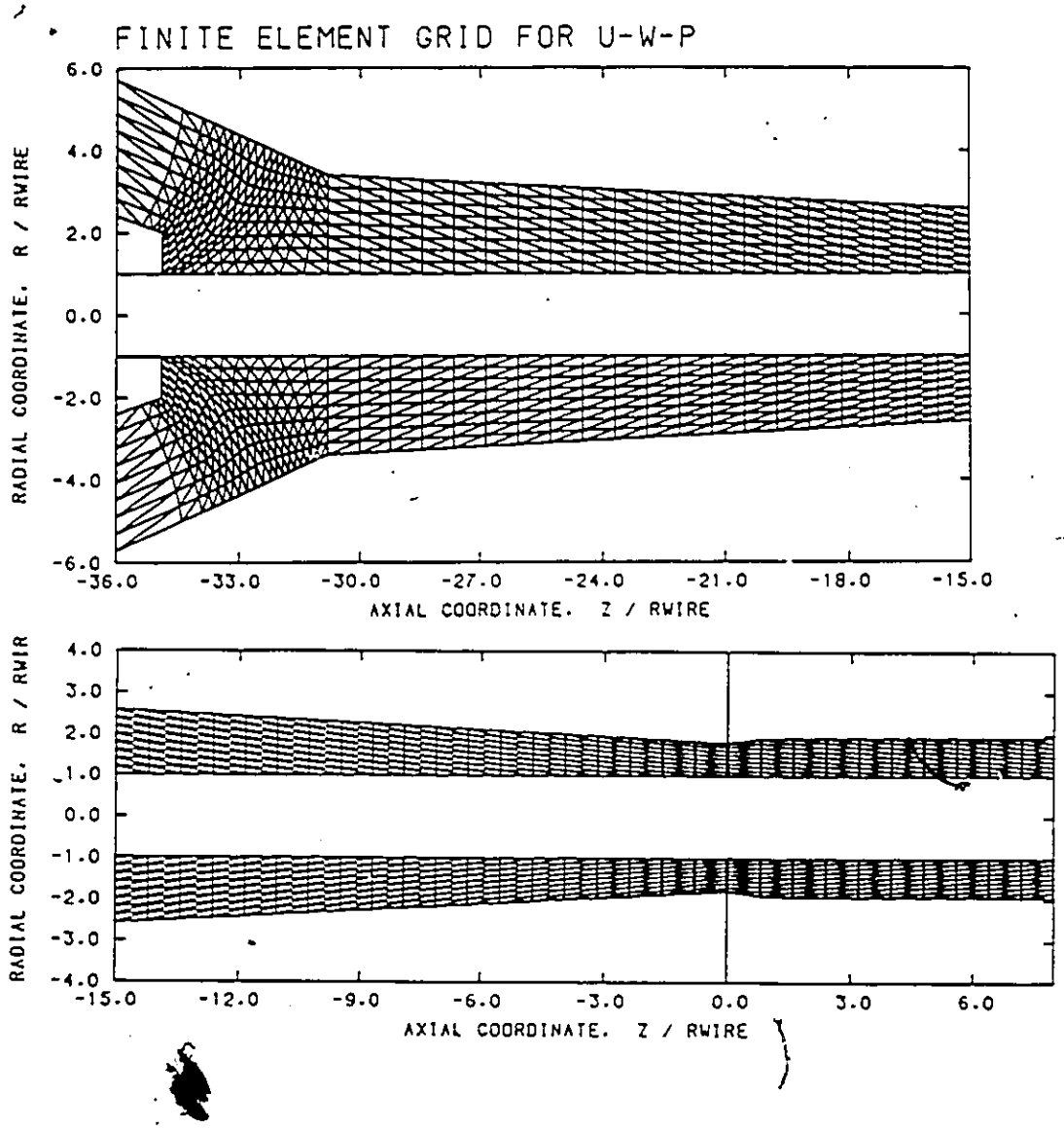

Figure 5.18: Finite Element Grids for u-w-p Formulation in the Nonisothermal Analysis of Du Pont's Die (GS=7.9R_w).

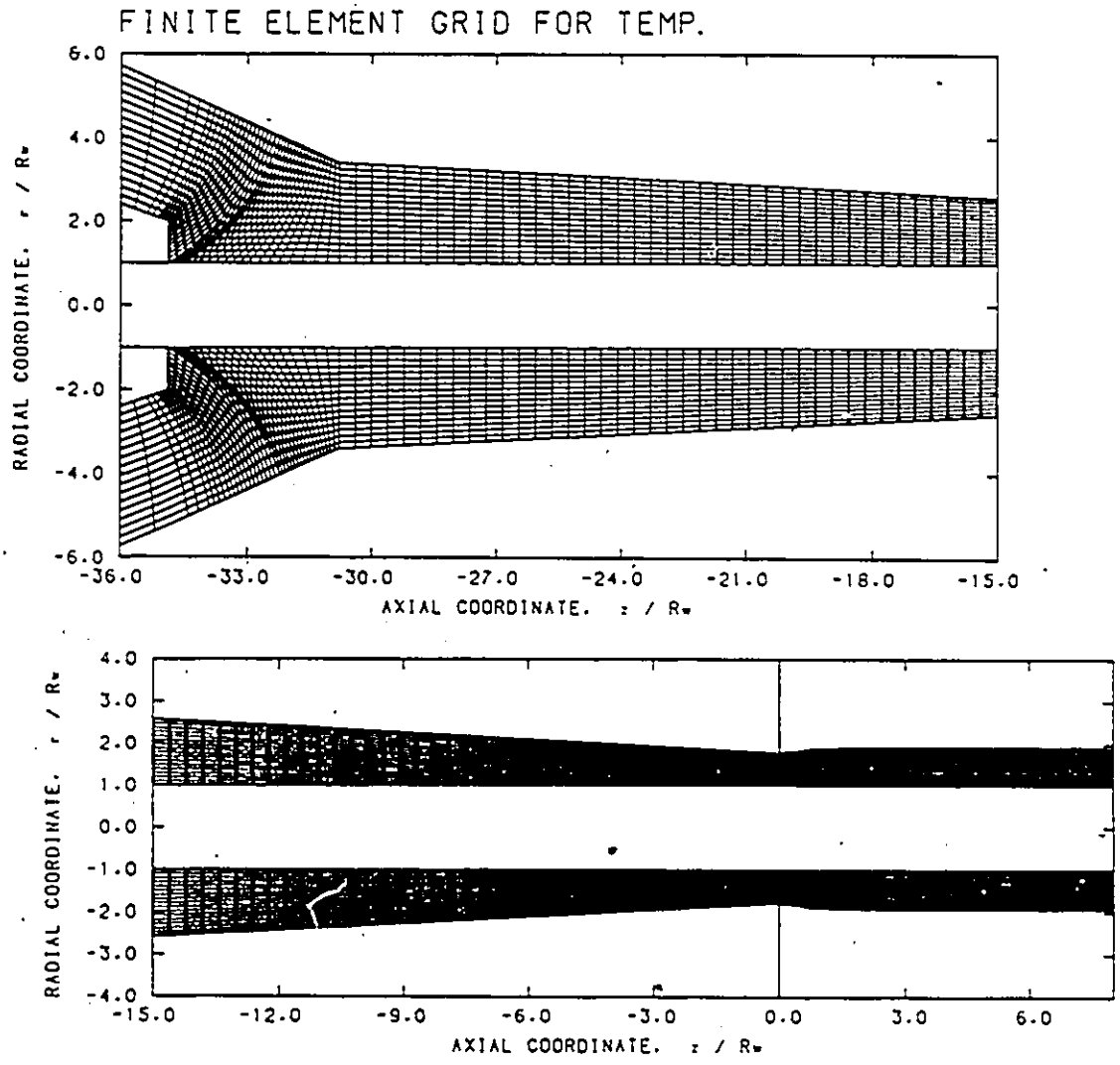

Figure 5.19: Finite Element Grids for Temperature/Stream Function Formulation in the Nonisothermal Analysis of Du Pont's Die (GS=$7.9R_w$).

Table 5.1: Overall Pressure Drop vs. Wire Speed for LDPE. Comparison between FEM and Experimental Results (Du Pont's Die, 22 AWG Wire, GS=$7.9R_w$).

Wire Speed	FEM, nonisothermal			Experimental
V_w (cm/s)	$Bi = \infty$	$30 < Bi < 130$	$Bi = 0$	Haas and Skewis (1974)
100	44.99	14.82	13.78	11.72
500	25.26	24.48	21.43	23.44
1000	30.43	28.87	25.13	29.65
2000	35.69	32.74	28.50	33.78

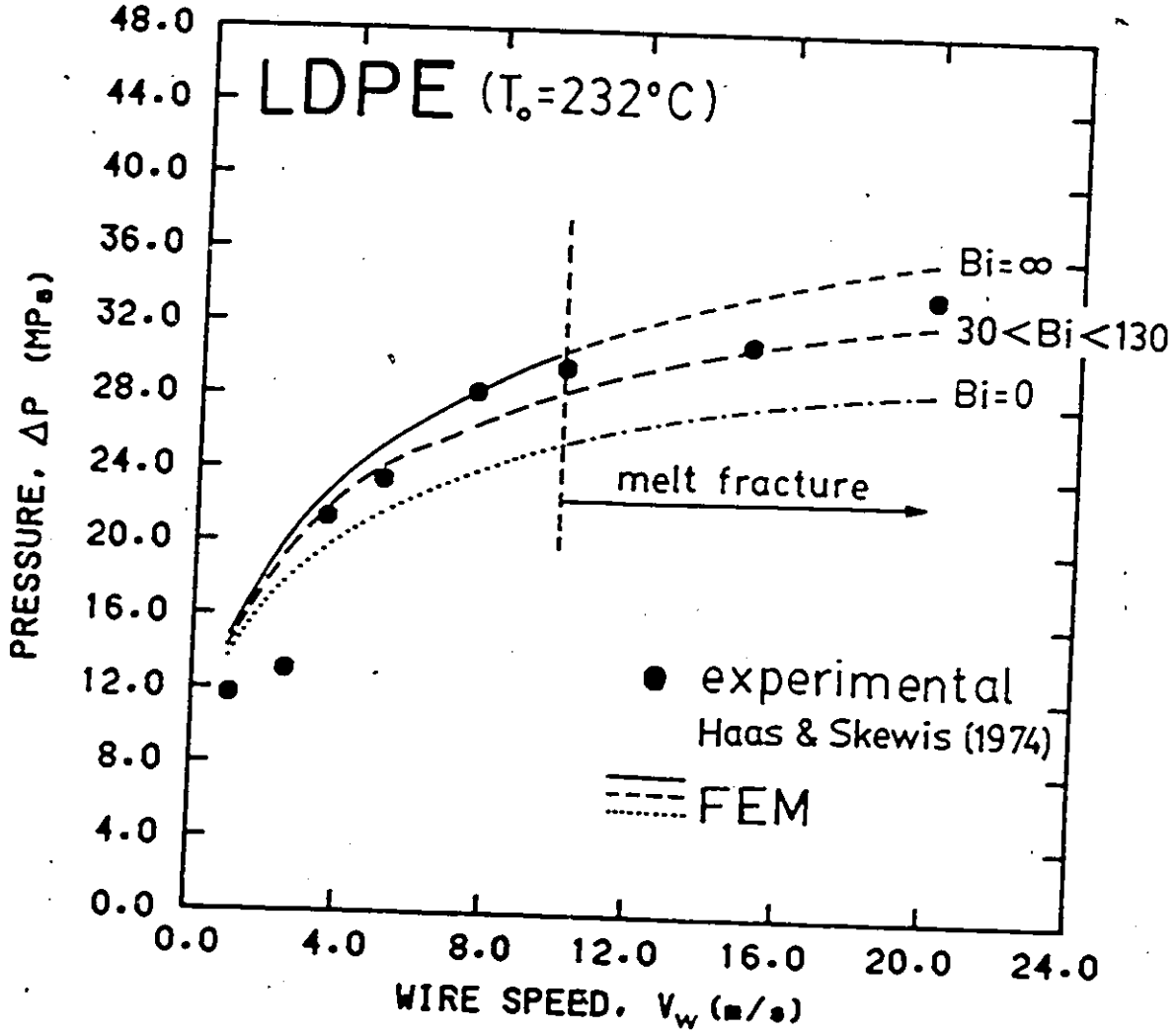

Figure 5.20: Comparison of Experimental Data with Predictions from the Nonisothermal FEM Analysis (Du Pont's Die, GS=7.9R_w).

be seen, the FEM results compare well with the experimental data. The isothermal wall condition ($Bi = \infty$) gives results which are always higher than the experimental data; thus it provides an upper limit at different wire speeds. On the other hand, the adiabatic wall condition ($Bi = 0$) provides the lower limit at high enough speeds ($V_w > 350\ cm/s$). Finally, the results based on heat balances ($30 < Bi < 130$) are in between these two extreme thermal boundary conditions, and they represent the experimental data better. Thus, heat balances are a better model for the thermal boundary conditions. This has also been pointed out by Winter (1977, 1978), who claimed that in actual wire-coating processes, $10 < Bi < 100$. Incidentally, this Bi range agrees well with the range found out from the calculations ($30 < Bi < 130$).

Wagner (1987) has analyzed the same die design ($7.9R_w$ GS) with a different formulation and discretization (Mitsoulis, 1984) using the isothermal wall condition ($Bi = \infty$). His results for the overall pressure drop, however, showed some deviation from the present work (see Figure 5.21). A look at his radial temperature profile at the exit for $V_w = 2000\ cm/s$ shows severe oscillations of $\pm 100°C$ (Figure 5.22). A plot of current results on the same graph shows an oscillation-free profile. Evidently, the unreliable tempera-

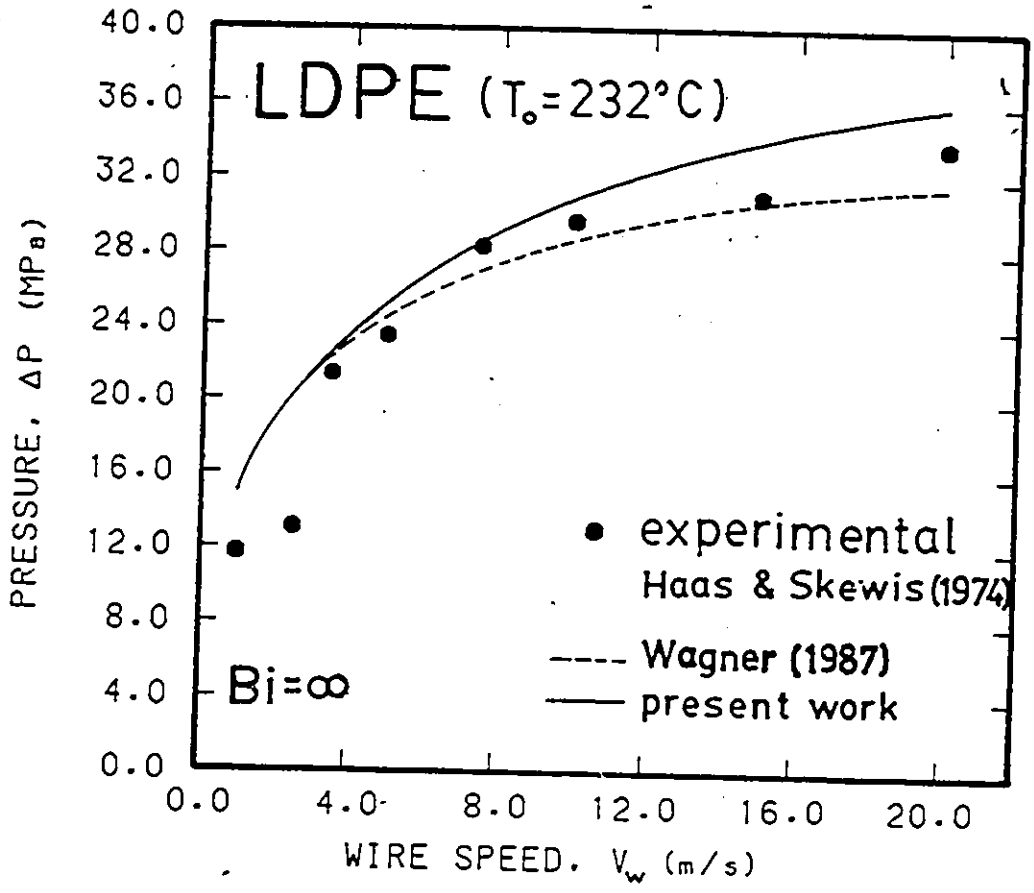

Figure 5.21: Comparison between Results from Nonisothermal Analysis for Present and Previous Work (Wagner, 1987) (GS=7.9R_w, $Bi = \infty$).

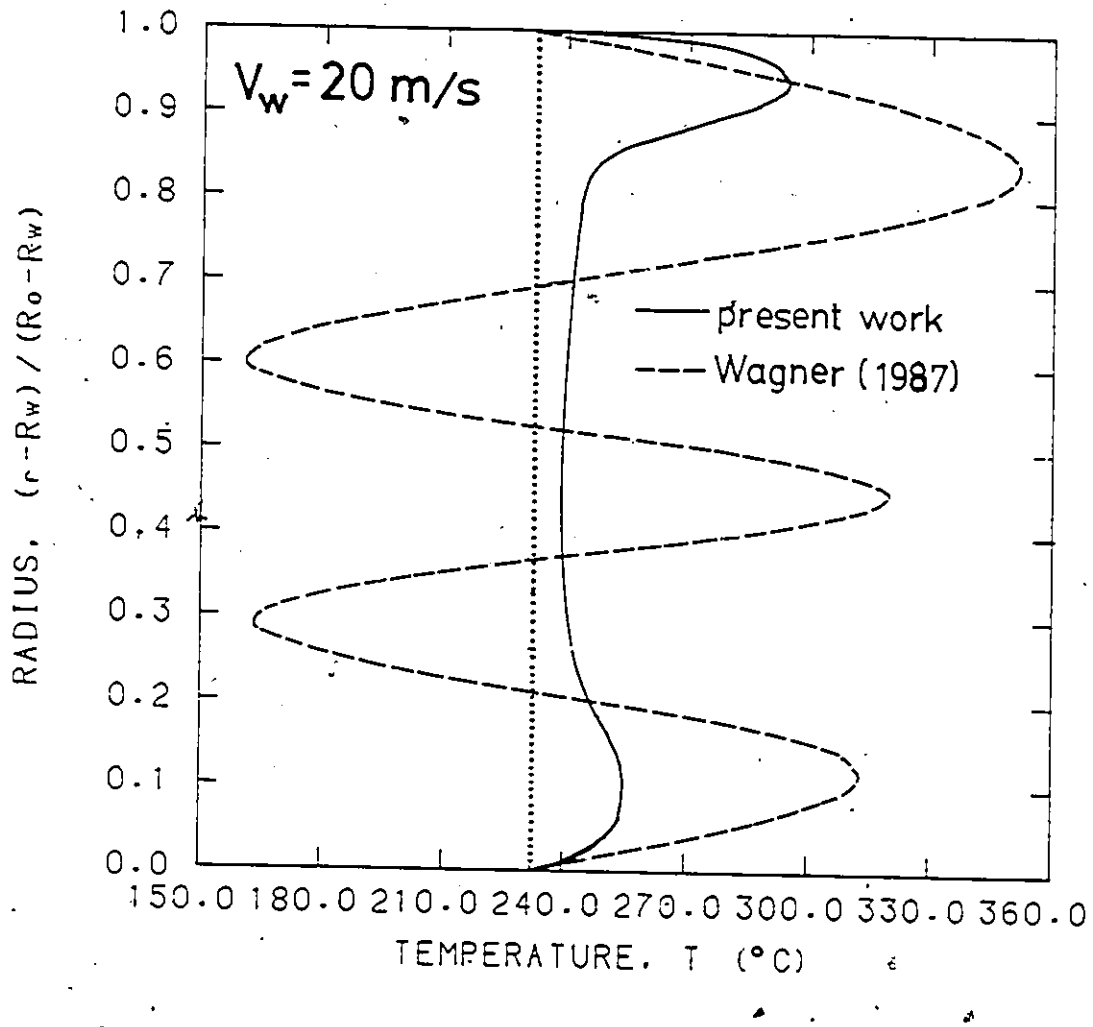

Figure 5.22: Comparison between Radial Temperature Profiles at the Die Exit Obtained from Present and Previous Work (Wagner, 1987) (GS=7.9R_w, $V_w = 2000\ cm/s$, $Bi = \infty$).

ture field obtained by Wagner (1987) is the cause for the discrepancies in the overall pressure drop. However, it is seen that despite the erroneous temperature field, the overall pressure results are not very much off. This agrees with Wagner's assertion that local oscillations do not greatly affect such global quantities as pressures, wire tension, etc. Of course, the current temperature formulation and discretization with its superior performance gives more reliable and better results.

For the temperature field, we have different radial profiles for either set of boundary conditions. Figure 5.23 shows a typical developing profile for the intermediate case of thermal boundary conditions ($30 < Bi < 130$) in which the unknown boundary temperatures are found from thermal balances. The temperatures grow higher close to the die walls due to viscous dissipation but not at the die walls unless the die exit is approached. This is better illustrated in Figures 5.24 and 5.25, where the maximum temperature distribution and the die wall temperatures are plotted along the die length for different wire speeds. It is seen that near the exit, the temperatures follow the stress singularity that becomes more dramatic as the wire speed increases. The global maxima reach $337°C$ for 1000 cm/s and $397°C$ for 2000 cm/s, just before the exit, but it is doubtful whether the melt

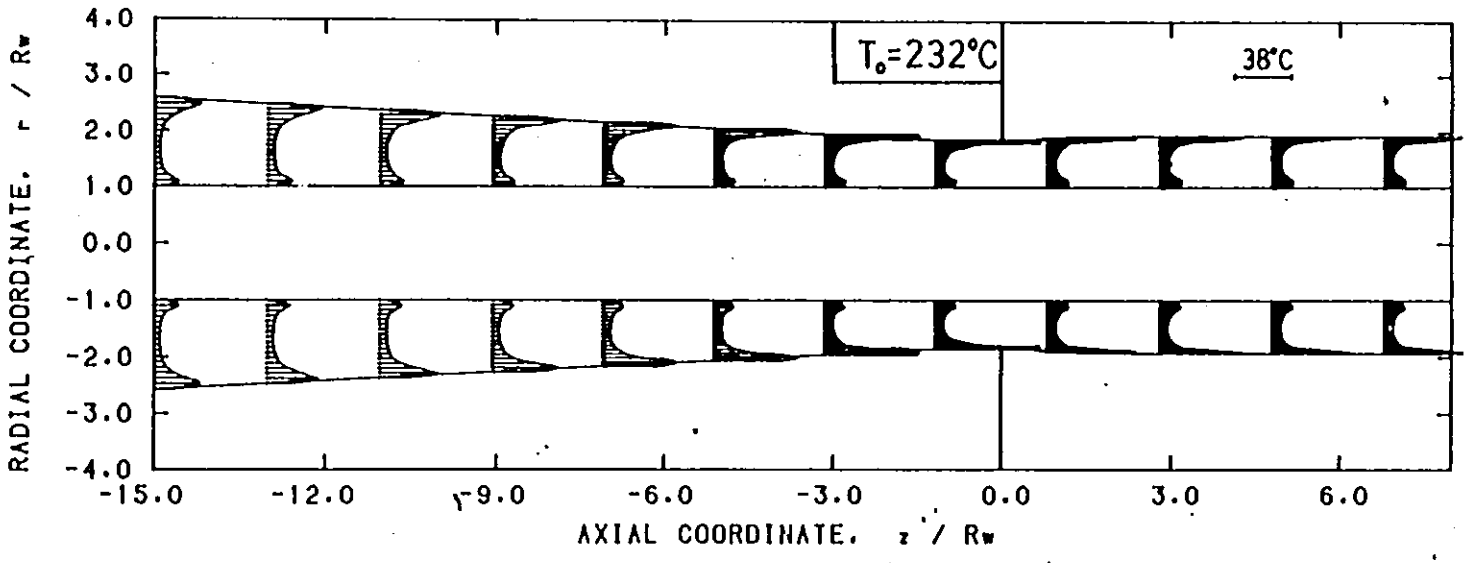

Figure 5.23: Temperature Profile Development along Du Pont's Die (GS=7.9R_w, $V_w = 1000\ cm/s$, $30 < Bi < 130$).

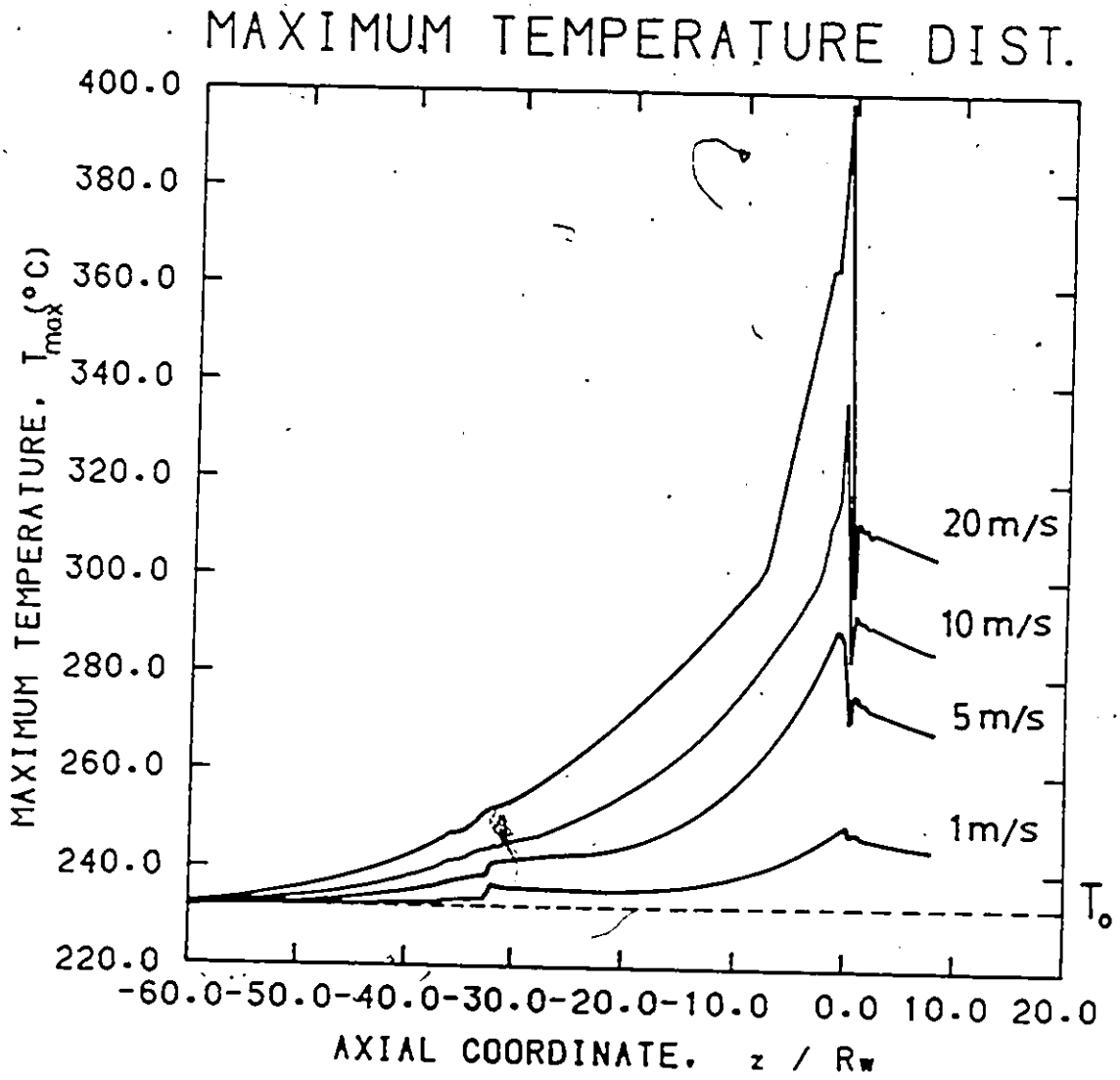

Figure 5.24: Maximum Temperature Distribution along Du Pont's Die for Different Wire Speeds (GS=7.9R_w, $30 < Bi < 130$).

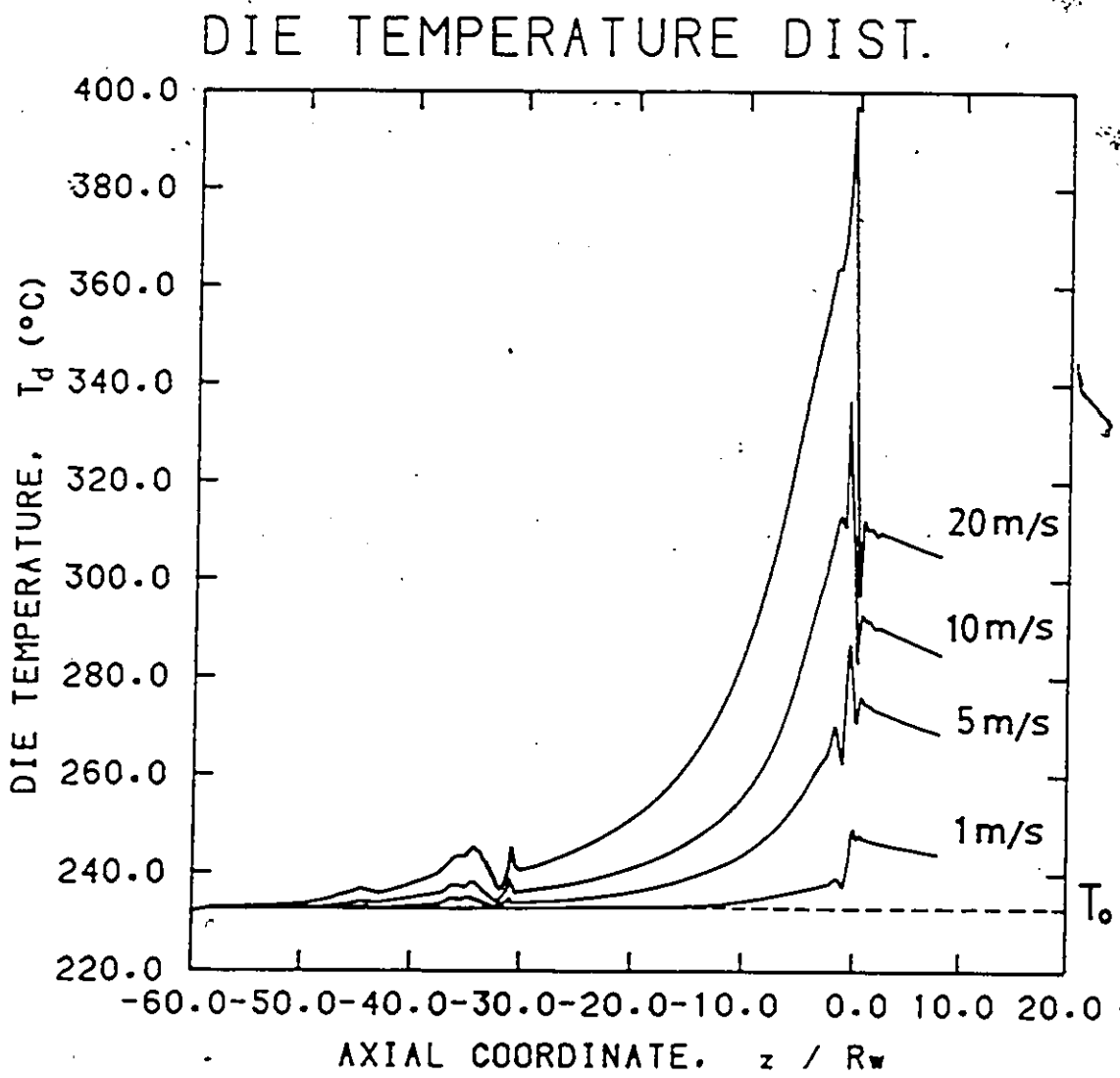

Figure 5.25: Die Wall Temperature Distribution along Du Pont's Die for Different Wire Speeds (GS=$7.9R_w$, $30 < Bi < 130$).

can sustain such temperatures without degrading. The experimental results also showed that wire speeds $V_w \geq 1000\ cm/s$ were causing increased wire-coating roughness (Haas and Skewis, 1974), which is an indication of the severity of these conditions.

It is also interesting to see that using heat balances on the wire surface leads to an increase in wire temperature of only about $1°C$ for the slowest speed of 100 cm/s (see Figure 5.26). Higher speeds reduce the rise, and therefore the wire exits with its temperature almost unaltered. Thus, due to the extremely short residence time in the die, the wire temperature stays approximately constant. The same conclusion was also reached by Winter (1978). This is not the case, though, when adiabatic walls are assumed ($Bi = 0$) as shown in Figure 5.27, where the wire temperature increases rapidly with wire speed. This is another indication that correct boundary conditions have to be used to obtain reliable results.

The radial temperature profiles at the die exit for the intermediate case ($30 < Bi < 130$) are shown in Figure 5.28 for four different wire speeds. The influence of changing from isothermal walls ($Bi = \infty$) to adiabatic walls ($Bi = 0$) is shown in Figure 5.29, where the three radial temperature profiles are compared at the die exit. Near the wire the actual profile

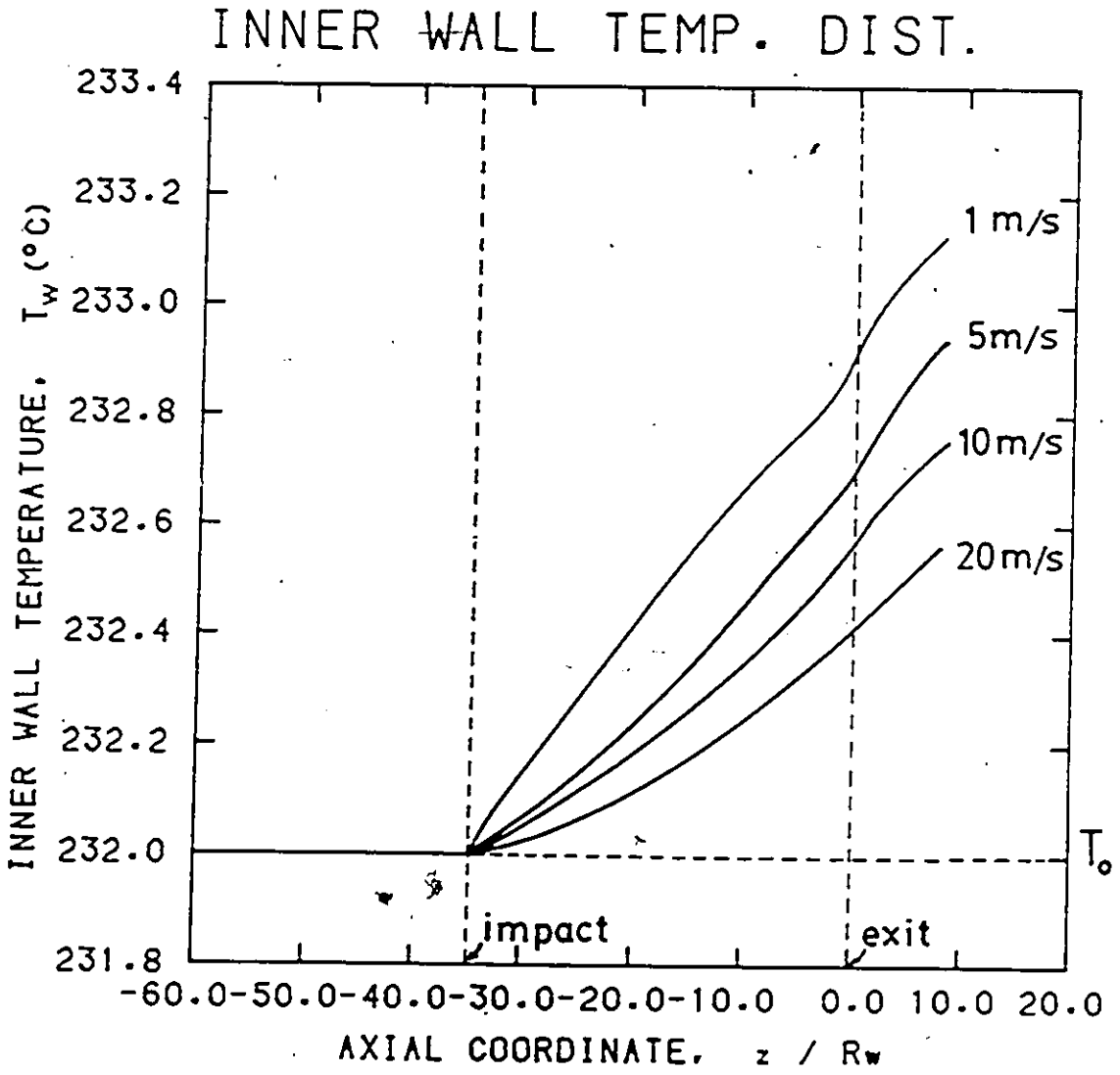

Figure 5.26: Torpedo Wall and Wire Surface Temperature Distribution along Du Pont's Die for Different Wire Speeds (GS=7.9R_w, $30 < Bi < 130$).

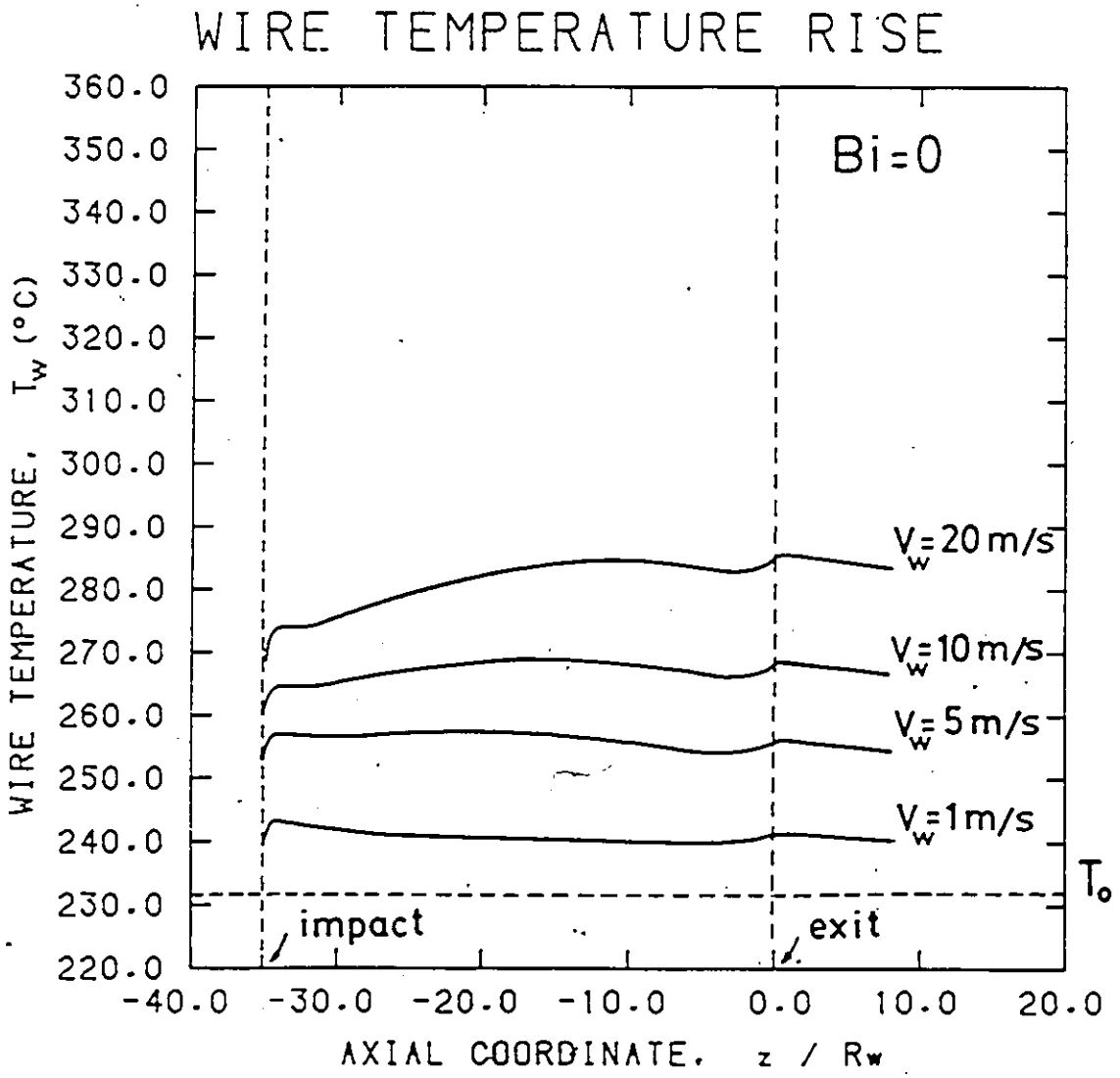

Figure 5.27: Wire Surface Temperature Distribution along Du Pont's Die for Different Wire Speeds (GS=7.9R_w, $Bi = 0$).

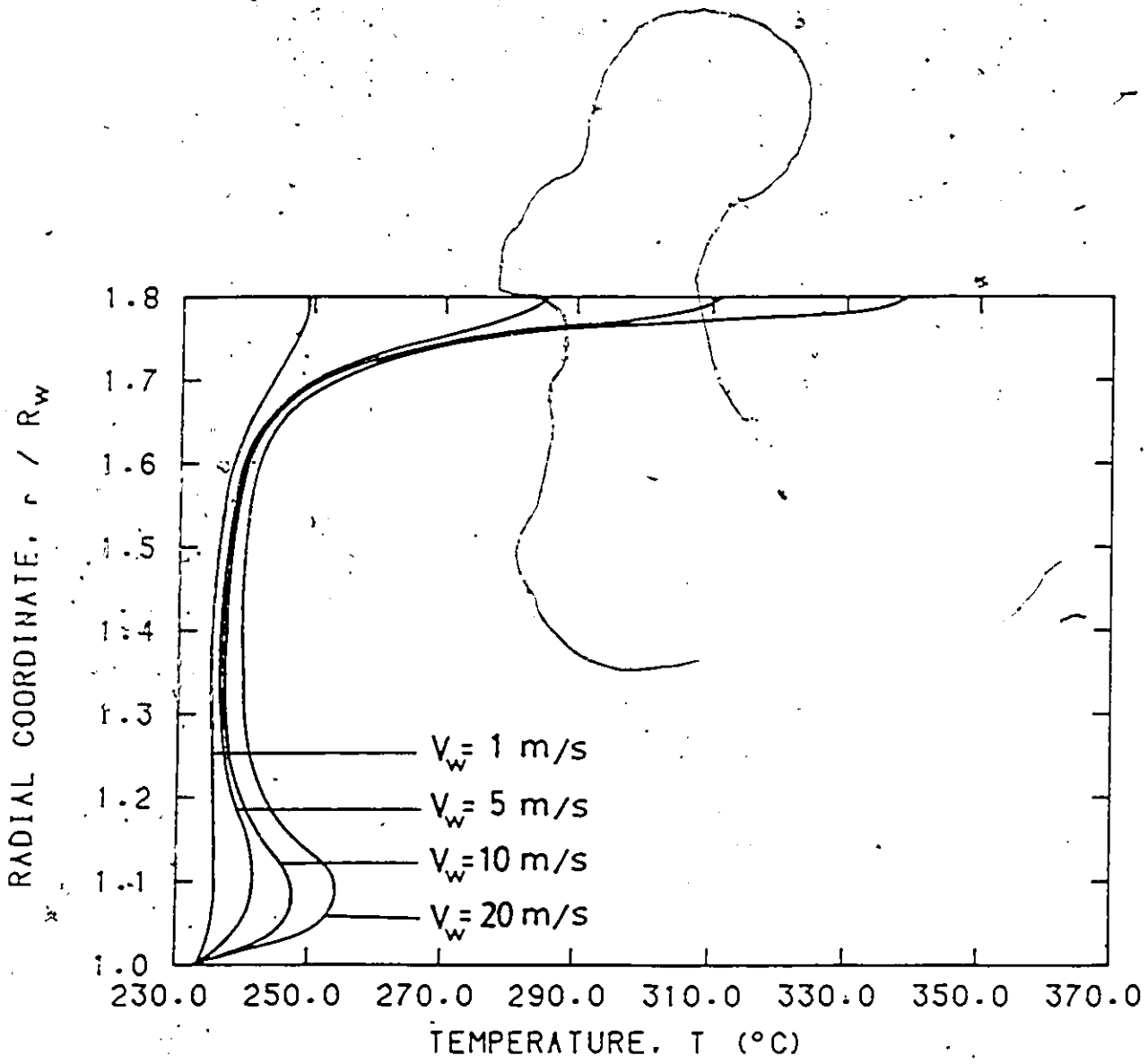

Figure 5.28: Radial Temperature Distribution at Du Pont's Die Exit ($z = 0$) for Different Wire Speeds (GS=7.9R_w, $30 < Bi < 130$).

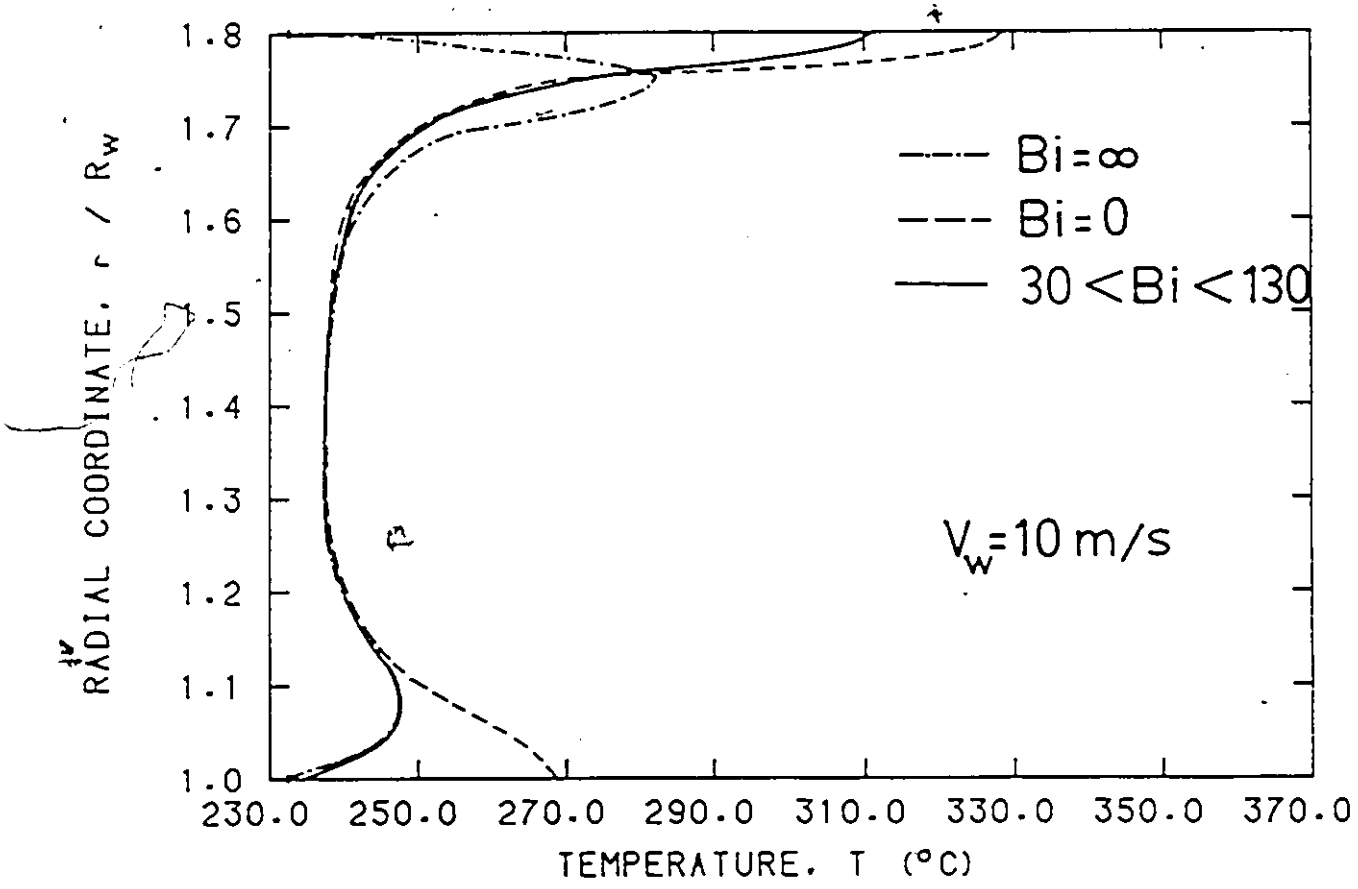

Figure 5.29: Radial Temperature Distribution at Du Pont's Die Exit ($z = 0$) Assuming Different Thermal Boundary Conditions (GS=7.9R_w, $V_w = 1000$ cm/s).

resembles that for isothermal walls, whereas near the die wall it approaches the adiabatic case. Adiabatic conditions cause the maxima to move to the walls and also increase considerably the maximum values. All these results are also in qualitative agreement with the nonisothermal calculations of Carley et al. (1979), Basu (1981) and Winter (1978). The shear stress profiles at both the torpedo wall/wire and die wall are shown in Figure 5.30 for the two extreme sets of thermal boundary conditions. Due to the higher temperatures developed under adiabatic conditions, the stress singularities at impact and exit are somewhat alleviated.

The influence of wire speed on wire tension is shown in Figure 5.31 under isothermal ($Bi = \infty$) and adiabatic boundary conditions ($Bi = 0$). Adiabatic conditions lower the maxima and shift them toward the exit. Higher speeds also shift the maxima toward the exit, in agreement with Pittman and Rashid (1986).

From the experimental values of pressure and assuming Newtonian behaviour, Haas and Skewis (1974) calculated shear rates and viscosities (hence shear stresses) for each wire speed. The finite element analysis shows that there are two regions of maximum stresses, at impact and at the die exit, where stress singularities exist (see Figure 5.30). The question,

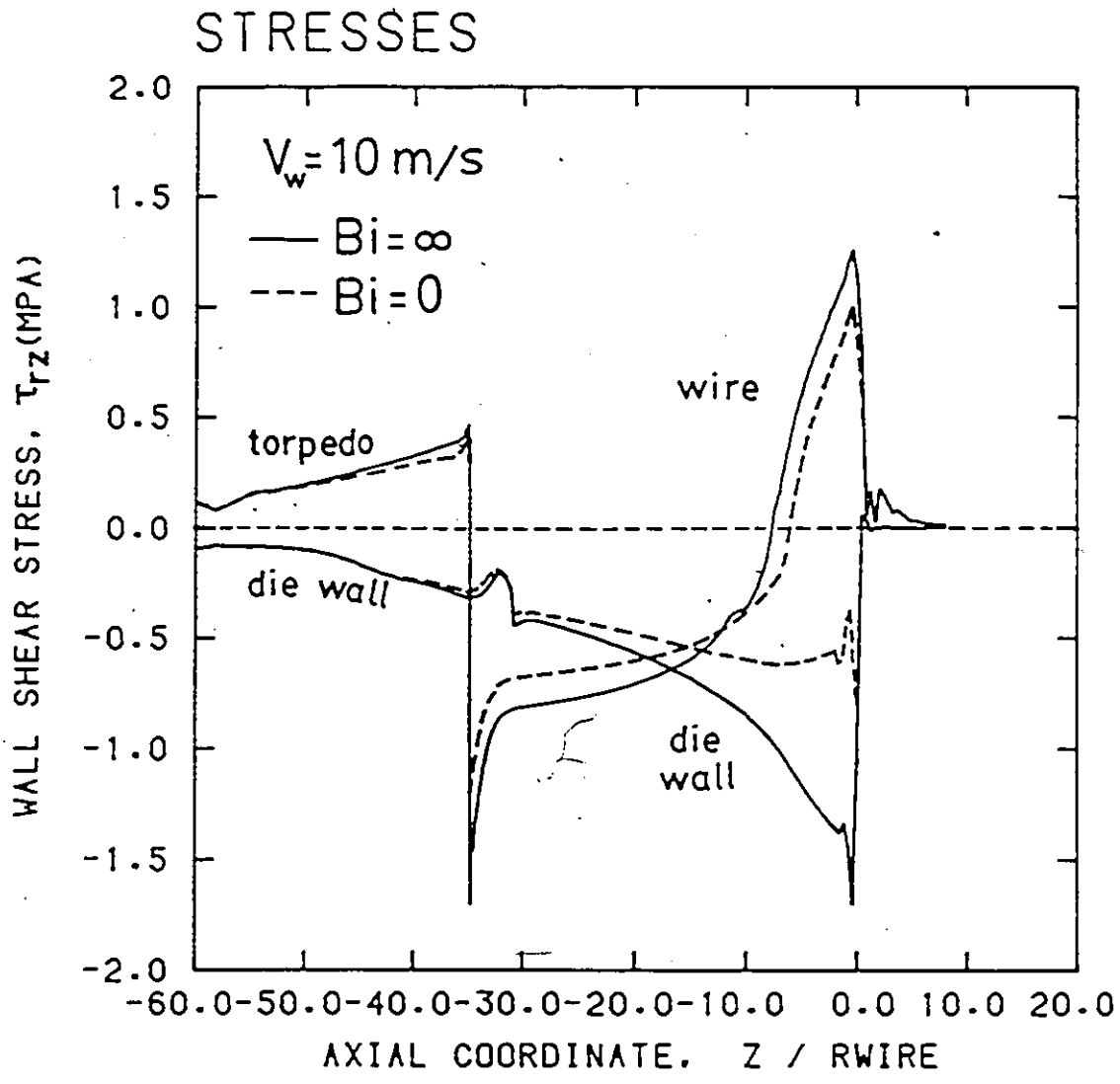

Figure 5.30: Shear Stress Distribution along the Torpedo/Wire and Die Wall in Du Pont's Die Assuming Different Boundary Conditions (GS=7.9R_w, $V_w = 1000\ cm/s$).

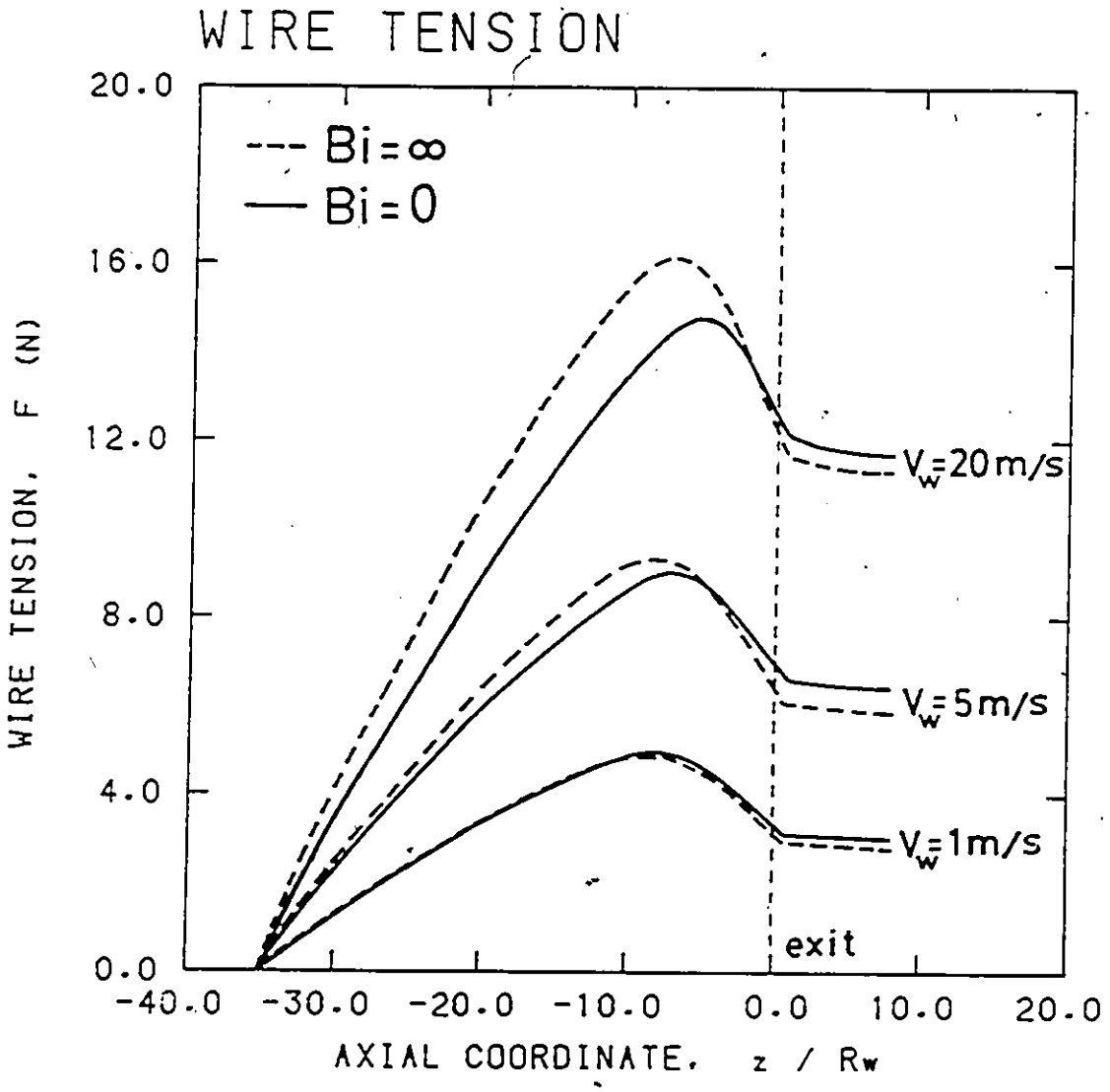

Figure 5.31: Wire Tension Distribution along Du Pont's Die for Different Wire Speeds and Thermal Boundary Conditions (GS=$7.9R_w$).

Table 5.2: Maximum Shear Rates ($\dot{\gamma}_{max}$) and Shear Stresses (τ_{max}) Calculated in Du Pont's Die for Different Wire Speeds (22 AWG Wire, GS=7.9R_w).

	Haas and Skewis (1974)		FEM Analysis			
Wire Speed V_w (cm/s)	$\dot{\gamma}_{max}$ (s^{-1})	τ_{max} (MPa)	$\dot{\gamma}_{max}$ (s^{-1})		τ_{max} (MPa)	
			$Bi=\infty$	$Bi=0$	$Bi=\infty$	$Bi=0$
100	16,000	0.18	17,700	16,600	0.60	0.55
500	80,000	0.35	84,700	71,600	1.03	0.85
1000	160,000	0.44	162,100	139,500	1.28	1.00
2000	320,000	0.51	311,700	284,000	1.58	1.16

therefore, arises as to which maximum stresses in the unit to consider. The stresses on the wire at exit are chosen, since the singularities at wire impact and die lip are still not well understood and their modelling is currently an active topic of research. Comparisons between the experimental predictions and the results from the nonisothermal FEM analysis are made in Table 5.2. Although the shear rates compare well (note the linear dependence on wire speed), the FEM stresses are always higher for both extreme cases of boundary conditions. The discrepancies may be attributed to the

assumptions involved (Newtonian vs. non-Newtonian fluid, temperature dependence, etc.). Nevertheless, all calculated values for the shear stress are above the critical shear stress values for melt fracture reported in the literature (Vlachopoulos and Alam, 1972). For LDPE, these range between 0.13 and 0.19 MPa (Wagner and Mitsoulis, 1985; Vlachopoulos and Alam, 1972). It should be noted, however, that critical stresses are given for fully developed flow in capillaries or slits preceded by flow in a sudden contraction, and not in a tapered annulus with the inner wall moving as is the case in wire coating.

The streamline pattern for all cases was virtually identical to the one shown in Figure 5.32, while a typical velocity profile development is shown in Figure 5.33. No recirculation is present in any case. The same was also found by Wagner (1987).

(b) Design B (GS=4.9R_w)

In an attempt to study the effect of different die designs on the field variables, a claimed "optimum" design (Haas and Skewis, 1974) of 4.9R_wGS (Design B) is also analyzed. A different mesh layout has to be used. The grids are shown in Figure 5.34 for the u-w-p formulation and in Figure 5.35

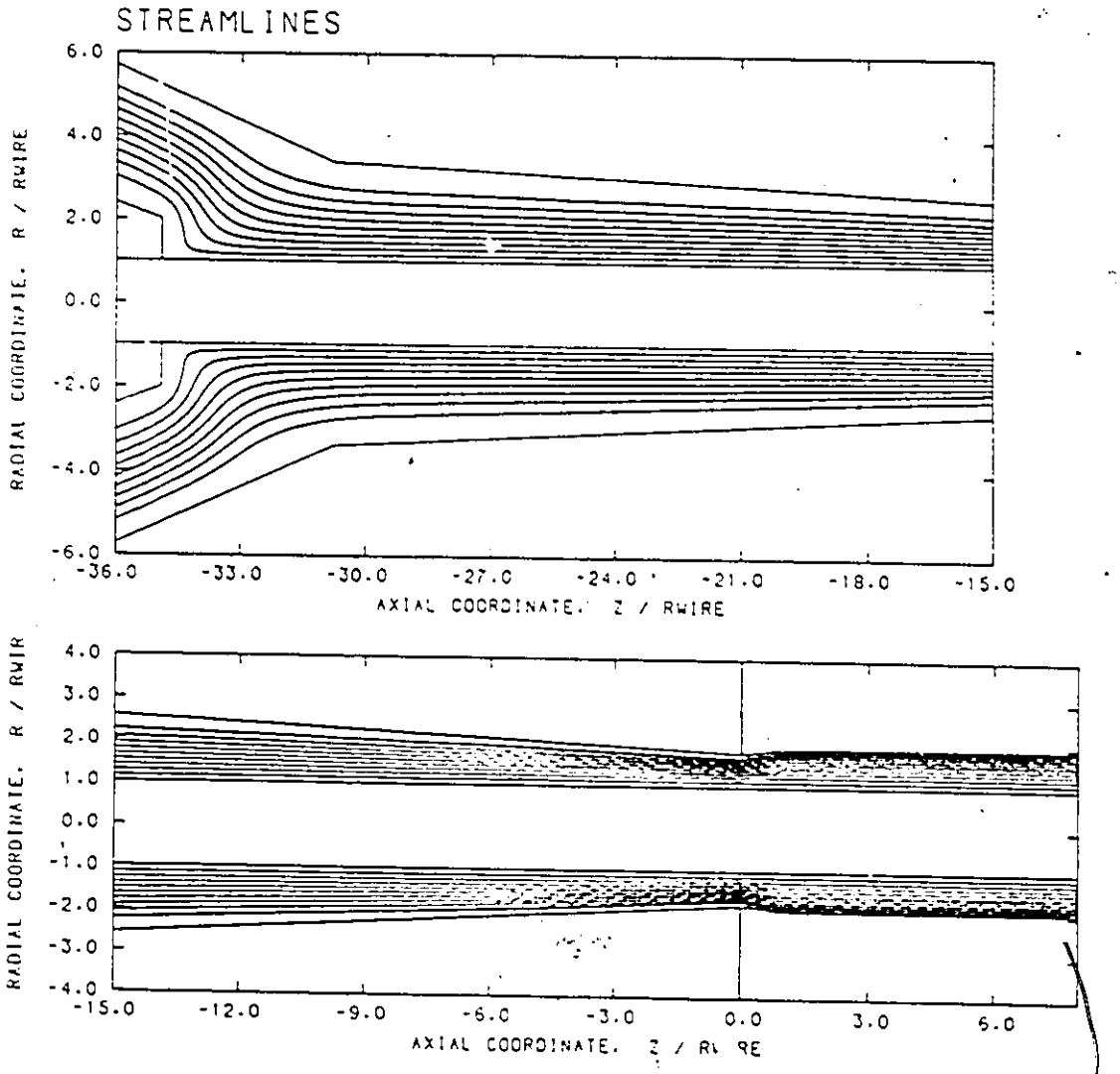

Figure 5.32: Typical Streamline Pattern Obtained from the Nonisothermal Analysis in Du Pont's Die (Normalized Streamlines between 0 and 1, GS=$7.9R_w$).

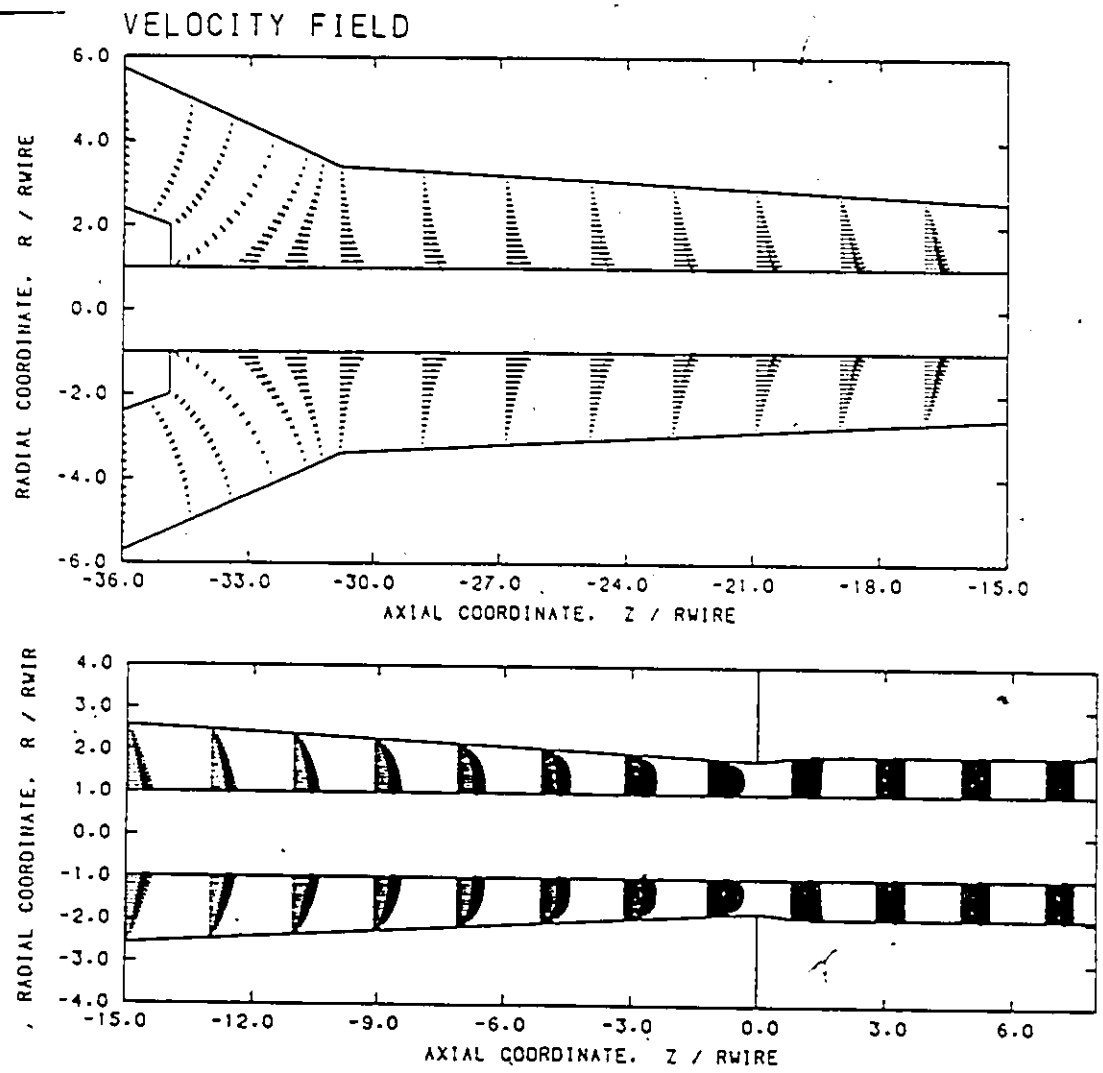

Figure 5.33: Typical Velocity Profile Development Obtained from the Non-isothermal Analysis in Du Pont's Die (Velocity Vectors Normalized by V_w, All Dimensions Drawn to Scale, GS=$7.9R_w$).

for the temperature/stream function formulation. The total number of elements and nodes employed are the same as for the $7.9R_w$-GS case. Four runs, for V_w = 100, 500, 1000 and 2000 cm/s, with intermediate thermal boundary conditions ($30 < Bi < 130$) were carried out.

The pressure profiles for the two designs operating at $V_w = 100$ cm/s and 2000 cm/s are plotted in Figure 5.36. For all cases, the overall pressure drop is higher for the $4.9R_w$-GS design. It is observed that this design always gives a higher pressure drop in the annular region due to a more restricted flow area. On the other hand, the die-region pressure drop is lower for the $4.9R_w$-GS design. However, the differences in die-region pressure drop tend to decrease as the wire speed is decreased, until they become almost equal at $V_w = 100$ cm/s.

Figure 5.37 shows the stresses at $V_w = 500$ cm/s for the two designs. There is, basically, no difference in the stresses in the die region. In addition, the stresses on the torpedo surface show similar characteristics for these designs. However, it is evident that the die wall stresses show different behaviour during the transition from the annular region to the die region. The $4.9R_w$-GS design gives a stress distribution which is steadily decreasing (more negative) before reaching the singularity point at the beginning

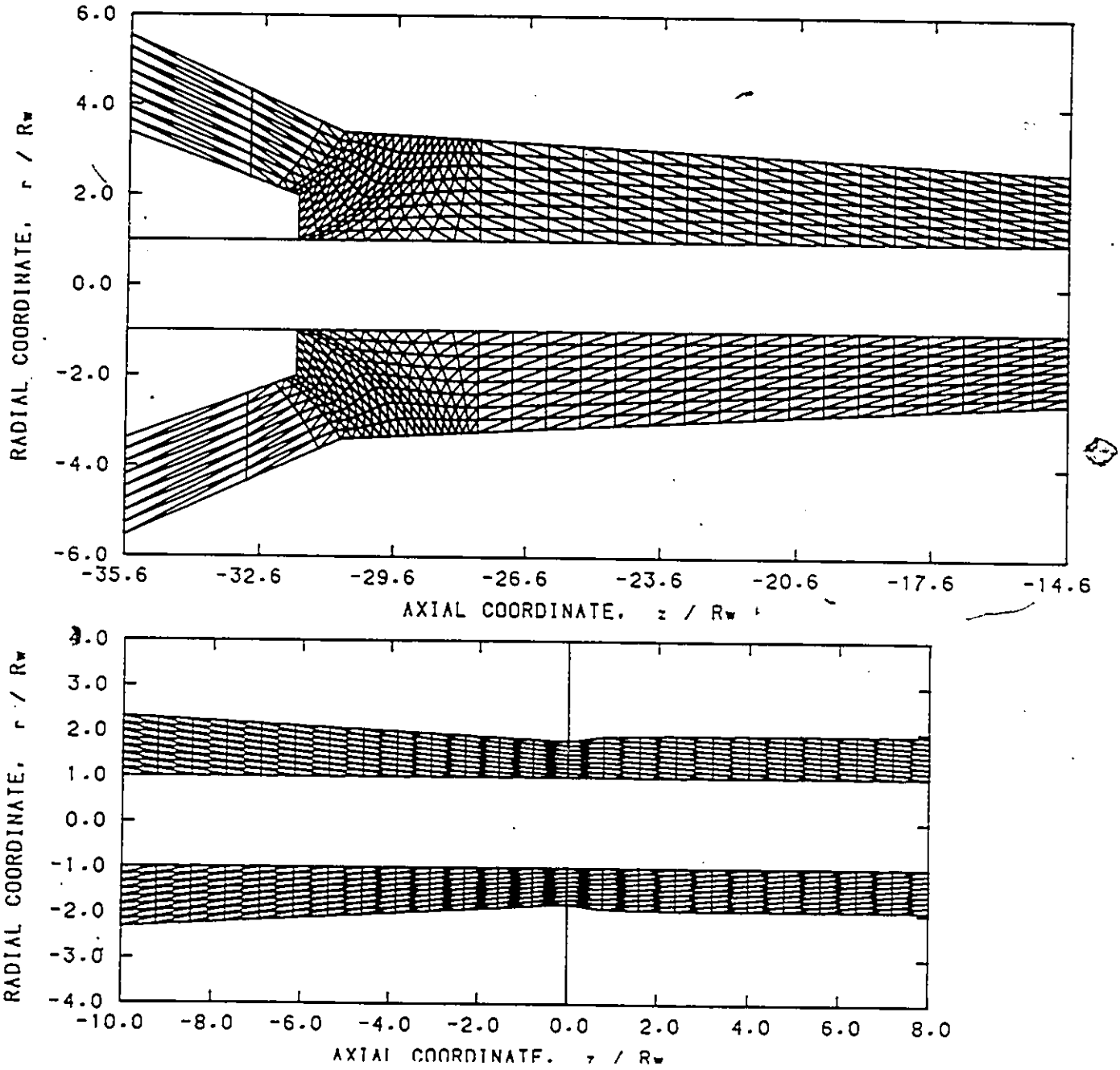

Figure 5.34: Finite Element Grids for u-w-p Formulation in Du Pont's Die (GS=4.9R_w).

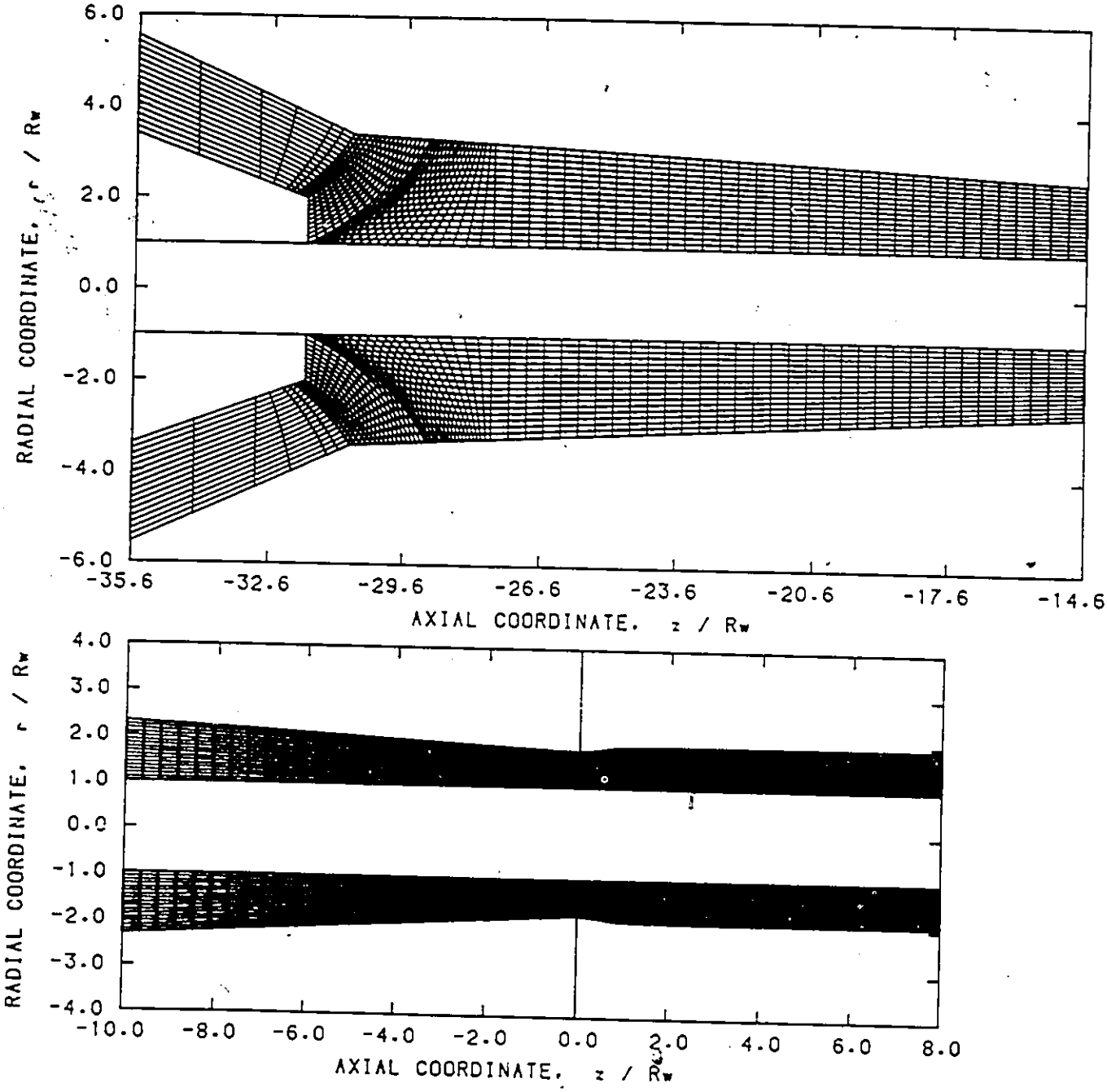

Figure 5.35: Finite Element Grids for Temperature/Stream Function Formulation in Du Pont's Die (GS=4.9R_w).

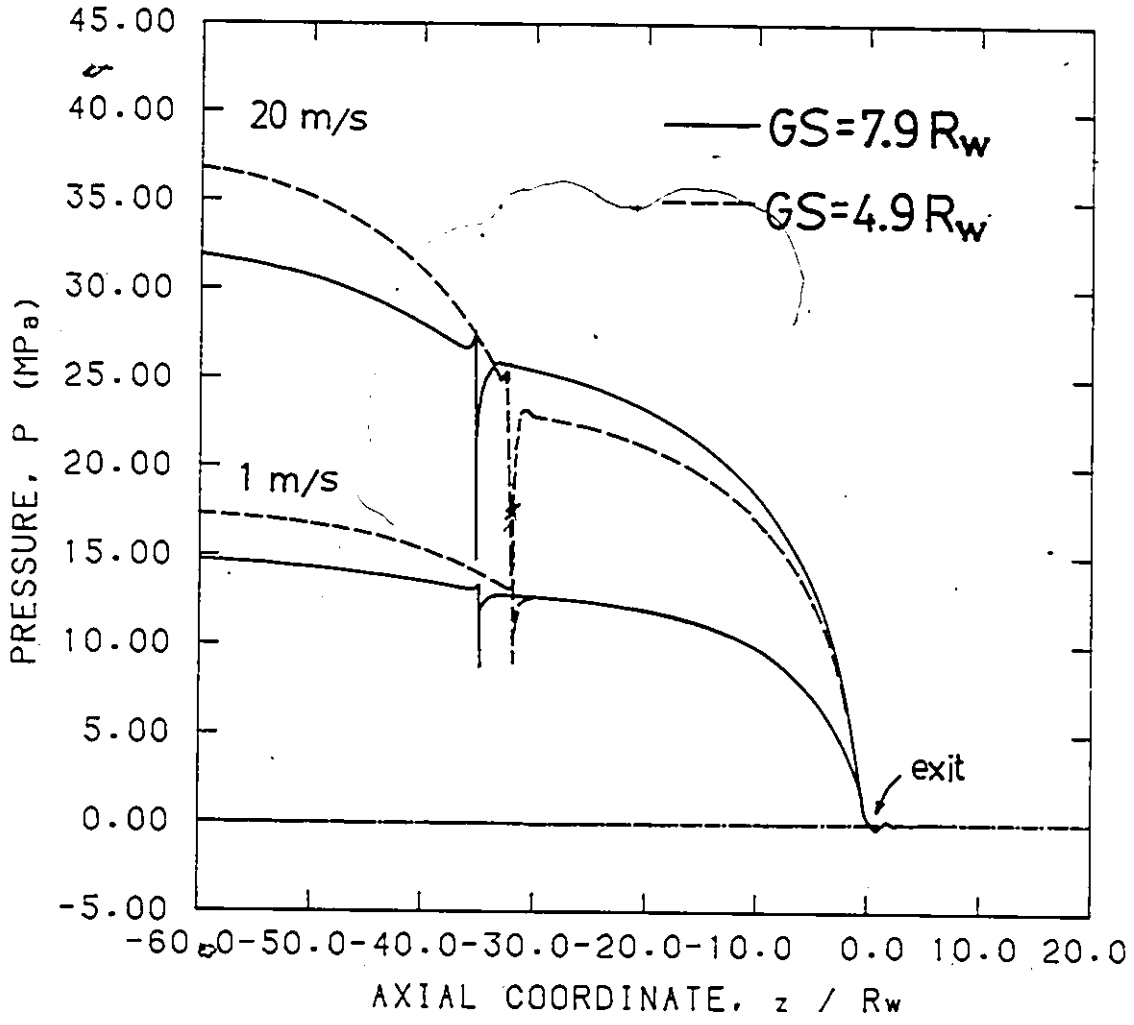

Figure 5.36: Pressure Distribution for Two Different Designs in Du Pont's Die ($30 < Bi < 130$, GS=$7.9R_w$ and $4.9R_w$).

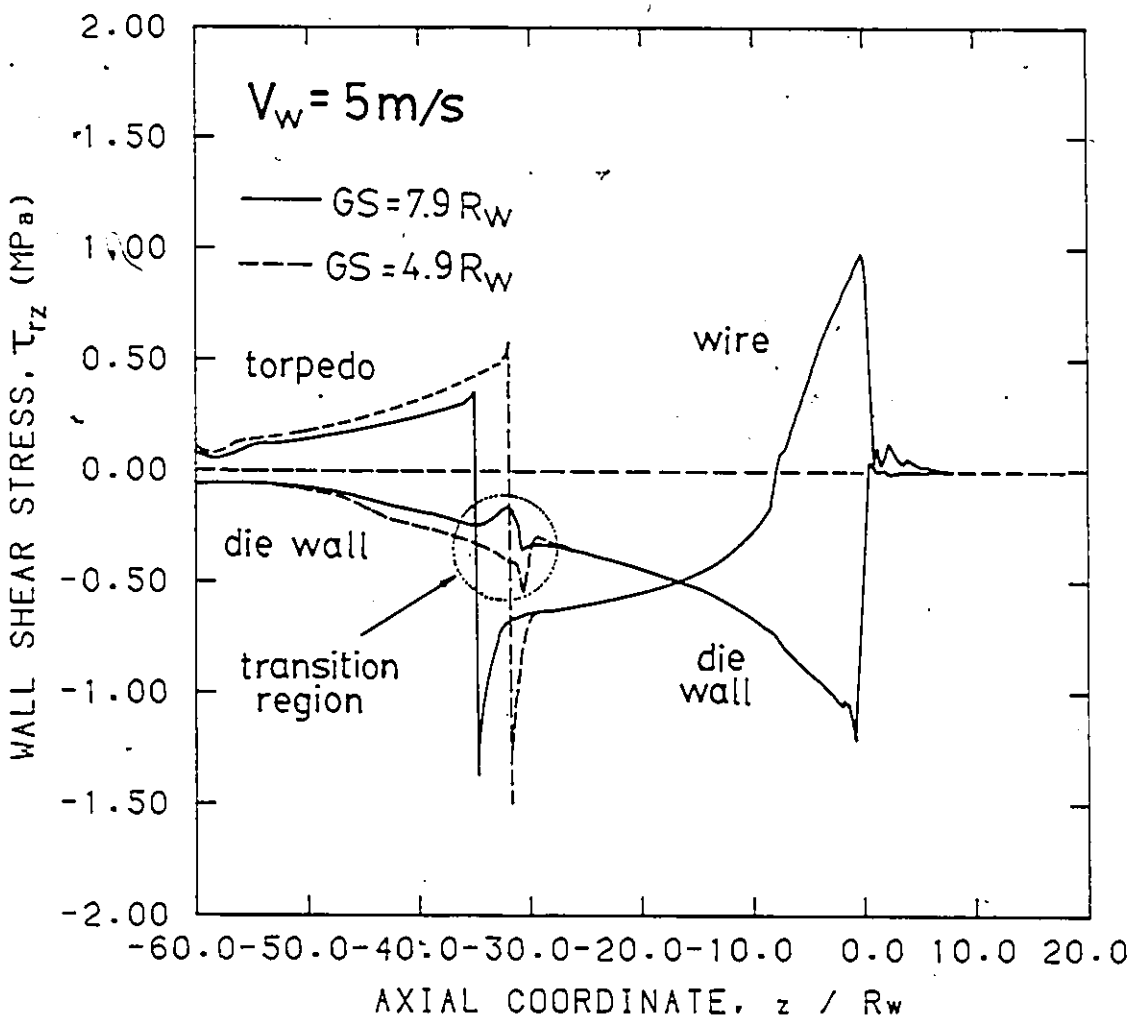

Figure 5.37: Stresses Distribution for Two Different Designs in Du Pont's Die (V_w = 500 cm/s, 30 < Bi < 130, GS=7.9R_w and 4.9R_w).

of the die region, thus giving a smooth profile. On the other hand, the $7.9R_w$-GS design gives a stress distribution which increases (less negative) in the beginning of the transition region followed by a decrease before the beginning of the die region, thus giving a "hump" in the transition region. The hump can be interpreted as a deceleration of the velocity followed by an acceleration (see Figure 5.8). Therefore, fluid particles undergoing such a change in stresses may be responsible for a rough coating exhibited by the $7.9R_w$-GS design. However, the absolute value for the stresses in the transition region is small compared to the stresses close to the die exit. The same pattern is observed for other wire speeds.

Maximum temperature profiles at $V_w = 1000\ cm/s$ for the two designs are shown in Figure 5.38. The $4.9R_w$-GS design gives higher maximum temperatures everywhere along the die, the largest difference being in the neighbourhood of the impact region. However, the maximum temperature, occurring close to the die exit, does not seem to be affected much.

The wire tension profiles for the two designs are very similar in shape (Figure 5.39). The $4.9R_w$-GS design gives a lower tension at any axial location, as expected, because the melt meets the wire farther down in the die.

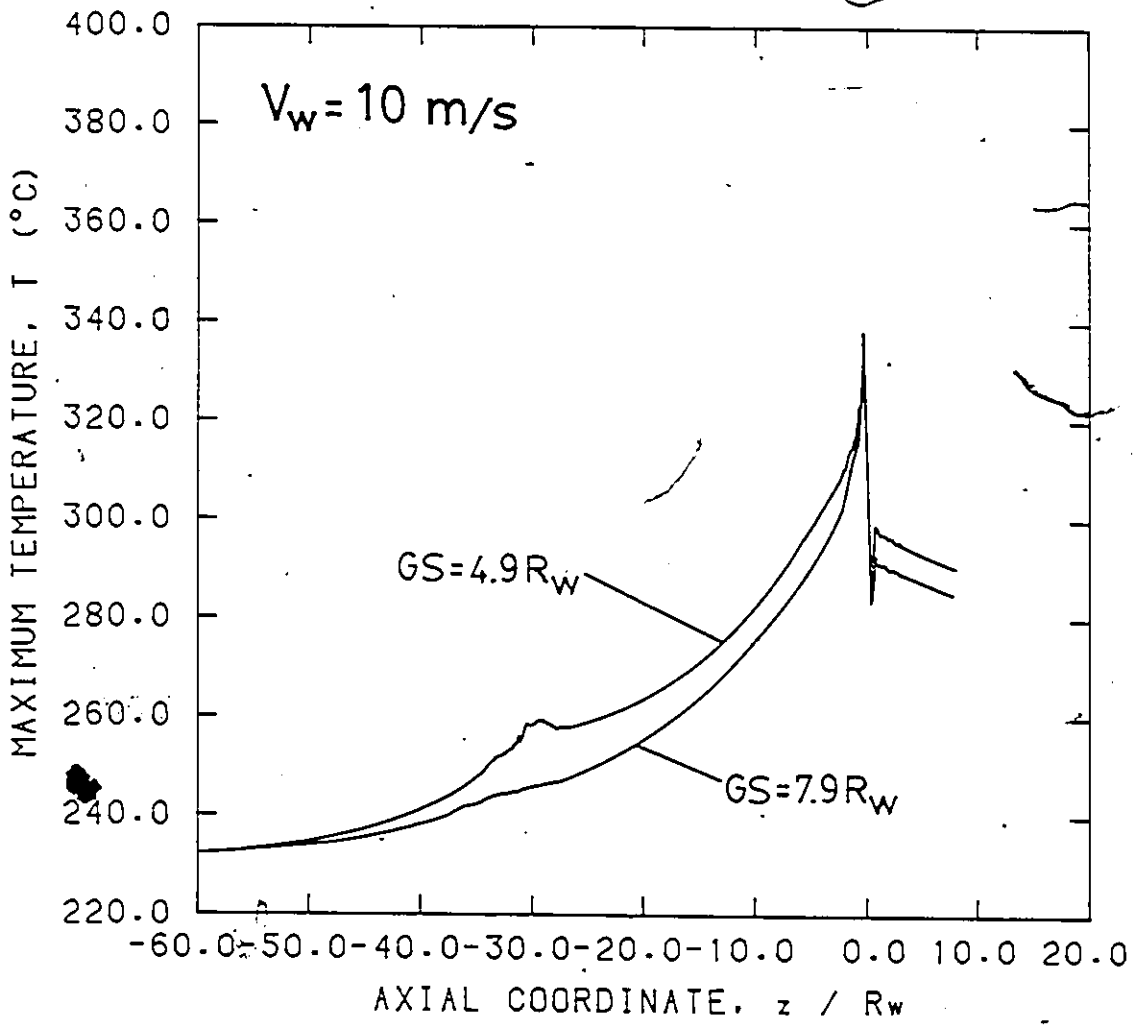

Figure 5.38: Maximum Temperature Distribution for Two Different Designs in Du Pont's Die ($V_w = 1000\ cm/s$, $30 < Bi < 130$, GS=$7.9R_w$ and $4.9R_w$).

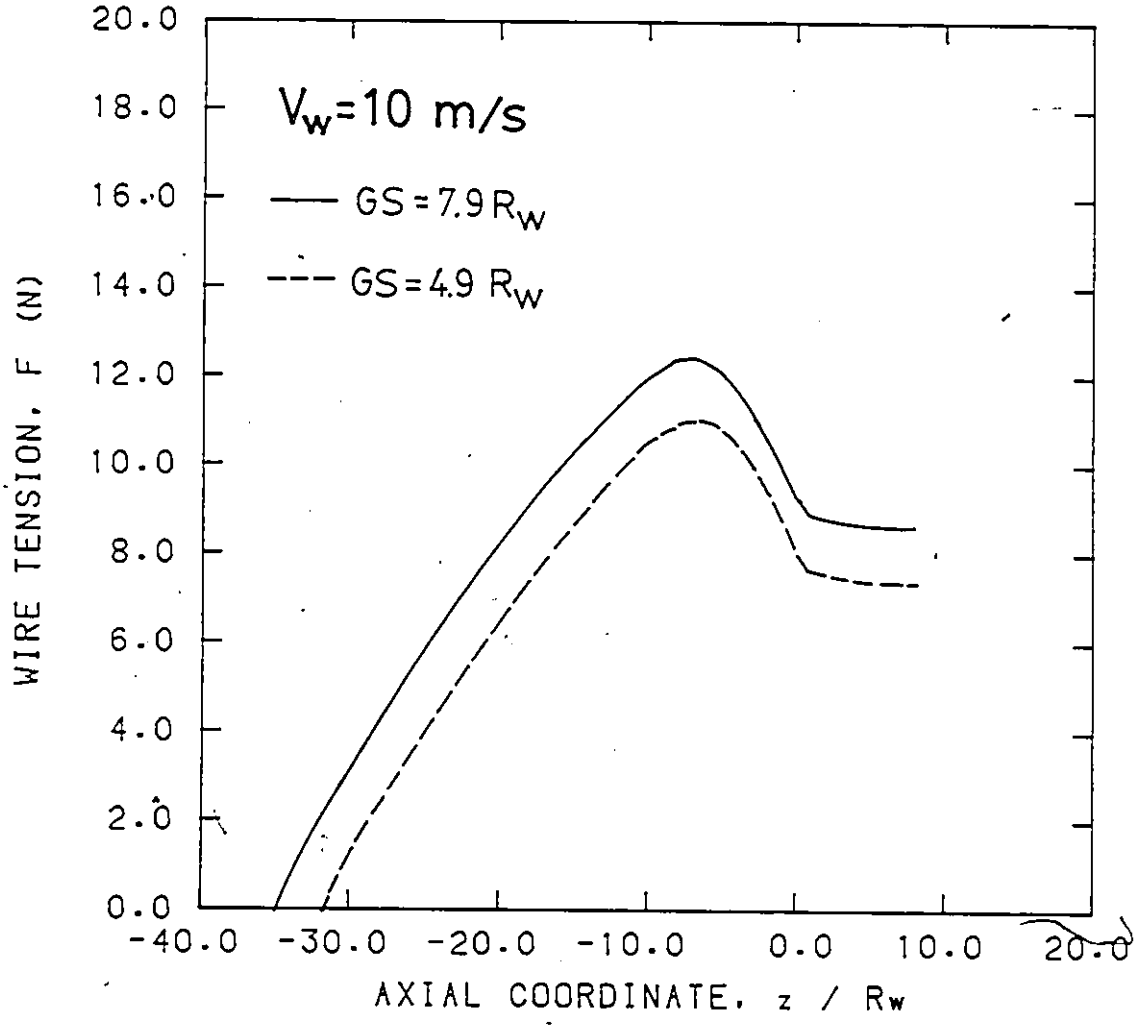

Figure 5.39: Wire Tension Distribution for Two Different Designs in Du Pont's Die ($V_w = 1000\ cm/s$, $30 < Bi < 130$, GS=$7.9R_w$ and $4.9R_w$).

A comparison between two typical streamline patterns is made in Figure 5.40. The difference in the flow field in the transition region (from annular to die region) is readily seen. The streamline closest to the die wall for the $4.9R_w$-GS design shows a more constrained flow. Such flow reduces the stagnant region close to the die wall, thus giving rise to a smoother die shear stress profile (as seen in Figure 5.37), avoiding the "hump" present in the $7.9R_w$-GS design. The flow field farther downstream is almost identical for the two cases. From the design viewpoint, the $4.9R_w$-GS design, although giving a higher pressure drop, is more desirable as it provides a more streamlined flow. This is believed to be the main reason for giving a reduced wire-coating roughness. Therefore, for design purposes, the torpedo must be set at such distance, so that a smooth shear stress distribution is achieved at the die wall, as well as a streamlined flow with no recirculation.

5.5 Concluding Remarks

The isothermal analysis of the two die designs ($4.9R_w$-GS and $7.9R_w$-GS) did not show significant differences. The increase in pressure for the $4.9R_w$-

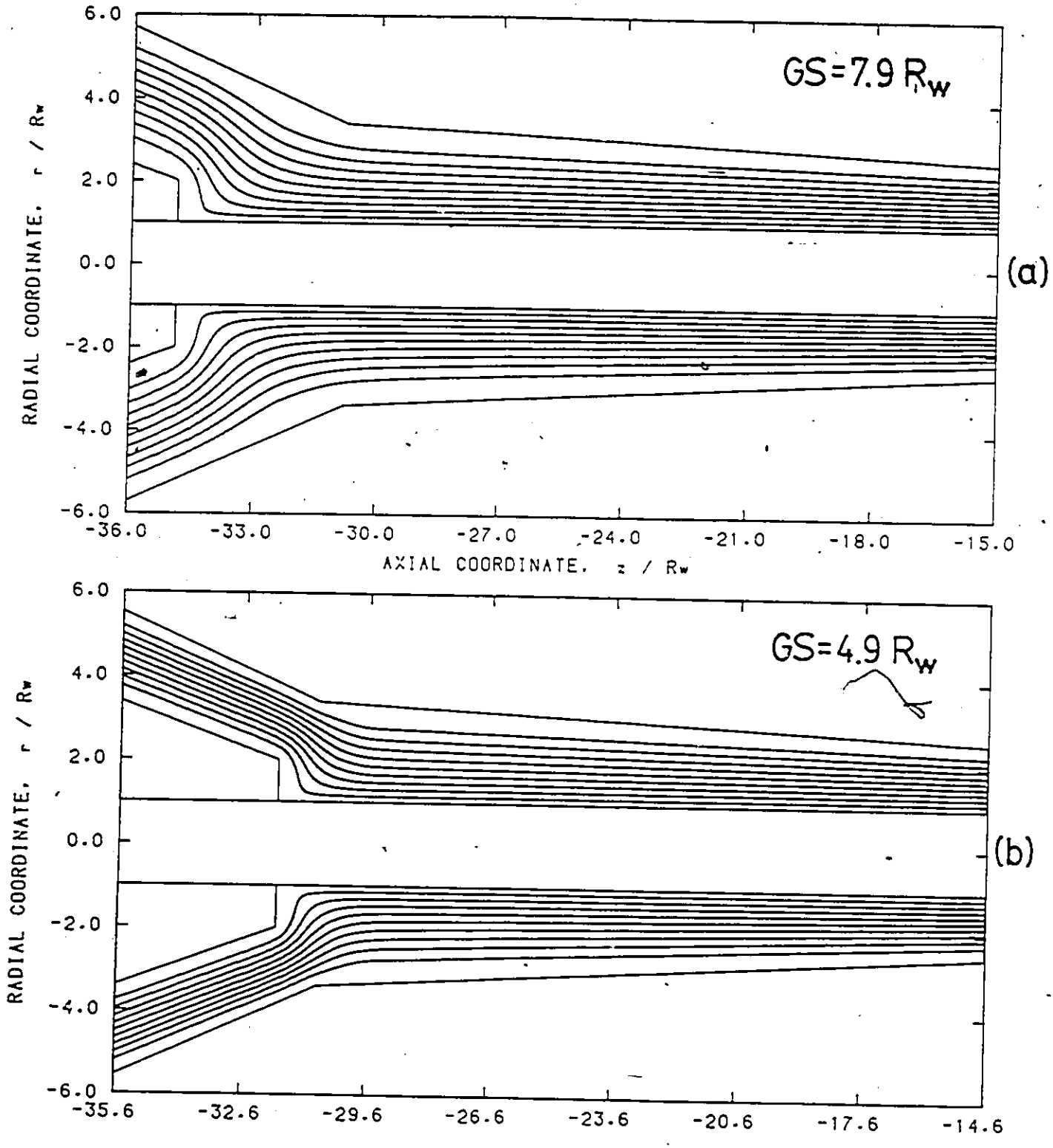

Figure 5.40: Streamline Patterns for Two Different Designs in Du Pont's Die ($V_w = 1000\ cm/s$, $30 < Bi < 130$). (a) GS=$7.9R_w$, (b) GS=$4.9R_w$.

GS design is predicted by either LAT or FEM. In addition, the suppression of recirculation for Newtonian fluids flowing in this design is predicted by LAT and supported by FEM through the visualization of flow field (streamlines). The die stresses predicted could be used as a criterion for determining the presence of recirculation, i.e. positive τ_{rz} at the die wall.

The nonisothermal analysis of Endo's die shows that the new temperature program developed did not present any difficulty in getting convergence as in the case of Carley et al. (1979). Its superior performance over other "upwinding" schemes using different discretization (for example Mizukami's, 1985) is readily seen. In addition, this analysis also shows that the inclusion of the radial convection term $v_r(\partial T/\partial r)$ is essential when performing the nonisothermal analysis. Neglecting this v_r-term tends to underestimate the maximum temperature and thus overestimate the pressure drop.

An accurate representation of the temperature field is crucial in the analysis of wire-coating extrusion dies for better predictions, as supported by the good agreement with the experimental data available. If isothermal flow field is assumed, gross overdesign should be expected. Although the heat-balance thermal boundary conditions are more realistic, an isother-

mal wall condition is recommended for designing purposes, since the latter always provides an overestimate of the pressure drop.

The nonisothermal analysis of the two designs ($4.9R_w$-GS and $7.9R_w$-GS) showed two major differences. The flow field for the $4.9R_w$-GS design showed a more "streamlined" flow, which may account for the better coating surface obtained experimentally. In addition, a smoother die stress distribution that resulted from the more constrained flow may also be part of the reason. Therefore, for design purposes, these two qualitative criteria should be considered.

Chapter 6

Computer-Aided Analysis and Design of Wire-Coating Coextrusion Dies

Isothermal and nonisothermal analyses of wire-coating coextrusion dies are performed. The isothermal analysis of power-law fluids flowing in a particular die design used by Han and Rao (1980) is performed to validate the LAT program developed for coextrusion flows. Then, a modified Du Pont's die that accomodates two fluids is analyzed assuming isothermal flows by using both LAT and FEM. The nonisothermal analysis is first performed

on a simple die design used by Basu (1981) and a comparison is made between his findings and FEM results. The analysis is then extended to an improved design for the modified Du Pont's die for typical polymer melts under a variety of flowrate ratios and operating conditions.

6.1 Introduction - The Wire-Coating Coextrusion Process

The process of coextrusion is a convenient one-step method for producing bilayered fibers, plastic films, tubes, etc. In insulating electrical wires, the wires are sometimes coextruded with an inner polymer layer with good electrical insulation properties, and an outer layer with good chemical resistance. It is also a common practice to coextrude a lubricant or a color compound on top of the first layer. Common problems encountered in single extrusion (melt fracture, swelling and excessive temperature rise) are also present in coextrusion. On top of that, there are problems of interfacial instability and migration and poor bonding between the surfaces.

Many experimental studies of coextrusion have been primarily concerned with the encapsulation phenomenon of the more viscous polymer

by the less viscous one (Lee and White, 1974; Han, 1975; Minagawa and White, 1975; Southern and Ballman, 1975). In addition, the interfacial instabilities were also investigated (Khan and Han, 1976, 1977; Han and Shetty, 1978; Schrenk et al., 1978; Kim and Han, 1983). The development of the interface along the length of the die has been experimentally studied by Everage (1975), Minagawa and White (1975) and White and Lee (1975). For wire-coating coextrusion, Han and Rao (1980) found that the interfacial instability is related to shear stress, viscosity ratio and first normal stress difference ratio at the interface.

Analytical studies on the encapsulation phenomenon have been performed by MacLean (1973) by using a minimum viscous dissipation approach. Everage (1973, 1975) has predicted the variation of interface position along the channel length as a function of viscosity ratio of the liquids. White and Lee (1975) concluded that the difference in viscosities of the fluids is the major factor in determining the shape of the interface. At the time of writing this thesis, Karagiannis et al. (1987) have used the FEM and the minimum viscous dissipation approach to determine the equilibrium interface shape in the cross section of complex die configurations.

Most numerical simulations of the coextrusion process have been done

by using the LAT for isothermal flow of power-law fluids. Han and Shetty (1976) analyzed the flow of multilayer film coextrusion. Han and Rao (1980) studied the wire-coating coextrusion process. Recently, the flows of two molten polymers in flat dies have been studied by Sornberger et al. (1986).

An improvement in the analysis was made when the FEM was used to simulate the full two-dimensional flow of polymer melts. Mitsoulis (1986) studied the extrudate swell of Newtonian fluids in tubular and annular geometries, while Mitsoulis and Heng (1987) extended the FEM analysis to power-law fluids.

The first attempt to perform the nonisothermal analysis of coextrusion flows seems to have been made by Uhland (1977). He studied the flow in tubular dies for power-law fluids. Following that, Basu (1981) has performed an analysis on wire-coating coextrusion dies using a more elaborate two-region (Newtonian and quadratic) viscosity function for three typical polymer melts (LDPE, HDPE and PS). Chin et al. (1984) and Sornberger et al. (1986) performed a similar analysis for flat-film coextrusion.

All the above studies are based on the simplification of the conservation equations according to LAT. Therefore, there exists a need to perform a full nonisothermal analysis of the coextrusion process. In this work, such

an analysis will be carried out for the wire-coating coextrusion process.

6.2 Mathematical Modelling of Wire-Coating Coextrusion

In the coextrusion wire-coating technique two different polymers are concentrically coated on the wire in a single step. The two melts are extruded from two different extruders and meet in a pressure die as shown in Figure 6.1.

The boundary conditions imposed are similar to those described in Section 5.2 and will not be repeated here. Additional boundary conditions for the interface have been included in Section 3.3.1.

The material properties employed in this analysis, except those for Newtonian fluids, are taken from Basu (1981). Two widely used and well characterized polymers are considered: (i) high density polyethylene (HDPE) (Union Carbide Corp., DMDJ 4306) and (ii) polystyrene (PS) (Dow Chemical Co., STYRON 678). The data for these polymers are summarized as follows:

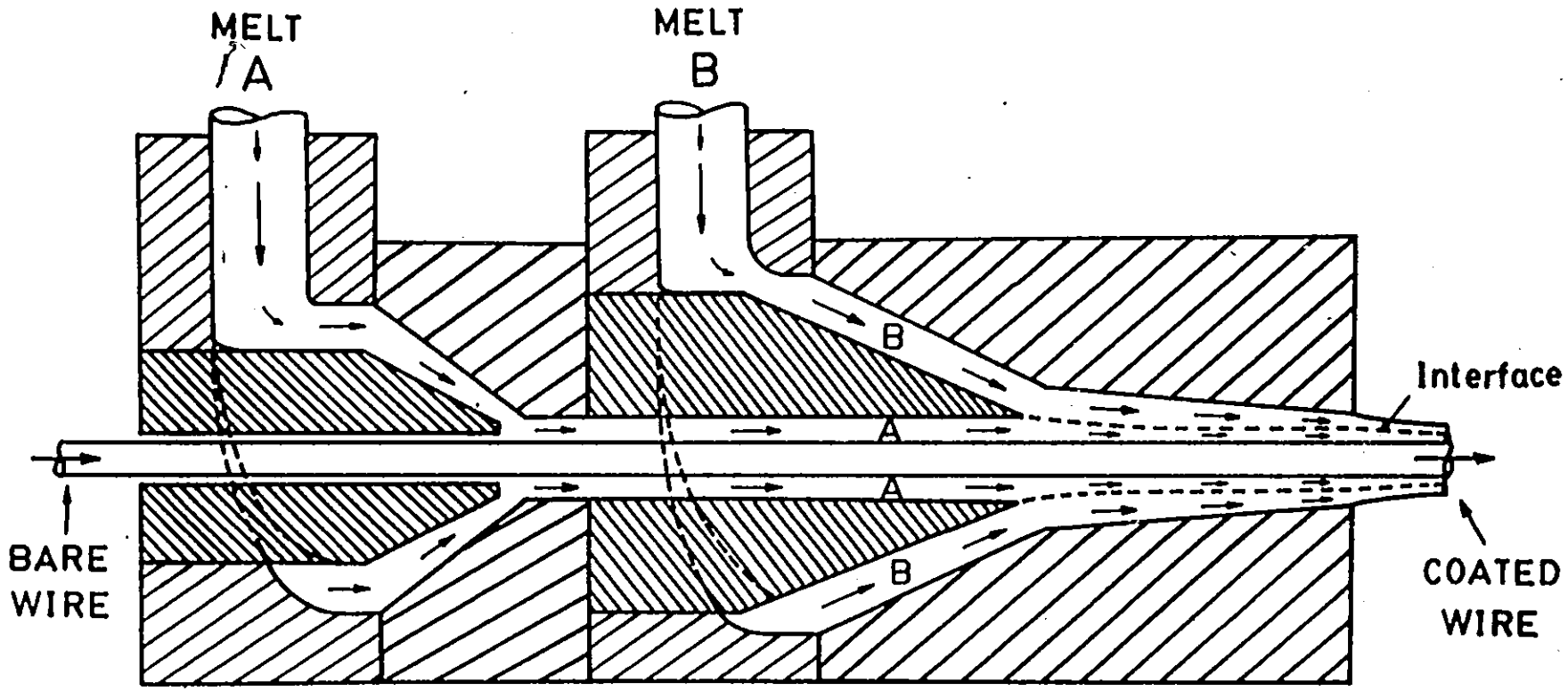

Figure 6.1: Schematic Representation of the Wire-Coating Coextrusion Process.

HDPE:	$\rho_a = 0.954$	g/cm^3 at room temperature
	$\rho_m = 0.8732 - 0.000291T$	g/cm^3 for $T > 150°C$
	$(C_p)_m = 3.5$	$J/g\ °C$
	$k_m = 0.005$	$J/cm\ s\ K$
PS:	$\rho_a = 1.05$	g/cm^3 at room temperature
	$\rho_m = 1.093 - 0.000605T$	g/cm^3 for $T > 150°C$
	$(C_p)_m = 1.425 + 0.00404T$	$J/g\ °C$
	$k_m = 0.00128$	$J/cm\ s\ K$

The viscosity was represented by two regions (Basu, 1981):

Newtonian region:

$$\mu = \mu_o \quad , \quad \tau \leq \tau_N \tag{6.1}$$

Quadratic region:

$$\log \dot{\gamma} = a + b(\log \tau) + c(\log \tau)^2 \quad , \quad \tau > \tau_N \tag{6.2}$$

where the correlated constants μ_o, a, b, and c are tabulated in Table 6.1 (Basu, 1981). The viscosity is given in *poise*.

Table 6.1: Correlated Constants for Viscosity Function (Basu, 1981).

	HDPE	PS
T_o $(°C)$	220	220
β (K^{-1})	0.01266	0.03
τ_N $(\frac{dynes}{cm^2})$	10^4	10^4
μ_o $(poise)$	2.098×10^6	1.406×10^4
a	-11.95	-1.318
b	2.405	-0.7287
c	5.073×10^{-4}	0.2553

The temperature dependence of viscosity was handled as follows (Basu, 1981):

$$\eta = \eta_o \exp\left[-\beta(T - T_o)\right] \tag{6.3}$$

where T_o is the reference temperature and η_o is the corresponding viscosity. The values of T_o and temperature shift factor β are tabulated in Table 6.1. Figure 6.2 shows the viscosity curves for these two polymer melts. As evidenced, HDPE is always more viscous than PS.

6.3 Isothermal Wire-Coating Coextrusion

6.3.1 Lubrication Approximation Theory

The isothermal analysis is carried out using the lubrication approximation theory (LAT) program developed for coextrusion processes. The details for this analysis have been discussed in Section 3.2. In order to check the validity of this program, a simple system of two power-law fluids flowing in a straight annular die is first considered.

The LAT program is checked against a numerical solution obtained by Han and Rao (1980). A straight annular die of radius 0.15875 *cm* was used to coat a wire of radius 0.06452 *cm* at a speed of 6.5 cm/s. The power-law

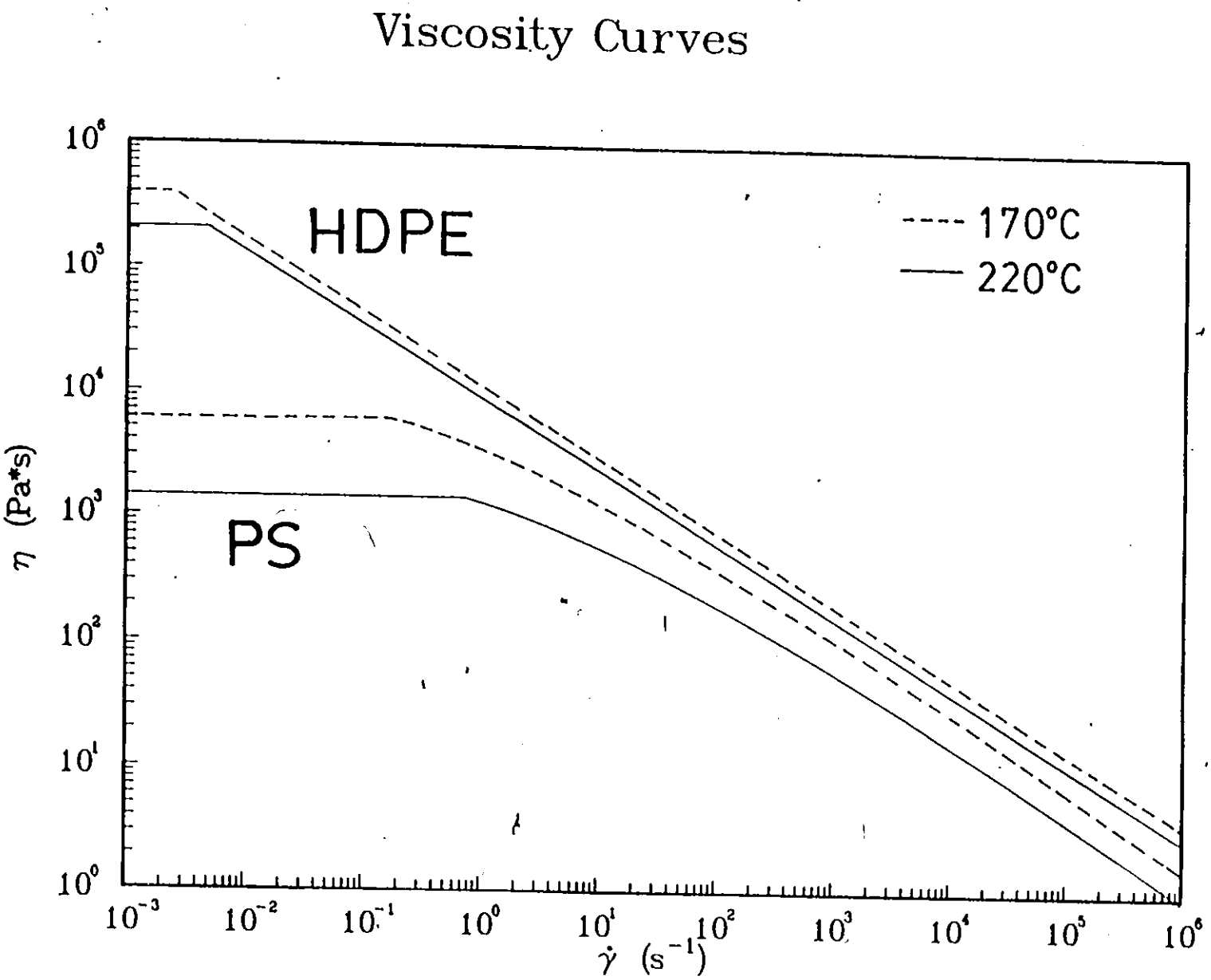

Figure 6.2: Shear Viscosity vs. Shear Rate Curves for HDPE and PS.

Table 6.2: Comparison of LAT Results for Two Power-Law Fluids between Present Study and Han and Rao's (1980).

	Present Study	Han and Rao	% Deviation
$-dp/dz$	3.10	3.15	1.6
λ	0.57	0.58	1.7
α	0.73	0.74	1.3

model is used to describe the viscosity functions (Han and Rao, 1980):

(inner layer) $m_i = 0.01007 \quad MPa \cdot s^n \quad , \quad n_i = 0.43$

(outer layer) $m_o = 0.00300 \quad MPa \cdot s^n \quad , \quad n_o = 0.45$

The required operating conditions are $Q_i = 0.3227\ cm^3/s$ and $Q_o = 0.6206\ cm^3/s$, and $T_o = 220°C$. The results obtained for this system are tabulated in Table 6.2 along with Han and Rao's results. As can be seen, the agreement is good with a maximum deviation of 1.7% from their results. The discrepancies can be attributed to different accuracy (double-precision variables are used in the current program) and grid density used (100 nodes in each layer are used in the current program).

Having established the accuracy of this program, we proceed with the analysis of a full wire-coating coextrusion die. Since no industrial designs

for coextrusion dies are available in the literature, we have taken Du Pont's die (see Figure 5.4) and modified it to accomodate two different fluids. We will refer to this die as the modified Du Pont's die (Design A). A diagram of the modified Du Pont's die is shown in Figure 6.3. The dimensions for this die have also been included. Note that this figure is similar to Figure 5.4. The only difference is that the lower section of the torpedo has been removed in order to accommodate a second fluid coming in from a separate extruder.

The flows of two polymers, namely HDPE and PS, are considered. The viscosity functions used have been summarized in Section 6.2. The operating conditions consist of applying a coating of thickness $0.8R_w$ on a 22-AWG wire ($R_w = 0.032\ cm$) at 1000 cm/s. The isothermal temperature is set at $T_o = 170°C$, as in Basu's analysis (1981). At this temperature, the HDPE melt is more viscous than the PS melt (see Figure 6.2). The effect of flowrate ratio, which is defined as:

$$\frac{Q_o}{Q_i} = \frac{\text{outer layer flowrate}}{\text{inner layer flowrate}} \tag{6.4}$$

on the flow behaviour of these two polymers is investigated.

Two different systems are considered: (i) PS forms the outer layer and

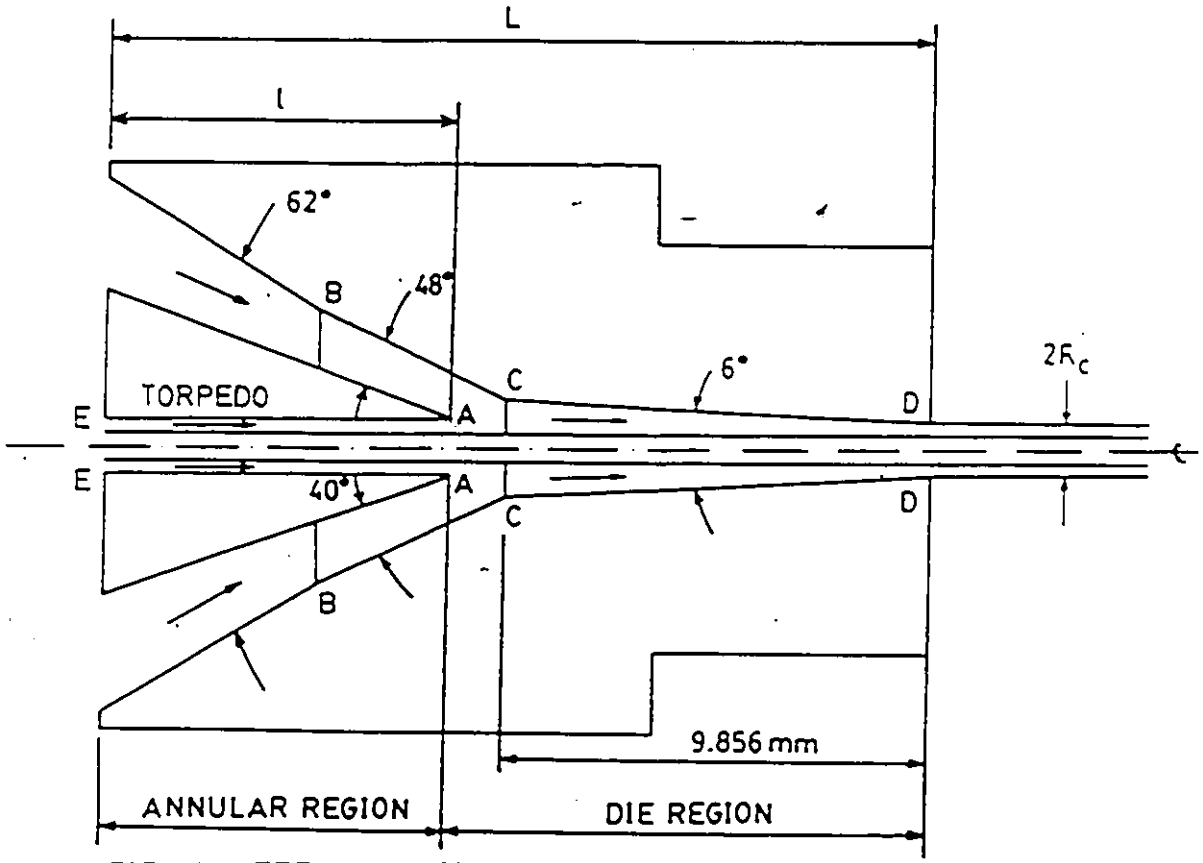

Figure 6.3: Modified Du Pont's Die Employed in the Isothermal Analysis of Wire-Coating Coextrusion (Design A). Changes in the Design Represented by *.

HDPE forms the inner layer (PS/HDPE), and (ii) HDPE forms the outer layer and PS forms the inner layer (HDPE/PS). Note that system (i) and (ii) mean that the less viscous and the more viscous component form the outer layer, respectively.

Four different flowrate ratios are used in this study: 0.4359, 0.7920, 1.333, and 2.246. These correspond to the arbitrarily chosen outer to inner layer coating thickness ratio of 1/3, 3/5, 1/1 and 5/3, respectively. Extreme thickness ratios are not used because they are not feasible in actual operation. The pressure and stress distribution curves are plotted in Figures 6.4 and 6.5, respectively.

Referring to Figure 6.4, for the PS/HDPE system, as the flowrate ratio is increased, the overall pressure drop for the outer layer increases. However, the same cannot be said about the inner layer. The pressure profile for the inner layer in the die region shows the same characteristics as for the outer layer. In the annular region, however, positive pressure gradients actually exist for the inner layer, suggesting inappropriate flowrate ratios have been used. On the other hand, when the more viscous component (HDPE) forms the outer layer (HDPE/PS system), the trend for the outer layer pressure drop in the die region and annular region is reversed. As the flowrate ratio

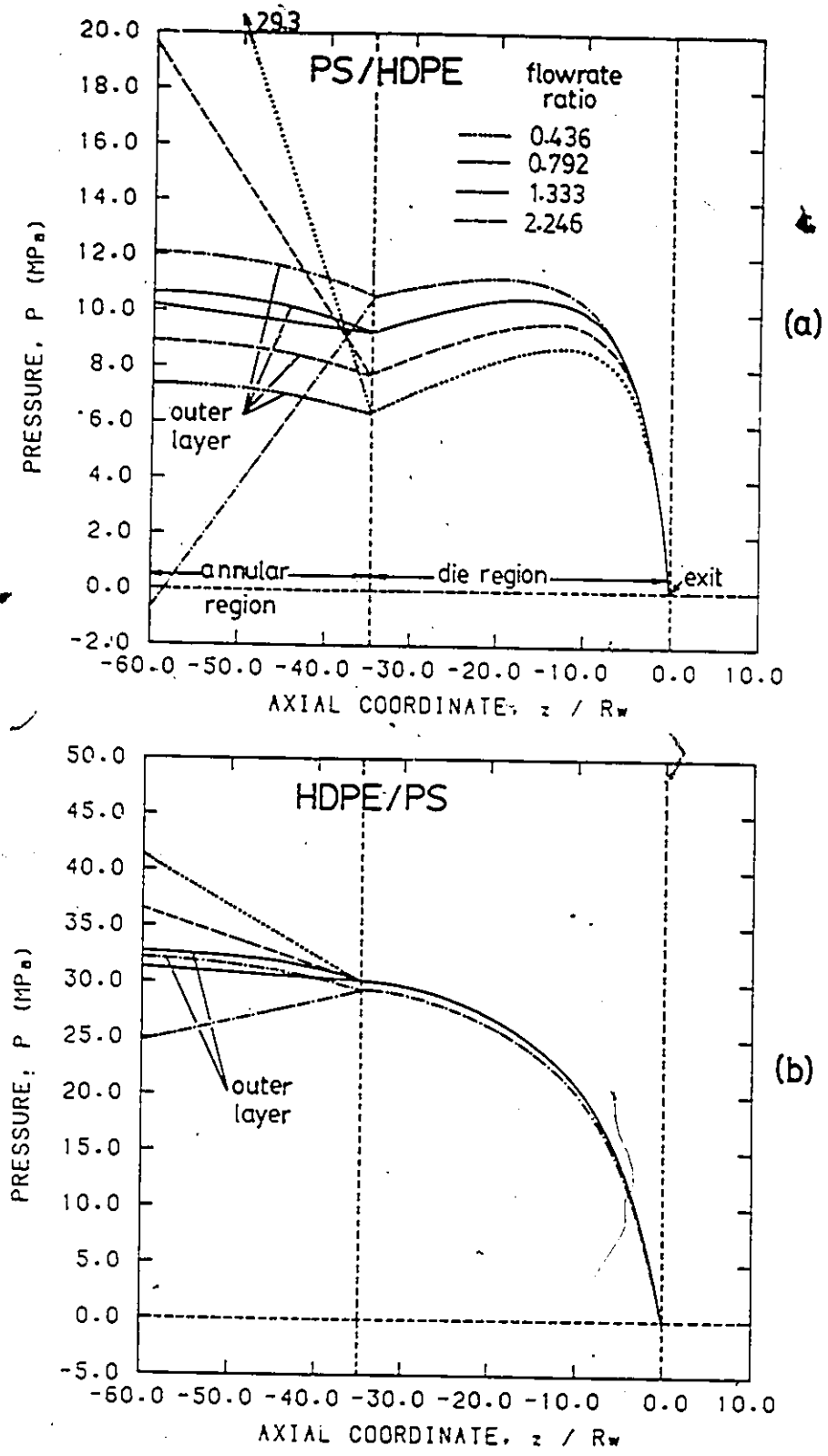

Figure 6.4: Pressure Profiles along Modified Du Pont's Die (Design A) Using LAT: (a) PS/HDPE. (b) HDPE/PS.

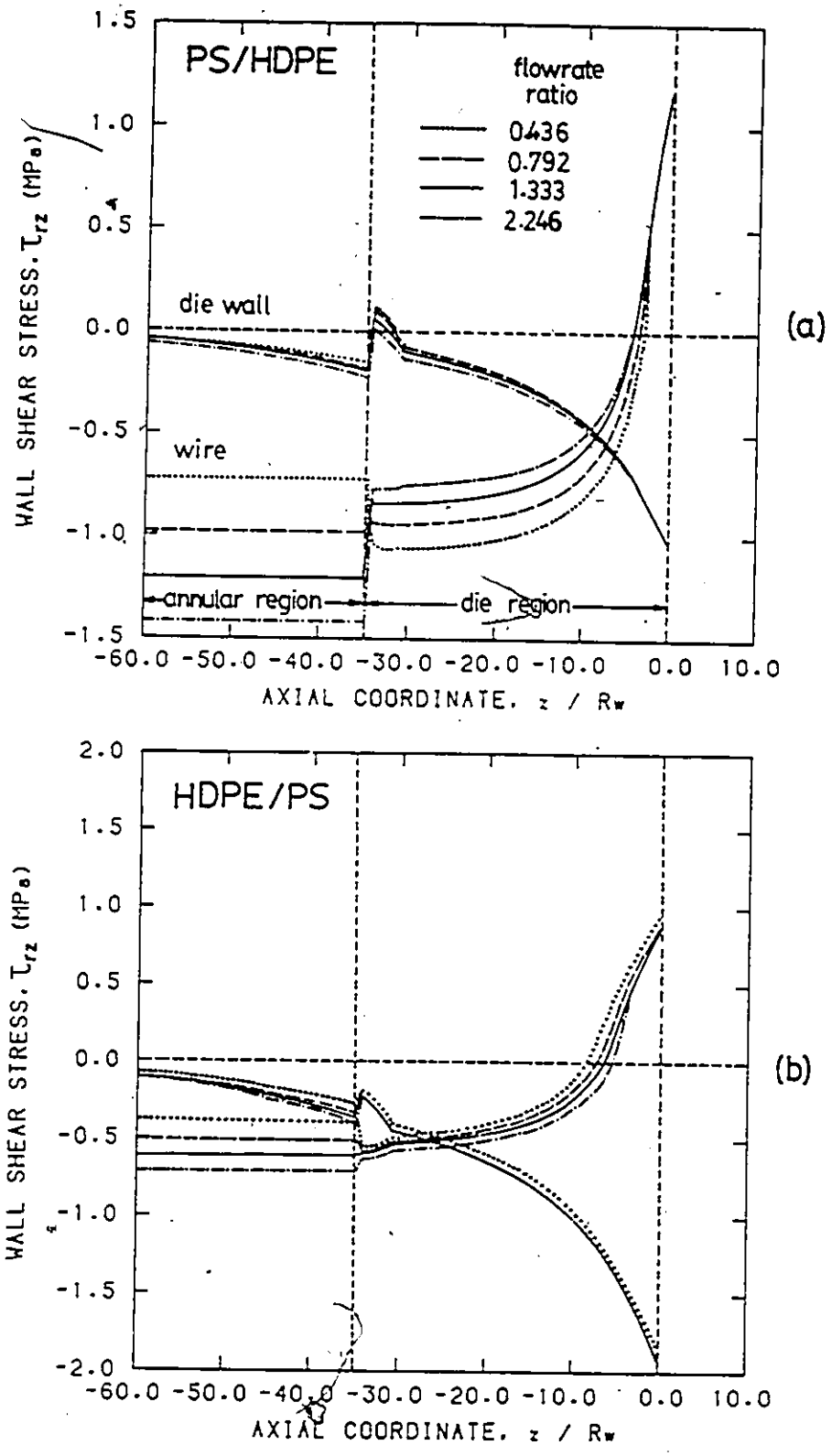

Figure 6.5: Shear Stress Profiles along the Die Wall and Wire in Modified Du Pont's Die (Design A) Using LAT: (a) PS/HDPE. (b) HDPE/PS.

increases, the pressure drop decreases. The same positive annular pressure gradient phenomenon for the inner layer exists.

A look at the stress for PS/HDPE system (Figure 6.5) suggests that as the flowrate ratio increases, the annular region stresses decrease (become more negative). In the die region, as the flowrate increases, the die wall shear stresses decrease and the wire shear stresses increase (become more positive). The stress distribution for the HDPE/PS system shows that all stresses decrease as the flowrate ratio increases. It is also interesting to note that positive shear stresses at the die wall exist for PS/HDPE system, indicating the presence of recirculation, which cannot be eliminated by simply changing the flowrate ratio.

In addition, these results show that for isothermal flows, changing flowrate ratio affects the inner fluid more than the outer fluid. Furthermore, when the outer fluid is less viscous than the inner fluid, the effects tend to be magnified. This analysis also reveals that higher pressure drop is required when the outer fluid is more viscous than the inner fluid.

6.3.2 Finite Element Analysis

It has been shown that the flowrate ratio has little effect on the suppression of recirculation present in the PS/HDPE system. Therefore, it would be interesting to investigate the effect of viscosity ratio, which is defined as:

$$\frac{\mu_o}{\mu_i} = \frac{\text{outer layer viscosity}}{\text{inner layer viscosity}} \tag{6.5}$$

on the suppression of recirculation. For such an analysis, Newtonian fluids are considered. The two-dimensional FEM analysis is used so that the quantitative amount of recirculation can be evaluated.

A total of seven viscosity ratios are investigated: 0.1, 0.2, 0.25, 0.5, 1.0, 1.25 and 2. Extreme viscosity ratios are not used because they are not practical in actual operation. The same operating conditions from the previous analysis are used, i.e. $V_w = 1000\ cm/s$ and $R_c = 1.8R_w$. In addition, the flowrate ratio is fixed at 0.9243, i.e. a thickness ratio of 0.70, or the coating thickness for the outer layer is only 70% of the inner.

A section of the u-w-p grid and stream function grid employed is shown in Figure 6.6. There are 432 u-w-p elements (864 stream function elements) and 1022 nodes (73 nodes along and 14 nodes across) with 7 nodes in each layer. The grids shown are the final ones after solution for the unknown a

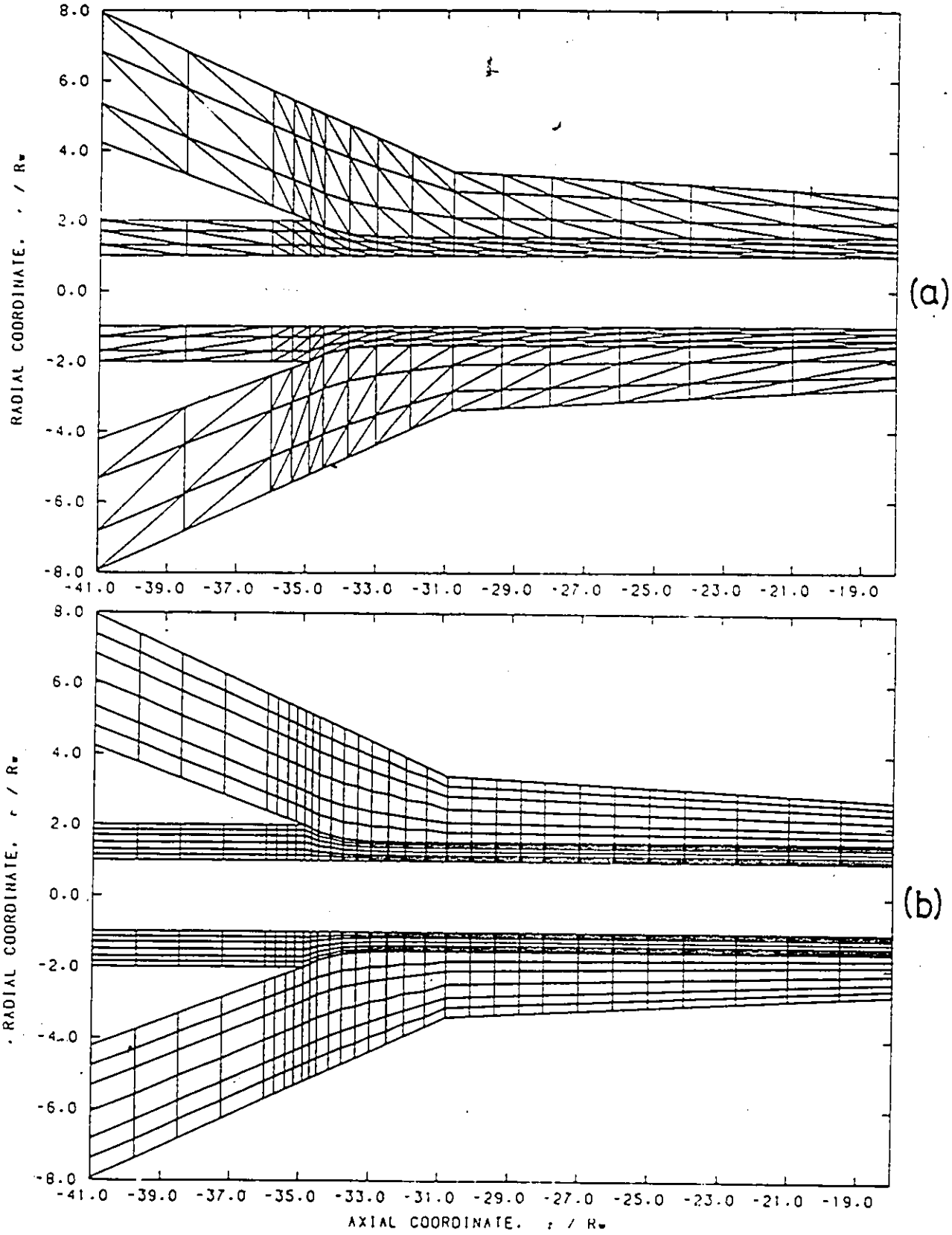

Figure 6.6: Finite Element Grid for Isothermal Analysis of Modified Du Pont's Die (Design A): (a) u-w-p Grid. (b) Stream Function Grid.

priori interface has been achieved. The initial interface location assumed consists of an arbitrary but judiciously chosen curve after the contact point followed by a flat line. This interface is then updated according to the procedure outlined in Section 3.4 with an underrelaxation factor $\lambda = 0.5$. In each case 7 iterations were required for convergence to occur.

Figure 6.7 shows a typical pressure distribution along the unit. In particular, the pressures along the outer wall of the inner channel and the inner wall of the outer channel are shown up to the contact point, after which the interface is formed. The discontinuity of pressures still exists when the two fluids first meet each other, then equalization occurs rather rapidly. Figure 6.8 shows a typical streamline pattern, where the streamlines have been normalized to take the values of -1 at the wire surface, 0 at the interface and the torpedo surfaces, and 1 at the die wall/free surface with increments of 0.25 in between. As can be seen, there is a large recirculation near the contact region, with 30% of the outer fluid recirculating.

The recirculation results for different viscosity ratios are plotted in Figure 6.9. It is evident that as the viscosity ratio increases, the amount of recirculation decreases at an exponential rate until it vanishes at $\mu_o/\mu_i \approx 1.5$, i.e. there is no recirculation when the outer fluid is approximately 1.5 times

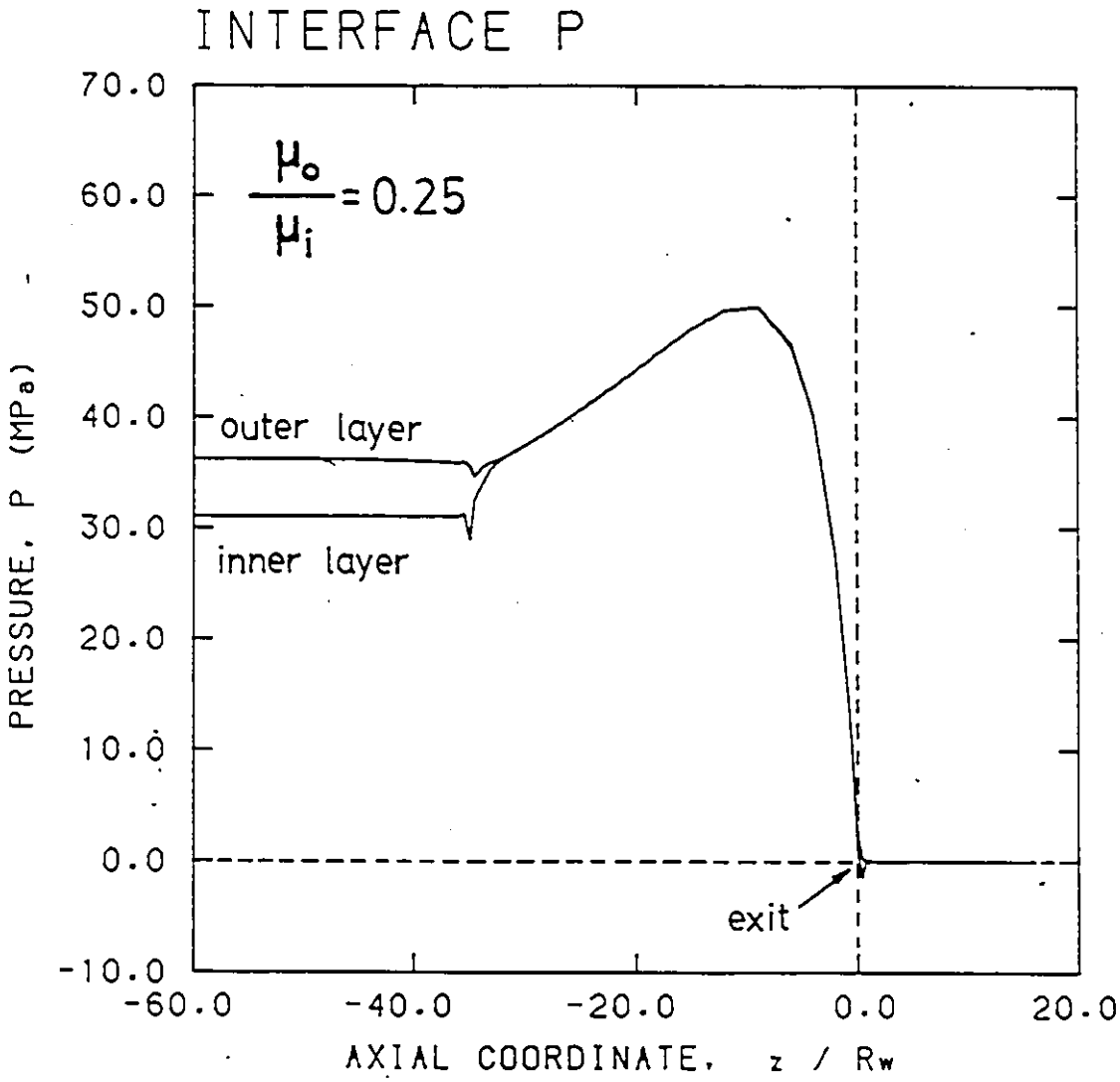

Figure 6.7: Pressure Profile for Isothermal Analysis of Two Newtonian Fluids in Modified Du Pont's Die (Design A).

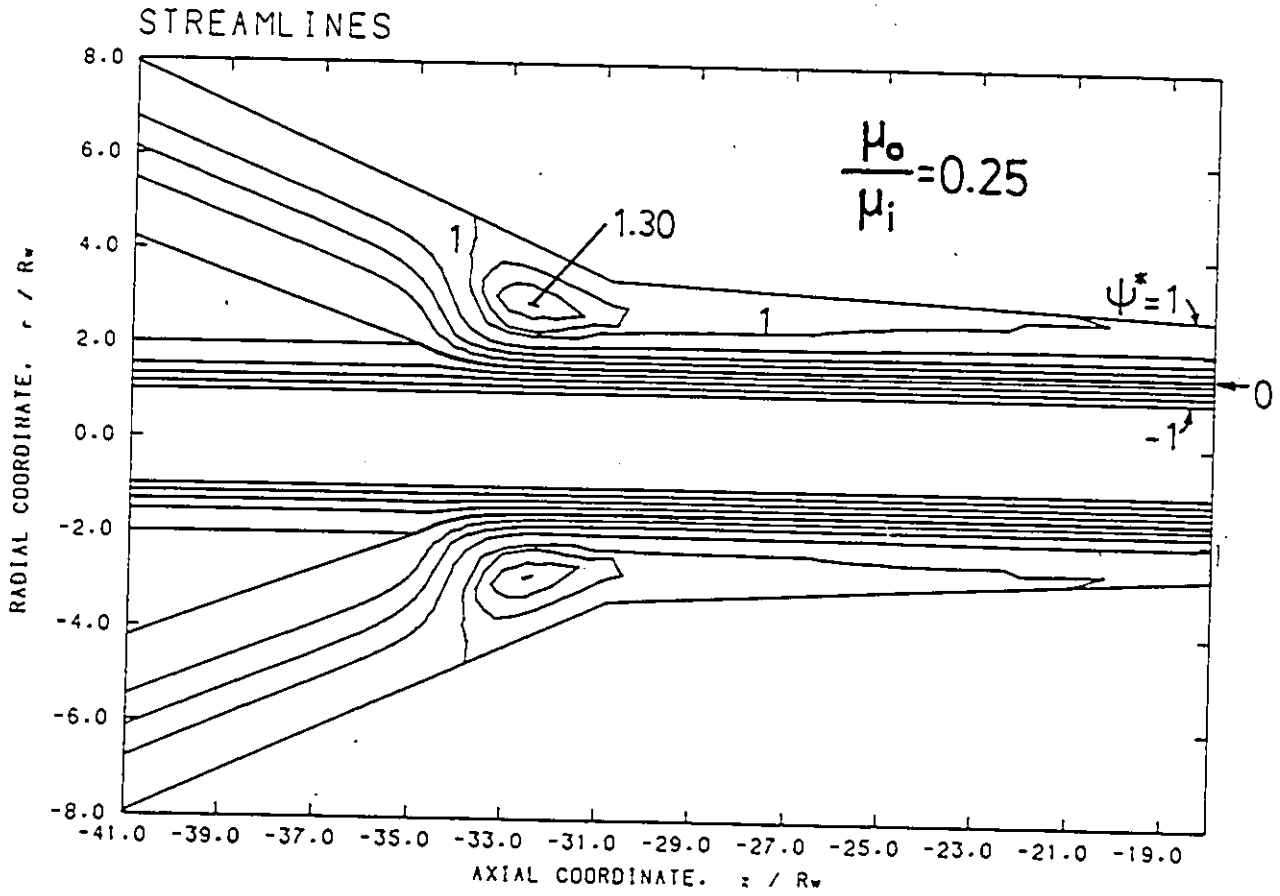

Figure 6.8: Streamline Pattern for Isothermal Analysis of Two Newtonian Fluids in Modified Du Pont's Die (Design A).

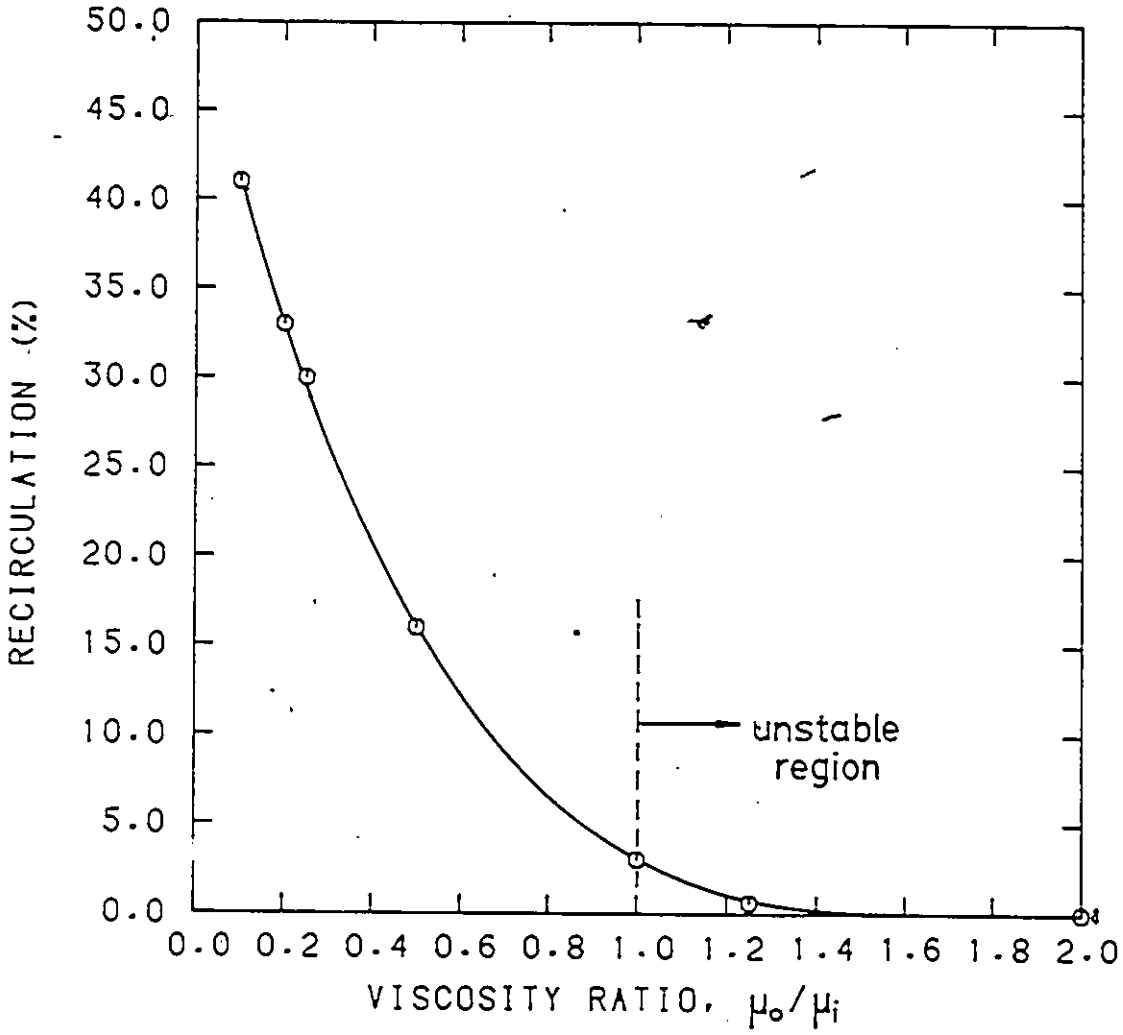

Figure 6.9: Recirculation as a Function of Viscosity Ratio for Isothermal Analysis of Two Newtonian Fluids in Modified Du Pont's Die (Design A).

more viscous than the inner fluid.

Therefore, the recirculation can be reduced by having a more viscous fluid outside. In certain cases, when the viscosity ratios are greater than a limiting value, the recirculation disappears. This phenomenon is also true if shear-thinning fluids are involved, as supported by the shear stress curves at the die wall for the HDPE/PS system (Figure 6.5(b)). However, when a more viscous fluid is on the outside, it has been shown experimentally that interfacial instabilities occur (Khan and Han, 1976; Han and Shetty, 1978; Kim and Han, 1983). Thus, $\mu_o/\mu_i > 1$ indicates an unstable region since this is not the preferential configuration.

This isothermal analysis has shown many interesting phenomena in wire-coating coextrusion. In actual situations, however, these flows are highly nonisothermal as discussed in Section 5.4. A full analysis is therefore necessary by solving the coupled momentum and energy equations, which will be discussed in the next section.

6.4 Nonisothermal Wire-Coating Coextrusion

This section presents a full nonisothermal analysis of wire-coating coextrusion. In particular, the present results will be first compared with the only other existing nonisothermal analysis based on the LAT simplification (Basu, 1981) and the errors will be discussed. Then, the full flow domain will be examined for a high-speed industrial coextrusion operation employing typical polymer melts in a new improved die design.

6.4.1 Comparison with Previous Results (Basu's Die)

The only nonisothermal study in wire-coating coextrusion dies has been performed by Basu (1981). His analysis was based on LAT for both the momentum and energy equations, i.e. neglecting all the v_r-components in both equations.

It has been found previously (Section 5.4.1) that a tapered die (Endo's die) gives large discrepancies when the radial convection term is excluded. It would be interesting to see if the flow of two polymers in a straight-channel wire-coating coextrusion die (Basu's die) gives the same type of

error. Since an interface is present, the effects of one-dimensional (LAT) vs. two-dimensional analysis (FEM) on the interface location are also investigated.

Basu's die consists of a wire ($R_w = 0.1026\ cm$) being coated from a cylindrical die ($R_c = 0.225\ cm$). Run No. 5 of his analysis is repeated here. The operating condition is to coat the wire with an inner layer (PS) having a thickness of 0.056 cm and an outer layer (HDPE) with a thickness of 0.013 cm at 1000 cm/s. The die considered is 2.43 cm long.

The flow is considered to be fully developed at $T_o = 170°C$ at the entry. The LAT is used to determine the velocity profile and locate the interface position. These, in turn, are used in the FEM analysis as entrance boundary conditions. Adiabatic-wall thermal boundary condition is assumed everywhere. The various dimensionless groups for this case are summarized as follows (refer to Appendix C for details of calculations):

$$\begin{array}{lllllll} \text{PS:} & Re & = & 0.27 & , & Pe & = & 91,500 \\ & Na & = & 483 & , & Gz & = & 2,100 \\ \text{HDPE:} & Re & = & 0.065 & , & Pe & = & 7,500 \\ & Na & = & 42 & , & Gz & = & 40 \end{array}$$

As can be seen, Pe and Na numbers are quite high, while Re numbers are

very low. Of course, due to adiabatic walls assumed, $Bi = 0$.

For the finite element analysis, the domain after the die exit is extended to a length of about $10R_w$ (see Figure 6.10). The finite element grid consists of 720 u-w-p elements (1440 temperature elements) with 73 nodes along and 22 nodes across the domain (11 nodes for each fluid). The nodes at the interface are double nodes (Figure 3.4). The initial interface location is assumed to be a horizontal line extending from the fully developed location imposed at the entry. Again, it is updated by the procedure detailed in Section 3.4 with an underrelaxation factor of 0.5. Approximately seven iterations are required for the solution to converge.

The streamline pattern from the nonisothermal finite element analysis is shown in Figure 6.11, where the streamlines have been normalized to take the values of -1 at the wire surface, 0 at the interface and 1 at the die wall/free surface with increments of 0.25 in between. Obviously, a rearrangement of the flow field occurs right at the exit in anticipation of the free surface, and therefore the interface location is higher than would be from Basu's analysis.

A comparison with Basu's results at the die exit with the presence of the free surface for the velocity and temperature profiles is given in Figures 6.12

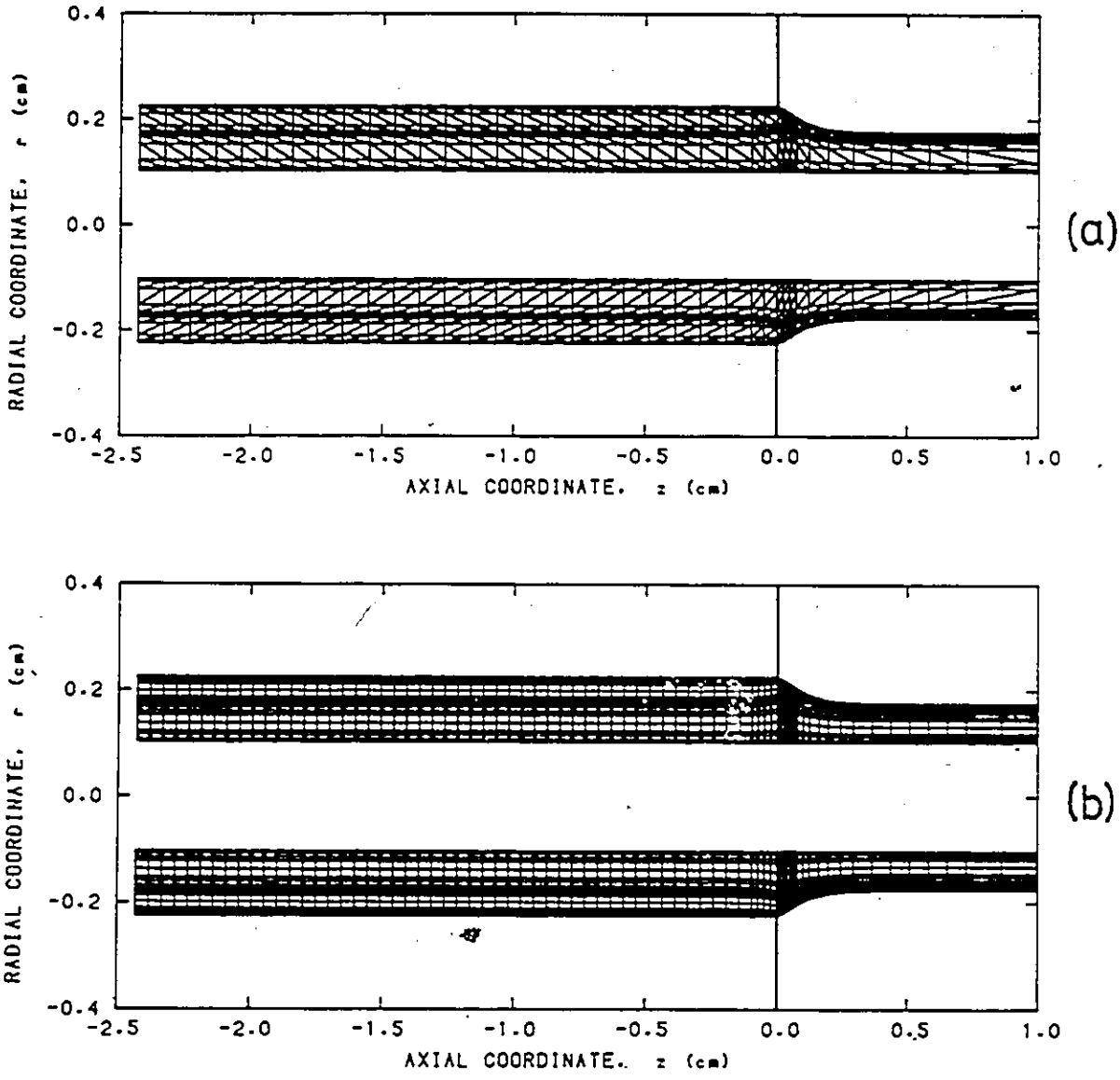

Figure 6.10: Finite Element Grid for Analysis of Basu's Die: (a) u-w-p Triangles, (b) Temperature Quadrilaterals.

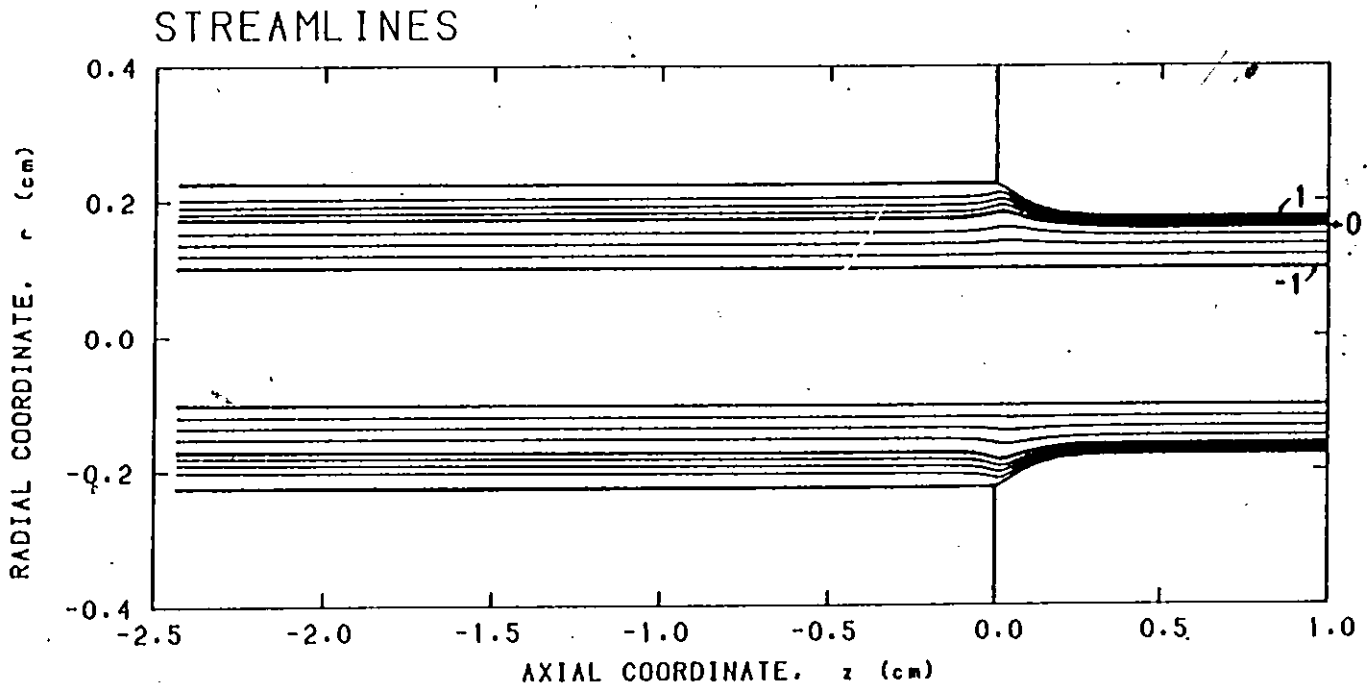

Figure 6.11: Streamline Pattern for Basu's Die.

and 6.13, respectively. It is seen that there are discrepancies due to the rearrangement of the profiles at the exit. When the free surface was ignored, the discrepancies were not great except for a higher temperature at the die wall found when the full energy equation is solved (extra heat contribution from the $v_r \partial T/\partial r$ term).

The interface pressure is shown in Figure 6.14, where the discontinuities near the die exit become evident. The overall pressure drop in the system was found to be 12.4 MPa which underestimates Basu's result of 13.5 MPa by 8%. When the free surface was ignored, the pressure was slightly higher (12.8 MPa). This shows that even for straight channels ($\phi = 0$), there are discrepancies when the radial components in the energy equation are ignored.

Again, it has been shown that solving the full two-dimensional momentum and energy equations is necessary when non-fully developed flows are anticipated, for instance, shift of interfaces due to temperature gradients and free surface flows. In addition, the inclusion of the radial convection term in the energy equation gives higher temperatures at the die wall. These effects would be magnified as the Pe and Na numbers and the taper angle ϕ become larger.

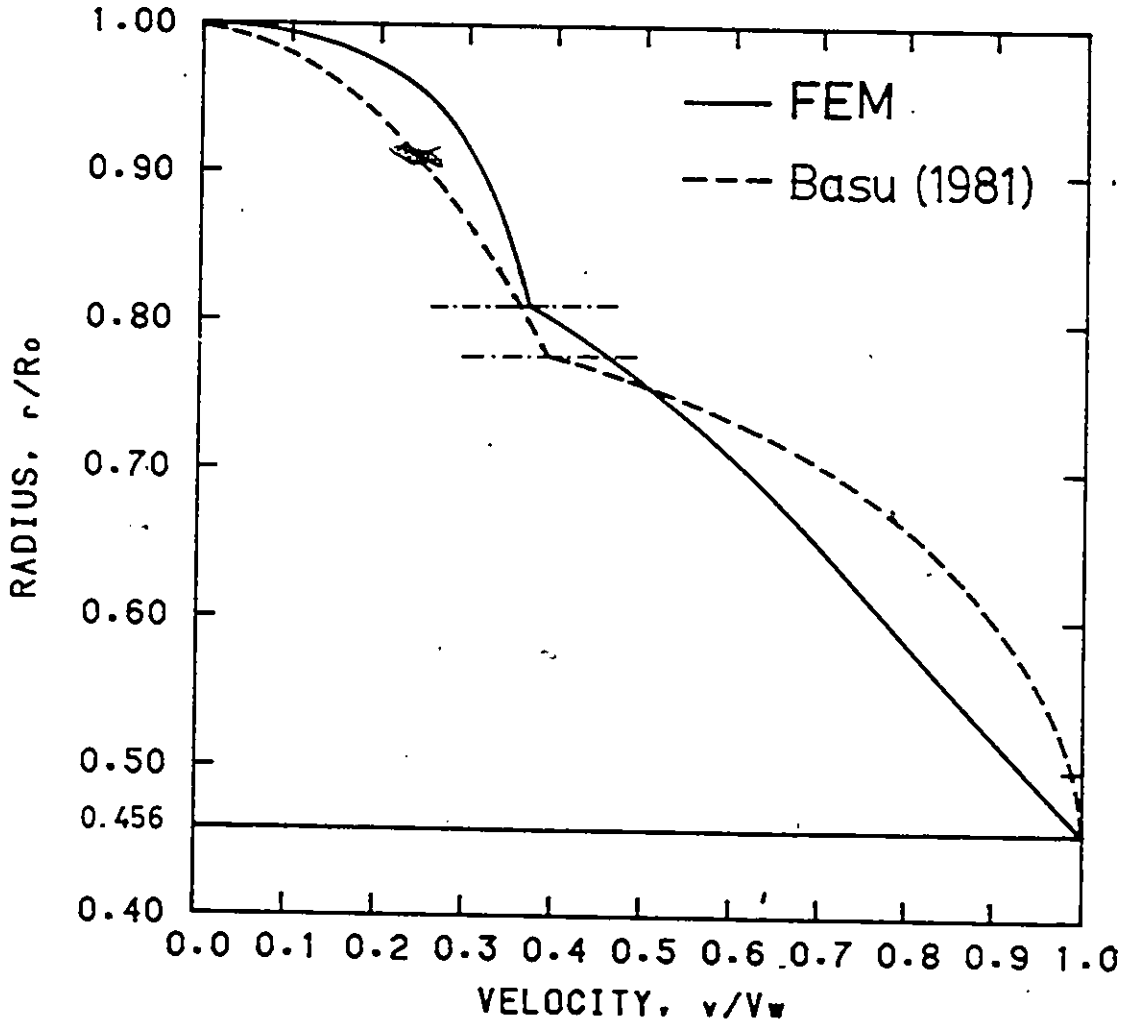

Figure 6.12: Comparison of Velocity Profiles at Die Exit between Present Study and Basu's Results (Run No. 5, 1981).

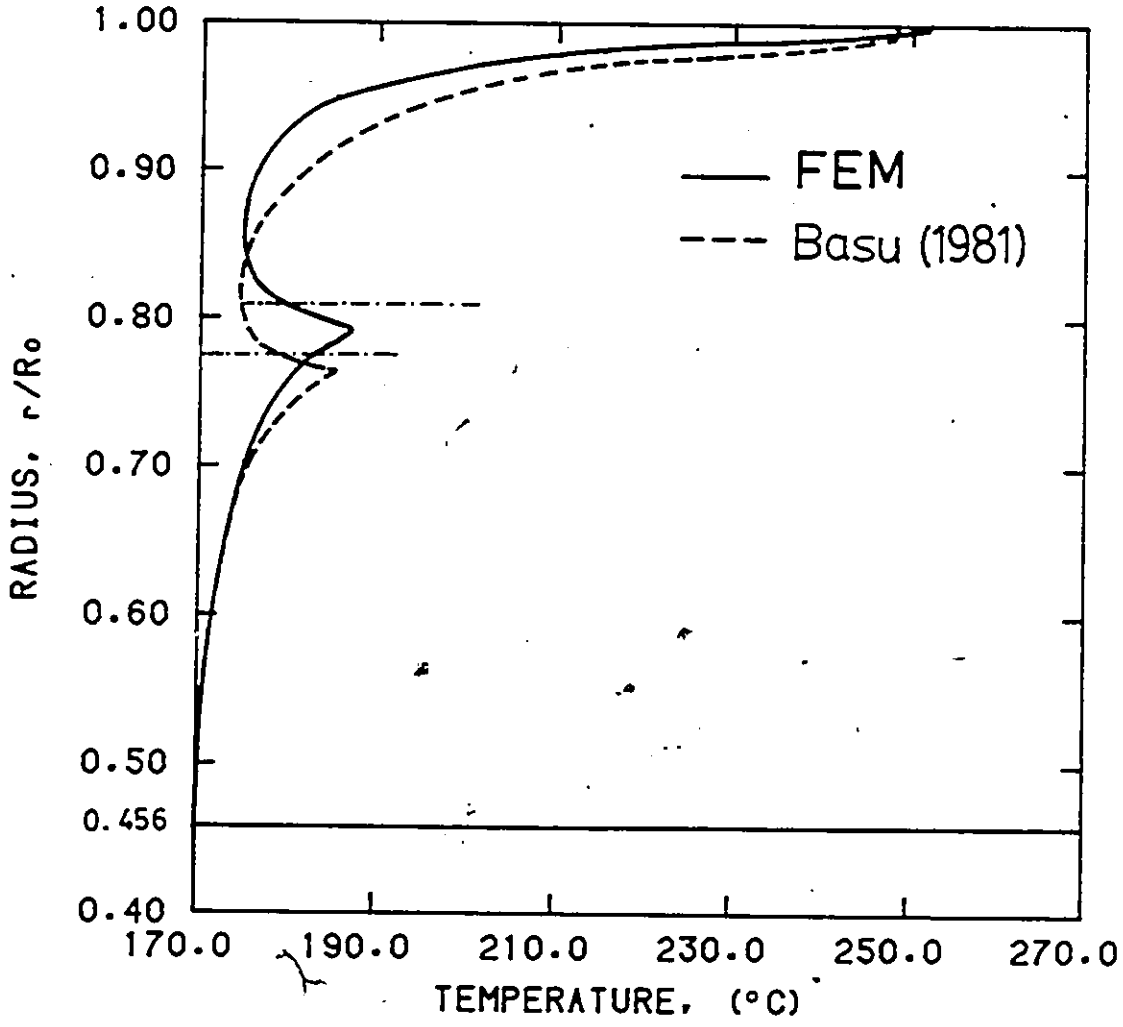

Figure 6.13: Comparison of Temperature Profiles at Die Exit between Present Study and Basu's Results (Run No. 5, 1981).

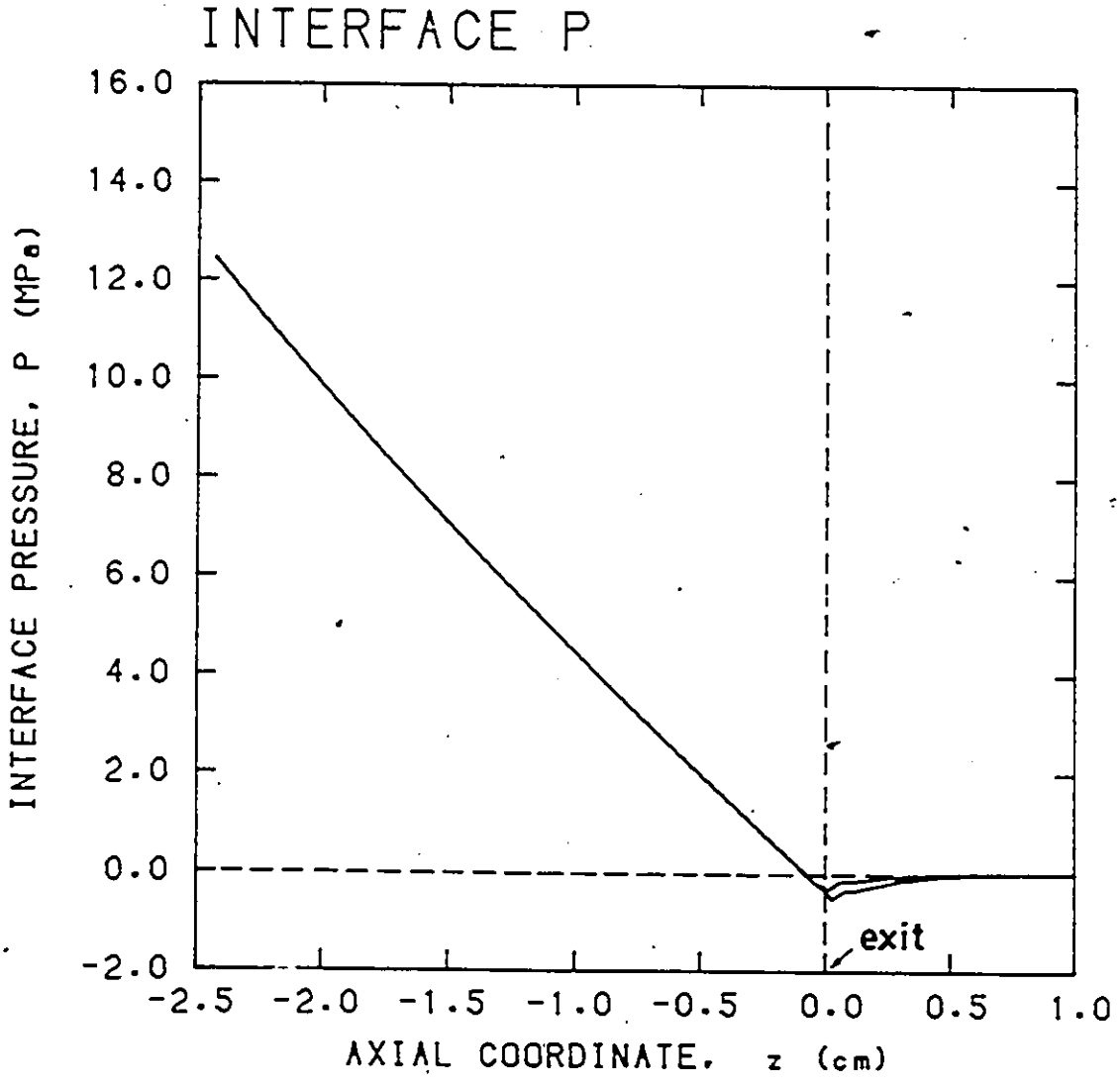

Figure 6.14: Pressure Distribution along the Interface in Basu's Die.

6.4.2 Influence of Die Design and Thermal Boundary Conditions (Modified Du Pont's Die)

After analyzing the simple die design considered by Basu (1981), we proceed to perform a thorough nonisothermal analysis of a full die. This die is required to provide streamlined flows, as discussed in Section 5.4.2. In addition, it must also provide an interface which does not change drastically in the axial direction. Such requirement ensures that additional stresses are not introduced due to the radial movements.

The physical properties of the polymers used have been summarized in Section 6.2. Two polymers, namely HDPE and PS, are employed. In addition, the boundary conditions have been discussed in the same section.

The effects of thermal boundary conditions and wire speed on the field variables are investigated. Since there are two different melts, the effects of entrance temperature on the field variables are also examined. This additional parameter is expressed as:

$$\frac{(T_o)_o}{(T_o)_i} = \frac{\text{entrance temperature for the outer layer}}{\text{entrance temperature for the inner layer}} \tag{6.6}$$

For each run, the required final cold coated wire radius is $1.8R_w$, i.e. overall coating thickness is 80% of the wire radius. The final thickess of the inner

layer is arbitrarily taken to be three times as thick as the outer layer, i.e. a thickness ratio of 1/3. The volumetric flowrate of the individual melt is then calculated at the corresponding entry melt temperature.

Special care must be taken in designing an improved die configuration. The previous analysis in Chapter 5 has shown that streamlined flows can be achieved by constraining the flow area available in the die. In the present case, the flow area in the die region can be reduced by reducing the final tapered angle. In addition, the flow area in the impact region can be further restricted by moving the torpedo deeper into the die, i.e. reducing the gum space GS. Both measures have been taken in redesigning the modified Du Pont's die. Preliminary runs have shown that a die design given in Figure 6.15, and thereafter called modified Du Pont's Die (Design B), tends to provide streamline flows and levelled interfaces for the operating conditions desired.

Three sets of runs are performed to determine the effects of various thermal boundary conditions and wire speeds of the field variables. These sets are:

1. $(T_o)_o = (T_o)_i = 220°C$, isothermal walls and $V_w = 100$, 500, 1000 and 2000 cm/s.

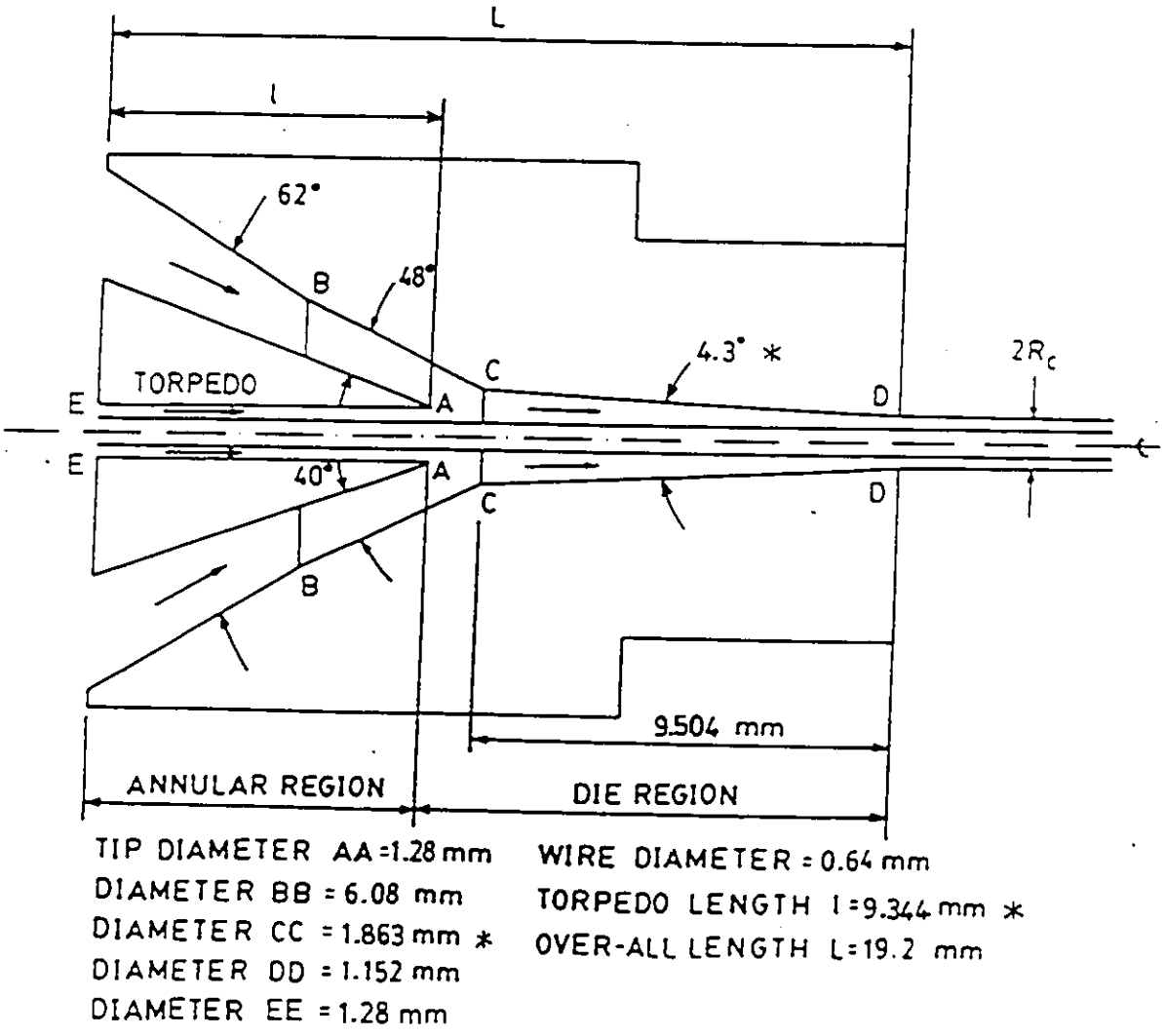

Figure 6.15: Modified Du Pont's Die Employed in the Nonisothermal Analysis of Wire-Coating Coextrusion (Design B). Changes in the Design Represented by *.

2. $(T_o)_o = (T_o)_i = 220°C$, adiabatic walls and $V_w = 100$, 500, 1000 and 2000 cm/s.

3. $(T_o)_o = 220°C$, $(T_o)_i = 200°C$, adiabatic walls and $V_w = 1000$ cm/s, and

   $(T_o)_o = 200°C$, $(T_o)_i = 220°C$, adiabatic walls and $V_w = 1000$ cm/s.

For all these runs, PS and HDPE will always form the outer and inner layers, respectively, i.e. PS/HDPE. Experimental results have shown that this is the favourable configuration, as discussed in Section 6.3.2.

The FEM grid employed consists of 780 u-w-p elements (1560 bilinear quadrilaterals) and 1738 nodes, with 79 nodes along the die length and 22 nodes radially (11 nodes for each fluid). Some typical final grids used are shown in Figure 6.16 for the u-w-p formulation and in Figure 6.17 for the temperature/stream function formulation.

A typical interfacial pressure distribution is shown in Figure 6.18. Slight pressure discontinuities exist immediately after the contact point and at the exit. However, the pressure discontinuities are not very distinct due to an interface which is almost horizontal, as shown in Figure 6.19. Such interface yields interfacial pressure which is almost continuous, as explained

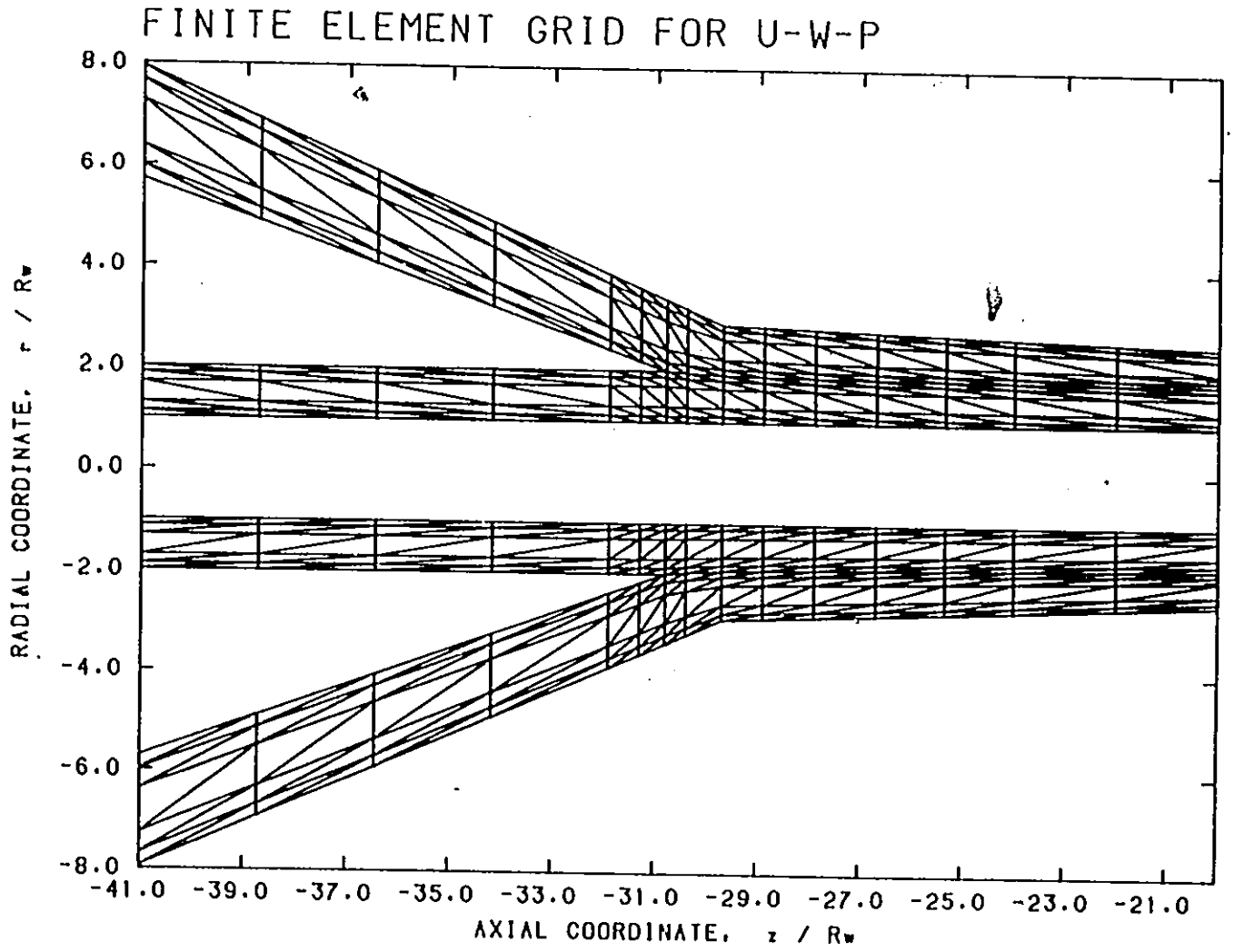

Figure 6.16: Finite Element Grids for u-w-p Formulation in the Nonisothermal Analysis of Modified Du Pont's Die (Design B).

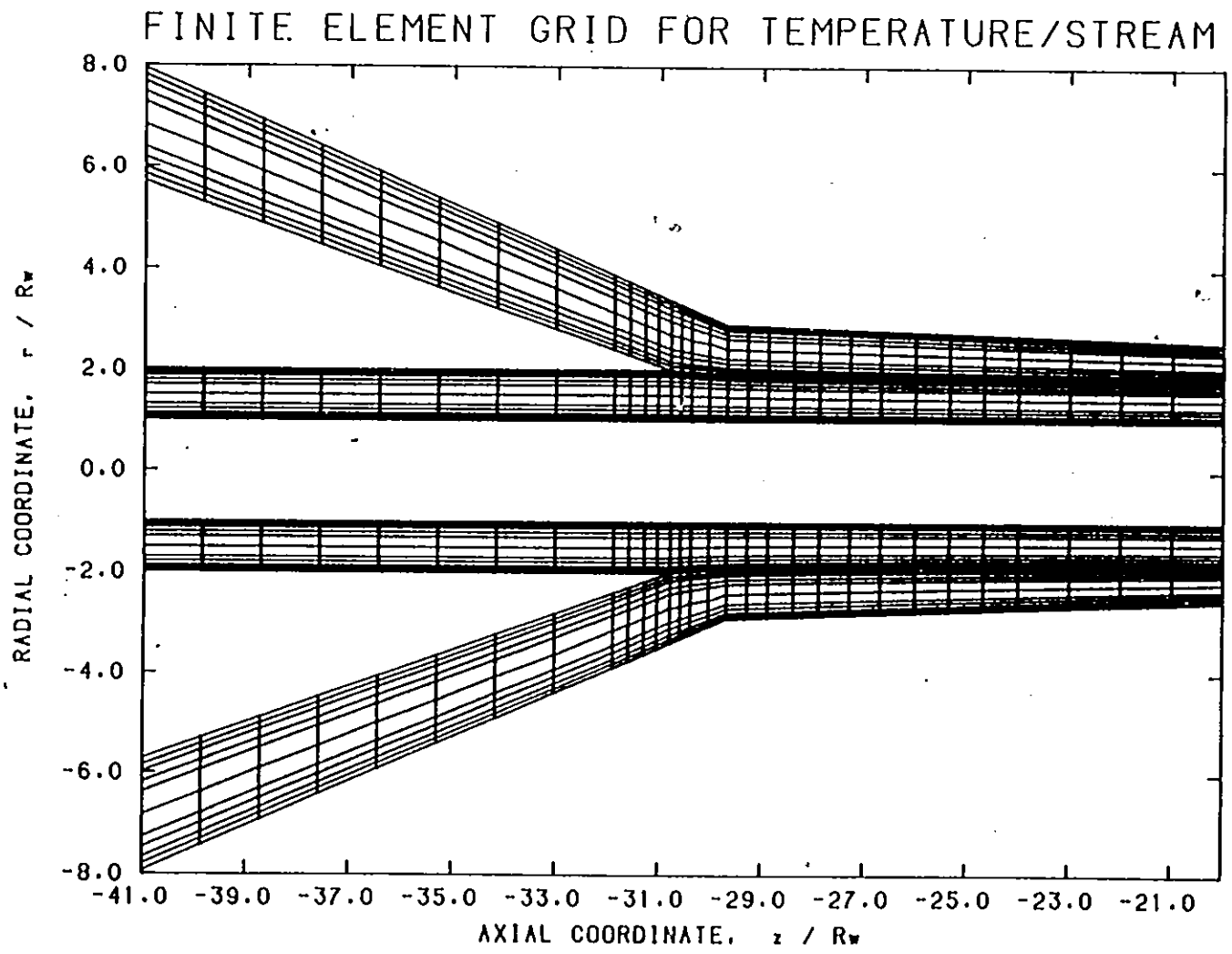

Figure 6.17: Finite Element Grids for Temperature/Stream Function Formulation in the Nonisothermal Analysis of Modified Du Pont's Die (Design B).

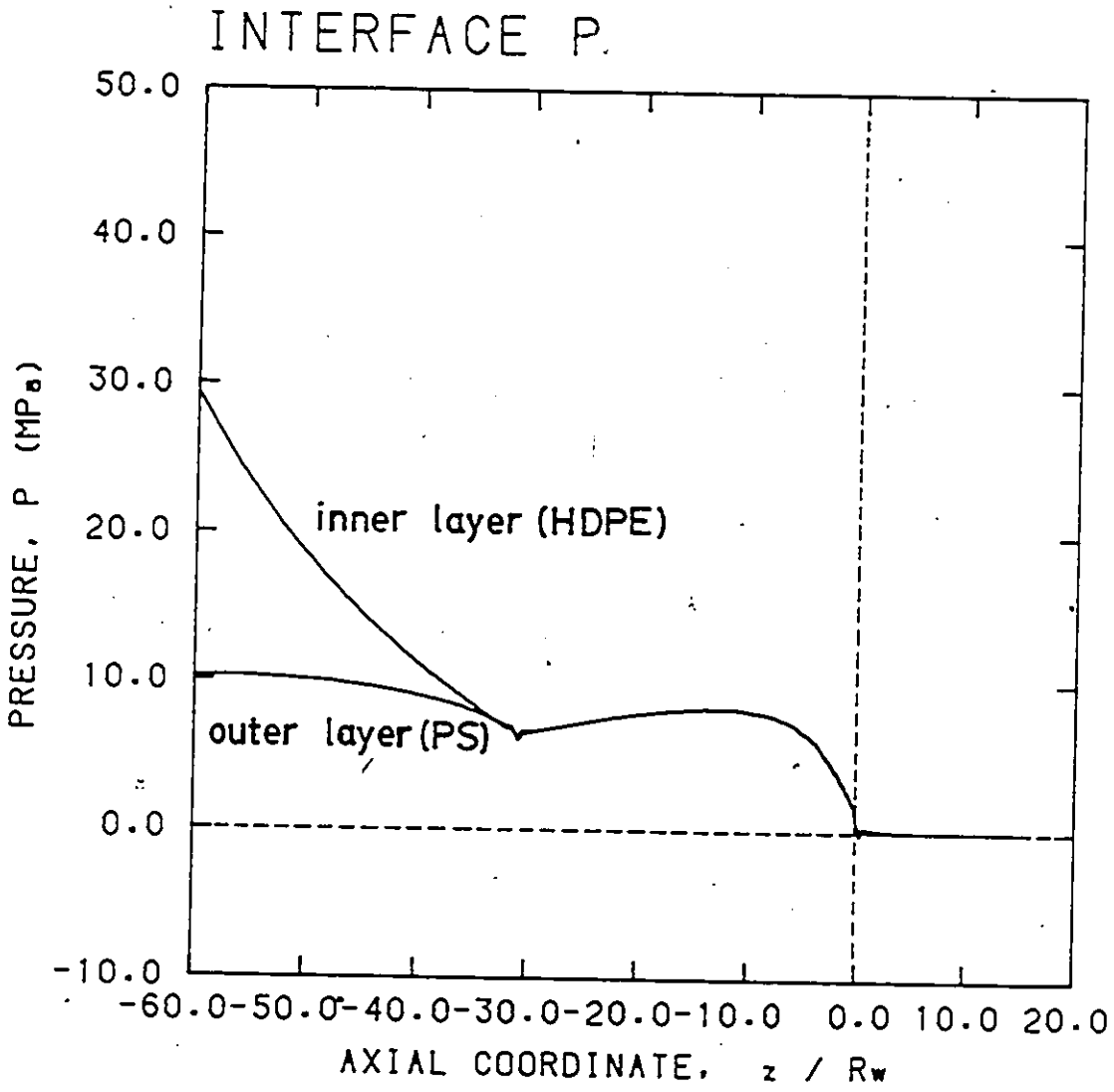

Figure 6.18: Pressure Distribution in Modified Du Pont's Die (Design B) (PS/HDPE, $V_w = 2000\ cm/s$, $Bi = 0$ and $(T_o)_o = (T_o)_i = 220°C$).

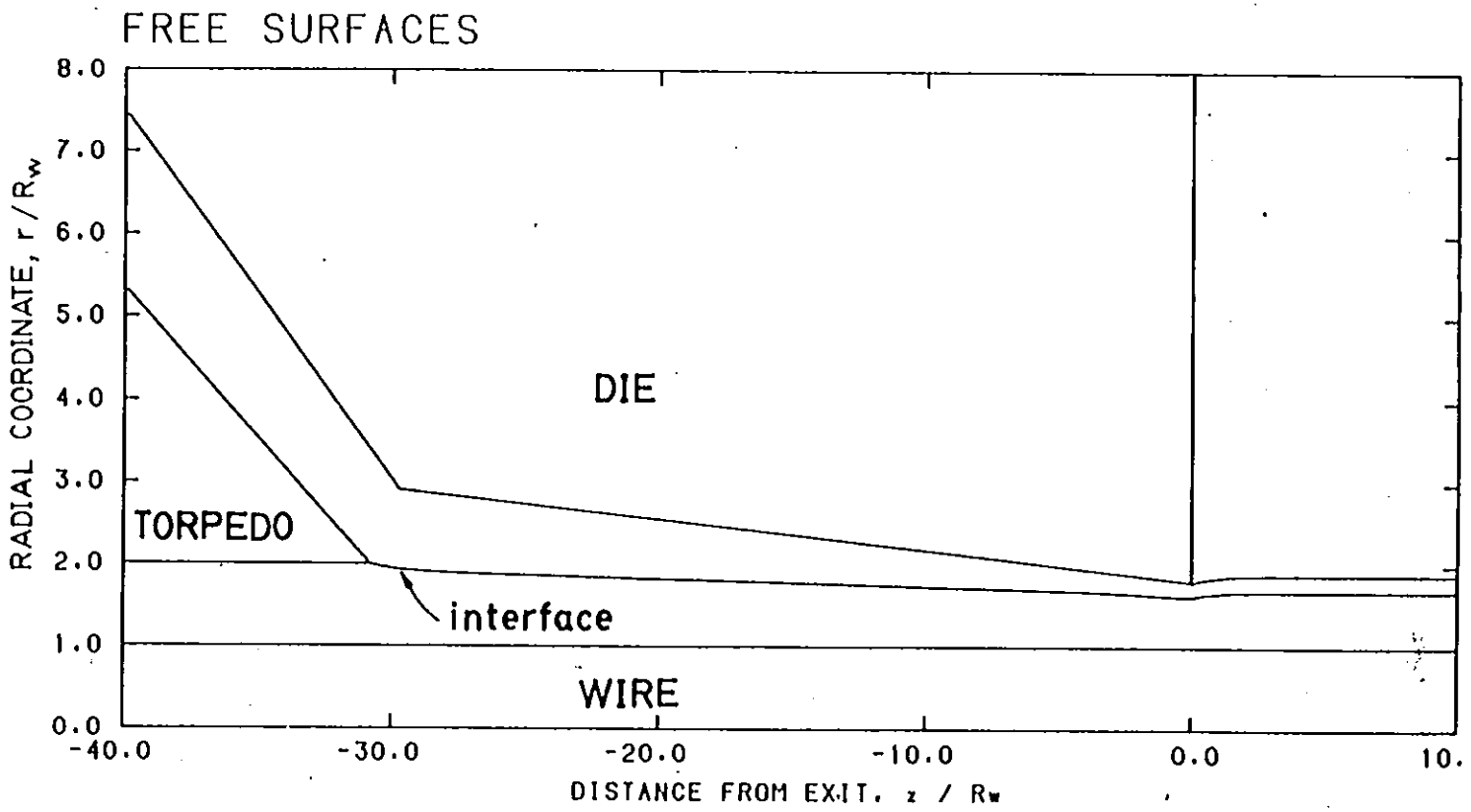

Figure 6.19: Interface Location in Modified Du Pont's Die (Design B)

(PS/HDPE, $V_w = 2000\ cm/s$, $Bi = 0$ and $(T_o)_o = (T_o)_i = 220°C$).

in Section 2.6.

The overall pressure drops for the isothermal and adiabatic boundary conditions are plotted in Figure 6.20. The pressure drop for the inner layer is always higher than the outer layer because of the higher flowrate and viscosity of the former. The effects of the thermal boundary conditions are readily seen. The adiabatic boundary condition always yields a lower pressure drop, consistent with the results presented in Section 5.4.2. Two typical radial temperature profiles at the exit are shown in Figure 6.21. Again, the higher temperatures at the die wall for the adiabatic case lower the viscosities and thus the pressure drop. In addition, the higher interfacial temperatures achieved by the adiabatic case should also contribute to the lowering of pressure drop.

Another interesting phenomenon is the steeper shear rate at the die wall and an interface which is closer to the die wall for the adiabatic case, as illustrated in Figure 6.22. In this case the profile away from the wall is flatter since the flowrate must be conserved. The shifting of the interfaces progressively toward the wall as the die wall temperature increases is evident in Figure 6.23. Note also that there is an additional maximum in temperature as compared to the single-layer wire-coating analysis per-

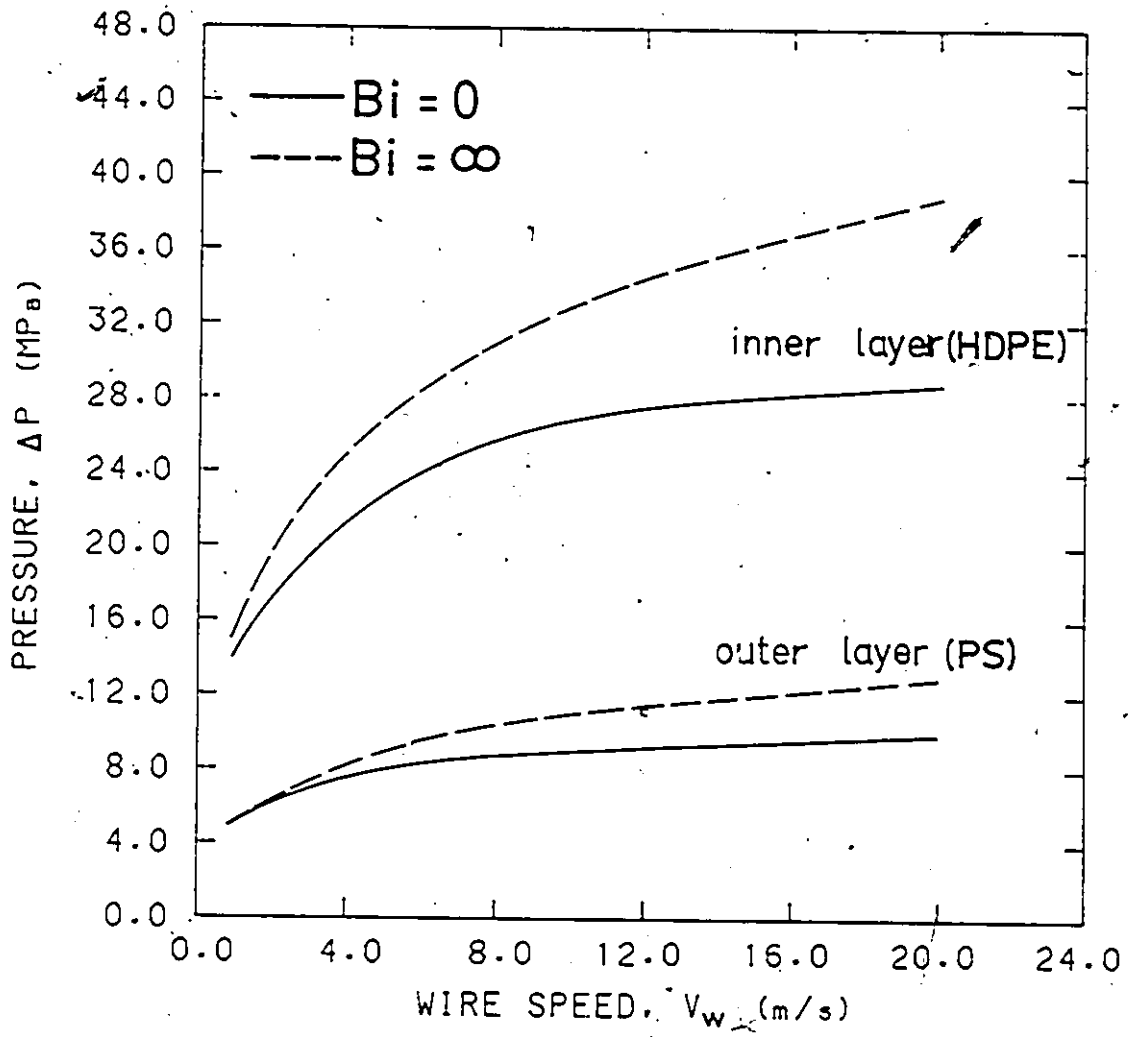

Figure 6.20: Overall Pressure Drop in the Nonisothermal Analysis of Modified Du Pont's Die (Design B) (PS/HDPE, $(T_o)_o = (T_o)_i = 220°C$).

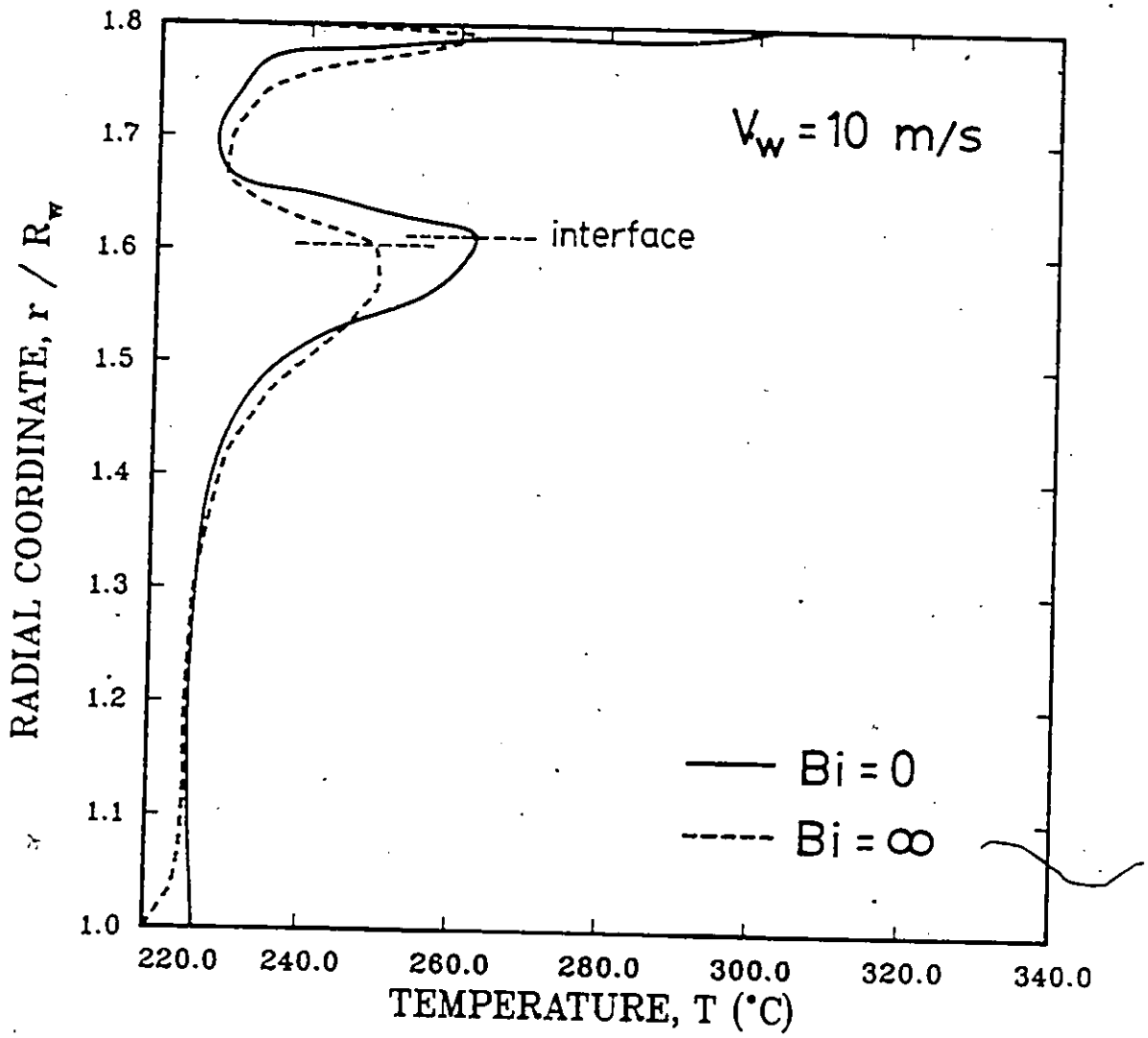

Figure 6.21: Radial Temperature Distribution at Modified Du Pont's (Design B) Die Exit ($z = 0$) Assuming Different Thermal Boundary Conditions (PS/HDPE, $V_w = 1000\ cm/s$, $(T_o)_o = (T_o)_i = 220°C$).

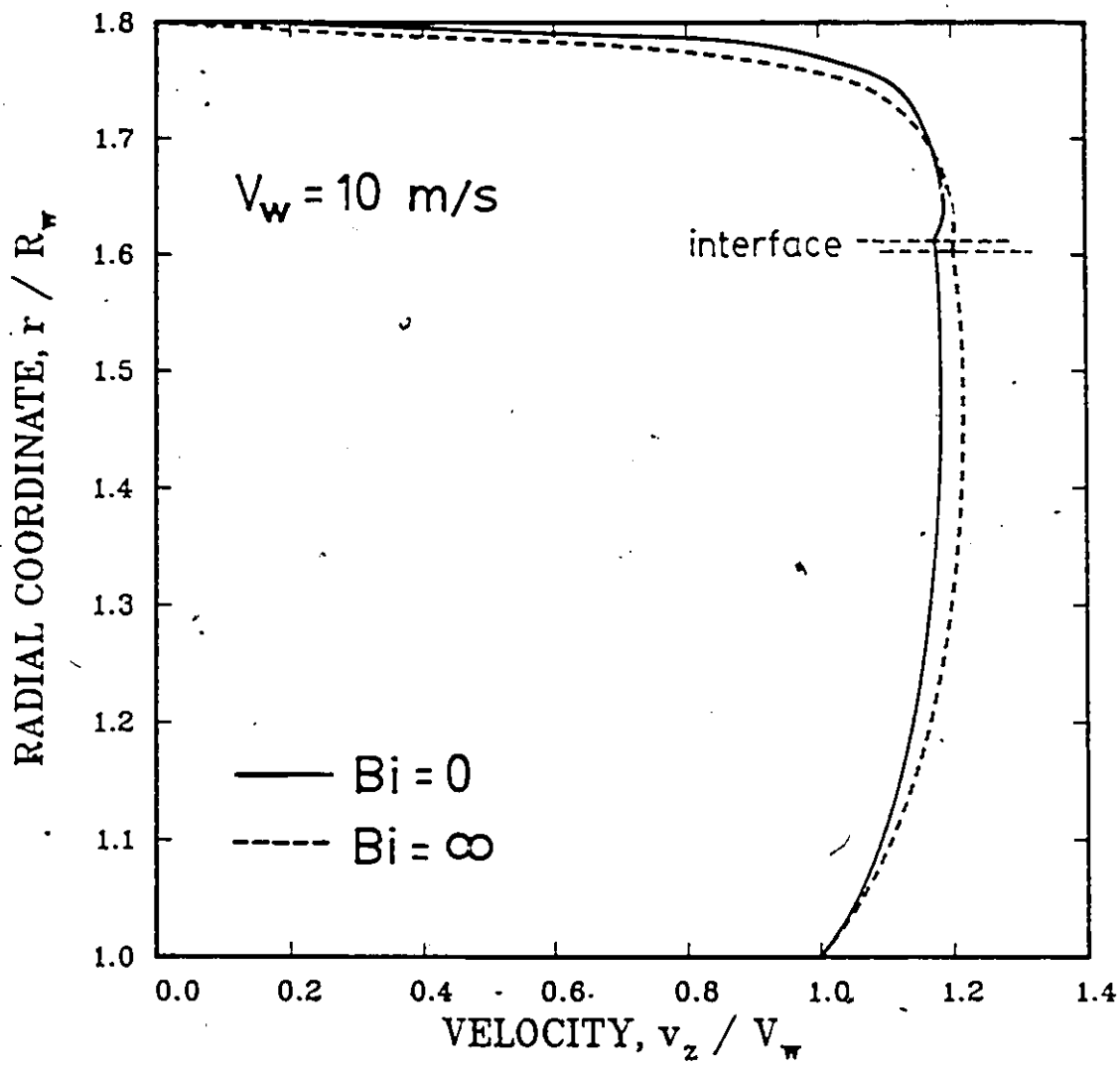

Figure 6.22: Radial Velocity Profile at Modified Du Pont's (Design B) Die Exit ($z = 0$) Assuming Different Thermal Boundary Conditions (PS/HDPE, $V_w = 1000\ cm/s$, $(T_o)_o = (T_o)_i = 220°C$).

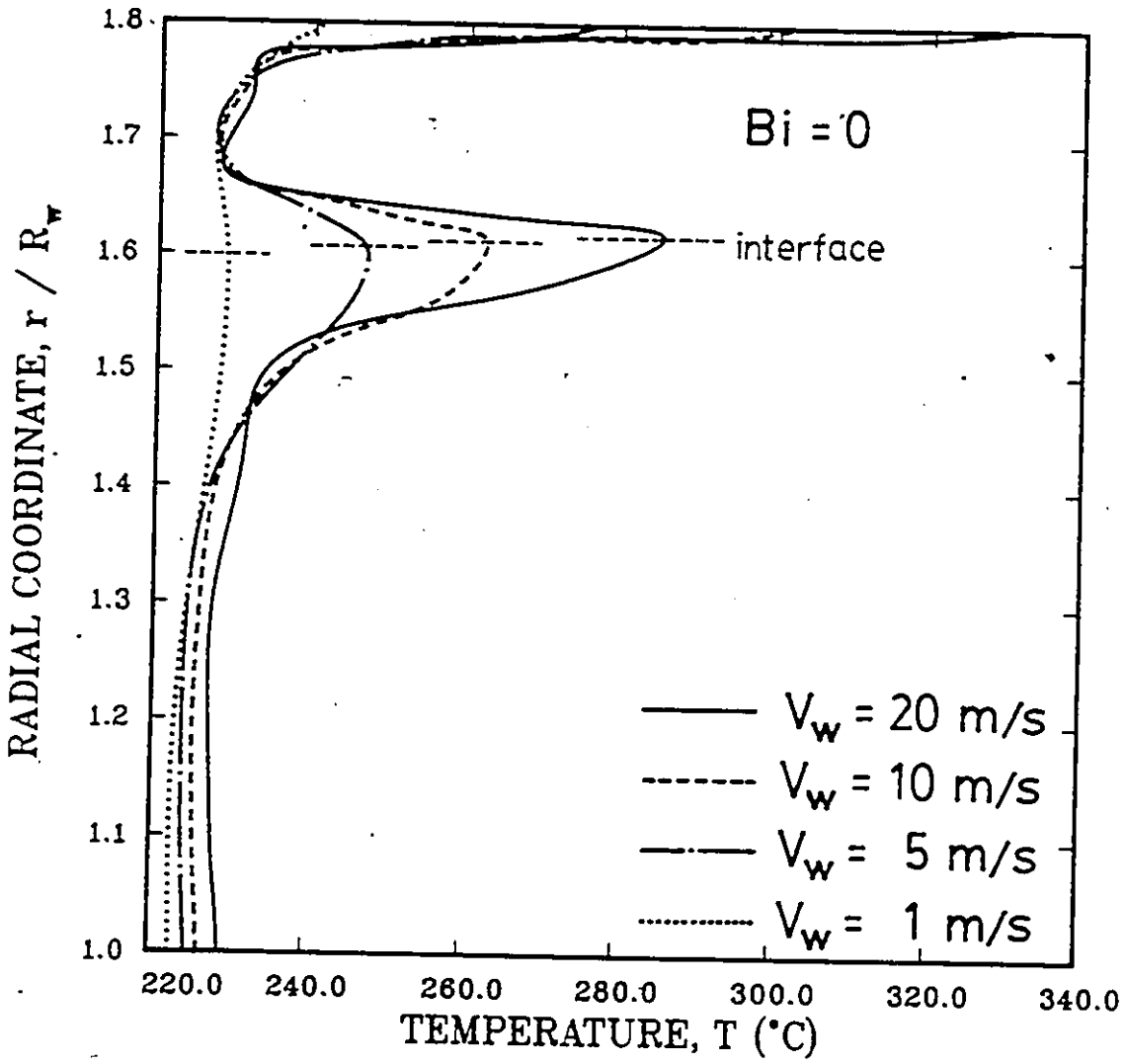

Figure 6.23: Radial Temperature Distribution at Modified Du Pont's (Design B) Die Exit ($z = 0$) for Different Wire Speeds (PS/HDPE, $Bi = 0$, $(T_o)_o = (T_o)_i = 220°C$).

formed in Section 5.4.2. This local maximum occurs in the neighborhood of the interfaces regardless of the thermal boundary condition. As can be seen, the temperature field is a strong function of wire speed.

The strong dependence of the temperature field on wire speed is also evident in Figure 6.24. These maximum temperature curves show two temperature peaks, one at the contact region and another at the exit region. The tremendous temperature rise before the contact point is due to the high viscous dissipation generated at the inner wall of the torpedo. This high temperature continues to dominate at the interface after the contact point. However, the temperature at the interface is considerably lower than that before the contact point. It is also interesting to mark that the maximum temperature is declining slowly in this region. At approximately seven wire radii from the exit, the temperature at the die wall starts to dominate. This temperature increases until reaching a peak at the exit. Both the adiabatic and isothermal wall cases look similar. Quantitatively, however, the adiabatic condition gives temperatures which are much higher than the ones obtained from the isothermal wall condition. The difference grows larger as the wire speed increases. Such discrepancy is also reflected in the pressure drop (Figure 6.20); as the wire speed increases the gap between

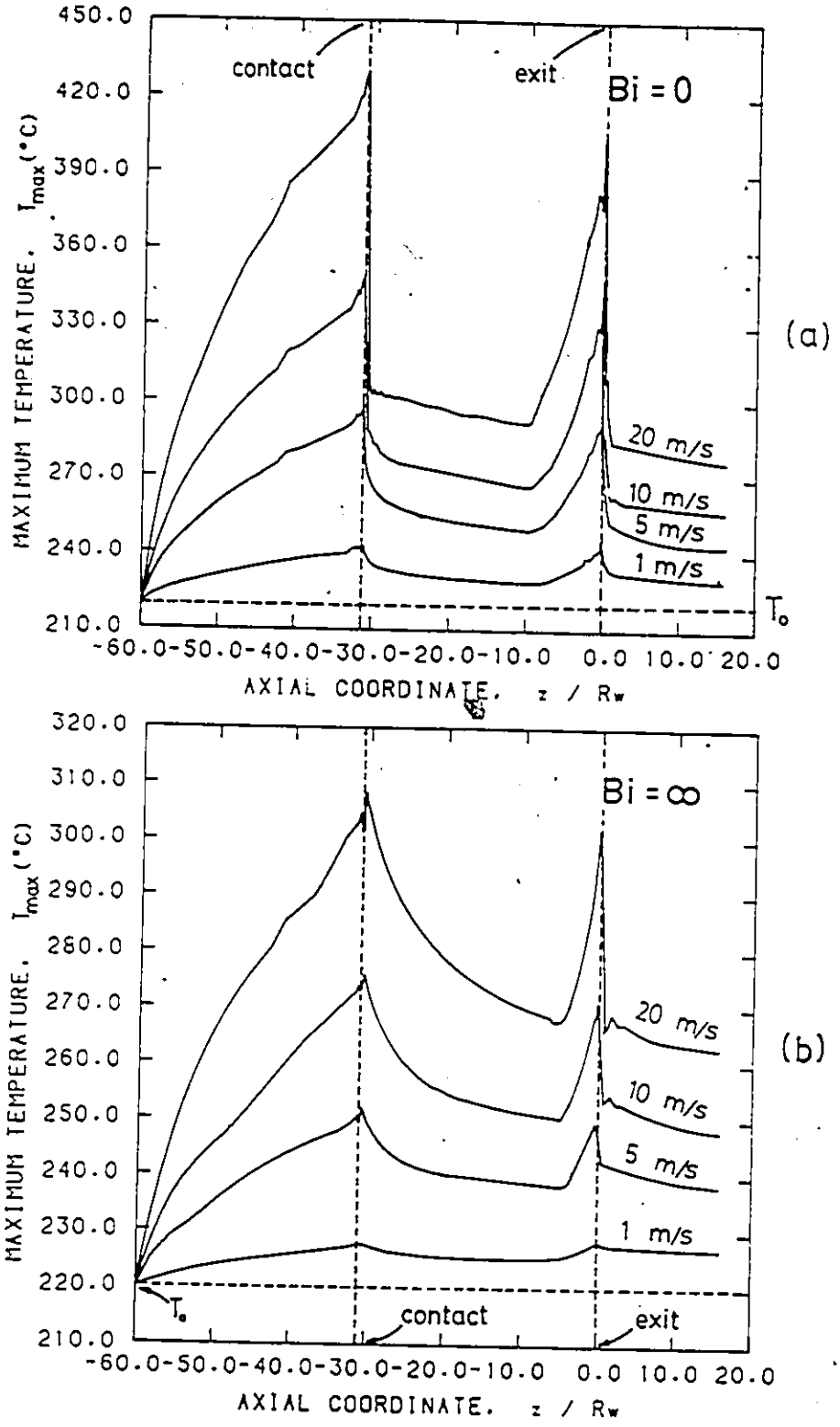

Figure 6.24: Maximum Temperature Distribution along Modified Du Pont's Die (Design B) for Different Wire Speeds (PS/HDPE, $(T_o)_o = (T_o)_i = 220°C$): (a) $Bi = 0$. (b) $Bi = \infty$.

these two conditions grows considerably.

The wire temperature rise for the adiabatic case is also included in Figure 6.25. Although the wire temperature rise is also a function of wire speed, the absolute rise is relatively insignificant as the maximum rise is less than $10°C$ from the inner inlet melt temperature $(T_o)_i$.

Two typical stress distributions for both the adiabatic and isothermal wall conditions are included in Figure 6.26. Along the wire surface, the latter condition tends to give more positive stresses before the contact region and when approaching the exit (approximately ten wire radii from the exit). In between these two regions, little differences are observed. Along the die wall, however, the stresses show discrepencies only when approaching the exit from approximately ten wire radii. In this case, the isothermal condition tends to give more negative stresses. The smooth die shear stresses also indicate that the flows are streamlined. This is indeed true as indicated in Figure 6.27.

The effects of entry melt temperatures are also investigated. Two different temperatures are used: 200 and $220°C$. The outer and inner layer temperatures are individually reduced to $200°C$ from the original $220°C$. The radial temperature profiles at the exit for these cases are plotted in

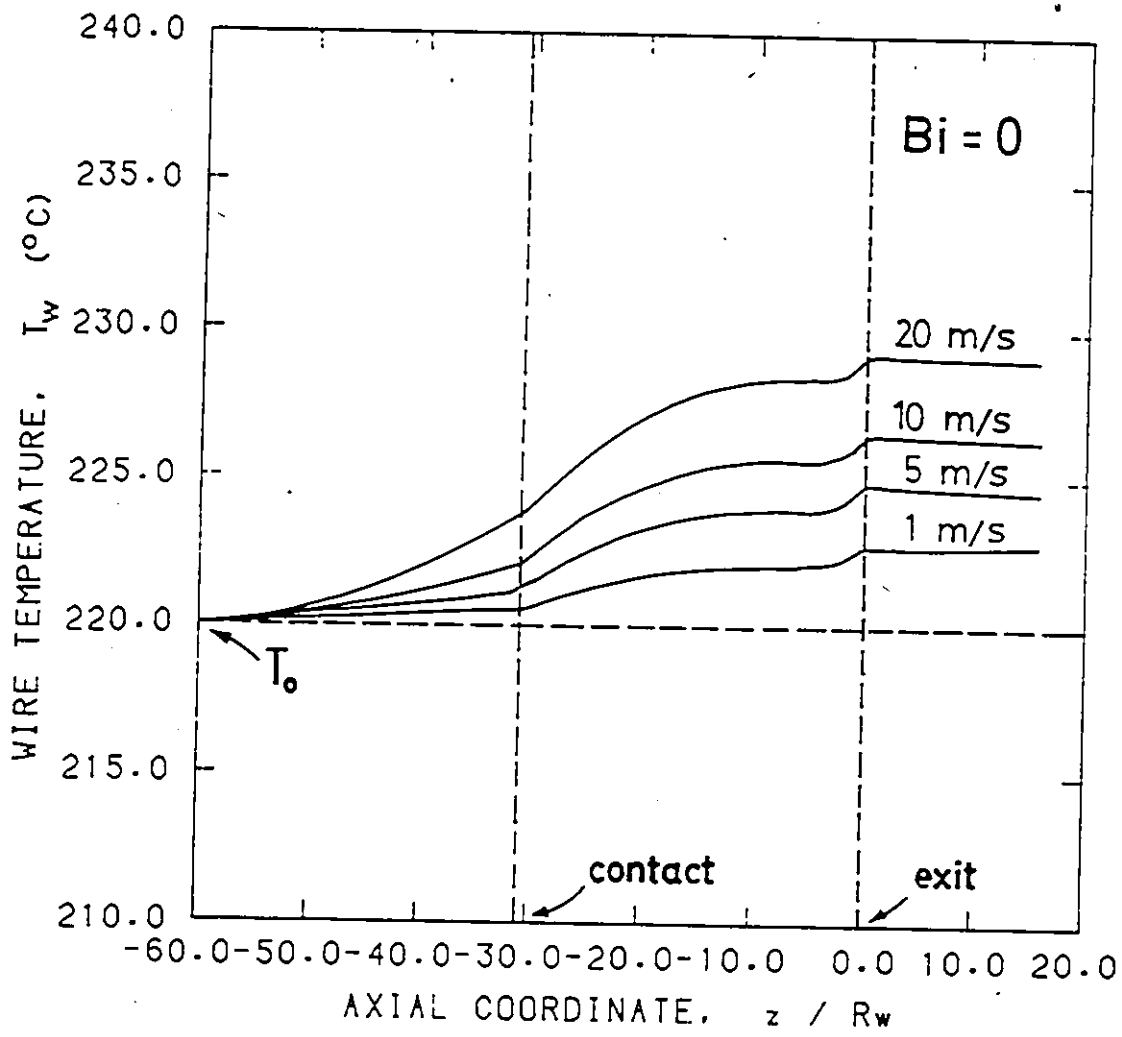

Figure 6.25: Wire Surface Temperature Distribution along Modified Du Pont's Die (Design B) for Different Wire Speeds (PS/HDPE, $(T_o)_o = (T_o)_i = 220°C$, $Bi = 0$).

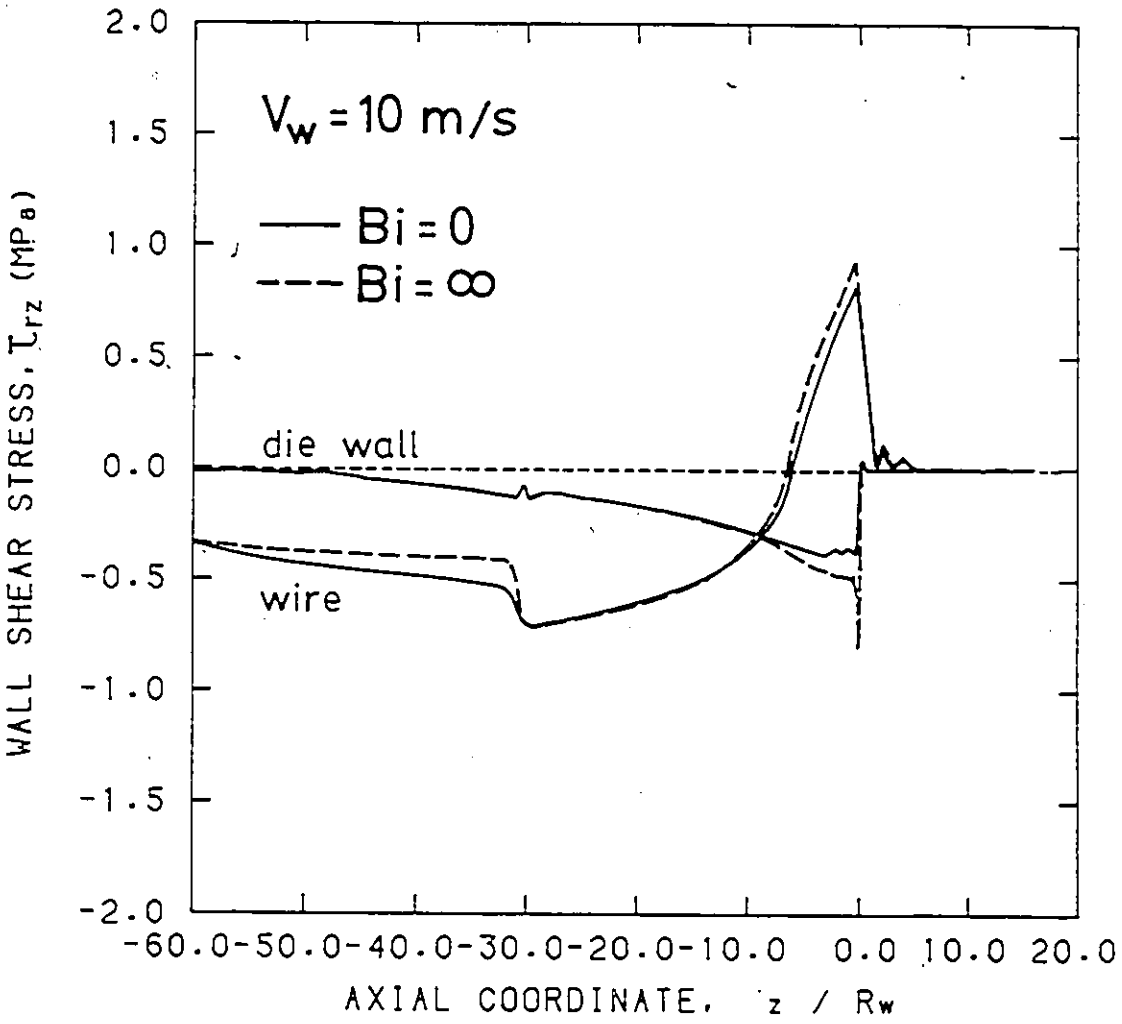

Figure 6.26: Shear Stress Distribution along the Torpedo/Wire and Die Wall in Modified Du Pont's Die (Design B) Assuming Different Thermal Boundary Conditions (PS/HDPE, $(T_o)_o = (T_o)_i = 220°C$, $V_w = 1000$ cm/s).

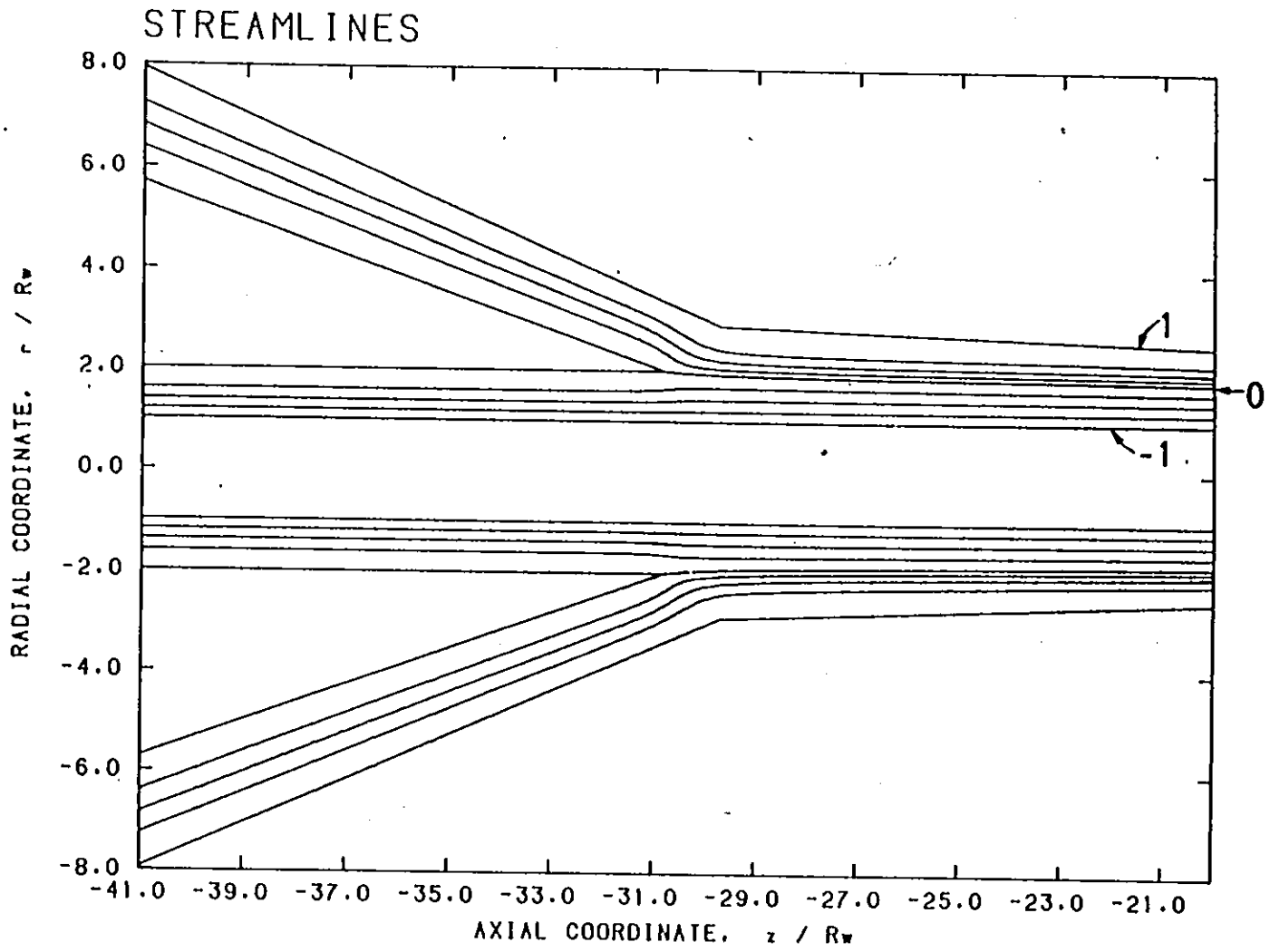

Figure 6.27: Typical Streamline Pattern Obtained from the Non-isothermal Analysis in Modified Du Pont's Die (Design B) (PS/HDPE, $(T_o)_o = (T_o)_i = 220°C$).

Figure 6.28. When the outer and inner entry temperatures are 220°C and 200°C, respectively (i.e. 220°C/200°C), the temperature profile for the inner layer shows considerable difference in temperature from the original case (220°C/220°C). However, the temperatures for the outer layer show little difference. For the 200°C/220°C case, the reverse is true. Although the temperatures are significantly different for the bulk of the outer layer, at a boundary layer very close to the wall, the temperatures are essentially the same. As a result, for the range of temperatures involved, the entry temperatures do not affect the die wall temperatures notably. Again, this fact is reflected in the same interface location obtained for all three cases.

A summary of the overall pressure drops is included in Table 6.3. As can be seen, the pressure drops are only affected when the entry temperature of the outer layer is changed. A drop of 20°C for the outer layer changes the outer and inner layer pressure drops by 22% and 4%, respectively.

6.5 Concluding Remarks

The isothermal analysis of PS and HDPE melts in modified Du Pont's die (Design A) has been carried out by LAT. It has been shown that the

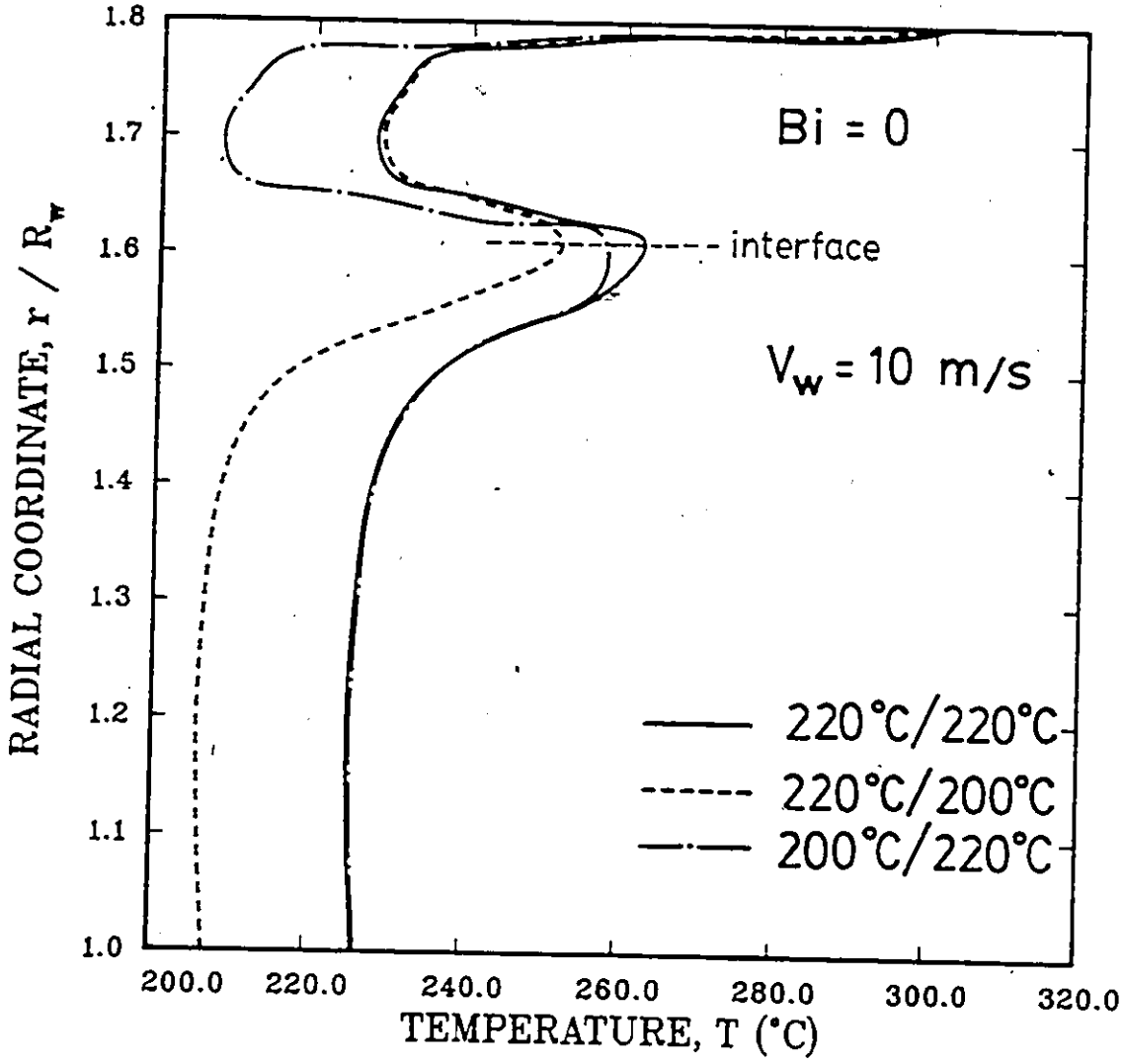

Figure 6.28: Radial Temperature Distribution at Modified Du Pont's (Design B) Die Exit ($z = 0$). Assuming Different Entry Melt Temperatures ($V_w = 1000\ cm/s$, $Bi = 0$).

Table 6.3: Overall Pressure Drop vs. Entry Melt Temperature Ratio for Modified Du Pont's Die (Design B) (PS/HDPE, $V_w = 1000\ cm/s$, $Bi = 0$).

$(T_o)_o/(T_o)_i$	$\Delta P\ (MPa)$	
	Inner Layer (HDPE)	Outer Layer (PS)
220/220	27.00	9.00
220/200	27.00	9.00
200/220	28.00	11.00

flowrate ratios do not significantly affect the various field variables of the outer layer. As a result, the recirculation present in this die cannot be successfully eliminated for the practical range of flowrates involved. On the other hand, the pressure and stress distributions in the annular region for the inner layer are significantly affected. The pressure distribution shows impractical operating conditions at certain flowrate ratios. FEM analysis on Newtonian fluids has shown that viscosity ratios can be used as a criterion to reduce the recirculation present in this die. However, elimination of the recirculation is not possible for the practical range of viscosity ratios. These analyses show that the manipulation of flowrate and viscosity ratios as a

means of eliminating recirculation is not very practical and, therefore, a new die design would have to be considered.

The nonisothermal analysis of Basu's die shows that the interface location is higher than would be from his analysis due to a rearrangement of the flow field right at the exit. In addition, the temperatures obtained are higher than his results, which is believed to be the main reason for a lower pressure drop. The difference in temperatures indicates that the radial convection term $v_r \partial T/\partial r$ should be included in the nonisothermal analysis, even when only straight channels are involved.

The nonisothermal analysis of modified Du Pont's die (Design B) indicates that the shape of the interface can be controlled by appropriate design of the location of the torpedo. In addition, streamlined flows can be obtained by modifying the overall die design to constrain the flow. The isothermal boundary condition yields pressure drops which are higher than the ones obtained from assuming adiabatic conditions due to a lower temperature reached in the neighborhood of the die wall. The temperature, and thus the pressure drop, was found to be a strong function of the wire speed. In addition, the interface location moves closer to the wall as the die wall temperature increases. For the range of the entry melt temperatures

considered, the die wall temperatures are not affected much. As a result, the field variables are not notably affected.

Chapter 7

Conclusions and Recommendations

A series of polymer melt flows in extrusion dies with axisymmetric geometries have been successfully analyzed by both the Lubrication Approximation Theory (LAT) and Finite Element Method (FEM). Newtonian and shear thinning (inelastic) fluids have been considered in this study under isothermal or nonisothermal conditions with or without free surfaces/interfaces. Computer programs based on the LAT and FEM for axisymmetric flows of single or dual layers have been developed. The LAT, being a less elaborate program, requires only little data preparation and

consumes relatively little computing resources to run. The FEM, on the other hand, requires elaborate data preparation and uses a tremendous amount of computer resources. Despite this, the flexibility and generality of FEM outweight its disadvantages.

A special numerical scheme called "Streamline-Upwind/Petrov-Galerkin Scheme" has been implemented in the FEM. Such scheme ensures the reliability of the solutions for highly convected flows. In addition, the more realistic heat balance boundary conditions have also been included in the program, and this allows the examination of various thermal boundary conditions. Furthermore, a special "double-node" technique has been implemented to handle the dual-layer flows.

Problems that have been solved include:

1. Isothermal flow through an orifice.

2. Isothermal flow through converging and diverging annular dies.

3. One-dimensional heat transfer without source term.

4. One-dimensional convective heat transfer with source term.

5. Wire coating.

6. Wire-coating coextrusion.

The following well-known inelastic fluid models were used:

1. Newtonian model.

2. Power-law model.

3. Quadratic model.

4. Full quadratic model incorporating temperature dependence.

A temperature-dependent viscosity has been included and the coupling of the momentum and energy equations has been dealt with a numerical iterative scheme. For the nonlinear problems, the relaxation method with a relaxation factor (λ) of 1.0 and 0.5 has been employed in FEM. The nonlinearity is present in: conservation equations ($\lambda = 1.0$), free surfaces ($\lambda = 1.0$ or 0.5) and interfaces ($\lambda = 0.5$). On the other hand, the nonlinearity in LAT has been handled by a full Newton-Raphson iterative scheme.

The isothermal flow through an orifice was solved for the Newtonian model. The results for a special case, an infinite capillary, showed excellent agreement with other solutions from the literature. New results for a

variable die length showed the discrepancy between Newtonian and non-Newtonian viscoelastic fluids.

Extrudate swell values were obtained for the isothermal flow of Newtonian fluids through converging and diverging annular extrusion dies. The shapes of the free surfaces showed the dependence on the diameter ratio and taper angle of the dies. For diverging dies a thickness contraction occurs for angles greater than 30°, while the diameter swell increases rapidly. For converging dies the design is limited to angles that do not allow contact of the inner free surfaces. The results showed that the diameter swell is highest for the diverging, followed by the straight and then the converging dies.

The one-dimensional heat transfer with or without source term was analyzed to examine the accuracy of several upwinding schemes. The results showed that only the Streamline-Upwind/Petrov-Galerkin scheme on bilinear quadrilateral elements produced an excellent agreement with the analytical solutions, thus, indicating the necessity to use this scheme in highly convected flows.

Several wire-coating extrusion dies were analyzed. Two die designs used by Du Pont Co. and a design by Endo (1976) were examined. Although

LAT gave reasonable results for isothermal flows, the actual wire-coating process proved to be highly nonisothermal. The inclusion of the radial convection term in the energy conservation equation was necessary. In addition, the use of the upwinding scheme was essential in order to obtain reliable solutions. The temperature field was found to be a strong function of thermal boundary conditions. Comparisons with experimental results showed that the heat balance boundary condition was a more realistic one between the extreme cases of adiabatic and isothermal walls. On the other hand, the isothermal wall boundary condition always overestimates the overall pressure drop, thus making it a proper choice for designing purposes. The flow characteristics were very much dependent on the die design. A more constrained design was found to give more streamlined flows and thus smoother stress distributions. Comparison with experimental findings suggested that a more streamlined flow is responsible for a smoother coating surface.

Wire-coating coextrusion dies for two-layer flows were also examined. Several die designs were analyzed, one given by Basu (1981) and also modifications of Du Pont's die to account for the presence of two fluids. The isothermal analysis of the modified Du Pont's die (Design A) using LAT

and FEM showed that recirculation existed and could not be practically suppressed by means of changing flowrate and viscosity ratios. However, it was apparent that the amount of fluid recirculating decreased as the flowrate or viscosity ratios was increased. Again, the analysis of Basu's die showed that the inclusion of the upwinding scheme in solving the equations was necessary. To meet successfully certain operating conditions and criteria, the modified Du Pont's die was redesigned (Design B) to give a flat interfacial configuration and smooth die shear stress. The die thus designed successfully met the criterion of a streamlined flow for all operating conditions under investigation. The analysis then showed that die wall temperatures increased as the wire speed was increased. This effect was more pronounced in the case of adiabatic conditions than isothermal wall conditions. In addition, the die wall temperature brought the interfaces closer to the die as it increased with wire speed. However, the major factor in determining the location of the interfaces has been the flowrate ratio which is a function of the entry melt temperature and the operating requirements. For the range of entry melt temperatures considered, the overall results did not vary much except for the temperature field. The examination of different temperatures indicated that the field variables were

mainly affected by the flow behaviour of the outer layer.

The numerical simulation has proven to be a powerful tool in understanding the complex polymer flows through extrusion dies. Such understanding can lead to effective design of various dies, as shown in the case of wire coating. For an even better modelling of such flows, however, further considerations will have to be undertaken. Some recommendations for further work in the field include:

A. From the numerical point of view:

A1. Using in the FEM the False Position or the Newton-Raphson iterative scheme rather than the Picard successive substitution so that faster convergence can be achieved for non-linear problems, as it was done with the LAT.

A2. Modifying the finite element formulation from u-w-p into u-w-p-T-h, thus solving simultaneously for temperatures T and the location of free surfaces/interfaces h along with the velocities u and w and pressure p. This will enable faster and easier processing of the program as well as handling of cases with complex free surfaces/interfaces.

A3. Extending the present studies to planar geometries, such as sheet and film extrusion, coating coextrusion, etc.

A4. Developing a scheme to accomodate viscoelastic constitutive equations on top of the purely viscous (inelastic) ones used in this work; such a scheme should be capable of keeping track of the strain history present in the viscoelastic integral constitutive equations.

B. From the rheological point of view:

B1. Including viscoelastic properties of polymer melts, such as normal stresses and elongational viscosity along with the shear viscosity. In this case, an appropriate viscoelastic constitutive equation would have to be implemented.

B2. Considering such complications as melt compressibility at high pressures and slip at the die wall at high shear rates.

B3. Performing studies on a variety of polymer melts used in coextrusion of multi-layered products.

There is also the need for more reliable data on shear viscosity, elongational viscosity and normal stresses for a wide range of shear rates to

better characterize the polymer melts. In addition, more experimental data on various extrusion processes are required to compare with results from numerical simulations, especially in the field of coextrusion.

Bibliography

[1] Acierno, D., Dalton, J.N., Rodriguez, J.M., White, J.L., "Rheological and Heat Transfer Aspects of the Melt Spinning of Monofilament Fibers of Polyethylene and Polystyrene", *J. Appl. Polym. Sci.*, **15**, 2395-2415 (1971).

[2] Agur, E.E., Vlachopoulos, J., "Numerical Simulation of a Single-Screw Plasticating Extruder", *Polym. Eng. Sci.*, **22**, 1084-1094 (1982).

[3] Allan, W., "Newtonian Die Swell Evaluation for Axisymmetric Tube Exits Using a Finite Element Method", *Int. J. Num. Meth. Eng.*, **11**, 1621-1632 (1977).

[4] Bagley, E.B., Storey, S.H., "Shear Rates and Velocities of Flow of Polymers in Wire Covering Dies", *Wire Wire Prod.*, **38**, 1104-1110 (1963).

[5] Basu, S., "A Theoretical Analysis of Non-Isothermal Flow in Wire-Coating Co-Extrusion Dies", *Polym. Eng. Sci.*, **21**, 1128-1138 (1981).

[6] Ben-Sabar, E., Caswell, B., "A Stable Finite Element Simulation of Convective Transport", *Int. J. Num. Meth. Eng.*, **14**, 545-565 (1979).

[7] Bird, R.B., Armstrong, R.C., Hassager, O., *Dynamics of Polymeric Liquids*, Vol. 1, Wiley, New York (1977).

[8] Bird, R.B., Stewart, W.E., Lightfoot, E.N., *Transport Phenomena*, Wiley, New York (1960).

[9] Brooks, A.N., Hughes, T.J.R., "Streamline Upwind/Petrov-Galerkin Formulations for Convection Dominated Flows with Particular Em-

phasis on the Incompressible Navier-Stokes Equations", *Comp. Meth. Appl. Mech. Eng.*, **32**, 199-259 (1982).

[10] Bush, M.B., Tanner, R.I., "Numerical Solution of Viscous Flows Using Integral Equation Methods", *Int. J. Num. Meth. Fluids*, **3**, 71-92 (1983).

[11] Carley, J.F., In *Processing of Thermoplastic Materials: chap. 4*, ed. E.C. Bernhardt, Reinhold, New York (1959).

[12] Carley, J.F., Endo, T., Krantz, W.B., "Realistic Analysis of Flow in Wire-Coating Dies", *Polym. Eng. Sci.*, **19**, 1178-1187 (1979).

[13] Caswell, B., Tanner, R.I., "Wirecoating Die Design Using Finite Element Methods", *Polym. Eng. Sci.*, **18**, 416-421 (1978).

[14] Chang, P-W., Patten, T.W., Finlayson, B.A., "Collocation and Galerkin Finite Element Methods for Viscoelastic Fluid Flow-II", *Comput. Fluids*, **7**, 285-293 (1979).

[15] Chin, H.B., Kim, Y.J., Han, C.D., "A Study on Non-Isothermal Flat-Film Coextrusion", *Polym. Eng. Rev.*, 4, 281-311 (1984).

[16] Crochet, M.J., Bezy, M., "Elastic Effects in Die Entry Flow", In *Rheology, Vol. 2: Fluids*, ed. G. Astarita, G. Marrucci, L. Nicolais, pp. 53-58, New York (1980).

[17] Crochet, M.J., Davies, A.R., Walters, K., *Numerical Simulation of Non-Newtonian Flow*, Elsevier, Amsterdam (1984).

[18] Crochet, M.J., Keunings, R., "Die Swell of a Maxwell Fluid: Numerical Prediction", *J. Non-Newtonian Fluid Mech.*, **7**, 199-212 (1980).

[19] Crochet, M.J., Keunings, R., "Numerical Simulation of Die Swell: Geometrical Effects", *Proc. 2nd World Congr. Chem. Eng.*, Montreal, **6**, 285-295 (1981).

[20] Crochet, M.J., Keunings, R., "Finite Element Analysis of Die Swell of a Highly Elastic Fluid", *J. Non-Newtonian Fluid Mech.*, **10**, 339-356 (1982a).

[21] Crochet, M.J., Keunings, R., "On Numerical Die Swell Calculation", *J. Non-Newtonian Fluid Mech.*, **10**, 85-94 (1982b).

[22] Crochet, M.J., Keunings, R., "Numerical Simulation of Viscoelastic Flow in Some Polymer Processing Applications", *Numerical Analysis of Forming Processes*, ed. Zienkiewicz et al., Wiley (1983).

[23] Crochet, M.J., Walters, K., "Numerical Methods in Non-Newtonian Fluid Mechanics", *Ann. Rev. Fluid Mech.*, **15**, 241-260 (1983).

[24] Everage, A.E., "Theory of Stratified Bicomponent Flow of Polymer Melts", *Trans. Soc. Rheol.*, **17**, 629-646 (1973).

[25] Everage, A.E., "Theory of Stratified Bicomponent Flow of Polymer Melts. II. Interface Motion in Transient Flow", *Trans. Soc. Rheol.*, **19**, 509-522 (1975)

[26] Fenner, R.T., *Extruder Screw Design*, Iliffe, London (1970).

[27] Fenner, R.T., Williams, J.G., "Analytical Methods of Wire-Coating Die Design", *Trans. J. Plast. Inst.*, **35**, 701-706 (1967).

[28] Haas, K.U., E.I. DuPont de Nemours & Co., Inc., Victoria, TX, private communication, 1986.

[29] Haas, K.U., Skewis, F.H., "The Wire Coating Process: Die Design and Polymer Flow Characteristics", *SPE 32nd ANTEC*, Tech. Papers, **20**, 8-12 (1974).

[30] Han, C.D., "A Study of Coextrusion in a Circular Die", *J. Appl. Polym. Sci.*, **19**, 1875-1883 (1975).

[31] Han, C.D., Rao, D., "Studies on Wire Coating Extrusion. I. The Rheology of Wire Coating Extrusion", *Polym. Eng. Sci.*, **18**, 1019-1029 (1978).

[32] Han, C.D., Rao, D., "Studies on Wire Coating Extrusion. II. The Rheology of Wire Coating Coextrusion", *Polym. Eng. Sci.*, **20**, 128-139 (1980).

[33] Han, C.D., Shetty, R., "Studies on Multilayer Film Coextrusion I. The Rheology of Flat Film Coextrusion", *Polym. Eng. Sci.*, 16, 697-703 (1976).

[34] Han, C.D., Shetty, R., "Studies on Multilayer Film Coextrusion II. Interfacial Instability in Flat Film Coextrusion", *Polym. Eng. Sci.*, 18, 180-186 (1978).

[35] Heng, F.L., "Wire-Coating Analysis Using the Lubrication Approximation", *Internal Report*, Dept. Chem. Eng., Univ. of Ottawa, Ottawa, ON, Canada (1986).

[36] Holman, J.P., *Heat Transfer*, McGraw-Hill, New York (1981).

[37] Huebner, K.H., Thornton, E.A., *The Finite Element Method for Engineers*, Wiley, New York (1982).

[38] Hughes, T.J.R., Brooks, A., "A Multi-Dimensional Upwind Scheme with No Crosswind Diffusion", *Proceedings of a Symposium on FEM for Convection Dominated Flows*, ASME Winter Annual Meeting, New York, 19-35 (1979).

[39] Hughes, T.J.R., Brooks, A., "A Theoretical Framework for Petrov-Galerkin Methods with Discontinuous Weighting Functions: Application to the Streamline-Upwind Procedure", In *Finite Elements in Fluids, Vol. 4: Chap. 3*, ed. R.H. Gallagher, D.H. Norrie, J.T. Oden, Zienkiewicz, O.C., pp. 47-65, New York (1982).

[40] Karagiannis, A., Mavridis, H., Hrymak, A.N., Vlachopoulos, J., "Interface Determination in Multilayer Extrusion", *SPE 45th ANTEC*, Tech. Papers, 45, 106-108 (1987).

[41] Khan, A.A., Han, C.D., "On the Interface Deformation in the Stratified Two-Phase Flow of Viscoelastic Fluids", *Trans. Soc. Rheol.*, 20, 595-621 (1976).

[42] Khan, A.A., Han, C.D., "A Study on the Interfacial Instability in the Stratified Flow of Two Viscoelastic Fluids through a Rectangular Duct", *Trans. Soc. Rheol.*, 21, 101-131 (1977).

[43] Kim, Y.J., Han; C.D., "A Study on Sandwich Flat-Film Coextrusion", *Polym. Eng. Rev.*, 2, 339-361 (1983).

[44] Lee, B.L., White, J.L., "An Experimental Study of Rheological Properties of Polymer Melts in Laminar Shear Flow and of Interface Deformation and Its Mechanisms in Two-Phase Stratified Flow", *Trans. Soc. Rheol.*, 18, 467-492 (1974).

[45] Leonard, B.P., "A Survey of Finite Differences of Opinion on Numerical Muddling of the Incomprehensible Defective Confusion Equation", In *AMD Vol. 34 : Finite Element Methods for Convection Dominated Flows*, ed. T.J.R. Hughes, New York (1979).

[46] MacLean, D.L., "A Theoretical Analysis of Bicomponent Flow and the Problem of Interface Shape", *Trans. Soc. Rheol.*, 17, 385-399 (1973).

[47] Maron, M.J., *Numerical Analysis—A Practical Approach*, Macmillan, New York (1982).

[48] Martin, H.C., Carey, G.F., *Introduction to Finite Element Analysis*, McGraw-Hill, New York (1973).

[49] Mavridis, H., Hrymak, A.N., Vlachopoulos, J., "Finite-Element Simulation of Stratified Multiphase Flows", *AIChE J.*, 33, 410-422 (1987).

[50] McKelvey, J.M., *Polymer Processing*, Wiley, New York (1962).

[51] Meissner, J., "Deformationsverhalten der Kunststoffe im Flüssigen und im festen Zustand", *Kunststoffe*, 61, 576-582 (1971).

[52] Middleman, S., *Fundamentals of Polymer Processing*, McGraw-Hill, New York (1977).

[53] Middleman, S., Gavis, J., "Expansion and Contraction of Capillary Jets of Newtonian Liquids", *Phys. Fluids*, 4, 355-365 (1961).

[54] Minagawa, N., White, J.L., "Co-Extrusion of Unfilled and TiO_2-Filled Polyethylene: Influence of Viscosity and Die Cross-Section on Interface Shape", *Polym. Eng. Sci.*, 15, 825-830 (1975).

[55] Mitsoulis, E., *Finite Element Analysis of Two-Dimensional Polymer Melt Flows*, Ph.D. Thesis, McMaster Univ. (1984).

[56] Mitsoulis, E., "Extrudate Swell in Double-Layer Flows", *J. Rheol.*, **30(S)**, S23-S44 (1986a).

[57] Mitsoulis, E., "Extrudate Swell of Newtonian Fluids from Annular Dies", *AIChE J.*, **32**, 497-500 (1986b).

[58] Mitsoulis, E., "Finite Element Analysis of Wire Coating", *Polym. Eng. Sci.*, **26**, 171-186 (1986c).

[59] Mitsoulis, E., "Fluid Flow and Heat Transfer in Wire Coating: A Review", *Adv. Polym. Tech.*, **6**, 467-487 (1986d).

[60] Mitsoulis, E., "The Numerical Simulation of Boger Fluids: A Viscometric Approximation Approach", *Polym. Eng. Sci.*, **26**, 1552-1562 (1986e).

[61] Mitsoulis, E., Heng, F.L., "Numerical Simulation of Coextrusion from a Circular Die", *J. Appl. Polym. Sci.*, **34**, 1713-1725 (1987).

[62] Mitsoulis, E., Vlachopoulos, J., "Non-Isothermal Creeping Flow through Parallel Plates and a Sudden Planar Contraction", *Can. J. Chem. Eng.*, **62**, 837-844 (1984a).

[63] Mitsoulis, E., Vlachopoulos, J., "The Finite Element Method for Flow and Heat Transfer Analysis", *Adv. Polym. Tech.*, **4**, 107-121 (1984b).

[64] Mitsoulis, E., Vlachopoulos, J., Mirza, F.A., "Simulation of Extrudate Swell from Long Slit and Capillary Dies", *Polym. Proc. Eng.*, **2**, 153-177 (1984).

[65] Mizukami, A., "An Implementation of the Streamline-Upwind/Petrov-Galerkin Method for Linear Triangular Elements" *Comp. Meth. Appl. Mech. Eng.*, **49**, 357-364 (1985).

[66] Nguyen, H., Boger, D.V., "The Kinematics and Stability of Die Entry Flows", *J. Non-Newtonian Fluid Mech.*, **5**, 353-368 (1979).

[67] Nickell, R.E., Tanner, R.I., Caswell, B., "The Solution of Viscous Incompressible Jet and Free-Surface Flows Using Finite-Element Methods", *J. Fluid Mech.*, 65, 189-206 (1974).

[68] Omodei, B.J., "Computer Solutions of a Plane Newtonian Jet with Surface Tension", *Comput. Fluids*, 7, 79-96 (1979).

[69] Omodei, B.J., "On the Die-Swell of an Axisymmetric Newtonian Jet", *Comput. Fluids*, 8, 275-289 (1980).

[70] Orbey, N., Dealy, J.M., "Isothermal Swell of Extrudate from Annular Dies; Effects of Die Geometry, Flow Rate, and Resin Characteristics", *Polym. Eng. Sci.*, 24, 511-518 (1984).

[71] Pearson, J.R.A., *Mechanics of Polymer Processing*, Elsevier, New York (1985).

[72] Perry, R.H., Green, D., *Perry's Chemical Engineers Handbook*, McGraw-Hill, Singapore (1984).

[73] Phuoc, H.B., Tanner, R.I., "Thermally-Induced Extrudate Swell", *J. Fluid Mech.*, 98, 253-260 (1980).

[74] Pittman, J.F.T., Rashid, K., "Numerical Analysis of High-Speed Wire-Coating", *Plast. Rubber Proc. Appl.*, 6, 153-159 (1986).

[75] Rao, D.A., *A Study of Wire Coating Extrusion*, Ph.D. Thesis, Polytechnic Institute of New York (1979).

[76] Roache, P.J., *Computational Fluid Dynamics*, Hermosa Publishers, Albuquerque, NM (1976).

[77] Schrenk, W.J., Bradley, N.L., Alfrey, T., Maack, H., "Interfacial Flow Instability in Multilayer Coextrusion", *Polym. Eng. Sci.*, 18, 620-623 (1978).

[78] Sornberger, G., Vergnes, B., Agassant, J.F., "Coextrusion Flow of Two Molten Polymers Between Parallel Plates: Non-Isothermal Computation and Experimental Study", *Polym. Eng. Sci.*, 26, 682-689 (1986).

[79] Sornberger, G., Vergnes, B., Agassant, J.F., "Two Directional Coextrusion Flow of Two Molten Polymers in Flat Dies", *Polym. Eng. Sci.*, **26**, 455-461 (1986).

[80] Southern, J.H., Ballman, R.L., "Stratified Bicomponent Flow of Polymer Melts in a Tube", *Appl. Polym. Symp.*, **20**, 175-189 (1973).

[81] Southern, J.H., Ballman, R.L., "Additional Observations on Stratified Bicomponent Flow of Polymer Melts in a Tube", *J. Polym. Sci.*, **13**, 863-869 (1975).

[82] Tadmor, Z., Gogos, C.G., *Principles of Polymer Processing*, Wiley, New York (1979).

[83] Tanner, R.I., "Die-Swell Reconsidered: Some Numerical Solutions Using a Finite Element Program", *Appl. Polym. Symp.*, **20**, 201-208 (1973).

[84] Tanner, R.I., "Finite Element and Boundary Element Methods in Polymer Processing Operations", *Proceedings of the 4th International Symposium on Finite Elements in Fluids*, Tokyo, 355-361 (1982).

[85] Tanner, R.I., "Computer Simulation of LDPE Extrusion", *SPE 45th ANTEC*, Tech. Papers, **45**, 103-105 (1987).

[86] Taylor, C., Hood, P., "A Numerical Solution of the Navier-Stokes Equations Using the Finite Element Technique", *Comput. Fluids*, **1**, 1-10 (1973).

[87] Tzoganakis, C., Dept. Chem. Eng., McMaster Univ., Hamilton, ON, private communication, 1986.

[88] Uhland, E., "Stratified Two-Phase Flow of Molten Polymers in Circular Dies", *Polym. Eng. Sci.*, **17**, 671-681 (1977).

[89] Viriyayuthakorn, M., Caswell, B., "Finite Element Simulation of Viscoelastic Flow", *J. Non-Newtonian Fluid Mech.*, **6**, 245-267 (1980).

[90] Vlachopoulos, J., "Should You Use Finite Difference or Finite Element Methods for Polymer Flow Problems ?", *SPE 35th ANTEC*, Montreal, Tech. Papers Vol. 23, 519-520 (1977).

[91] Vlachopoulos, J., "Extrudate Swell in Polymers", *Rev. Def. Beh. Mat.*, **3**, 219-248 (1981).

[92] Vlachopoulos, J., Alam, M., "Critical Stress and Recoverable Shear for Polymer Melt Fracture", *Polym. Eng. Sci.*, **12**, 184-192 (1972).

[93] Wagner, R.E., *Finite Element Analysis of Wire Coating*, M.A.Sc. Thesis, Univ. of Ottawa (1987).

[94] Wagner, R., Mitsoulis, E., "Effect of Die Design on the Analysis of Wire Coating", *Adv. Polym. Tech.*, **5**, 305-325 (1985).

[95] White, J.L., Lee, B.L., "Theory of Interface Distortion in Stratified Two-Phase Flow", *Trans. Soc. Rheol.*, **19**, 457-479 (1975).

[96] Winter, H.H., "Viscous Dissipation in Shear Flows of Molten Polymers", *Adv. Heat Trans.*, **13**, 205-267 (1977).

[97] Winter, H.H., "Thermal Capacitance and Cooling Length in the Wire Coating Process", *SPE 36th ANTEC*, Tech. Papers, **24**, 462-465 (1978).

APPENDIX A

Streamline-Upwind/Petrov-Galerkin Scheme

This appendix presents in detail the formulation of the Streamline-Upwind/ Petrov-Galerkin (SU/PG) scheme for two-dimensional bilinear isoparametric Lagrangian quadrilaterals.

The SU/PG scheme involves changing the weighting functions $W_i = N_i$ for the convection and the heat of dissipation terms in Equation 3.42 to other appropriate weighting functions $W_i \neq N_i$ that take into account the streamlined flow and achieve the suppression of oscillations in the temperature solution.

Referring to Figure A.1, the weighting function is evaluated at the Gaussian integration points (A, B, C and D). At each Gaussian point, the new weighting function W_i is given by (Hughes and Brooks, 1979);

$$W_i = N_i + \tilde{k}\frac{\hat{v}_r}{|\overline{v}|}\frac{\partial N_i}{\partial r} + \tilde{k}\frac{\hat{v}_z}{|\overline{v}|}\frac{\partial N_i}{\partial z} \tag{A.1}$$

where

$$\hat{v}_r = \frac{v_r}{|\overline{v}|}, \qquad \hat{v}_z = \frac{v_z}{|\overline{v}|} \tag{A.2}$$

$$|\overline{v}|^2 = v_r^2 + v_z^2 \tag{A.3}$$

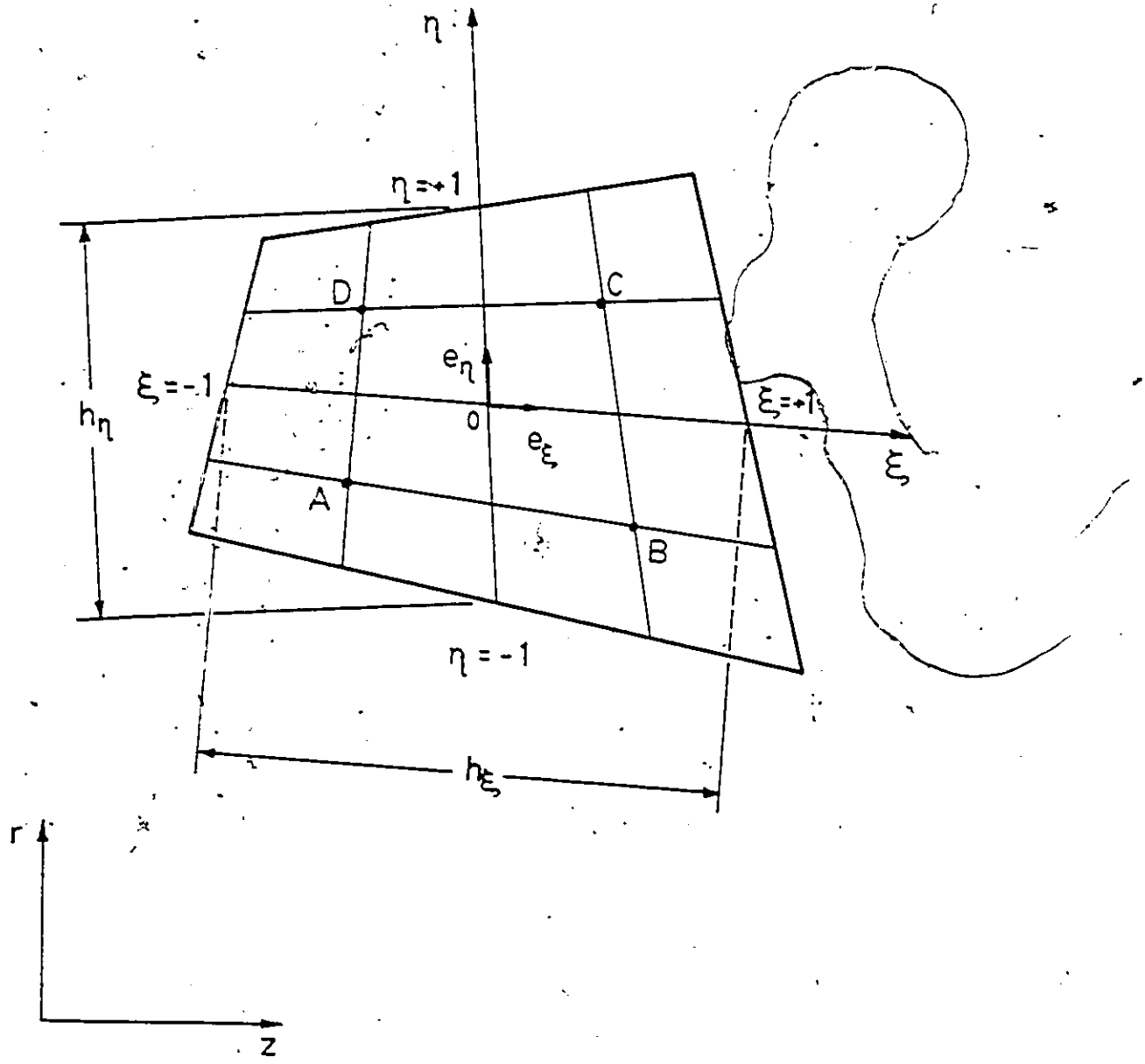

Figure A.1: Typical Four-Node Quadrilateral Finite Element Geometry.

$$\tilde{k} = \left(\tilde{\xi} u_\xi h_\xi + \tilde{\eta} u_\eta h_\eta\right)/2 \tag{A.4}$$

$$\tilde{\xi} = \coth \alpha_\xi - \frac{1}{\alpha_\xi} \quad , \quad \tilde{\eta} = \coth \alpha_\eta - \frac{1}{\alpha_\eta} \tag{A.5}$$

$$\alpha_\xi = u_\xi h_\xi/(2k) \quad , \quad \alpha_\eta = u_\eta h_\eta/(2k) \tag{A.6}$$

$$u_\xi = \overline{e}_\xi \cdot \overline{v} \quad , \quad u_\eta = \overline{e}_\eta \cdot \overline{v} \tag{A.7}$$

where the unit vectors, $\overline{e}_\xi$ and $\overline{e}_\eta$, and element lengths h_ξ and h_η, are defined as shown in Figure A.1; $\tilde{k}$ is a scalar artificial diffusivity; $\hat{v}_r$, $\hat{v}_z$ and $|\overline{v}|$ are as defined above; k is the thermal conductivity of the fluid. The interpolation functions N_i are as defined in Equation 3.45, and their derivatives are obtained by using Equation 3.46.

APPENDIX B

Derivation of Heat-Balance Boundary Conditions

This appendix presents the derivation of heat-balance boundary conditions at the die wall and at the wire surface.

B.1 Die Wall

Figure B.1 shows a schematic diagram of a tapered channel. If the channel is considered locally straight, the tapered solid boundary can be represented by a series of discontinuous straight sections as shown by the dotted lines. If the inner and outer wall temperatures are held constant at T and T_s, respectively, it may be assumed that the heat flows only in the radial direction and Fourier's law of heat conduction applies (Holman, 1981):

$$\dot{q} = -k_w A \frac{dT}{dr} = -2\pi k_w \Delta x r \frac{dT}{dr} \qquad \text{(B.1)}$$

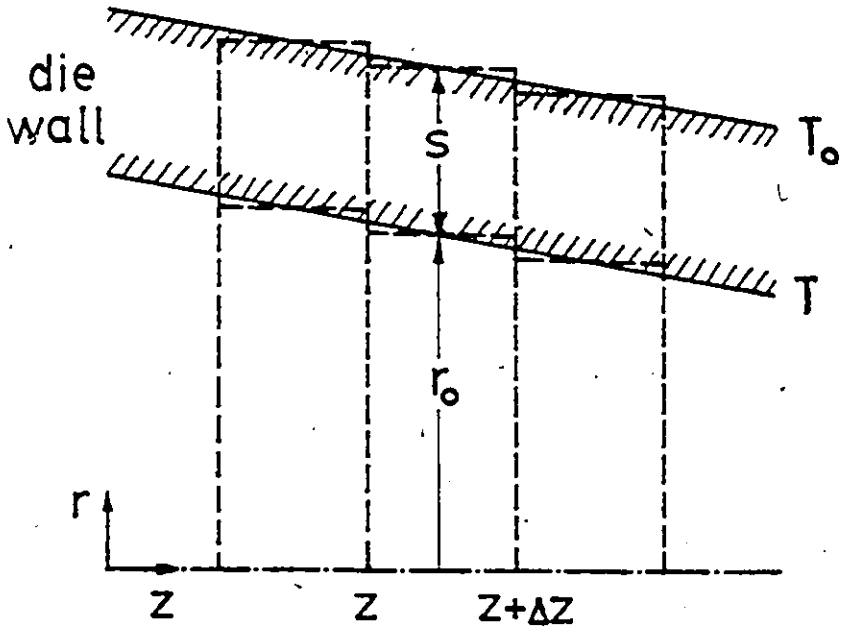

Figure B.1: Schematic Diagram of a Tapered Channel.

with the boundary conditions:

$$\begin{aligned} T &= T \quad \text{at} \quad r = r_o \\ T &= T_s \quad \text{at} \quad r = r_o + s \end{aligned} \tag{B.2}$$

where $\dot{q}$ is the constant rate of heat flowing through the cylinder, k_w is the thermal conductivity of the wall, A is the surface area that the heat flows through, Δz is the length of the cylinder, s is the thickness of the cylinder, and r_o is the inner radius of the cylinder. Rearranging Equation B.1 yields:

$$\frac{1}{2\pi k_w \Delta z}\frac{dr}{r} = -\frac{dT}{\dot{q}} \tag{B.3}$$

Integrating Equation B.3 subjected to boundary conditions yields:

$$\frac{1}{2\pi k_w \Delta z}\ln\left(\frac{r_o + s}{r_o}\right) = \frac{1}{\dot{q}}(T - T_s) \tag{B.4}$$

where k_w is assumed constant. Rearranging Equation B.4 yields:

$$\dot{q} = \frac{2\pi k_w \Delta z}{\ln(1 + s/r_o)}(T - T_s) \tag{B.5}$$

The heat flux at the inner wall can be obtained by dividing Equation B.5 by $A = 2\pi r_o \Delta z$. As a result, the heat flux at the inner wall is:

$$\overline{q} = \frac{k_w}{r_o \ln(1 + s/r_o)}(T - T_s) \tag{B.6}$$

For inner wall temperature which is not constant, $T|_z \neq T|_{z+\Delta z} \neq T$, Equation B.6 is not applicable. However, if Δz is small enough such that

$T|_z \approx T|_{z+\Delta z} \approx T$, Equation B.6 can be used as an approximation for the heat flux at the die wall.

B.2 Wire

Figure B.2 shows a schematic diagram of a moving annulus (wire) surrounded by a polymer melt. The time required for heat conduction in the metal is very much smaller than the time required for heat conduction in the polymer melt, as evidenced by the following ratio (Winter, 1977, 1978):

$$\frac{R_w^2}{k_w/\rho_w C_{pw}} \Big/ \frac{h^2}{k/\rho C_p} \ll 1 \tag{B.7}$$

As a result, the temperature of the wire is practically uniform in each cross-section. The transport properties with and without the subscript w are for the wire and melt, respectively; R_w is the wire radius; h is defined in Figure B.2. In addition, the Peclet number for the wire is:

$$Pe = \frac{\rho_w C_{pw} V_w R_w}{k_w} \gg 1 \tag{B.8}$$

where V_w is the wire speed. Therefore, the only component which is significant in the energy equation (2.20) is the axial convection component. The

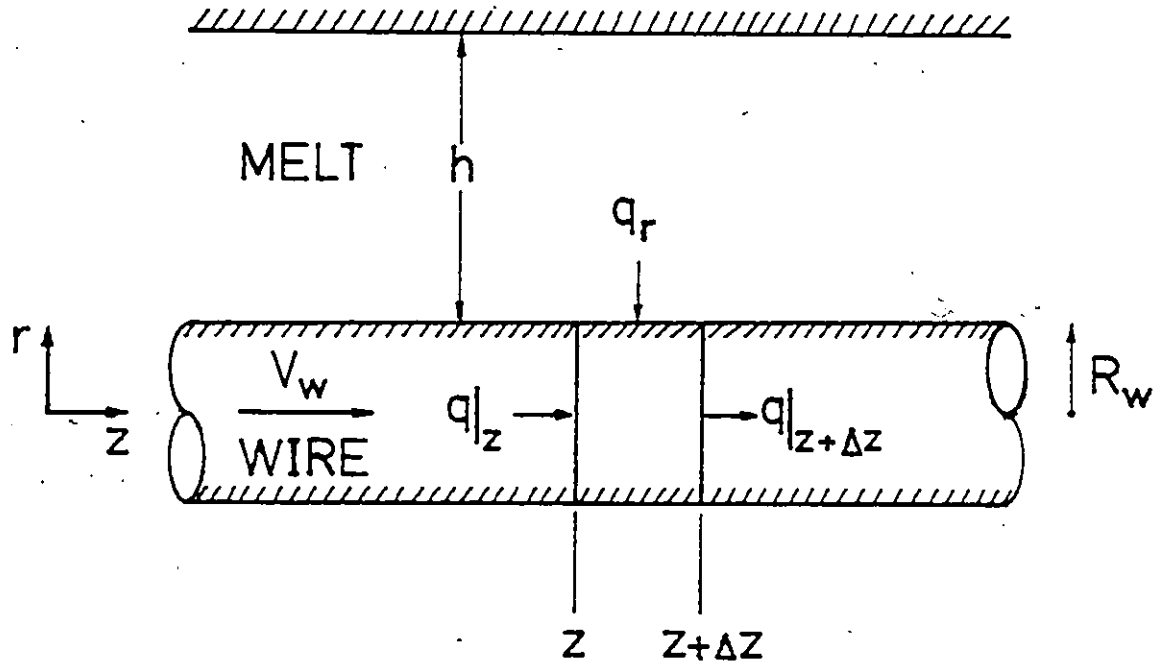

Figure B.2: Schematic Diagram of a Moving Annulus (Wire).

heat balance on the shell indicated in Figure B.2 gives:

$$\text{heat rate in} = \text{heat rate out} \tag{B.9}$$

or

$$q_r \cdot (\text{surface area}) = (q|_{z+\Delta z} - q|_z) \cdot (\text{cross sectional area}) \tag{B.10}$$

or

$$q_r \cdot 2\pi R_w \Delta z = \pi R_w^2 \left(\rho_w C_{pw} V_w \, T|_{z+\Delta z} - \rho_w C_{pw} V_w \, T|_z\right) \tag{B.11}$$

Rearranging Equation B.11 and assuming constant ρ_w and C_{pw} gives:

$$q_r = \frac{R_w}{2}(\rho_w C_{pw}) V_w \frac{(T|_{z+\Delta z} - T|_z)}{\Delta z} \tag{B.12}$$

Taking the limit as $\Delta z \rightarrow 0$ gives:

$$q_r = \frac{R_w}{2}(\rho_w C_{pw}) V_w \frac{dT}{dz} \tag{B.13}$$

which is the final heat balance equation at the wire surface.

APPENDIX C

Calculations of Dimensionless Groups

This appendix shows the detailed calculations of *Re*, *Pe*, *Na* and *Gz* numbers for Endo's (Section 5.4.1) and Basu's (Section 6.4.1) dies. The determination of a reference viscosity is essential in order to calculate these quantities. The viscosity is related to the temperature through some exponential relationship. The shifting factor β for such a relationship can be a function of temperature (Endo) or a constant (Basu). The shifting of viscosity curves is achieved at constant stress, i.e.

$$\eta_2 = \eta_1 \exp[-\beta(T_2 - T_1)] \tag{C.1}$$

as illustrated in Figure C.1

C.1 Endo's Die

In order to calculate the dimensionless groups, a characteristic velocity, length and temperature have to be chosen. These are (referring to data provided in Section 5.4.1):

$$V = V_w = 2032\ cm/s \tag{C.2}$$

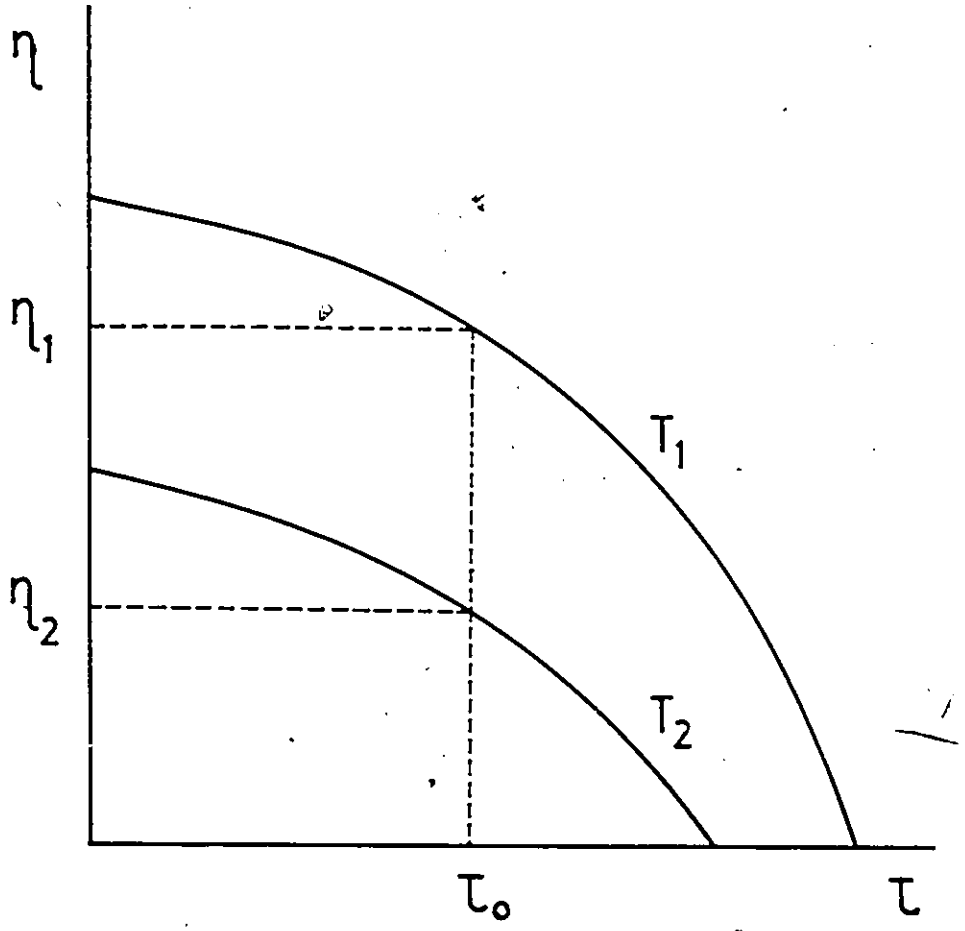

Figure C.1: Schematic Diagram Showing the Shifting of Viscosity Curves for Different Temperatures at Constant Shear Stress.

$$H = R_w = 0.0322\ cm \tag{C.3}$$

$$T = T_m = 227\ ^\circ C = 500\ K \tag{C.4}$$

where V_w is the wire speed, R_w is the wire radius and T_m is the entry melt temperature. Following that, a few additional characteristic variables are calculated at T_m:

$$\beta = \frac{E_\tau}{RT_\circ T_m} = \frac{48,900}{(8.310)(479)(500)} = 0.02457\ K^{-1} \tag{C.5}$$

$$\bar{\dot{\gamma}} = \frac{V_w}{R_w} = \frac{2032}{0.0322} = 63,100\ s^{-1} \tag{C.6}$$

$$\begin{aligned} \bar{\eta} &= m|_{T_m}\,\bar{\dot{\gamma}}^{n-1} = m|_{T_\circ} \exp\left[\frac{E_\tau}{RT_\circ T_m}(T_\circ - T_m)\right]\bar{\dot{\gamma}}^{n-1} \\ &= (0.01009)\exp[0.02457(479-500)](63,100)^{0.333-1} \\ &= 3.786 \times 10^{-6}\ MPa \cdot s = 37.86\ poise \end{aligned} \tag{C.7}$$

where $T_\circ$ is the reference temperature for the viscosity, m is the consistency index, β is the temperature shift factor, $\bar{\dot{\gamma}}$ is the characteristic shear rate, and $\bar{\eta}$ is the characteristic shear viscosity. The additional transport properties required are calculated at T_m:

$$\rho = (1.143 + 0.00089 \times 227)^{-1} = 0.7435\ g/cm^3 \tag{C.8}$$

$$C_p = 2.827\ J/g \cdot ^\circ C \tag{C.9}$$

$$k = 0.00329\ J/cm \cdot s \cdot ^\circ C \tag{C.10}$$

Finally, the dimensionless groups can be evaluated as (referring to Section 2.5 for definitions):

$$Pe = \frac{\rho C_p V_w R_w}{k} = 41,800 \quad \text{(C.11)}$$

$$Na = \frac{\beta \bar{\eta} V_w^2}{k} 0.00329 = 117 \quad \text{(C.12)}$$

$$Re = \frac{\rho V_w R_w}{\bar{\eta}} = 1.3 \quad \text{(C.13)}$$

$$Gz = Pe \cdot \frac{R_w}{L} = 1,060 \quad \text{(C.14)}$$

where L is the axial length of the die.

C.2 Basu's Die

Two polymers are involved in Basu's die: PS (polymer A) and HDPE (polymer B). The following data are available (referring to Section 6.4.1):

$$V_w = 1000\ cm/s \quad \text{(C.15)}$$

$$T_m = 170\ ^\circ C \quad \text{(C.16)}$$

$$h_A = 0.056\ cm \quad \text{(C.17)}$$

$$\beta_A = 0.03\ K^{-1} \quad \text{(C.18)}$$

$$h_B = 0.013\ cm \quad \text{(C.19)}$$

$$\beta_B = 0.01266\ K^{-1} \quad \text{(C.20)}$$

Letting the characteristic velocity be the wire speed V_w, characteristic temperature be the entry melt temperature T_m, and characteristic length be the corresponding thickness of each layer in the coated wire h, the characteristic shear rates can be calculated as:

$$\bar{\dot{\gamma}}_A = \frac{V_w}{h_A} = 17,860\ s^{-1} \tag{C.21}$$

$$\bar{\dot{\gamma}}_B = \frac{V_w}{h_B} = 76,920\ s^{-1} \tag{C.22}$$

To obtain the characteristic viscosity $\bar{\eta}$ at T_m, $\bar{\dot{\gamma}}$ must first be evaluated at T_m as follows:

$$\bar{\dot{\gamma}}|_{T_m} = \bar{\dot{\gamma}} \exp[-\beta(T_m - T_o)] \tag{C.23}$$

where T_o is the reference temperature for the viscosity. The $\bar{\eta}$ can thus be obtained by finding the root of the quadratic viscosity function as:

$$a(\log \tau)^2 + b(\log \tau) + c = 0 \tag{C.24}$$

or

$$\log \tau = \frac{-b + \sqrt{b^2 - 4ac}}{2a} \tag{C.25}$$

and

$$\bar{\eta} = \frac{\tau}{\bar{\dot{\gamma}}} \tag{C.26}$$

and the results are:

$$\bar{\dot{\gamma}}_A|_{T_m} = 17,860 \exp[-0.03(170-220)] = 80,000\ s^{-1} \quad \text{(C.27)}$$

$$\bar{\dot{\gamma}}_B|_{T_m} = 76,920 \exp[-0.01266(170-220)] = 144,800\ s^{-1} \quad \text{(C.28)}$$

and:

$$\log \tau_A = f(\bar{\dot{\gamma}}_A|_{T_m}) = 6.566 \quad \text{(C.29)}$$

$$\log \tau_B = f(\bar{\dot{\gamma}}_B|_{T_m}) = 7.104 \quad \text{(C.30)}$$

As a result,

$$\bar{\eta}_A = \tau_A/\bar{\dot{\gamma}}_A = 206\ poise = 2.06 \times 10^{-5}\ MPa \cdot s \quad \text{(C.31)}$$

$$\bar{\eta}_B = \tau_B/\bar{\dot{\gamma}}_B = 165\ poise = 1.65 \times 10^{-5}\ MPa \cdot s \quad \text{(C.32)}$$

the additional transport properties required are calculated at T_m:

$$\begin{aligned} \rho_A &= 0.9902 \ , \ \rho_B &= 0.8237 \quad g/cm^3 \\ (C_p)_A &= 2.112 \ , \ (C_p)_B &= 3.5 \quad J/g \cdot {}^\circ C \\ k_A &= 0.00128 \ , \ k_B &= 0.005 \quad J/cm \cdot s \cdot {}^\circ C \end{aligned} \quad \text{(C.33)}$$

Finally, the dimensionless groups can be evaluated as (referring to Section 2.5 for definitions):

$$\begin{aligned} Pe_A &= 91,500 \quad , \quad Pe_B = 7,500 \\ Na_A &= 483 \quad , \quad Na_B = 41.8 \\ Re_A &= 0.269 \quad , \quad Re_B = 0.0649 \\ Gz_A &= 2,110 \quad , \quad Gz_B = 40.1 \end{aligned} \tag{C.34}$$

APPENDIX D

Evaluation of Heat Transfer Coefficient

This appendix presents the evaluation of heat transfer coefficient h_T based on Acierno et al.'s experimental results (1971).

Acierno et al. (1971) reported a Nusselt number (Nu) of

$$Nu = \frac{h_T R_c}{k_{air}} = 0.72 \tag{D.1}$$

based on an integral boundary-layer analysis of forced convection of an LDPE melt extruded into the air. Assuming that the temperature on the wire surface is held constant at $350°C$ (average maximum temperature at the exit of Du Pont's die for $V_w = 2000\ cm/s$ in Figure 5.24) and the ambient temperature is at $20°C$, an arithmetic average film temperature (Holman, 1981) can be calculated as:

$$T_f = 185°C \tag{D.2}$$

or 458 K. Evaluating k_{air} at this temperature via linear interpolation yields (Holman, 1981):

$$k_{air} = 0.000376\ J/cm\,s°C \tag{D.3}$$

Knowing that the final coated wire radius is $R_c = 1.8R_w$ $(= 1.8 \times 0.032\ cm)$ allows the heat transfer coefficient h_T to be calculated:

$$h_T = 0.0047\ J/cm^2\, s°C \tag{D.4}$$